



UNIVERSITY OF  
BIRMINGHAM

# CRYSTAL GROWTH OF FUNCTIONAL OXIDES USING AN IMAGE FURNACE

By

**SEYED MOJTABA KOOHPAYEH**

A thesis submitted to the University of Birmingham for the degree of

**DOCTOR OF PHILOSOPHY**

School of Engineering  
Department of Metallurgy and Materials  
The University of Birmingham

**July 2007**

UNIVERSITY OF  
BIRMINGHAM

**University of Birmingham Research Archive**

**e-theses repository**

This unpublished thesis/dissertation is copyright of the author and/or third parties. The intellectual property rights of the author or third parties in respect of this work are as defined by The Copyright Designs and Patents Act 1988 or as modified by any successor legislation.

Any use made of information contained in this thesis/dissertation must be in accordance with that legislation and must be properly acknowledged. Further distribution or reproduction in any format is prohibited without the permission of the copyright holder.

# SYNOPSIS

The present study is concerned with the single crystal growth of functional oxides by the floating zone technique using a four mirror image furnace. This thesis attempts to extend our knowledge of the subject by firstly studying the optical floating zone method as a *technique* in terms of the experimental growth parameters and then by *performing* crystal growth and characterization on a number of functional oxides such as rutile ( $\text{TiO}_2$ ), Co-doped rutile and rare earth orthoferrite crystals ( $R\text{FeO}_3$ ,  $R=\text{Er}$  and  $\text{Y}$ ).

When growing high quality, large and homogeneous crystals using an image furnace, finding the optimum growth parameters (such as growth speed, rotation rate, gas pressure and type of atmosphere) is a crucial first step since it has been found that these parameters can all affect the eventual crystal quality and properties. Comprehensive characterization of an image furnace revealed that the growth behaviour, and consequently, the quality of the as-grown crystal, can be explained by the effects that varying these growth parameters have upon the temperature profiles within growing crystals.

Characterization of as-grown crystals has been performed using a combination of different techniques such as scanning electron microscopy, energy dispersive x-ray analysis, x-ray diffractometry, back reflection x-ray Laue, polarised optical microscopy and vibrating sample magnetometry.

The best quality  $\text{TiO}_2$  crystals were prepared when neither the growing crystal nor the feed rod were rotated during crystal growth. When rotation was employed, this was found to introduce sub-grain boundaries in crystals when the linear growth rate was low, or bubble inclusions when the linear rate was high. The use of lower molten zone temperatures was found to give pale-yellow crystals, while crystals grown using higher molten zone temperatures tended to have the blue colour characteristic of oxygen deficient material.

A study of Co-doped  $\text{TiO}_2$  single crystals, prepared from the melt using the FZ technique, revealed that Co does not dissolve into the rutile matrix and that the type of atmosphere used during FZ affects the type of cobalt-based second phases formed.

Magnetization measurements of Co-doped rutile bulk samples (both single crystals prepared using the FZ technique and polycrystalline powders prepared using a solid state reaction) also indicated that the magnetic properties depend upon the material preparation conditions. An oxygen deficient environment during the preparation of Co-doped  $\text{TiO}_2$  powders and single crystals was crucial for the observation of room temperature ferromagnetism, since preparation in oxygen rich conditions led to the formation of paramagnetic material that included the second phase  $\text{CoTiO}_3$ .

Finally, growth of  $\text{ErFeO}_3$  and  $\text{YFeO}_3$  single crystals by the FZ technique revealed that the best quality crystals were prepared when the growth rate was 6 mm/h or less, since the use of higher growth rates (12, 18 and 24 mm/h) was found to result in the formation of second phase inclusions within the crystals. The magnetic properties of these crystals, as represented by the hysteresis loops, showed that crystals of both materials grown at higher rates have significantly lower coercivities; this was attributed to the effect of the second phase in nucleating reverse magnetic domains and so aiding the demagnetization process.

# ACKNOWLEDGEMENTS

I would like to thank people who helped me to complete this study. In particular, I want to express my deepest admiration and gratitude to my supervisors, Professor J.S. Abell and Dr. D. Fort, for their intellectual inspiration, outstanding support and encouragement throughout this project. I feel deeply indebted to them, many thanks for always keeping me in the right path of my research and for pointing the obvious parts I was unable to see. In fact, I had the most rewarding three years working with my supervisors.

I am also grateful to Dr. A. Williams, Dr T.W. Button and A. Bevan for their comments, helpful discussions, and their provision of ceramic and magnetic laboratory facilities.

Many thanks are due to all of the technical staff who collaborated in this research work, with special mentions to Mr. A. Bradshaw and Mr. J. Sutton for their help, assistance and guidance.

Sincere thanks to my supervisors, EPSRC, Department of Metallurgy & Materials, and the University of Birmingham for provision of my scholarship.

Finally, I would like to thank to my family, my wife, Zahra, who has been a great support to me in my life and my research effort and our little baby daughter, *Mahshid*, who has brought joy to our life.

# CONTENTS

<b>LIST OF TABLES</b>	ix
<b>LIST OF FIGURES</b>	x
<b>ABBREVIATIONS</b>	xviii
<b>CHAPTER 1: INTRODUCCION</b>	<b>1</b>
1.1. The importance of crystal growth in science and technology	1
1.2. Scope of thesis	2
1.3. Crystal structures	3
1.3.1. Defects in crystals	5
1.4. Crystal growth phenomena	8
1.5. Historical development of crystal growth methods from melt	8
1.6. Fundamentals of the floating zone technique	11
1.6.1. Crystal growth by the floating zone technique using image furnaces	15
1.7. Magnetism	17
1.7.1. Classification of magnetic materials	17
1.7.2. Spontaneous magnetization	20
1.7.3. Magnetization and hysteresis loops	20
1.7.4. Physical origin of ferromagnetism	21
1.7.4.1. Domain walls	25
1.7.4.2. Intersection of domain walls with crystal imperfections	26
1.7.5. Units	26
<b>CHAPTER 2: LITERATURE REVIEW</b>	<b>28</b>
2.1. Influence of growth parameters when using image furnaces	28
2.1.1. Feed rod characteristics	28
2.1.2. Crystallization rate or growth speed	30
2.1.3. Growth atmosphere and gas pressure	32
2.1.4. Temperature gradient and molten zone temperature	35
2.1.5. Rotation rate	37

2.1.6. Conclusions drawn from a survey of the literature regarding FZ growth parameters and their potential effects	37
2.2. Rutile ( $\text{TiO}_2$ )	41
2.2.1. Introduction	41
2.2.2. Features of rutile single crystals	42
2.2.3. Bulk crystal growth of rutile ( $\text{TiO}_2$ )	44
2.3. Cobalt-doped $\text{TiO}_2$ and its magnetic properties	46
2.3.1. Introduction	46
2.3.2. Current state of affairs	47
2.3.3. Magnetic properties of Co-doped $\text{TiO}_2$ bulk samples	48
2.4. Rare earth orthoferrites	52
2.4.1. Introduction	52
2.4.2. Features of orthoferrites	52
2.4.3. Bulk crystal growth of rare earth orthoferrites	56
2.4.3.1. Phase diagram information for rare earth orthoferrites	56
2.4.3.2. Growth of rare earth orthoferrites by the flux method	57
2.4.3.3. Growth of rare earth orthoferrites by the Czochralski and Bridgman techniques	59
2.4.3.4. Growth of rare earth orthoferrites by the floating zone method	60
2.5. Summary of conclusions reached from the literature review	61
2.5.1. Image furnace characterization	61
2.5.2. $\text{TiO}_2$	61
2.5.3. Co-doped $\text{TiO}_2$	61
2.5.4. Rare earth orthoferrites	62
<b>CHAPTER 3: EXPERIMENTAL PROCEDURES</b>	<b>63</b>
3.1. Introduction	63
3.2. Materials and feed rod preparation	63
3.2.1. Rutile ( $\text{TiO}_2$ ) feed rods	63
3.2.2. Co-doped $\text{TiO}_2$ (rutile) powders and feed rods	64
3.2.3. Orthoferrite ( $R\text{FeO}_3$ , $R=\text{Y}$ and $\text{Er}$ ) feed rods	64
3.3. Crystal growth	66
3.3.1. The optical floating zone furnace (image furnace)	66
3.4. Sample characterization techniques	68

3.4.1. Back-reflection X-ray Laue technique	68
3.4.1.1. Cutting aligned single crystals	71
3.4.2. X-ray diffractometry	72
3.4.3. Optical microscopy	73
3.4.4. Scanning electron microscopy (SEM)	74
3.4.5. Magnetization measurements	76
3.4.6. Density measurements	77
<b>CHAPTER 4: FZ SYSTEM CHARACTERIZATION (RESULTS AND DISCUSSION)</b>	<b>78</b>
4.1. Introduction	78
4.2. Temperature	78
4.3. Effect of lamp power on the temperature distribution	81
4.4. Effect of gas type on the temperature distribution	82
4.5. Effect of gas pressure on the temperature distribution	84
4.6. Effect of zoning rate on the temperature distribution	87
4.7. Temperature characterization of the FZ system using density measurements	89
4.8. Effect of gas pressure on sample temperatures	91
4.9. Summary of FZ system characterization and likely influences of growth parameters related to 'temperature' profiles	91
<b>CHAPTER 5: RUTILE (RESULTS AND DISCUSSION)</b>	<b>95</b>
5.1. Introduction	95
5.2. Feed rod preparation	95
5.3. Crystal growth	96
5.4. Influence of growth parameters	97
5.4.1. Effect of growth rate	97
5.4.2. Effect of oxygen pressure	101
5.4.3. Effect of rotation rate	102
5.4.4. Effect of molten zone temperature	106
5.5. Summary	109
<b>CHAPTER 6: CO-DOPED RUTILE (RESULTS AND DISCUSSION)</b>	<b>110</b>
6.1. Introduction	110
6.2. Co-doped TiO <sub>2</sub> powders	111



6.2.1. Preparation of Co-doped TiO <sub>2</sub> powders	111
6.2.2. Magnetic properties of Co-doped rutile powders	114
6.3. Co-doped rutile single crystals	115
6.3.1. Feed rod preparation	115
6.3.2. Crystal growth	116
6.3.3. Magnetic properties of Co-doped rutile single crystals	126
6.4. Summary	130
<b>CHAPTER 7: RARE EARTH ORTHOFERRITES (RESULTS AND DISCUSSION)</b>	<b>131</b>
7.1. Introduction	131
7.2. Erbium orthoferrite (ErFeO <sub>3</sub> )	131
7.2.1. Feed rod preparation of ErFeO <sub>3</sub>	131
7.2.2. Crystal growth	135
7.2.2.1. Effect of growth rate on the microstructure of ErFeO <sub>3</sub>	137
7.2.2.2. Effect on crystal quality of increasing oxygen pressure to 5 bar	142
7.2.2.3. Effect of reducing the rotation rate of growing crystal to zero	144
7.2.3. Magnetic properties of ErFeO <sub>3</sub> crystals	145
7.2.3.1. Effect of growth rate on magnetic properties	146
7.2.3.2. Effect of increasing the oxygen pressure during FZ growth on magnetic properties	149
7.2.3.3. Magnetocrystalline anisotropy measurements of ErFeO <sub>3</sub> single crystals	150
7.3. Yttrium orthoferrite (YFeO <sub>3</sub> )	152
7.3.1. Feed rod preparation	152
7.3.2. Crystal growth	152
7.3.2.1. Effect of growth rate on the microstructure of YFeO <sub>3</sub> crystals	154
7.3.2.2. Effect of increasing the oxygen pressure to 5 bar during FZ	156
7.3.2.3. Effect of reducing the rotation rate of the growing crystal to zero	157
7.3.3. Magnetic properties of YFeO <sub>3</sub> crystals	158
7.3.3.1. Effect of growth rate on magnetic properties	158
7.3.3.2. Magnetocrystalline anisotropy measurements of YFeO <sub>3</sub> single crystals	158
7.4. Summary	160
<b>CHAPTER 8: CONCLUSIONS AND FUTURE WORK</b>	<b>161</b>
8.1. Conclusions	161

8.1.1. Image furnace characterization	161
8.1.2. Rutile ( $\text{TiO}_2$ )	162
8.1.3. Co-doped $\text{TiO}_2$	163
8.1.4. Rare earth orthoferrites ( $R\text{FeO}_3$ , $R=\text{Er}$ and $\text{Y}$ )	164
8.2. Suggestions for future work	165
8.2.1. FZ system characterization	165
8.2.2. Rutile	165
8.2.3. Co-doped rutile	166
8.2.4. Rare earth orthoferrites ( $R\text{FeO}_3$ , $R=\text{Er}$ and $\text{Y}$ )	166
<b>Appendix A.</b> Summary of the crystals grown by the FZ method using image furnaces since 1990 with particular reference to the growth conditions	168
<b>Appendix B.</b> Summary of findings from Co-doped $\text{TiO}_2$ thin films	182
<b>Appendix C.</b> Publications resulting from the work described in this thesis	190
<b>References</b>	191

# LIST OF TABLES

<b>Table 1.1.</b> The 14 Bravais lattices	4
<b>Table 1.2.</b> Summary of different types of magnetic behaviour	19
<b>Table 2.1.</b> Bulk properties of rutile ( $\text{TiO}_2$ )	43
<b>Table 2.2.</b> Crystallographic constants of orthoferrites ( $R\text{FeO}_3$ )	54
<b>Table 2.3.</b> Thermal expansion of $\text{ErFeO}_3$ and $\text{YFeO}_3$ lattice parameters	54
<b>Table 2.4.</b> The Neel temperature in rare earth orthoferrites	55
<b>Table 4.1.</b> Lamp power required to melt different copper rods	79
<b>Table 5.1.</b> EDX analysis of yellow and blue rutile single crystals	108
<b>Table 7.2.</b> EDX analysis results from the inclusion shown in Fig. 7.9. The results are given in terms of both atomic % and as a formula normalized to give a Fe value of unity.	140
<b>Table 7.2.</b> Summary of the defects produced at different growth conditions in $\text{ErFeO}_3$	142

# LIST OF FIGURES

<b>Fig.1.1.</b> Diagram of low-angle grain boundary made up of an array of dislocations	7
<b>Fig.1.2.</b> Modification of Verneuil's principles of nucleation control and increasing crystal diameters in other crystal-growth techniques [2]	9
<b>Fig.1.3.</b> Scheme of the floating zone technique, (a) formation of the molten zone, (b) and (c) growth by moving the molten zone through the feed rod	12
<b>Fig.1.4.</b> Schematic of a pseudobinary phase diagram for incongruent and congruent melting materials (left), and the travelling solvent floating zone technique (TSFZ) to grow an incongruent melting material (right)	14
<b>Fig.1.5.</b> Schematic illustration of the optical floating zone melting with one ellipsoidal mirror	16
<b>Fig.1.6.</b> Hysteresis loop for a ferro- or ferrimagnet	21
<b>Fig.1.7.</b> Reduction of the magnetostatic energy by domain formation in a ferromagnet, (a) single domain, (b) two domains, (c) four domains and (d) closure domains	23
<b>Fig.1.8.</b> The magnetocrystalline anisotropy of cobalt	24
<b>Fig.1.9.</b> Schematic representation of a 180° domain wall	25
<b>Fig.2.1.</b> The tetragonal crystal structure of rutile; unit cell dimensions: $a=b=4.584 \text{ \AA}$ , $c=2.953 \text{ \AA}$ [181]	42
<b>Fig.2.2.</b> Phase diagram of the Ti-O system. The region $\text{Ti}_2\text{O}_3\text{-TiO}_2$ contains $\text{Ti}_2\text{O}_3$ , $\text{Ti}_3\text{O}_5$ , seven discrete phases of $\text{Ti}_n\text{O}_{2n-1}$ (Magneli phases: homologous series of shear structures in phase regions previously believed to be continuous solid solutions) and $\text{TiO}_2$ [185]	44
<b>Fig.2.3.</b> Magnetization vs. magnetic field curves at room temperature for $\text{Ti}_{1-x}\text{Co}_x\text{O}_2$ powders, (a) ref. [224] and (b) ref. [225]	50
<b>Fig.2.4.</b> Solubility limits of different transition metal ions in anatase and rutile thin films [228]	51
<b>Fig.2.5.</b> phase relations in the system $\text{CoO-TiO}_2$ [229]	51
<b>Fig.2.6.</b> Crystal structure of orthoferrites ( $\text{RFeO}_3$ ) [250]	53
<b>Fig.2.7.</b> Magnetization curves of $\text{ErFeO}_3$ (left) and $\text{YFeO}_3$ (right) single crystals grown by the flux technique [255]	55
<b>Fig.2.8.</b> Phase diagrams of (a) $\text{ErFeO}_3$ [256] and (b) $\text{YFeO}_3$ [257]	56
<b>Fig.3.1.</b> Experimental layout of the present investigation	63

<b>Fig.3.2.</b> Photographs of the hydraulic press and furnaces used to prepare feed rods	65
<b>Fig.3.3.</b> Schematic of the four mirror image furnace	66
<b>Fig.3.4.</b> Four mirror image furnace in two views, (a) outside and (b) and inside	67
<b>Fig.3.5.</b> Schematic of the optical FZ technique with more attention to the shafts, sample holders and movements	68
<b>Fig.3.6.</b> Scheme of the Laue technique in the back-reflection geometry	69
<b>Fig.3.7.</b> A typical map including Laue patterns prepared for rutile crystals	70
<b>Fig.3.8.</b> Schematic of a goniometer on the X-ray Laue set. Once aligned the crystal, still on the goniometer, was transferred to the cutter.	71
<b>Fig.3.9.</b> Photograph of the diamond blade cutter, used to prepare oriented samples from as-grown single crystals.	72
<b>Fig.3.10.</b> Scanning electron microscopy used in this study	76
<b>Fig.3.11.</b> VSM and detection coil set-up	77
<b>Fig.4.1.</b> Pt-13%Rh thermocouple set up for temperature measurements	80
<b>Fig.4.2.</b> Temperature vs. distance plots measured from the position of maximum temperature down the $\text{YFeO}_3$ sample at different lamp powers (10, 20, 30, 40 and 50%). Increasing the lamp power increases the temperature nonlinearly along the sample. All measurements were performed at zoning rate of 20 mm/h under 1 bar oxygen pressure.	81
<b>Fig.4.3.</b> Average increase in temperature vs. lamp power; the higher is the applied power the larger is the temperature gradient along the sample.	82
<b>Fig.4.4.</b> Temperature profiles at different atmospheres. All measurements were performed at zoning rate of 20 mm/h and lamp power of 30%. The pressure was 1 bar for oxygen, helium and argon, while the pressure in vacuum condition was $1.3 \times 10^{-5}$ bar.	83
<b>Fig.4.5.</b> Effect of increasing the lamp power (from 30.0 to 34.5%) on the temperature profile for helium. All measurements were performed at zoning rate of 20 mm/h and the pressure of 1 bar.	83
<b>Fig.4.6.</b> Temperature distributions along the growth axis at two different oxygen pressures of 1 and 5 bar. These experiments were performed at the same zoning rate of 10 mm/h and 30% of lamp power. Increasing the oxygen pressure in the growth chamber decreases the temperature along the sample.	84
<b>Fig.4.7.</b> Temperature distribution curves along the growth axis under two oxygen pressures of 1 bar (at 30% lamp power) and 5 bar (at 32% lamp power). Increasing the lamp power by 2% under 5 bar oxygen pressure equalizes the maximum temperature, but it does not match the temperature	

distribution along the sample for the run under 1 bar and 30% lamp power. These experiments were performed at zoning rate of 10 mm/h. 85

**Fig.4.8.** Differential temperature curve measured from the temperature profiles for two oxygen pressures of 1 bar (at 30% lamp power) and 5 bar (at 32% lam power). Although increasing the lamp power by 2% equalizes the hottest zone temperature, a differential temperature between the profiles of up to 90 °C is still observed at distances a few millimeters from the hottest zone. 86

**Fig.4.9.** Temperature distribution along the growth axis at two different zoning rates of 10 and 20 mm/h. These experiments were performed under 1 bar oxygen pressure and 30% lamp power. 88

**Fig.4.10.** Temperature distribution along the growth axis at two different zoning rates of 10 and 20 mm/h. These experiments were performed under 5 bar oxygen pressure and 30% lamp power. 88

**Fig.4.11.** Density of  $\text{YFeO}_3$  polycrystalline rods sintered at different temperatures 89

**Fig.4.12.** Changes in density along  $\text{YFeO}_3$  polycrystalline rods heated at 55% of the lamp power at two oxygen pressures of 1 and 5 bar. Increasing the gas pressure gives lower density rods as a result of decreasing the temperature in the sample (temperature data were obtained from Fig.4.11). 90

**Fig.4.13.** A schematic of the optical FZ technique in two stages, before growth and during growth 92

**Fig.5.1.** XRD patterns from the starting  $\text{TiO}_2$  powder (in anatase structure) and after sintering at 1600 °C for 8h in air, which changed it to the rutile structure. 96

**Fig.5.2.** A typical as-grown rutile single crystal (left) and a view through a longitudinal section cut from such a crystal (right) to illustrate its transparency (the writing is below the crystal). 97

**Fig.5.3.** XRD from a crushed rutile single crystal 97

**Fig.5.4.** Polarised light photographs (taken in transmission mode) of polished cross sections of as-grown rutile crystals prepared using different growth rates (left) with corresponding back reflection Laue pictures taken from the crystals (right). The growth rates used were 5, 10, 15, 20 and 27 mm/h. For all of these growths, the oxygen pressure was  $5 \times 10^5$  Pa and the rotation rate was 30 rpm. At lower growth rates, subgrain boundaries are evident together with spot splitting on the Laue photographs. Higher growth rates gave better quality pictures, but the samples contain bubbles. 99

**Fig.5.5.** Growth direction of rutile crystals grown at growth rates of 5 and 20 mm/h. The growth rate did not affect significantly on the growth direction. 100

- Fig.5.6.** X-ray rocking curve of the (200) Bragg diffraction peak measured on the rutile single crystal grown at 27 mm/h (Fig. 5.4e). 100
- Fig.5.7.** Polarised light transmission micrographs of rutile crystals illustrating the effect of changing the oxygen pressure during growth at two different pull rates. The upper two micrographs were from crystals grown at 5 mm/h under an oxygen pressure of  $1 \times 10^5$  Pa (left) and  $5 \times 10^5$  Pa (right). The lower micrographs were from crystals grown at 20 mm/h under an oxygen pressure of  $1 \times 10^5$  Pa (left) and  $5 \times 10^5$  Pa (right). For all four growths, the rotation rate was 30 rpm. 101
- Fig.5.8.** Polarised light transmission micrographs of longitudinal sections from rutile crystals grown at rotation rates of 0, 5, 10, 20 and 30 rpm. The same growth rate of 27 mm/h and oxygen pressure of  $1 \times 10^5$  pa was used for all these crystals. Increasing the rotation rate clearly increased the number of bubbles within the crystals. 103
- Fig.5.9.** Polarised light transmission micrograph from a cross section (left) and X-ray Laue picture from the surface (right) of an as-grown rutile crystal prepared at a rate of 5 mm/h with zero rotation, under  $1 \times 10^5$  Pa oxygen. 104
- Fig.5.10.** Diagram illustrating the interrelationship between the growth and rotation rates and the defects found in rutile crystals grown using the image furnace. 104
- Fig.5.11.** Rutile crystal grown at a lower temperature using 71 % of the available halogen lamp power (left) showing a pale yellow colour and a similar crystal grown at a higher temperature using 75 % of the available halogen lamp power (right), which is blue in colour. 108
- Fig.6.1.** XRD patterns taken from  $\text{CoO}+\text{TiO}_2$  (anatase) powder synthesized at  $1100^\circ\text{C}$  for 8 h in oxygen. The Co content varied from 2 to 8% with respect to titanium. XRD reference data for rutile and  $\text{CoTiO}_3$  are also given. These patterns show that synthesized powders mainly comprise the rutile structure with small amounts of  $\text{CoTiO}_3$  second phase. 112
- Fig.6.2.** XRD patterns taken from  $\text{Co}+\text{TiO}_2$  (anatase) powder synthesized at  $1100^\circ\text{C}$  for 8 h in vacuum. The Co content varied from 2 to 8% with respect to titanium. These patterns show that the material has the rutile structure with no detectable segregation of other phases such as Co, cobalt oxides,  $\text{CoTiO}_3$  and  $\text{CoTi}_2\text{O}_5$ . 113
- Fig.6.3.** Magnetization measurements performed on powders synthesized in oxygen and vacuum for Co contents between 2 and 8% shown in Fig. 6.1 and Fig. 6.2 respectively. 115

- Fig.6.4.** Backscattered images taken from the cross sections of the feed rod ( $\text{TiO}_2 + \text{CoTiO}_3$ ) with the Co content of 8% near to the molten zone, the molten zone and growing crystal at the beginning of growth procedure. 117
- Fig.6.5.** Typical 4%Co: $\text{TiO}_2$  single crystals grown in oxygen (a) and argon (b). These growths were carried out under 5 bar gas pressure at a growth rate of 5 mm/h, with rotation rates of 15 rpm for the growing crystal and 0 rpm for the feed rod. 118
- Fig.6.6.** Laue diffraction photographs taken from the cross and longitudinal sections of the crystals grown in oxygen (a) and in argon (b). These X-ray Laue pictures indicated that both crystals exhibited an equally high crystalline quality, and the growth direction was [001]. 118
- Fig.6.7.** The XRD pattern taken from the crushed 4%Co-doped  $\text{TiO}_2$  single crystal grown under 5 bar oxygen pressure 119
- Fig.6.8.** The XRD pattern taken from the crushed 4%Co-doped  $\text{TiO}_2$  single crystal grown under 5 bar argon pressure 120
- Fig.6.9.** SEM back scattered micrographs of a *cross section* cut from a 4%Co: $\text{TiO}_2$  single crystal grown at 5 mm/h in *oxygen*. Growth in oxygen led to the formation Co-Ti-O phases which were identified as  $\text{CoTiO}_3$  by XRD (Fig. 6.8). EDX chemical mapping images are also given. 122
- Fig.6.10.** SEM back scattered micrographs of a *longitudinal section* cut from a 4%Co: $\text{TiO}_2$  single crystal grown at 5 mm/h in *oxygen*. Growth in oxygen led to the formation Co-Ti-O phases which were identified as  $\text{CoTiO}_3$  by XRD. EDX chemical mapping images are also given. 123
- Fig.6.11.** SEM back scattered micrographs of a *cross section* cut from a 4%Co: $\text{TiO}_2$  single crystal grown at 5 mm/h in *argon*. Growth in argon led to the formation Co rich particles. EDX chemical mapping images are also given. 124
- Fig.6.12.** SEM back scattered micrographs of a *longitudinal section* cut from a 4%Co: $\text{TiO}_2$  single crystal grown at 5 mm/h in *argon*. Growth in argon led to the formation Co rich particles oriented along the growth direction. EDX chemical mapping images are also given. 125
- Fig.6.13.** M-H curves measured at room temperature for 4%Co: $\text{TiO}_2$  (rutile) crystals grown in oxygen and argon. Room temperature ferromagnetism with magnetization  $0.24 \text{ Am}^2 \text{ kg}^{-1}$  ( $\sim 0.083 \mu_B/\text{Co atom}$ ) was observed in crystals grown in argon, while a weak paramagnetic behaviour was obtained from crystals grown in oxygen. 126
- Fig.6.14.** Preparation routs and magnetic properties of Co-doped rutile powders and single crystals 127



- Fig.7.1.** Effect of calcining temperature and time for converting the constituents to the  $\text{ErFeO}_3$  structure. The starting materials were thoroughly ground and mixed for 2 h by hand. 132
- Fig.7.2.** (a) XRD reference data for  $\text{ErFeO}_3$ , and (b) XRD patterns taken from the starting materials,  $\text{Er}_2\text{O}_3$  and  $\text{Fe}_2\text{O}_3$ , and  $\text{ErFeO}_3$  synthesized at  $1200^\circ\text{C}$  for 20h. 133
- Fig.7.3.** XRD patterns taken from  $\text{ErFeO}_3$  powders synthesized at  $1200^\circ\text{C}$  for 20 h, as a function of different mixing times for the starting materials. 134
- Fig.7.4.** The formation of a large bubble which was led to collapse the molten zone during crystal growth of  $\text{ErFeO}_3$  using low compacted feed rods sintered at  $1500^\circ\text{C}$ . 135
- Fig.7.5.** Molten zone shapes during crystal growth of  $\text{ErFeO}_3$ , (a) when only the mirror moves, and (b) when both the feed rod and mirror move at the same direction 136
- Fig.7.6.** A typical  $\text{ErFeO}_3$  single crystal grown using the four mirror image furnace (left), and a Laue diffraction taken from the cross section of the crystal (right) showing the high quality of the crystal with  $[391]$  as the growth direction. 137
- Fig.7.7.** SEM image taken from the surface of  $\text{ErFeO}_3$  crystal where the growth rate has been changed from 12 mm/h to 18 mm/h. As the growth rate increases the surface becomes rough and non uniform. 138
- Fig.7.8.** SEM back scattered micrographs of cross sections cut from  $\text{ErFeO}_3$  crystals grown at (a) 3 mm/h, (b) 6 mm/h, (c) 12 mm/h, (d) 18 mm/h and (e) 24 mm/h. Increasing the growth speed resulted in the formation of second phase inclusions in the crystals. All these experiments were performed under 1 bar oxygen pressure, with rotation rates of 15 rpm for the growing crystal and 0 rpm for the feed rod. 139
- Fig.7.9.** A typical back scattered SEM micrograph taken from  $\text{ErFeO}_3$  crystal grown at a higher zoning rate (24 mm/h) showing in greater detail one of the inclusions within the  $\text{ErFeO}_3$  matrix. This inclusion has two areas (lighter and darker) of different compositions as measured by EDX. 140
- Fig.7.10.** Back scattered images of cross sections cut from  $\text{ErFeO}_3$  crystals grown under 5 bar oxygen pressure at 6, 12 and 18 mm/h. Increasing the gas pressure added defects such as second phases (in the crystal grown at 6 mm/h) and cracks (in crystals grown at 12 and 18 mm/h). Rotation rates of 15 rpm for the growing crystal and 0 rpm for the feed rod were applied during these experiments. 143

<b>Fig.7.11.</b> Back scattered images of cross sections cut from $\text{ErFeO}_3$ crystals grown with rotation rate of zero for both the growing crystal and the feed rod. These experiments were performed under 1 bar oxygen pressure at 6, 12, 18 and 24 mm/h. Reducing the rotation rate to zero led to cracks in all crystals.	145
<b>Fig.7.12.</b> (a) Magnetization curves and (b) coercivity measurements for disk shaped samples cut directly from the cross sections of $\text{ErFeO}_3$ crystals grown at different rates. During these measurements, the [391] direction within the disk was parallel to the field. The errors indicated in the coercivity values are due to sample alignment uncertainties during the magnetization measurements.	146
<b>Fig.7.13.</b> Magnetization vs. field plots along the principal crystallographic directions for $\text{ErFeO}_3$ single crystals grown at 6 and 12 mm/h. When the field is along the 'c' direction, the slower grown crystal shows a significantly wider hysteresis loop compared to the faster grown crystal.	147
<b>Fig.7.14.</b> Magnetization measurements at 0.4 MA/m between room temperature and $600^\circ\text{C}$ from crystals grown at 6 mm/h and 12 mm/h	149
<b>Fig.7.15.</b> Magnetization vs. field plots along the principal crystallographic directions for $\text{ErFeO}_3$ single crystals grown at 6 mm/h under two oxygen pressures of 1 and 5 bar	150
<b>Fig.7.16.</b> Magnetocrystalline anisotropy of high quality $\text{ErFeO}_3$ crystals grown at 6 mm/h under 1 bar oxygen pressure with rotation rate of 15 rpm for the growing crystal	151
<b>Fig.7.17.</b> Magnetization and coercivity values for $\text{ErFeO}_3$ crystals measured from Fig. 7.16	151
<b>Fig.7.18.</b> XRD pattern taken from $\text{YFeO}_3$ powder after calcining at $1200^\circ\text{C}$ for 20 h (left), and XRD reference data for $\text{YFeO}_3$ (right)	152
<b>Fig.7.19.</b> Density values for $\text{YFeO}_3$ feed rods sintered at $1500\text{-}1700^\circ\text{C}$	153
<b>Fig.7.20.</b> A typical molten zone obtained during crystal growth of $\text{YFeO}_3$	153
<b>Fig.7.21.</b> A typical as grown $\text{YFeO}_3$ single crystal together with X-ray Laue diffraction patterns, taken from the surface and cross section, indicating the high quality of this crystal	154
<b>Fig.7.22.</b> Back scattered SEM images taken from the polished cross sections of $\text{YFeO}_3$ crystals (left) grown at 3, 6, 12 and 18 mm/h. SEM pictures taken from the surface of each crystal (middle images) along with X-ray Laue diffraction patterns (right) are also shown. All these experiments were performed under 1 bar oxygen pressure with rotation rate of 15 rpm for the growing crystal and 0 rpm for the feed rod.	155

**Fig.7.23.** Backscattered SEM images of cross sections cut from  $\text{YFeO}_3$  crystals grown under 5 bar oxygen pressure at 3, 6, 12 and 18 mm/h. Increasing the gas pressure caused the formation of defects such as second phases (crystal grown at 6 mm/h) and cracks (crystals grown at 12 and 18 mm/h). Rotation rates of 15 rpm for the growing crystal and 0 rpm for the feed rod were applied during these experiments. 156

**Fig.7.24.** Magnetization vs. field plots measured from  $\text{YFeO}_3$  crystals grown at 3 and 12 mm/h. The slower grown crystal shows a wider hysteresis loop compared to the faster grown crystal. 158

**Fig.7.25.** Magnetocrystalline anisotropy of high quality  $\text{YFeO}_3$  crystals grown at 3 mm/h under 1 bar oxygen pressure with rotation rate of 15 rpm for the growing crystal 159

**Fig.7.26.** Magnetization and coercivity values for  $\text{YFeO}_3$  crystals measured from Fig. 7.25 159

# ABBREVIATIONS

FZ = Floating Zone

TSFZ = Travelling Solvent Floating Zone

XRD = X-ray Diffraction

FWHM = Full Width at Half Maximum

SEM = Scanning Electron Microscopy

SE = Secondary Electron

BSE = Back Scattered Electron

EDX/EDS = Energy Dispersive X-ray Spectroscopy

EBSD = Electron Back Scattered Diffraction

TEM = Transmission Electron Microscopy

VSM = Vibrating Sample Magnetometer

FM = Ferromagnetism

R = Rare earth

RT = Room Temperature

V = Velocity

T = Tesla, Temperature

$T_m$  = Melting temperature

$T_c$  = Curie temperature, Superconducting transition temperature

$T_N$  = Neel temperature

M = Magnetization

B = Magnetic induction

$B_s$  = Saturation induction

$B_r$  = Residual induction

H = Applied magnetic field

$H_c$  = Coercivity

$\chi$  = Susceptibility

$\mu_B$  = Bohr magneton

$\alpha$  = Thermal expansion coefficient

rpm = Revolutions per minute

# CHAPTER 1: INTRODUCTION

## 1.1. The importance of crystal growth in science and technology

The discovery and development of novel, complex materials with interesting and potentially useful properties is crucial to scientific progress and economic growth. Indeed, science is increasingly charted by the discovery and development of new materials, while several recent Nobel prizes (e.g. quantum hall effects, conducting polymers and high temperature superconductors) have resulted from the synthesis and development of materials with exciting properties.

History indicates that the discovery process is often driven by purely scientific interests, with the technological benefit being realized at a later time. Virtually every modern technology is materials limited; for example, the properties of the materials currently in use limit the switching speeds in computers, the optical transmission of digitized light signals, the magnetic memory density in computers and the temperature, current and magnetic field at which a superconductor can function in electric power generation and distribution.

Thus, research into advanced, often complex, materials with enhanced properties is paramount in the agenda of condensed matter physicists, materials scientists and chemists, while the ability to make high quality single crystals of advanced materials is often one of the critical steps on the path to achieve a material's full functionality as well as to completely elucidate its properties. Using good quality, homogenous single crystal forms of material is the best way to determine comprehensively the physical, chemical and structural properties of a crystalline phase together with any anisotropic characteristics. Indeed, it could be argued that the provision of high quality single crystals is the key to the future of much condensed matter science, for without them only a limited understanding of fundamental physical properties of crystalline materials can be achieved.

Thus, despite major world wide investment in *characterization* facilities to investigate the properties of new materials, the productivity of these facilities and their researchers is often limited by the ready availability of newly discovered *materials* particularly in the form of high quality crystals. Despite this clear link between groups that grow high

quality crystals of novel bulk materials and groups that perform specialized characterization measurements, an imbalance has arguably developed between the supply and demand for crystals, a disparity exacerbated by the shortage of specialists and crystal growth laboratories. The negative consequences of such an imbalance have been recognized by some countries. Japan, in particular, has invested in major crystal growth facilities such as the Institute of Solid State Physics at the University of Tokyo which houses about 15 optical floating-zone furnaces and the Universities of Tohoku, Kyoto, and Nagoya which each operate five such furnaces. Furthermore, a new “Center for Crystal Science and Technology” was recently established at Yamanashi University.

With commendable foresight for the time, the University of Birmingham set up a specialist crystal growth unit as far back as the 1960s with the initial aim of preparing high purity crystals of the rare earth metals. By the new millennium this remit had broadened to encompass the vast majority of metallic elements, alloys and intermetallic compounds using a variety of crystal growth techniques including Bridgman, Czochralski, flux growth, tri-arc and float zoning.

In 2002, the group acquired a crystal growth image furnace which gave it the means to expand its activities from almost exclusively metallic systems to non-conductors, such as oxides. To fully exploit the potential of this new equipment, it was decided to initially spend some time characterizing the furnace, both from an experimental point of view and via a thorough review of the relevant literature. This seemed an ideal project for a PhD student; thus, the studies described in this thesis commenced in 2003.

The material chosen for the initial tests on the equipment was rutile ( $\text{TiO}_2$ ) as it was presumed that this would be a relatively straightforward compound with which to take a first step with the ‘new’ technology; indeed, the image furnace manufacturers had used rutile to demonstrate the equipment when they commissioned it. This presumption, however, proved to be far from the case....

## **1.2. Scope of thesis**

This thesis reports the float-zone (FZ) growth and characterization of crystals of functional oxides such as  $\text{TiO}_2$ , Co-doped  $\text{TiO}_2$  and orthoferrites  $R\text{FeO}_3$  ( $R=\text{Er}$  and  $\text{Y}$ ).

For this purpose, the thesis is divided into eight chapters as follows:

Chapter 1 (*introduction*) contains information regarding crystal structures, crystal growth phenomena, growth techniques from melt, the floating zone method, crystal growth using image furnaces and finally a description of the magnetic properties of materials.

The *literature review* in chapter 2 covers four subject areas. The first part of the chapter reports the influence of those FZ growth parameters (growth speed, gas pressure, type of atmosphere, rotation rate, temperature and feed rod characteristics) that have been identified as being most important in reports of crystal growths using the image furnace technique; (As part of this review appendix A lists almost all the reported crystal growths using the image furnace).

The second section reviews the *crystal growth of rutile* ( $\text{TiO}_2$ ) and describes the typical defects which have been reported during the FZ growth of this material. Following this is an overview of the literature concerning bulk crystalline samples of *cobalt-doped  $\text{TiO}_2$*  and their magnetic properties, while the literature survey concludes with the crystal growth history of *orthoferrite crystals* along with their basic magnetic properties.

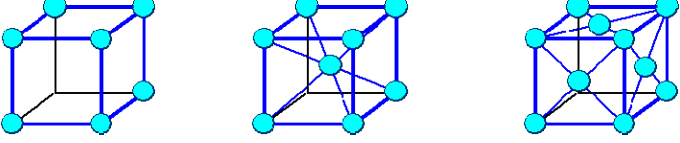

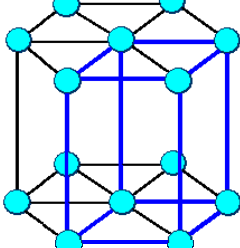
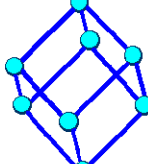
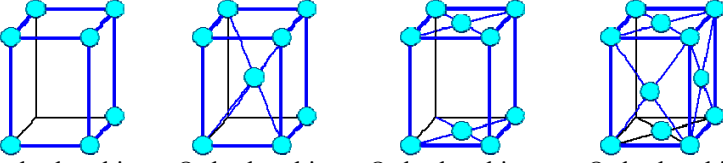

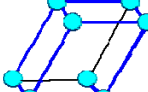
The *experimental procedures* used in this work are described in chapter 3, which deals with the techniques used to perform the crystal growth and characterization of the above materials.

Chapters 4-7 present the *results and discussion* and follow the four main topic areas described in the literature review. Thus, these chapters cover firstly the characterization of the FZ equipment (chapter 4), followed by the systematic growth, preparation and characterization of bulk crystalline oxides of  $\text{TiO}_2$  (chapter 5), Co-doped  $\text{TiO}_2$  (chapter 6) and orthoferrites  $R\text{FeO}_3$ ,  $R=\text{Er}$  and  $\text{Y}$ , (chapter 7). Finally, *conclusions* have been drawn in chapter 8 and suggestions are given for *future work*.

### 1.3. Crystal structures

An ideal crystal is a repetition of identical structural units in three dimensional space. The periodicity is described by a crystal lattice, which is a mathematical description of points at specific coordinates in space. The classification of lattices according to basic symmetry groups yields the 14 *Bravais lattices*, which are commonly used to describe lattice types as shown in Table 1.1.

**Table 1.1.** The 14 Bravais lattices

Crystal system and base vectors	Angles between axes	Bravais Lattices
Cubic $a_1 = a_2 = a_3$	$\alpha = \beta = \gamma = 90^\circ$	 <p>cubic primitive      cubic body centered (bcc)      cubic face centered (fcc)</p>
Tetragonal $a_1 = a_2 \neq a_3$	$\alpha = \beta = \gamma = 90^\circ$	 <p>Tetragonal primitive      Tetragonal body centered</p>
Hexagonal $a_1 = a_2 \neq a_3$	$\alpha = \beta = 90^\circ$ $\gamma = 120^\circ$	 <p>Hexagonal (elementary cell continued to show hex. symmetry)</p>
Rhombohedral $a_1 = a_2 = a_3$	$\alpha = \beta = \gamma \neq 90^\circ$	 <p>Rhombohedral</p>
Orthorhombic $a_1 \neq a_2 \neq a_3$	$\alpha = \beta = \gamma \neq 90^\circ$	 <p>Orthorhombic primitive      Orthorhombic body centered      Orthorhombic base face centered      Orthorhombic face centered</p>
Monoclinic $a_1 \neq a_2 \neq a_3$	$\alpha = \beta = 90^\circ$ $\gamma \neq 90^\circ$	 <p>Monoclinic primitive      Monoclinic base face centered</p>
Triclinic $a_1 \neq a_2 \neq a_3$	$\alpha \neq \beta \neq \gamma \neq 90^\circ$	



All possible lattices can be described by a set of three linearly independent vectors  $\underline{a}_1$ ,  $\underline{a}_2$ , and  $\underline{a}_3$ , the unit vectors of the lattice, and a set of integers  $k$ ,  $l$  and  $m$  so that each lattice point, identified by a vector  $\mathbf{r}$ , can be obtained from:

$$\mathbf{r} = k \mathbf{a}_1 + l \mathbf{a}_2 + m \mathbf{a}_3$$

Following the discovery of the diffraction of X-rays by metallic crystals by Von Laue in 1912, the use of diffraction techniques (X-ray, neutron and electron) has become of great importance in the analysis of crystal structures. Not only can they reveal the main features of the lattice structure, i.e. the lattice parameters and type of structure, but also other details such as the arrangement of different kinds of atoms in crystals, the presence of imperfections, sub-grains and grain sizes, the orientation and the degree of any lattice distortion.

### 1.3.1. Defects in crystals

The term *defect* is generally used to describe any deviation from an orderly array of lattice points in crystals. It is an unfortunate fact that however well they are prepared, all crystals contain defects. Imperfections that have influence on the physical and mechanical properties of a crystal can arise from defects in the crystalline structure or from chemical impurities or inclusions.

The deviation from the periodic arrangement of the lattice can be localized to the vicinity of only a few atoms, such as point defects (vacancies or mis-placed atoms) or it can extend through microscopic regions of the crystal (for example, line defects or planar defects).

A *vacancy*, or vacant lattice site, exists when an atom is missing from a normal lattice position. Any crystalline material above 0 K will contain vacancies as an equilibrium part of its structure. The number of vacancies will increase exponentially with temperature, so that in a typical metal crystal lattice, for example, of the order of 1 site in  $10^4$  will be vacant at temperatures approaching its melting point. Generally such vacancies will be randomly distributed, and as such have marginal effect on properties, but if a crystal is cooled too quickly, before the higher number of vacancies characteristic of elevated temperatures have time to ‘anneal out’, they can agglomerate to form voids.

An atom that is trapped inside the crystal at a point intermediate between normal lattice positions is called an *interstitial atom*. While interstitial defects do not occur normally as a result of thermal activation, they can occur, for example, as a result of bombardment with high energy nuclear particles (radiation damage).

The presence of *impurity atoms* (either at a lattice position or at an interstitial position in atomic scale) or *second phases* in a crystal can affect its quality in two ways; (i) they can affect its chemical or physical properties, (ii) second phase inclusions can limit crystal size by acting as nucleation sites for secondary grain formation during crystal growth. The effect that an impurity can have on physical properties can be out of all proportion to its numerical presence; for example, a strongly magnetic impurity can drastically alter the properties of a non-magnetic host, while the dopant levels in many semi-conductor crystals (i.e. B in Si) have a fundamental influence at concentrations that would be classed as insignificant levels for many impurities in many other systems. Second phase inclusions can arise not just from impurities, but from other phases within a binary (or ternary, etc.) system. As such they can not be classed as impurities and are not always undesirable as their presence at elevated temperatures may be an essential part of the solidification process, but crystal size may again be limited by them.

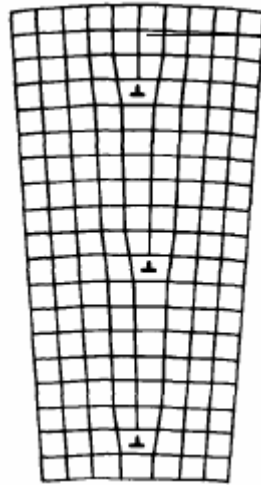
*Dislocations* (the most important line defects) form if a crystal is mechanically or thermally strained. It is perhaps surprising that a metal crystal would be considered to be well-annealed if it had a dislocation density of  $10^6$  cm of dislocation lines per  $\text{cm}^3$ , while a heavily deformed metal can have dislocation densities approaching  $10^{12}$   $\text{cm}/\text{cm}^3$ .

Surface, or planar, defects arise from the clustering of line defects into a plane. Low angle grain boundaries, grain boundaries, the stacking fault between two close-packed regions of a crystal and twinned regions are examples of planar defects.

*Sub-boundaries* or *low angle grain boundaries* are definite substructures that can exist within the grains surrounded by high-energy grain boundaries. A low angle grain boundary contains a relatively simple arrangement of dislocations, and the difference in orientation across the boundary may be less than a degree. Low angle grain boundaries can be produced in a number of ways, for example, during crystal growth, during high temperature creep deformation, or as the result of a phase transformation. Perhaps the most general method of producing a substructure network is by introducing a small

amount of deformation and following this with an annealing treatment to rearrange the dislocations into subgrain boundaries. (For this to occur, the amount of deformation and the temperature must be low enough to prevent the formation of new grains by recrystallization or polygonization).

Low angle grain boundaries can be detected using X-ray techniques or, in many materials, by metallographic procedures. A schematic of a low angle grain boundary constituted of a regular arrangement of dislocations is shown in Fig. 1.1.



**Fig.1.1.** Diagram of low-angle grain boundary made up of an array of dislocations

*Twins* may also be produced by mechanical deformation or as the result of annealing following plastic deformation when a portion of the crystal takes up an orientation that is related to the orientation of the rest of the untwinned lattice in a definite symmetrical way. Twinning is most easily achieved in metals of close-packed hexagonal structure where, because of the limited number of slip systems, twinning is an essential and unavoidable mechanism of deformation in polycrystalline specimens. In single crystals the orientation of the specimen, the stress level and the temperature of deformation are all important factors in the twinning process.

Errors, or faults, in the stacking sequence of the planes of atoms in crystals can also be produced in most metals by plastic deformation. This defect is called a *stacking fault* and occurs most readily in fcc metals.

*Cracks* in crystals are another type of defect that can form as a result of mechanical or thermal stresses. The latter is more likely in crystal growth processes where a sharp

temperature gradient is present in the growing crystal or if a crystal is cooled (or heated) too quickly. Thermal stresses, in particular, together with the anisotropic thermal expansion of a crystal or the presence of second phase inclusions (as nucleation sites for cracks) are probable origins of cracking in crystals.

#### **1.4. Crystal growth phenomena**

In principal, single crystals can be grown by the assemblage of their constituents from any other surrounding phase containing the constituents in a disordered form: solution, melt, vapour, or even another solid phase, although the latter is not an effective way to obtain a crystal.

Although classical thermodynamics is concerned with equilibrium states of systems, in crystal growth non-equilibrium conditions have to be assumed. However, thermodynamic descriptions of steady-state and transient processes can be acceptably accurate as long as these processes are slow in comparison with the kinetics of the atoms and concentration gradients are not too steep [1].

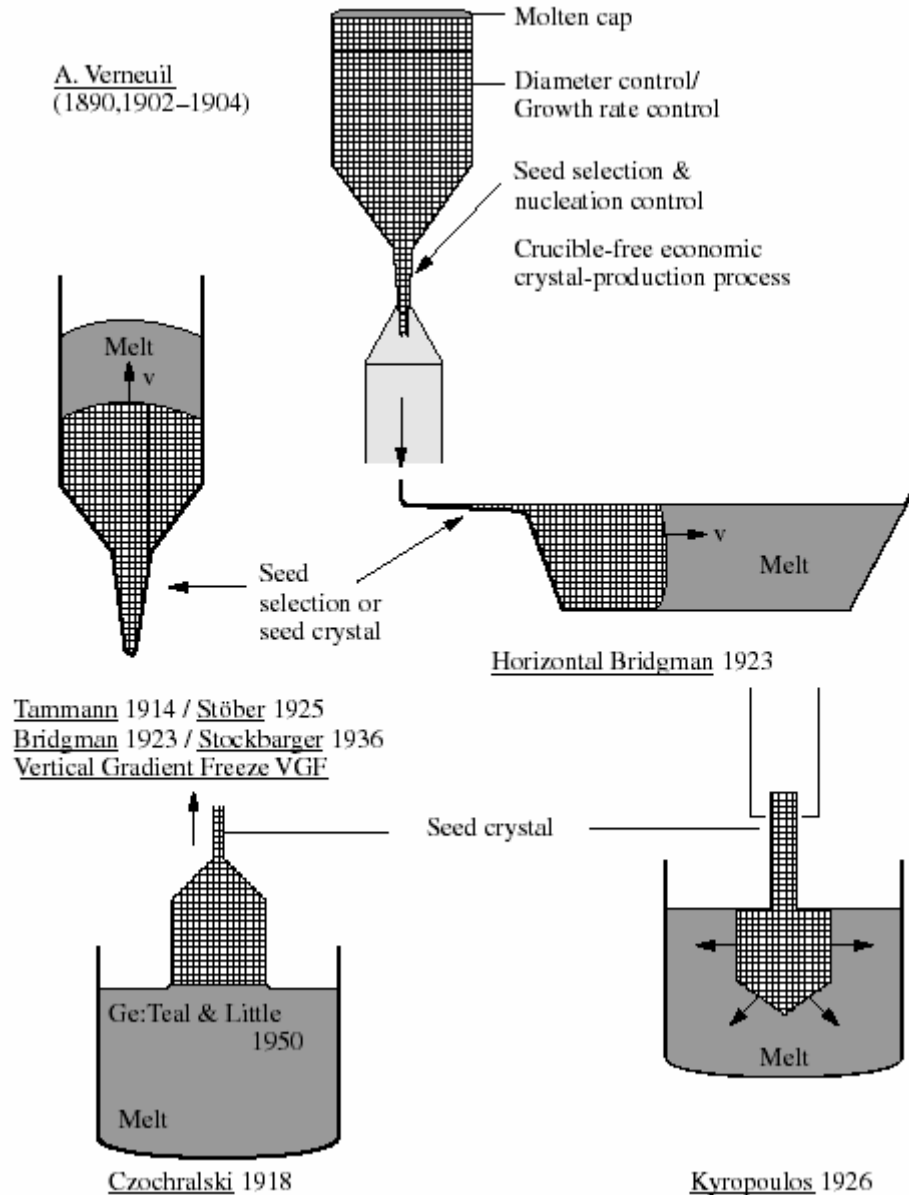
Overall, crystal growth combines studies of phase equilibria and thermodynamics, nucleation phenomena, solute partitioning, hydrodynamics and fluid motion, heat and mass transfer, interface attachment kinetics, interface morphology and defect generation. Because such a highly complex task has to adhere to so many different areas of knowledge, more often than not its practical solution can be perceived as an art [1].

#### **1.5. Historical development of crystal growth methods from melt**

Industrial crystal production started with Verneuil in 1902 who, with the flame-fusion growth process named after him, achieved for the first time control of nucleation and thus prepared single crystals of ruby and sapphire (which have melting points above 2000 °C). By first forming a neck (Fig. 1.2), followed by enlargement of the crystal diameter, not only was seed selection achieved in a crucible-free process, but also the structural perfection of the growing crystal could be controlled to some extent.

The principles of the Verneuil method with nucleation, growth rate and diameter control have been applied in most of the growth processes developed in the following years: Tammann 1914, Stober 1925, Bridgman 1923, Stockbarger 1936, vertical-gradient-freeze

growth of Ramsberger and Malvin 1927, and in the Czochralski process 1918/1950 [2] (see Fig. 1.2).



**Fig.1.2.** Modification of Verneuil's principles of nucleation control and increasing crystal diameters in other crystal-growth techniques [2]

The pioneering work by Bridgman was directed toward the growth of single crystals of mainly low-melting point metals. This technique is characterized by the relative translation of the crucible containing the melt to the axial temperature gradient in a

vertical furnace. (A similar vertical configuration was employed by Stockbarger to grow single crystals of lithium fluoride. In one variant of the method, he utilized two furnaces mounted coaxially and separated by a baffle having a central hole of just sufficient diameter to allow the crucible to be lowered through. In this technique, the upper furnace was at a temperature sufficient to melt the charge and the temperature of the lower one empirically adjusted to give the best crystal quality). Horizontal Bridgman has also been employed due to some advantages, for example, the seeding step is generally more easily observed in the horizontal mode, and the removal of the ingot from the crucible is easier because the crystal-crucible interface is half that of vertical crucibles. Additionally, in some situations, it is necessary to achieve a steady state equilibrium with a gaseous species, such as arsenic vapour in the growth of GaAs. This is easier to achieve in a horizontal boat configuration where the distance from the vapour to the growth interface is fairly constant over the entire length of the crystal, while in the vertical mode, this distance varies with the fraction of the melt solidified [3].

Crystal pulling, a method named after Czochralski [2], was first developed as a technique for growing single crystals of useful size and perfection by Teal and Little. Since 1950's, its application has been extended to the growth of silicon and a wide range of semiconductors, metals, oxides and halides. In its simplest form, the technique consists of a crucible which contains the charge material to be crystallized surrounded by a heater capable of melting the charge. A seed crystal (attached to a pull rod) is lowered until the end of the seed crystal is dipped into the melt while the melt temperature is carefully adjusted until a meniscus is supported by the end of the seed. Once a thermal steady state has been achieved, the pull rod is slowly lifted and rotated, and crystallization onto the end of the seed occurs.

Kyropulos method is another bulk crystal growth technique which is usually used to produce large sapphire boules of a cylindrical form by cooling the crystal in the same zone of growth inside the crucible and sprouting the crystal into the melt. Such method allows to grow crystals with minimal mechanical stress [3].

Flux growth, the most commonly used term for crystal growth from high temperature solutions, is a method which allows the growth of single crystals of a wide range of materials. In this technique, the components of the desired materials are dissolved in a

solvent called flux. The flux growth process analogous to crystal growth from aqueous solutions, but the solvent solidifies before reaching room temperature. The main advantage of this method is that the crystals are grown below the melting temperature. If the material melts incongruently, i.e. decomposes before melting, or exhibits a phase transition below the melting point, one has indeed to look for growth temperatures lower than these phase transitions. Flux growth might be used when the melting temperature is very high, and useful when the vapour pressure at the melting temperature is too high. Thermal strain is also minimized due to the relatively low growth temperature and very slow cooling rates. The main disadvantage of the technique is the low growth rate because the growth rate of crystals from the flux is generally more than hundred times smaller than in melt growth, thus, crystals from the flux are in general of small size. Crystal extraction from the flux is also quite difficult (it is usually performed by tapping with a hammer). A further disadvantage is the unavoidable presence of ions of the flux as impurities in the crystals [3].

In the early 1950's, crucible-free zone melting (the floating zone method) was introduced (after a first representation in a patent of Theuerer) by Keck and Golay as well as by Emeis for preparing high-purity silicon for semiconductor devices [3]. This technique circumvented the problems resulting from the use of crucibles, in particular, pick up of impurities from the crucible material (a common problem with Czochralski growth). The technique has now become probably the most popular method for the growth of materials with high or very high melting points for which no crucible material is available. The crystals grown by this technique (compared to the flux technique) are quite large and crystals can be extracted easily because there is no crucible or flux around the crystal. However, it should be noted that the FZ technique is often more complicated and difficult to control, while the equipment is generally more complex and expensive, than the Czochralski method [3].

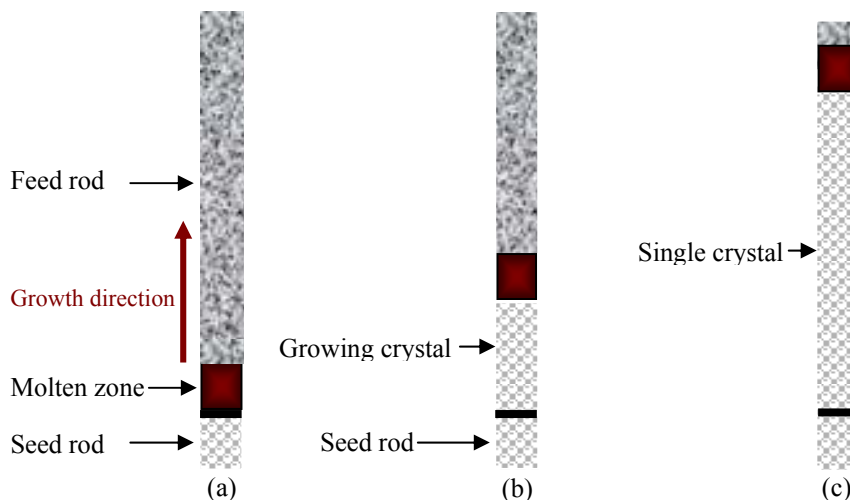
### **1.6. Fundamentals of the floating zone technique**

In the FZ technique, the sample is in the form of a free-standing rod, clamped only at its ends, in which a relatively small length is melted at any one time by a suitable heating method. This 'molten zone' is suspended like a drop between the two solid parts of the

rod, leading to the designation floating zone or float zone melting. This molten zone is moved along the rod by the motion of either the heater or the rod itself (Fig. 1.3). A single crystal can be generated by spontaneous nucleation or by using a single-crystalline seed crystal as the initial part of the rod [3].

As shown in the Fig. 1.3, the molten zone established between the two vertical cylindrical rods is supported against gravity essentially by the surface tension of the liquid and the stability of such a configuration plays an important role in the technique. In general, a molten zone is more stable the higher the surface tension of the material and the lower its specific weight.

The dependence of the shape and stability of a molten zone on surface tension and density have been studied in mathematical analyses of the subject [3]. However, the mathematical conclusions reached are based on assumptions such as a flat solid/liquid interface, no motion of the zone, and only consider the molten zone size (length and radius), density of the liquid and surface tension [4], so they have limited value in reality as these assumptions do not represent actual growth conditions. In addition, surface tension data are not usually available for the high melting temperature materials, and can vary during a growth procedure due to possible changes in melt composition, temperature or other parameters.



**Fig.1.3.** Scheme of the floating zone technique, (a) formation of the molten zone, (b) and (c) growth by moving the molten zone through the feed rod

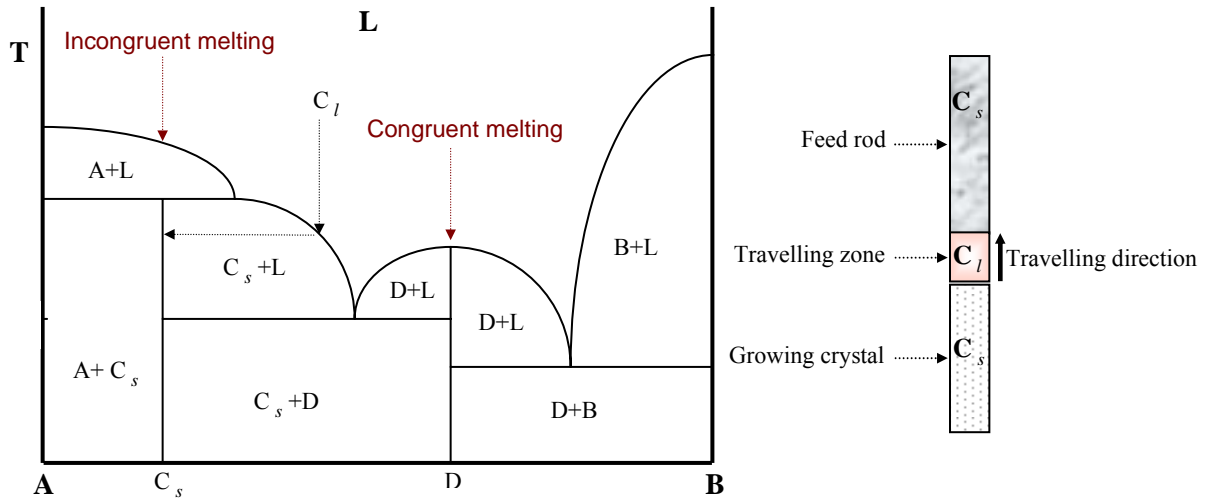


Actual operating experience with the floating zone technique indicates that the stability of a molten zone is complicated since many experimental parameters, including both materials properties (such as composition, thermal conductivity, volatility and viscosity) and growth parameters (such as feed rod characteristics, growth speed, gas pressure around the molten zone, rotation rate, molten zone temperature, direction of zone travel and shape of the solid/liquid interface) can influence the stability conditions.

Once a stable molten zone is achieved, the reaction or reactions involved in the floating zone become the crucial issues determining the formation of a phase or phases in the growing crystal. While the application of phase diagrams is indispensable in all forms of crystal growth, their usefulness in the float zone technique is magnified by the absence of crucibles and the close control that is possible of other growth parameters such as composition, crystallization rate, atmosphere, temperature and atmospheric pressure. In addition, the FZ method permits growth of doped crystals with an exactly adjustable dopant concentration. These factors allow phase diagrams to be used more reliably than is perhaps the case with some other growth methods. It is worth mentioning that volatilization losses during crystal growth can also be decreased compared with other techniques due to the shorter times that any particular part of the material is in the molten state in the FZ technique, although some volatilization may still occur, of course, in parts of the sample below the melting point in the solid state.

Although the FZ technique is generally used for congruently melting materials (where the feed rod, molten zone and the growing crystal all have the same composition), the technique can also be employed to grow some '*incongruently melting*' materials, depending on the phase stability of the material. In this case, the feed rod and growing crystal have different compositions to the molten zone and the technique is called travelling solvent floating zone (TSFZ). For most incongruently melting compounds (as shown in Fig. 1.4 where letters A and B are used as two different phases to form a pseudobinary phase diagram, L is the liquid phase, and letters D and  $C_s$  define congruently and non-congruently melting compounds respectively in the phase diagram) any attempted float-zone growth of a crystal of concentration  $C_s$ , from a molten zone of the same concentration does not give a crystal of concentration  $C_s$  because, as the liquid is cooled below the liquidus, the first solid to appear will be of composition A. To obtain

a solid of composition  $C_s$ , the composition of the liquid (molten zone) has to be changed to, for example,  $C_l$  where the first solid to form during FZ growth will have concentration  $C_s$ .



**Fig.1.4.** Schematic of a pseudobinary phase diagram for incongruent and congruent melting materials (left), and the travelling solvent floating zone technique (TSFZ) to grow an incongruent melting material (right)

In the TSFZ technique, the common methodology to produce a molten zone with a composition different to the feed and seed rods, is to attach a small ‘solvent disk’ of composition  $C_l$  to the top part of the seed rod (where the feed and seed rods are joined to produce a molten zone). The molten zone then retains this composition as zoning progresses since the solidification of crystal of composition  $C_s$  from the molten zone is balanced by introduction of feed rod material (also of composition  $C_s$ ) into the zone.

In the FZ technique, the first heating methods used to produce a molten zone were electron bombardment and induction melting. Electron beam melting had the advantage that very high temperatures could be obtained, although a vacuum environment was necessary so limiting the technique to lower vapour pressure materials. With induction heating, a gaseous environment was possible, but very high temperatures and sharp temperature gradients were more difficult to achieve [4]. Both techniques, however, had

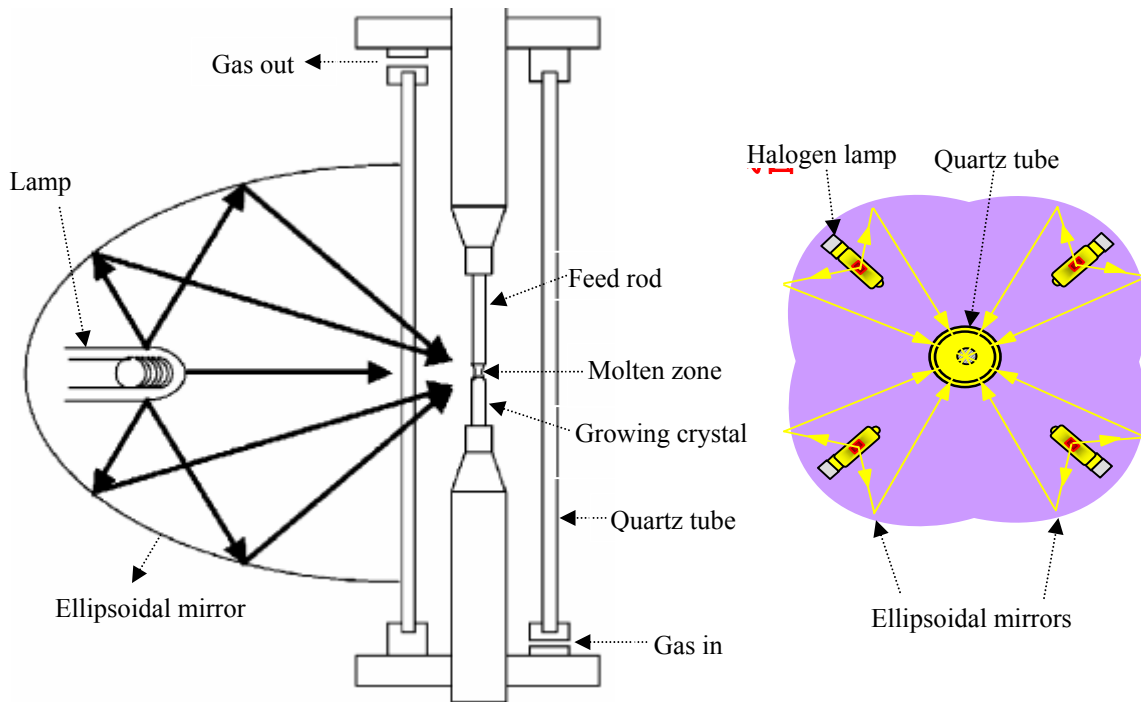
the fundamental disadvantage that they were only applicable to samples that were electrical conductors.

To overcome these difficulties, another heating technique developed for float zone melting was the radiation coming from an optical source which was focused onto the molten zone by means of a concave mirror. Firstly, Kooy and Couwenberg melted rods of ferrite  $\text{MnFe}_2\text{O}_4$  and other oxides using the light of the carbon-arc lamp from a film projector [3]. Subsequently, optical or radiation furnaces specifically constructed for floating zone techniques have become available. In particular, the development of infra red image furnaces in Japan in the late 1980's used ellipsoid mirror furnace designs that, due to their compactness and high efficiency, became used in space laboratories. This variation of the float zoning technique is probably the most advanced to date in terms of design and energy efficiency.

#### **1.6.1. Crystal growth by the floating zone technique using image furnaces**

Early designs of image furnaces or optical furnaces for floating zone melting had 1 or 2 mirrors, but the image furnaces made since the late 1990's generally have four mirrors to both increase the power of the furnace and also to obtain more uniform sample heating. In all image furnaces, the basic concept is that ellipsoidal mirror(s) are used to focus the light from halogen or Xenon lamp(s) onto the sample to produce the molten zone, making the technique suitable for both conducting and non-conducting materials. Also, the use of light heating is particularly convenient and efficient for oxides and semiconductors that absorb infrared easily.

Fig. 1.5 shows image furnaces consisting of one and four ellipsoidal mirror(s) or reflector(s) to focus the light onto a small part of the sample to create a molten zone. In image furnaces, the sample is protected from air by a large diameter, clear quartz tube which both prevents any evaporant settling on the mirror and allows control of the growth atmosphere and gas pressure around the growing crystal.



**Fig.1.5.** Schematic illustration of the optical floating zone melting with one ellipsoidal mirror (left) and four ellipsoidal mirrors (right)

Several experimental parameters (e.g. crystallization rate, atmosphere, gas pressure, temperature) can be controlled when growing crystals using image furnaces. Optimizing these parameters is the key to achieving growth stability and, consequently, good crystal properties. Therefore, scientists who work with image furnaces require knowledge of the possible effects of these parameters and any correlations between them; also they need to have adequate control of the overall growth procedure for which practical experience is vital. The importance of the controllable growth parameters will be discussed in detail in the literature review section with reference to previous crystal growths.

Thus, crystal growth by the optical floating zone technique using image furnaces has been extensively utilized to grow single crystals of oxides (optical, magnetic, and superconducting...) which play an important role in modern materials science and technology, e.g. such as active media in lasers, electronic and optical devices, catalysts, solid oxide fuel cells, oxygen sensors, memory and magnetic devices, magneto-optical sensors and other field of engineering.

The research work presented in this thesis attempts to extend our knowledge of the subject by firstly studying the optical floating zone method as a *technique* in terms of the

experimental growth parameters, and then to *perform* crystal growth and characterization on a number of functional oxides such as TiO<sub>2</sub> (Rutile), Co-TiO<sub>2</sub> and orthoferrite crystals (RFeO<sub>3</sub>, R=Er and Y). Since the magnetic properties of cobalt-doped rutile and orthoferrite crystals are of particular interest, a description of magnetic materials follows.

## 1.7. Magnetism

Magnetism is an extremely complex subject and only the briefest overview of those areas relevant to the work presented in this thesis can be given here. Thus, the detailed physics that explains, or attempts to explain, the origin of different types of magnetism is not covered in any depth.

### 1.7.1. Classification of magnetic materials

When a material is placed in a magnetic field, the extent to which it is affected is described by its magnetization (M). This magnetization is a measure of the magnetic moment per unit volume of material, but can also be expressed per unit mass, the specific magnetization ( $\sigma$ ). The magnetic field that is applied to the material is called the applied field (H) and is the total field that would be present if it were applied to a vacuum.

Another important parameter is the magnetic induction (B), which is the total flux of magnetic field lines through a unit cross sectional area of the material, considering both lines of force from the applied field and from the magnetization of the material. B, H and M are related by equation 1.1 in cgs units. 
$$B=H+4\pi M \quad \text{Eq. 1.1}$$

The magnetization (M) is a characteristic property of the material, and is related to the susceptibility per unit volume of the material which is defined as: 
$$\chi=M/H \quad \text{Eq. 1.2}$$

Those materials for which  $\chi$  is negative, such as copper, silver and gold, are repelled by the field and are termed *diamagnetic* materials. Most materials, however, have positive  $\chi$  values (i.e. they are attracted by the field) and the majority are either *paramagnetic* (when  $\chi$  is small) or *ferromagnetic* (when  $\chi$  is very large). Unlike diamagnets or paramagnets, magnetization exists in ferromagnets even without an external magnetic field since the atomic magnetic moments align naturally.

All materials can be classified in terms of their magnetic behaviour as falling into one of five categories depending on their bulk magnetic susceptibility as shown in Table 1.2.

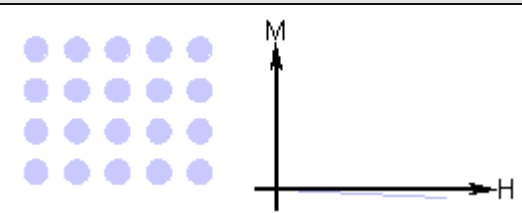
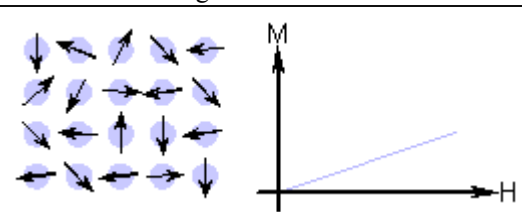
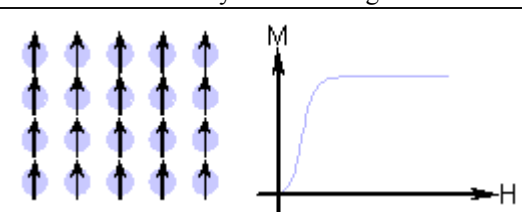
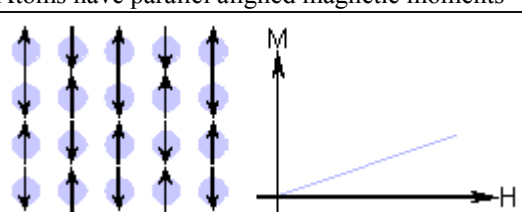
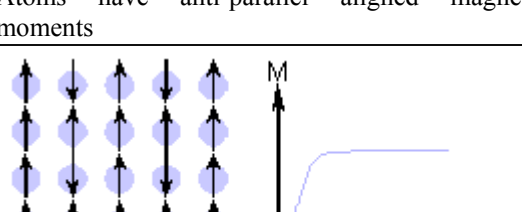
The two most common types of magnetism are *diamagnetism* and *paramagnetism*, which account for the magnetic properties of most of the periodic table of elements at room temperature.

Of the elements, only Fe, Co, Ni and Gd are ferromagnetic at and above room temperature. As ferromagnetic materials are heated, the thermal agitation of the atoms means that the degree of alignment of the atomic magnetic moments decreases until the agitation becomes so great that the material becomes paramagnetic; the temperature of this transition is the *Curie temperature*,  $T_C$  (Fe:  $T_C = 770^\circ\text{C}$ , Co:  $T_C = 1131^\circ\text{C}$  and Ni:  $T_C = 358^\circ\text{C}$ ).

The only other type of magnetism observed in pure elements at room temperature (in chromium) is *antiferromagnetism*. Antiferromagnetic materials are similar to ferromagnetic materials except that neighbouring atoms have anti-parallel alignment of their atomic magnetic moments. Therefore, the magnetic field cancels out and the material appears to behave a similar way to a paramagnetic material. Like ferromagnetic materials, these materials become truly paramagnetic above a transition temperature, known as the Néel temperature,  $T_N$ . (Cr:  $T_N = 37^\circ\text{C}$ ).

Finally, some materials can be classified as *ferrimagnetic* although this is not observed in any pure element but can be found in compounds such as mixed oxides known as ferrites, from which ferrimagnetism derives its name. Within these materials the unequal atomic moments are aligned parallel in some of the crystal sites and anti-parallel in others, resulting in a net positive moment.

**Table 1.2.** Summary of different types of magnetic behaviour [290]

Type of Magnetism	Susceptibility	Atomic & Magnetic Behaviour	Example & Susceptibility
Diamagnetism	Small & Negative	 <p>Atoms have no magnetic moment</p>	Au $-2.74 \times 10^{-6}$ Cu $-0.77 \times 10^{-6}$
Paramagnetism	Small & Positive	 <p>Atoms have randomly oriented magnetic moments</p>	$\beta$ -Sn $0.19 \times 10^{-6}$ Pt $21.04 \times 10^{-6}$ Mn $66.10 \times 10^{-6}$
Ferromagnetism	Large & Positive Function of applied field, microstructure dependent.	 <p>Atoms have parallel aligned magnetic moments</p>	Fe $\sim 100,000$
Antiferromagnetism	Small & Positive	 <p>Atoms have anti-parallel aligned magnetic moments</p>	Cr $3.6 \times 10^{-6}$
Ferrimagnetism	Large & Positive Function of applied field, microstructure dependent	 <p>Atoms have mixed parallel and anti-parallel aligned magnetic moments</p>	Ba ferrite $\sim 3$

### 1.7.2. Spontaneous magnetization

Historically, the term ‘ferromagnet’ was used for any material that could exhibit spontaneous magnetization (a net magnetic moment in the absence of an external magnetic field). This general definition is still in common use. More recently, however, different classes of spontaneous magnetization have been identified when there is more than one magnetic ion per primitive cell of the material, leading to a stricter definition of "ferromagnetism" that is often used to distinguish it from ferrimagnetism. In particular, a material is "ferromagnetic" in this narrower sense only if *all* of its magnetic ions add a positive contribution to the net magnetization.

While some of the ‘magnetic’ materials studied in this thesis are not true ferromagnets (strictly the rare earth orthoferrites are classed as canted antiferromagnets), their behaviour is similar to that of a weak ferromagnet, so many of the characteristics of ferromagnetic materials, explained in the following pages, are relevant to them.

### 1.7.3. Magnetization and hysteresis loops

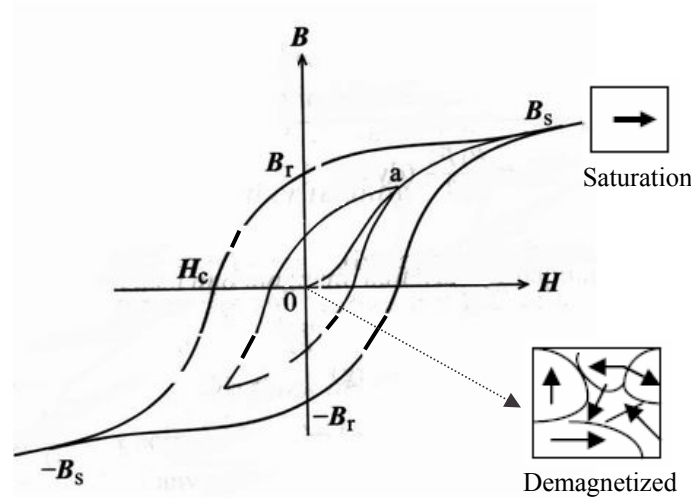
If  $H$  is the magnetic field necessary to induce a magnetic field of strength  $B$  inside a ferromagnetic material, upon removal of the magnetic field ( $H$ ), the magnetization is not reduced to zero. In fact, ferro- and ferrimagnets continue to show interesting behavior when the field is reduced to zero and then reversed in direction. The graph of  $B$  (or  $M$ ) versus  $H$  which is traced out, is called a Hysteresis loop (Fig. 1.6).

As shown in Fig. 1.6, as the field is increased in the positive direction, the magnetic induction follows the curve from 0 to  $B_s$  (saturation induction). Although the magnetization is constant after saturation,  $B$  continues to increase since  $B=H+4\pi M$ . When the magnetic field is reduced to zero after saturation, the induction decreases from  $B_s$  to  $B_r$  (residual induction or retentivity), and the reversed magnetic field required to reduce the induction to zero is called the coercivity ( $H_c$ ).

Depending on the value of the coercivity, ferromagnetic materials are classified as either hard or soft. A soft magnet is one which is easy both to magnetize and demagnetize, and a low value of  $H$  is sufficient to induce a large field  $B$  in the material, while only a small field  $H_c$  is required to remove it (these materials have narrow hysteresis loops). A hard



magnet is a material that is magnetized and demagnetized with difficulty and has a wider hysteresis loop because it needs a larger magnetic field to reduce its induction to zero.



**Fig.1.6.** Hysteresis loop for a ferro- or ferrimagnet

#### 1.7.4. Physical origin of ferromagnetism

The property of ferromagnetism is due to the direct influence of two effects from *quantum mechanics*: *spin* and the *Pauli exclusion principle*.

The spin of an electron, combined with its orbital angular momentum, results in a magnetic dipole moment and creates a magnetic field. In many materials (specifically, those with filled electron shells), however, the total dipole moment of all the electrons is zero (e.g., the spins are in up/down pairs that cancel each other out). Only atoms with partially filled shells (e.g., unpaired spins) can experience a net magnetic moment in the absence of an external field.

While these permanent dipoles (often called simply ‘spins’ even though they also generally include orbital angular momentum) tend to align parallel to an external magnetic field (i.e. paramagnetism), ferromagnetism involves an additional phenomenon: the dipoles tend to *align spontaneously*, without any applied field. This is a purely quantum-mechanical effect.

According to classical electromagnetism, two nearby magnetic dipoles will tend to align in *opposite* directions (which would create an antiferromagnetic material). In a ferromagnet, however, they tend to align in the *same* direction because of the Pauli

principle: two electrons with the same spin state cannot lie at the same position, and thus feel an effective additional repulsion that lowers their electrostatic energy. This difference in energy is called the *exchange energy* and induces nearby electrons to align.

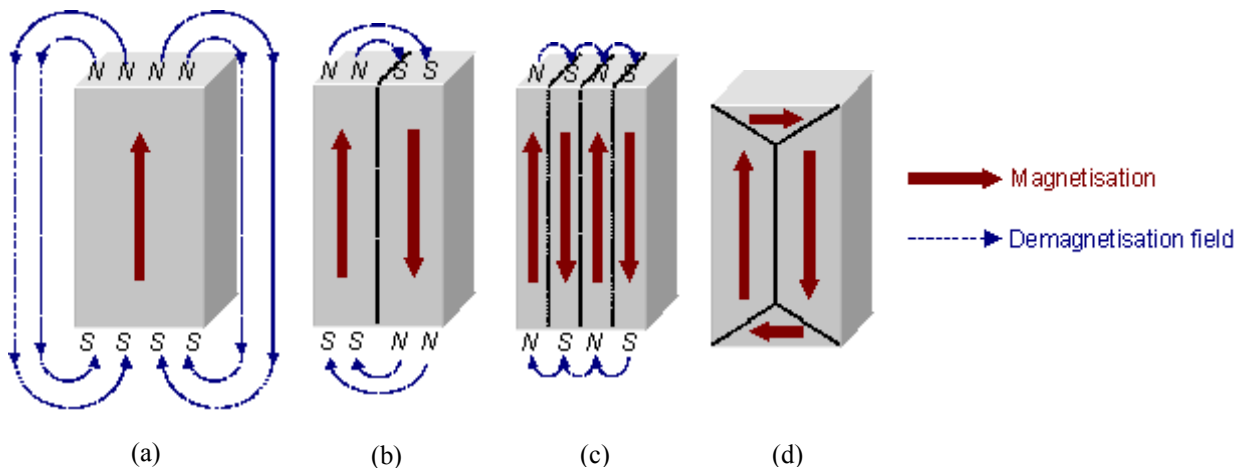
The exchange interaction between magnetic atoms may often be indirect and take place via an intermediate non-magnetic atom such as oxygen. Under some circumstances, the coupling between magnetic atoms can cause antiparallel alignment of the spins of neighbouring atoms leading to antiferromagnetism. Thus, an antiferromagnet comprises two interpenetrating lattices of similar magnetic ions which cancel each other out. In a ferrimagnet, two such interpenetrating lattices have antiparallel magnetizations of unequal magnitude so that there remains a resultant magnetic moment in the direction of the stronger magnetic sub-lattice.

At long distances (over many thousands of ions), the exchange energy advantage is overtaken by the classical tendency of dipoles to anti-align. This is why, in an equilibrated (non-magnetized) ferromagnetic material, the dipoles in the whole material are not aligned. Rather, they organize into magnetic domains (also known as *Weiss domains*) that are aligned (magnetized) at short range, but at long range adjacent domains are anti-aligned. Therefore, ferromagnetic domains are small regions in ferromagnetic materials within which all the magnetic dipoles are aligned parallel to each other. When a ferromagnetic material is in its demagnetized state, the magnetization vectors in different domains have different orientations, and the total magnetization averages zero, while the process of magnetization causes the domains to orient in the same direction.

Since the exchange energy provides a strong driving force for parallel alignment, it might be expected that ferromagnetic materials should be composed of one single domain, with all dipoles aligned in the same direction. However, while a single domain would certainly minimize the exchange contribution to the total energy, there are a number of other contributions to the total magnetic energy of a ferromagnet. The formation of domains allows a ferromagnetic material to minimize its *total* magnetic energy, of which the exchange energy is just one component. The other main contributors to the magnetic energy are the *magnetostatic energy*, which is the principal driving force for domain formation, and the *magnetocrystalline* and *magnetostrictive energies*, which influence the shape and size of domains.

*Magnetostatic energy:*

A uniformly magnetized block of ferromagnetic material containing a single domain has a macroscopic magnetization, as shown in Fig. 1.7.a. The magnetization causes the block to behave as a magnet, with a magnetic field around it. It is apparent from the figure that the field acts to magnetize the block in the opposite direction from its own magnetization, and for this reason, it is called the demagnetizing field ( $H_d$ ). The demagnetizing field causes a magnetostatic energy which depends on the shape of the sample. In general if the sample has a high length to diameter ratio (and is magnetised in the long axis) then the demagnetising field and the magnetostatic energy will be low.



**Fig.1.7.** Reduction of the magnetostatic energy by domain formation in a ferromagnet, (a) single domain, (b) two domains, (c) four domains and (d) closure domains [290].

The break up of the magnetisation into two domains, as illustrated in Fig. 1.7.b, reduces the magnetostatic energy by half. In fact if the magnet breaks down into  $N$  domains then the magnetostatic energy is reduced by a factor of  $1/N$ , hence figure Fig. 1.7.c has a quarter of the magnetostatic energy of Fig. 1.7.a. Fig. 1.7.d shows a closure domain structure where the magnetostatic energy is zero, however, this is only possible for materials that do not have a strong uniaxial anisotropy, and the neighbouring domains do not have to be at  $180^\circ$  to each other.

*Magnetocrystalline energy:*

The magnetization in ferromagnetic crystals tends to align along certain preferred crystallographic directions known as ‘easy’ axes (since it is easiest to magnetize a

demagnetized sample to saturation if the external field is applied along that direction). Fig. 1.8 shows schematic magnetization curves for a ferromagnetic single crystal of cobalt, which has a hexagonal structure that can be magnetized easily in the  $[0001]$  direction, but has hard directions of magnetization in the  $\langle 10\bar{1}0 \rangle$  type directions. In both cases the same saturation magnetization is achieved, but a much larger applied field is required to reach saturation along the hard axis than along the easy axis.

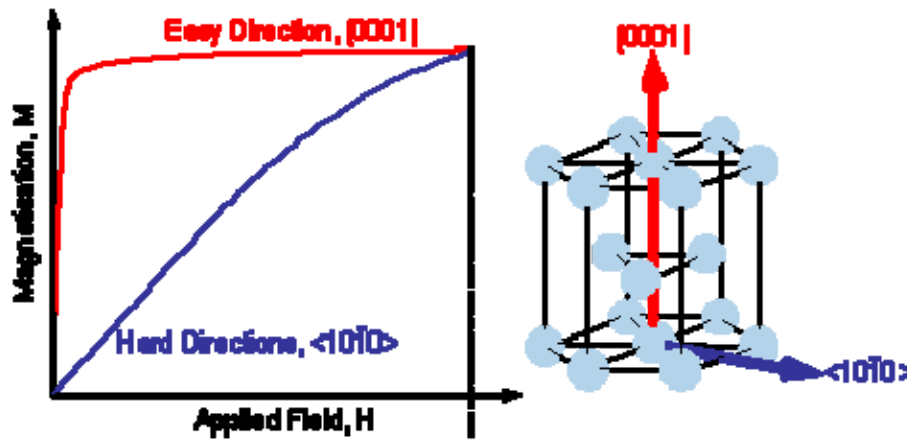


Fig.1.8. The magnetocrystalline anisotropy of cobalt [290]

The phenomenon that causes the magnetization to align itself along a preferred crystallographic direction is magnetocrystalline anisotropy. The magnitude and type of magnetocrystalline anisotropy affect properties such as magnetization and hysteresis curves in magnetic materials. Therefore, the nature of the magnetic anisotropy is an important factor in determining the suitability of a magnetic material for a particular application. The anisotropy can be either intrinsic to the material due to its crystal chemistry or shape, or it can be induced by careful choice of processing method.

A crystal is higher in energy when the magnetization points along the hard direction than along the easy direction, and the energy difference between samples magnetized along easy and hard directions is called the magnetocrystalline anisotropy energy. In fact, the area between the hard and easy magnetization curves in Fig. 1.8 is a measure of the magnetocrystalline energy for that material. To minimize the magnetocrystalline energy,

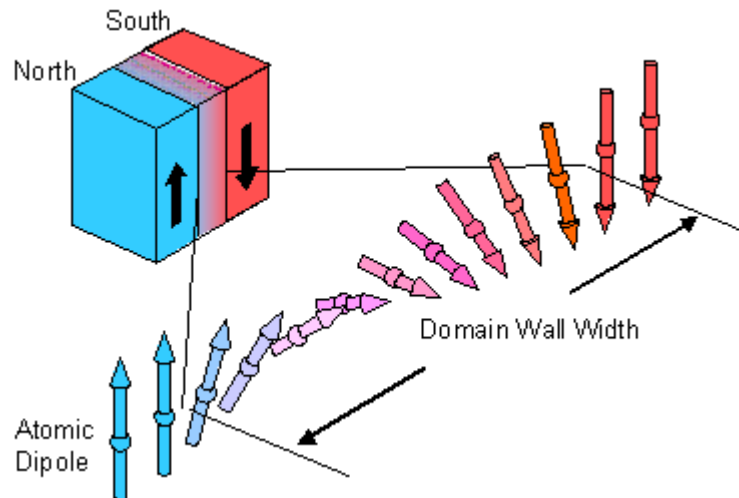
domains will form so that their magnetizations point along easy crystallographic directions.

*Magnetostrictive energy:*

When a ferromagnetic material is magnetized it undergoes a change in length known as its magnetostriction. Some materials, such as iron, elongate along the direction of magnetization and are said to have a positive magnetostriction. Others, such as nickel, contract and have negative magnetostriction. The length changes are very small (tens of parts per million), but do influence the domain structure due to elongation or contraction of domains.

### 1.7.4.1. Domain walls

The transition between two domains, where the magnetization flips, is called a *domain wall* (e.g., a Bloch/Néel wall, depending upon whether the magnetization rotates parallel/perpendicular to the domain interface) and is a gradual transition on the atomic scale (covering a distance of about 300 ions for iron). Domain walls usually undergo an angular displacement of  $90^\circ$  or  $180^\circ$  (Fig. 1.9).



**Fig.1.9.** Schematic representation of a  $180^\circ$  domain wall [290]

The width of domain walls is again determined by a balance between competing energy contributions. The exchange energy is optimized if adjacent magnetic moments are parallel, or as close to parallel as possible, to each other. This favours wide walls, so that the change in angle of the moments between adjacent planes of atoms can be as small as

possible. However, the magnetocrystalline anisotropy is optimized if the moments are aligned as closely as possible to the easy axes. This favours narrow walls with a sharp transition between the domains, so that few moments have unfavourable crystalline alignment in the transition region. In practice, a compromise is reached which minimizes the total energy across the boundary.

#### **1.7.4.2. Intersection of domain walls with crystal imperfections**

As described previously, at the coercive field, the vector component of the magnetization of a ferromagnet measured along the applied field direction is zero. Two primary modes of magnetization reversal, namely *rotation* and *domain wall motion*, are given for the demagnetization and coercivity mechanism.

When the magnetization of a material reverses by rotation, the magnetization component along the applied field is zero because the vector points in a direction orthogonal to the applied field, while when the magnetization reverses by domain wall motion, the net magnetization is small in every vector direction because the moments of all the individual domains sum to zero. Magnetization curves dominated by rotation and magnetocrystalline anisotropy are found in the relatively perfect magnetic materials typically used in fundamental research, while domain wall motion is a more important reversal mechanism in real engineering materials since defects such as grain boundaries and impurities serve as *nucleation sites* for reversed-magnetization domains.

Now, it is generally believed that crystal inhomogeneity plays a significant role in reducing the coercivity by nucleating domain walls. However, the detail of this nucleation process and the related inhomogeneous reversal modes, as well as the role of domain walls in determining coercivity is complex and still unclear since defects may pin domain walls in addition to nucleating them.

#### **1.7.5. Units**

In this thesis, the units used for magnetic measurements are in the S.I. system, and where appropriate the Bohr magneton ( $\mu_B$ ) is used as the unit for expressing the electron magnetic dipole moment of ferromagnetic atoms. The Bohr magneton is defined as:

$$\mu_B = \frac{eh}{4\pi m_e c} = 9.27400899 \times 10^{-24} \text{ Am}^2 \text{ or J/T} \quad \text{Eq. 1.3}$$

Where:

$e$  = electron charge =  $1.602 \times 10^{-19}$  C

$h$  = Planck's constant =  $6.626 \times 10^{-34}$  Js

$m_e$  = electron rest mass =  $9.109 \times 10^{-31}$  kg

$c$  = velocity of light =  $2.997924580 \times 10^8$  ms<sup>-1</sup>

(In the c.g.s. system of units this is written as  $\mu_B = \frac{eh}{2m_e c} = 0.927 \times 10^{-20}$  erg/O<sub>e</sub>)

## CHAPTER 2: LITERATURE REVIEW

As indicated previously, this literature review comprises four main parts. Initially, the literature relating specifically to the FZ technique is reviewed. Secondly, all aspects of the literature regarding  $\text{TiO}_2$  are covered, while the third and fourth parts review the literature pertaining to Co-doped  $\text{TiO}_2$  and rare earth orthoferrites.

### **2.1. Influence of growth parameters when using image furnaces**

Since the development of image furnaces, no systematic study is known to have been published that charts the effects that changes in the various experimental variables associated with the technique have upon single crystal growth. When starting work with an image furnace, such information would be really useful, but while the effects of individual growth parameters have been mentioned in publications for different materials, reports rarely give complete information explaining all aspects of the growth procedure.

In an attempt to collate such data to see if any trends are apparent, appendix A lists almost all the reported crystal growths using the image furnace technique since 1990 [6-177]. The growth conditions, where given in the literature, are also listed. (For further information regarding crystals grown using other crucible-free zone melting techniques, references 3 and 5 are particularly informative). This data is discussed below under headings that reflect the main experimental parameters that characterize FZ crystal growth.

#### **2.1.1. Feed rod characteristics**

The preparation of feed rods is the initial stage in growing crystals using the floating zone technique. The evidence from the literature clearly indicates that a well compacted, homogeneous in composition, straight and constant diameter feed rod is required to achieve and keep a perfectly stable molten zone over a long growth period and thereby grow a high quality crystal.

Any porosity in a feed rod made from compacted powders (the usual method for oxide materials) can be decreased by either sintering the rod at a relatively high temperature,



probably near the melting point, prior to loading into the image furnace, or pre-melting the feed rod by passing a zone in the image furnace prior to crystal growth (the twice scanning technique).

In general, the main effect that excess porosity in a starting feed rod has on the stability of the molten zone is due to either bubble formation in the melt zone or penetration of the melt into the feed rod. Crystal growth reports from a number of diverse materials such as  $\text{NiTa}_2\text{O}_6$  [29], Cr-doped  $\text{Mg}_2\text{SiO}_4$  [35] and  $\text{R}_{9.33}(\text{SiO}_4)_6\text{O}_2$  (R=Pr, Nd, Sm) [78,151] have illustrated that many bubbles originate from the pores in poorly compacted feed rods, which then enter the molten zone. The bubbles often coalesce to form a large one, which subsequently bursts making the molten zone seriously unstable. Sometimes, however, these bubbles do not join together and remain in the growing crystal as a defect, as reported in  $\text{Fe}_2\text{SiO}_4$  [39].

Molten zone penetration into the feed rod during growth is another problem that can occur in FZ growth. Decreasing any porosity in the feed rod has been found to be an effective way to reduce the penetration into the feed rod during growth of  $\text{Bi}_2\text{Sr}_2\text{CaCu}_2\text{O}_{8+\delta}$  [18],  $\text{NdBa}_2\text{Cu}_3\text{O}_{7-\delta}$  [68],  $\text{Nd}_{9.33}(\text{SiO}_4)_6\text{O}_2$  [78],  $\text{La}_{1.92}\text{Sr}_{0.08}\text{CuO}_{4+\delta}$  [80],  $\text{La}_{2-x}\text{Sr}_x\text{CuO}_4$  [84],  $\text{Bi}_2\text{Sr}_{2-x}\text{La}_x\text{CuO}_{6+\delta}$  [140],  $\text{Bi}_2(\text{Sr}_x\text{Ca}_{3-x})\text{Cu}_2\text{O}_y$  [141], R-doped  $\text{LuVO}_4$  (R=Nd, Tm, Yb) [167],  $(\text{La}_{1-x}\text{Ca}_x)_2\text{CaCu}_2\text{O}_{6+\delta}$  [177]. Infiltration or penetration of the melt into the feed rod is detrimental to the stability of the growth process due to a capillary effect in which the melt is partially absorbed by the voids within the feed rod and the volume of the melt is reduced. Excess reduction of the zone volume can lead to instability of the liquid zone, and can also change the zone composition particularly in the traveling solvent floating zone technique as has been reported in  $\text{Bi}_2(\text{Sr}_x\text{Ca}_{3-x})\text{Cu}_2\text{O}_y$  [141].

### 2.1.2. Crystallization rate or growth speed

The growth rate or crystallization rate is one of the most critical parameters which can affect crystal quality when using the FZ technique. It has been reported that varying the growth speed can affect the growing crystal in terms of size, formation of second phases or inclusions, cracks, composition, growth direction or crystal alignment, low angle grain boundaries, twin formation, bubbles and also influences the liquid/solid interface and molten zone stability.

The growth rate required may depend upon whether the material melts congruently or incongruently, relatively higher growth velocities generally being applied for congruently melting crystals [113]. However, some materials such as Bi-based cuprate oxides [111] melt incongruently, which means that the composition of the melt (molten zone) differs from that of the original solid (feed rod) and that of the growing crystal. When applying the travelling solvent floating zone (TSFZ) technique to grow these types of incongruent materials, these compositional differences cause solute diffusion at the solid/liquid interface, which takes place very slowly, and thus limits the crystal growth to a very slow rate. Crystals with narrow crystallization fields may also restrict the growth to an extremely slow rate.

The experimental results reported for growths of a range of materials at various growth velocities indicate that crystal growth at lower growth rates generally yields larger crystals, for example Bi-Sr-Ca-Cu-O [6,21,52],  $\text{Bi}_2\text{Sr}_2\text{CaCu}_2\text{O}_x$  [33],  $\text{La}_{2-x}\text{Sr}_x\text{CuO}_4$  [43],  $\beta_{II}\text{-Li}_3\text{VO}_4$  [54],  $\text{SrCu}_2(\text{BO}_3)_2$  [82],  $\text{Bi}_2\text{Sr}_{2-x}\text{La}_x\text{CuO}_{6+\delta}$  [140],  $\text{Bi}_2(\text{Sr}_x\text{Ca}_{3-x})\text{Cu}_2\text{O}_y$  [141],  $\text{Bi}_2\text{Sr}_2\text{Ca}_{1-x}\text{Pr}_x\text{Cu}_2\text{O}_y$  [142],  $\text{Sr}_3\text{Fe}_2\text{O}_{7-x}$  [155],  $(\text{La}_{1-x}\text{Sr}_x)_2\text{CaCu}_2\text{O}_{6+\delta}$  [176], and prevents crack formation in crystals of Nd-doped  $\text{YVO}_4$  [53],  $\beta_{II}\text{-Li}_3\text{VO}_4$  [54],  $\text{Ca}_{12}\text{Al}_{14}\text{O}_{33}$  [114],  $\text{La}_{1-x}\text{Sr}_x\text{MnO}_3$  [116],  $\text{SrFeO}_x$  [136],  $\text{Nd}_2\text{CuO}_4$  and  $\text{Nd}_{1.815}\text{Ce}_{0.185}\text{CuO}_4$  [145],  $\text{Ca}_2\text{Co}_{1-x}\text{Zn}_x\text{Si}_2\text{O}_7$  [143] and  $\text{CaMn}_{1-x}\text{Mo}_x\text{O}_3$  [158].

The formation of second phases or inclusions and inhomogeneity in composition are other possible defects that are reported to be influenced by the crystallization rate. Several studies have indicated that with many materials, slower growth speeds give crystals without (or sometimes with a reduced amount of) second phases or inclusions

such as  $\text{La}_{2-x}\text{Sr}_x\text{CuO}_{4-\delta}$  [26],  $\text{Bi}_2\text{Sr}_2\text{CaCu}_2\text{O}_x$  [33],  $\text{La}_{2-x}\text{Sr}_x\text{CuO}_4$  [43], Nd-doped  $\text{YVO}_4$  [53],  $\beta_{II}\text{-Li}_3\text{VO}_4$  [54],  $\text{Er:YVO}_4$  [90],  $\text{Bi}_2\text{Sr}_2\text{Ca}_2\text{Cu}_3\text{O}_{10+\delta}$  [111], Nd-doped  $\text{GdVO}_4$  [120],  $\text{La}_{2-x}\text{Ba}_x\text{CuO}_4$  [131],  $\text{Bi}_2\text{Sr}_{2-x}\text{La}_x\text{CuO}_{6+\delta}$  [140],  $\text{Ca}_2\text{Co}_{1-x}\text{Zn}_x\text{Si}_2\text{O}_7$  [143],  $(\text{La}_{1-x}\text{Sr}_x)_2\text{CaCu}_2\text{O}_{6+\delta}$  [176] and also give crystals with a more homogeneous composition in  $\text{La}_{2-x}\text{Ba}_x\text{CuO}_4$  [131] and  $\text{Bi}_2\text{Sr}_2\text{Ca}_{1-x}\text{Pr}_x\text{Cu}_2\text{O}_y$  [142].

However, depending on the material and its phase stability, faster growth rates are sometimes needed to obtain single phase crystals without inclusions, such as  $\text{CaSi}_2$  [15] and Nd-doped  $\text{YVO}_4$  [104], more stoichiometric crystals of  $\text{Bi}_2\text{Sr}_2\text{CaCu}_2\text{O}_{8+\delta}$  [101], or to avoid evaporation of components in  $\text{Nd}_{0.7}\text{Sr}_{0.3}\text{MnO}_3$ ,  $\text{La}_{0.5}\text{Ca}_{0.5}\text{MnO}_3$  [71],  $\text{Ca}_2\text{Co}_{1-x}\text{Zn}_x\text{Si}_2\text{O}_7$  [143] or decomposition of crystals, for example  $\text{GeNi}_2\text{O}_4$  and  $\text{GeCo}_2\text{O}_4$  [163].

One of the other clear influences of using lower growth rates concerns the formation of bubbles and voids in or on the surface of growing crystals. In this respect, it is reported that the formation of bubbles in crystals of  $\text{Nd}_{9.33}(\text{SiO}_4)_6\text{O}_2$  [78],  $\text{TiO}_2$  [95],  $\text{Ca}_{12}\text{Al}_{14}\text{O}_{33}$  [114],  $\text{Ca}_2\text{Co}_{1-x}\text{Zn}_x\text{Si}_2\text{O}_7$  [143],  $\text{Gd}_{3-x}\text{Y}_x\text{Fe}_5\text{O}_{12}$  [162] or voids on the surface of growing crystals of  $\text{Ca}_{2+x}\text{Y}_{2-x}\text{Cu}_5\text{O}_{10}$  [102] is prevented at lower growth rates.

Low angle grain boundaries and twin formation are other defects which can be sensitive to the growth rate. Published results have indicated that higher growth speeds for  $\text{TiO}_2$  single crystals [95] and lower rates for the crystals of  $\text{La}_{2-x}\text{M}_x\text{CuO}_4$  ( $\text{M}=\text{Ca}, \text{Sr}, \text{Ba}$ ) [57] and  $\text{Tb-Dy-Fe}$  [63] suppress the formation of low angle grain boundaries and twinning.

The reason given for using a higher growth rate for  $\text{TiO}_2$  crystals was to suppress the formation of low-angle grain boundaries whereby faster cooling of the grown crystal gave less time for the migration of the dislocations [95].

Growth rate can also affect the growth direction, preserving the crystal orientation during growth at lower rates in  $\text{Bi-Sr-Ca-Cu-O}$  [6] and  $\text{La}_{1-x}\text{Sr}_{1+x}\text{MnO}_4$  [130].

The nature of the liquid/solid interface (i.e. whether it has a planar or a cellular growth front) is another factor reported to affect crystal quality. In general, using a lower growth rate seems more likely to give a planar growth front, as reported in  $\text{Bi}_2\text{Sr}_2\text{CaCu}_2\text{O}_x$  [33], Bi-Sr-Ca-Cu-O [52],  $\text{Bi}_2\text{Sr}_{2-x}\text{La}_x\text{CuO}_{6+\delta}$  [140],  $\text{Bi}_2\text{Sr}_2\text{Ca}_{1-x}\text{Pr}_x\text{Cu}_2\text{O}_y$  [142],  $(\text{La}_{1-x}\text{Sr}_x)_2\text{CaCu}_2\text{O}_{6+\delta}$  [176] and can also provide more time for diffusion at the liquid/solid interface,  $\text{SrCu}_2(\text{BO}_3)_2$  [82], although crystal growth of Nd-doped  $\text{GdVO}_4$  by Shonai et al. [120] has indicated that in this material the growth front could be cellular in form even at a lower growth rate.

Besides these possible effects on the quality of crystals grown at different speeds, the stability of a molten zone can also be influenced by the growth rate. A more stable molten zone is reported upon lowering the growth rate for some materials such as  $\text{SrCuO}_2$  [75],  $\text{Y}_2\text{Cu}_2\text{O}_5$  [83],  $\text{La}_{2-x}\text{Ba}_x\text{CuO}_4$  [131], Zn-doped CuO [139] while for other crystals ( $\text{SrZrO}_3$  [122],  $\text{Bi}_2\text{Sr}_{2-x}\text{La}_x\text{CuO}_{6+\delta}$  [140] and  $\text{La}_{1-x}\text{Sr}_x\text{CoO}_{3+\delta}$  [164]) a higher rate increases stability.

In general, therefore, the growth rate is clearly one of the key parameters in the floating zone technique. For a successful growth, the growth speed needs to be precisely selected to obtain the best crystals, while most morphological changes occurring in the growing crystal can be explained on the basis of growth rate. The higher superconducting transition temperature ( $T_c$ ) obtained at lower growth rates in Bi-Sr-Ca-Cu-O [52],  $\text{Bi}_2\text{Sr}_2\text{Ca}_2\text{Cu}_3\text{O}_{10+\delta}$  [111] and  $\text{La}_{2-x}\text{Ba}_x\text{CuO}_4$  [131] clearly illustrates this link between the growth rate, crystal quality and properties.

### 2.1.3. Growth atmosphere and gas pressure

The type of atmosphere and its pressure during FZ crystal growth are other parameters that can be controlled during a growth and need to be selected according to the phase stability of the sample and thermodynamic data. In general, the growth atmosphere for oxides is selected to be pure oxygen (or oxygen mixed with argon) and for metallic samples is argon or vacuum due to potential oxidation at higher temperatures.

According to the literature, increasing the gas pressure around the sample increases the lamp power needed to melt the sample, leading to the general assumption that the melting point of the material increases under higher gas pressures, as reported for  $\text{Bi}_2\text{Sr}_2\text{CaCu}_2\text{O}_{8+x}$  [24,101,112],  $\text{La}_{2-x}\text{Sr}_x\text{CuO}_{4-\delta}$  [26],  $\text{Bi}_{2+x}\text{Sr}_{2-y}\text{CuO}_{6+\delta}$  [100],  $\text{CuO}$  [173] and  $(\text{La}_{1-x}\text{Sr}_x)_2\text{CaCu}_2\text{O}_{6+\delta}$  [176].

The other significant and functional effect of increasing the gas pressure is to reduce vapourization of volatile components from the sample both during heating before the melting temperature is attained and during the growth. This effect was found in crystal growth of materials such as  $\text{GeNi}_2\text{O}_4$  and  $\text{GeCo}_2\text{O}_4$  [163],  $\text{La}_{2-x}\text{Sr}_x\text{CuO}_{4-\delta}$  [26], A-doped  $\text{CuGeO}_3$  (A=Al, Mg, Ni, Si, Zn) [67],  $\text{Sr}_2\text{CuO}_2\text{Cl}_2$  [69], Nd-doped  $\text{YVO}_4$  [92],  $\text{La}_{1-x}\text{Sr}_x\text{MnO}_3$  [116],  $\text{Bi}_2\text{Sr}_{2-x}\text{La}_x\text{CuO}_{6+\delta}$  [140],  $\text{Na}_x\text{CoO}_2$  [147],  $\text{Pr}_5\text{Si}_3$  [149],  $\text{CaMn}_{1-x}\text{Mo}_x\text{O}_3$  [158] and R-doped  $\text{LuVO}_4$  (R=Nd, Tm, Yb) [167] where applying a higher gas pressure was beneficial to the growth of more stoichiometric single crystals of materials having higher vapour pressures.

Crystal growth investigations of the Bi-Sr-Ca-Cu-O system, a superconducting oxide, under different oxygen pressures, indicated a variation of both structure and superconducting transition temperature according to the applied pressure. In this system, increasing the oxygen pressure even slightly over the ranges 0.0005 to 1 bar [112] and 1 to 10 bar [24, 100, 101, 112], increased the lamp power required for melting leading to speculation that a higher melting temperature is achieved at higher gas pressures. Later, it was concluded that this apparent increase in the growth temperature decreased the surface tension and viscosity, and as a consequence, the stability of the molten zone was reduced [100-101]. However, an alternative report indicates that the molten zone stability is not sensitive to increases in oxygen pressure in the range from 0.0005 to 1 bar [112].

TSFZ crystal growth of this system also indicated that the content of Sr incorporated into the compound increased with increasing the pressure [24, 86, 100, 101], (easier incorporation of La into the  $\text{Bi}_2\text{Sr}_{2-x}\text{La}_x\text{CuO}_{6+\delta}$  structure [140] and higher Ca contents in  $\text{Sr}_{14-x}\text{Ca}_x\text{Cu}_{24}\text{O}_{41}$  single crystals [74] are also reported at higher oxygen pressures). In addition, a very distinct difference in the c-axis lattice parameter [24, 86, 100, 101,

112] and superconducting transition temperature [24, 101, 100, 112] of Bi-Sr-Cu-O crystals grown at different oxygen pressures is reported.

Second phase formation and inclusions are further defects whose introductions into the crystal are reported to be influenced by different types of atmospheres and pressures. For example, second phase formation was reported in  $\text{La}_{2-x}\text{Sr}_x\text{CuO}_{4-\delta}$  crystals at higher oxygen pressures, although crystal growth in air was successful [26]. Inclusions or second phases were found in  $\text{La}_2\text{NiO}_{4+\delta}$  crystals grown in argon, although no trace of other phases appeared after growth in air or in oxygen at pressures of 1, 3 and 5 bar [37]. In addition, the  $\text{Cr}^{+4}$  concentrations in Cr-doped  $\text{Mg}_2\text{SiO}_4$  crystals varied as a function of growth atmosphere [48], while deviation from the stoichiometric composition of  $\text{CuFeO}_{2+\delta}$  crystals was reported with increasing oxygen partial pressure in the surrounding atmosphere [60]. A pressure of 10 bar of argon was found to prevent formation of inclusions in  $\text{RB}_6$  single crystals [62]; fewer impurity phases were detected after applying a higher oxygen pressure for the growth of  $\text{Ca}_{2+x}\text{Y}_{2-x}\text{Cu}_5\text{O}_{10}$  crystals [102]. Rapid evaporation of components prevented growth in vacuum of  $\text{La}_{2-x}\text{Sr}_x\text{NiO}_{4+\delta}$  while the formation of second phases on the surface of crystals was found during growth in a flow of Ar gas at 1 bar, although growth was successful under a high pressure mixture of Ar+O<sub>2</sub> gas [117]. The precipitation of other phases on the surface of  $\text{ANb}_2\text{O}_6$  (A=Ni, Co, Fe, Mn) crystals [127], and other investigations on  $\text{La}_{2-x}\text{Ce}_x\text{CuO}_4$  [132], CaO-doped  $\text{YVO}_4$  [138] and Zn-doped  $\text{CaCu}_2\text{O}_3$  [171] also demonstrate the importance of the atmosphere and gas pressure during crystal growth using the floating zone method.

Sometimes higher gas pressures can be detrimental, however, as the occurrence of bubbles in the molten zone during crystal growth of  $\text{LuFe}_2\text{O}_4$  [7],  $\text{Bi}_2\text{Sr}_{2-x}\text{La}_x\text{CuO}_{6+\delta}$  [140] and in growing crystal of  $\text{Ca}_2\text{Co}_{1-x}\text{Zn}_x\text{Si}_2\text{O}_7$  [143], as well as molten zone penetration into the feed rod and more cracks in crystals of  $(\text{La}_{1-x}\text{Ca}_x)_2\text{CaCu}_2\text{O}_{6+\delta}$  [177] were also reported during growth under high oxygen pressures.

Attempts to prevent the formation of low angle grain boundaries in  $\text{TiO}_2$  (Rutile) single crystals grown by the FZ technique, have been made by controlling the oxygen partial

pressure of the growth atmosphere. The first work by Higuchi [10] indicated that an upper limit for the oxygen partial pressure of 0.01 bar was needed for growth of crystals without low angle grain boundaries, since growth under the pressure of 1 bar led to formation of such defects. However, other research by J.K. Park et al. [124] revealed that a single crystal of rutile grown under the oxygen pressure of 5 bar contained no low angle grain boundaries, yet applying pressures of 3, 4 and 8 bar led to crystals having the defect.

#### 2.1.4. Temperature gradient and molten zone temperature

The temperature distribution along the sample during growth is a natural characteristic of the FZ method and is reported to be an important factor in the technique.

A large temperature gradient along the growth direction can cause thermal stresses in the growing crystal which result in cracks developing and propagating, as reported in crystals of  $\text{NiAl}_2\text{O}_4$  [28],  $\text{Ba}_{1-x}\text{Sr}_x\text{TiO}_3$  [32], Cr-doped  $\text{Mg}_2\text{SiO}_4$  [35],  $(\text{Fe}_x\text{Mg}_{1-x})_2\text{SiO}_4$  [40],  $\beta_{II}\text{-Li}_3\text{VO}_4$  [54],  $\text{SrTiO}_3$  [137],  $\text{NiFe}_2\text{O}_4$  and  $\text{CoFe}_2\text{O}_4$  [160]. Attempts have been made to reduce thermal stresses and cracks in crystals using after-heaters (a heat source in connection with a lamp in crystal growth of  $\text{NiAl}_2\text{O}_4$  [28], or a tube-type furnace placed under the molten zone around the growing crystal of  $\text{NiFe}_2\text{O}_4$  and  $\text{CoFe}_2\text{O}_4$  [160]), or a heat reservoir around crystals during growing and cooling of  $\text{Ba}_{1-x}\text{Sr}_x\text{TiO}_3$  [32]. Growth of crack free crystals of Cr-doped  $\text{Mg}_2\text{SiO}_4$  and  $(\text{Fe}_x\text{Mg}_{1-x})_2\text{SiO}_4$  with this technique was also performed by other groups [35, 40].

Changes in the shape of the liquid/solid interface are also reported to be due to temperature gradients along the sample since the temperature of the crystal surface, just below the solid/liquid interface, relative to the temperature at the centre of the rod, is believed to control the shape of the interface. It is reported that if the longitudinal temperature gradient is very steep, the crystal, just below the solid/liquid interface, may not effectively absorb the heat from the lamp and can lose heat by radiation leading to a concave solid/liquid interface towards the melt. With a reduction in the temperature gradient, the surface of the crystal, just below the solid/ liquid interface, may retain the heat absorbed from the lamp more effectively and run at a higher temperature than the

centre. This could lead to a convex solid/liquid interface towards the melt [28]. However, while this theory was initially proposed to explain stable crystal growth in  $\text{NiAl}_2\text{O}_4$  with a lower temperature gradient along the crystal, no attempt was made to experimentally verify this interface shape (the same explanation was given in crystal growth of Cr-doped  $\text{Mg}_2\text{SiO}_4$  [35] and  $(\text{Fe}_x\text{Mg}_{1-x})_2\text{SiO}_4$  [40]).

Although the considerable temperature gradient applied to the sample in the FZ technique may be an inherent disadvantage due to possible crack formation, a steep temperature gradient can help to reduce the length of melting zone which can lead to a more stable zone, and also makes it possible to stabilize the growth conditions in the narrow crystallization field of crystals such as Bi-2223 crystals [99]. Successful crystal growths of  $\text{Ca}_2\text{CuO}_3$  [34],  $\text{Bi}_{12}\text{SiO}_{20}$  [56],  $\text{NdBa}_2\text{Cu}_3\text{O}_{7-\delta}$  [68],  $\text{Y}_2\text{Cu}_2\text{O}_5$  [83] and  $\text{Bi}_2\text{Sr}_2\text{Ca}_2\text{Cu}_3\text{O}_{10+\delta}$  [99, 111] are also reported using sharper temperature gradients.

On the whole, it can be concluded from the literature that the effect of the temperature gradient along a sample is a complicated subject that depends on several factors such as the type of image furnace, e.g. number of mirrors or lamps around the sample (FZ crystal growth using a four ellipsoidal mirror is expected to give a smaller radial temperature gradient in the sample than a single mirror or double mirror type image furnace), type of the lamps (xenon or halogen) [28], power of the lamps [99], lamp alignment), crystal properties (e.g. thermal conductivity, anisotropic thermal expansion [95], size,...), and other growth parameters (e.g. using a higher growth rate may alter the temperature gradient along the sample).

As well as the temperature distribution in the growing crystal, the molten zone itself can exhibit a range of temperatures (i.e. from the melting point upwards). If the maximum temperature in the zone is too high, however, this can lead to a long and unstable molten zone which collapses. Although a wide temperature range in the molten zone can be accommodated for lower density materials or those with lower thermal conductivity, float-zone growth at the lowest molten zone temperature at which stable and unperturbed growth of high quality crystals can be achieved, may still be desirable to prevent, for example, Mn evaporation during the growth of  $\text{La}_{1-x}\text{Sr}_{1+x}\text{MnO}_4$  [130].



### 2.1.5. Rotation rate

Independent rotation of the feed rod and the growing crystal in opposite directions (e.g. clockwise and counterclockwise) is another controllable experimental parameter during FZ. Rotation is usually used to ensure efficient mixing in the molten zone (liquid homogeneity) and a more homogeneous temperature distribution within the melt or, put another way, a more homogeneous heating environment around the sample, as reported in Ni-doped Bi-Sr-Ca-Cu-O [11],  $\text{Bi}_2\text{Sr}_2\text{CaCu}_2\text{O}_x$  [33],  $\text{Nd}_{0.7}\text{Sr}_{0.3}\text{MnO}_3$  and  $\text{La}_{0.5}\text{Ca}_{0.5}\text{MnO}_3$  [71],  $\text{Sr}_{14-x}\text{Ca}_x\text{Cu}_{24}\text{O}_{41}$  [74],  $\text{La}_{1.92}\text{Sr}_{0.08}\text{CuO}_{4+\delta}$  [80],  $\text{SrCu}_2(\text{BO}_3)_2$  [82],  $\text{Bi}_{2+x}\text{Sr}_{2-y}\text{CuO}_{6+\delta}$  [100],  $\text{Bi}_2\text{Sr}_2\text{Ca}_2\text{Cu}_3\text{O}_{10+\delta}$  [111] and  $\text{CaMn}_{1-x}\text{Mo}_x\text{O}_3$  [158].

It is reported that using a higher rotation rate, which enhances forced convection in the molten zone by transporting the heat absorbed on the melt surface, is an effective way to lower the convexity of the interface during growth of  $\text{R}_{9.33}(\text{SiO}_4)_6\text{O}_2$  (R=Pr, Nd, Sm) [151, 78], so giving a more stable molten zone. In addition, a more stable molten zone and a slightly convex growth front, which enhanced the morphological stability of the growing crystal, were achieved by controlling the rotation rate in Nd-doped  $\text{YVO}_4$  [104] and  $\text{Bi}_2(\text{Sr}_x\text{Ca}_{3-x})\text{Cu}_2\text{O}_y$  [141]. In general, however, the effect of this parameter has not been considered in many growths, possibly due to its complicated dynamic nature involving heat transformation, motion and force in the region near to the liquid/solid interface where the crystal is grown.

### 2.1.6. Conclusions drawn from a survey of the literature regarding FZ growth parameters and their potential effects

Overall, it can be concluded that the principal growth parameters (feed rod characteristics, growth rate, growth atmosphere and its pressure, temperature gradient and rotation rate) play key roles during growth of single crystals using image furnaces since crystal quality, growth stability and materials properties can all be affected by changing these experimental variables. The effect of these parameters becomes even more acute in the growth of ‘difficult’ materials, which may have unchangeable intrinsic properties such as high density, low surface tension or a complicated phase diagram.

The conclusions drawn from this survey of growth parameters and their possible influences during FZ growth are listed below.

### **Feed rod preparation**

- **Stability of molten zone**

A poorly compacted feed rod can lead to bubble formation in the molten zone or penetration of the melt into the feed rod.

- **Crystal quality**

A poorly compacted feed rod can lead to bubble formation in the growing crystal.

### **Growth rate**

- **Crystal size**

Crystal growth at lower growth rates generally yields larger crystals.

- **Second phases or inclusions and inhomogeneity in composition**

With many materials, slower growth rates give crystals with more homogeneous compositions or without second phases or inclusions. However, depending on the material and its phase stability, faster growth rates are sometimes needed to obtain crystals without inclusions.

- **Cracks**

Crack formation is reduced when lower growth rates are used.

- **Growth direction or crystal alignment**

Lower growth rates can lead to better crystal alignment and help to preserve the growth direction.

- **Low angle grain boundaries and twinning**

Both higher and lower growth speeds can suppress the formation of these defects, depending upon the material in question.

- **Bubbles**

A lower growth rate is favourable for growing bubble-free crystals.

- **Liquid/Solid interface**

In general, using a lower growth rate is more likely to give a planar growth front.

- **Molten zone stability**

The stability of a molten zone can be increased using either lower or higher growth speeds, depending upon the material in question.

### **Growth atmosphere and gas pressure**

- **Lamp power**

Increasing the gas pressure is reported to increase the lamp power needed to melt the sample.

- **Vapourization of volatile components**

Increasing the gas pressure reduces vapourization of volatile components from the sample.

- **Molten zone stability**

Increasing the gas pressure can reduce the molten zone stability in some materials.

- **Composition, crystal structure and properties**

The gas pressure can affect crystal composition (for example easier incorporation of doped elements could occur with increasing gas pressure), lattice parameters and crystal properties.

- **Second phase formation or inclusions**

Depending on the material, different growth atmospheres and gas pressures can affect the formation of second phases.

- **Bubbles**

Increasing the gas pressure can lead to bubble formation in the molten zone and growing crystal, as well as molten zone penetration into the feed rod.

- **Cracks**

More cracks in growing crystals sometimes occur at higher gas pressures.

- **Low angle grain boundaries**

Increasing or decreasing the gas pressure can lead to the formation of low angle grain boundaries in growing crystals, depending upon the material in question.

### **Temperature gradient and molten zone temperature**

- **Cracks**

Larger temperature gradients along the growth direction are more likely to cause cracking in the growing crystal due to thermal stresses.

- **Shape of the liquid/solid interface**

A sharper temperature gradient can lead to a concave solid/liquid interface toward the melt, while a reduction in the temperature gradient can give a convex interface.

- **Length and stability of the molten zone**

A steep temperature gradient helps to reduce the length of melting zone which can lead to a more stable molten zone.

- **Compositional homogeneity**

A lower molten zone temperature can help to prevent evaporation of components during growth and give a more homogeneous crystal.

### **Rotation rate**

- **Molten zone or liquid homogeneity**

Rotation is usually used to ensure efficient mixing in the molten zone.

- **Temperature distribution**

More homogeneous heating within the melt and around the sample can be achieved using rotation.

- **Liquid/solid interface**

Using a higher rotation rate can be a way of lowering the convexity of the interface, so giving a more stable molten zone.

## 2.2. Rutile ( $\text{TiO}_2$ )

### 2.2.1. Introduction

Titanium dioxide (Titania) crystallizes in three major allotropes: anatase (tetragonal,  $a=b=3.782 \text{ \AA}$  and  $c=9.502 \text{ \AA}$ ), brookite (orthorhombic,  $a=5.436 \text{ \AA}$ ,  $b=9.166 \text{ \AA}$  and  $c=5.135 \text{ \AA}$ ) and rutile (tetragonal,  $a=b=4.584 \text{ \AA}$  and  $c=2.953 \text{ \AA}$ ). The brookite and anatase crystalline phases, which although stable at low temperature, transform into rutile when the sample is calcined at temperatures above approximately  $800^\circ\text{C}$  then remain as rutile phase even after subsequent cooling to ambient temperatures. (Thermodynamic calculations based on calorimetric data predict that rutile is the stable phase at ambient temperatures and pressures up to 60 kbar). However, it is reported that brookite and anatase can be stabilized at higher temperatures if dopants are present during synthesis, so inhibiting their transformation into rutile [178].

Thermodynamic analyses of the nucleation of anatase and rutile from  $\text{TiO}_2$  melts have indicated that rutile crystallizes at temperatures slightly below melting point under conditions approaching equilibrium solidification, whereas the metastable anatase preferentially nucleates during rapid cooling at lower solidification temperatures with a high degree of undercooling [179]. Generally, however, rutile is the only form of significance in the context of bulk crystal growth due to the stability of the phase.

It has been demonstrated that some properties of titanium dioxide are very sensitive to its structure, crystalline form and oxidation state, which leads to several applications for the material. For example, titanium dioxide is a reducible metal oxide that exists in a variety of oxidation states, so it is used in many technical areas where high temperature reduction and oxidation processes play a role [180,178].

Applications for sintered titanium dioxide are limited by its relatively poor mechanical properties, although it finds a number of uses in electrical sensors and electrocatalysis. By far its most widely used application, however, is as a pigment for providing whiteness and opacity to products such as paints and coatings, where it is used in powder form. Titanium dioxide is also used in heterogeneous catalysis, as a photocatalist, in solar cells for the production of hydrogen and electric energy and as a gas or oxygen sensor.

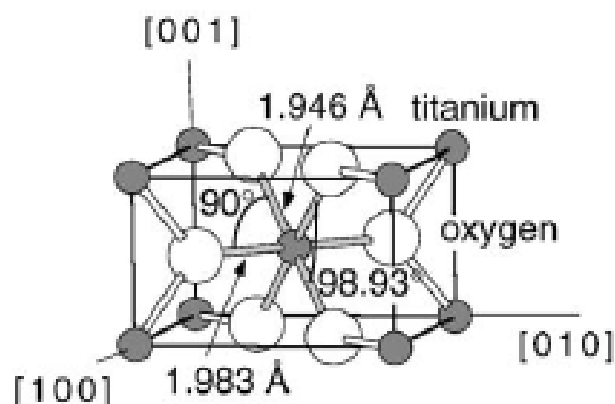
Because titania tends to lose oxygen and become sub stoichiometric even in mildly reducing atmospheres, becoming a semiconductor as it does so, the electrical resistivity of the material can be correlated with the oxygen content of the atmosphere to which it is exposed; hence, it can be used to sense the amount of oxygen or reducing species present in an atmosphere.  $\text{TiO}_2$  also finds uses as a corrosion-protective coating and as an optical coating [181].

While the anatase phase is chemically and optically active, making it suitable for catalysts and supports, rutile has the highest refractive index and ultraviolet absorption among the titania phases, thus it is employed in pigments, paints and ultraviolet absorbents [178].

### 2.2.2. Features of rutile single crystals

Because rutile crystals have a larger refractive index, larger birefringence characteristics and a wider transmission range than other forms of titania, rutile is more suitable for use in optical applications, including polarizers, polarizing prisms and optical isolators [181-182]. Rutile is also an excellent insulator at room temperature and has good mechanical properties with high thermal and chemical stability.

The crystal structure of rutile and some physical properties of the material are shown in Fig. 2.1 and Table 2.1 [181] respectively.



**Fig.2.1.** The tetragonal crystal structure of rutile; unit cell dimensions:  $a=b=4.584 \text{ \AA}$ ,  $c=2.953 \text{ \AA}$  [181]

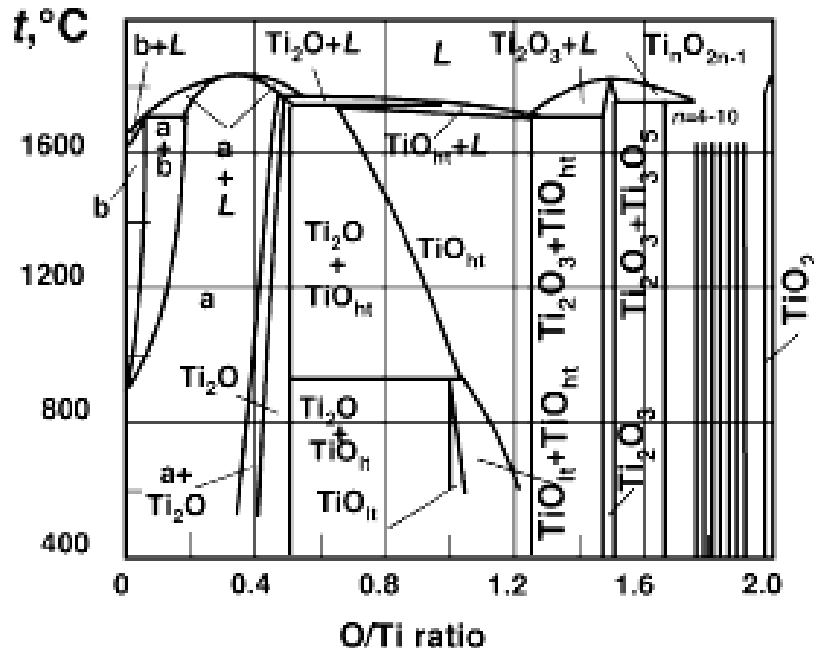
**Table 2.1.** Bulk properties of rutile (TiO<sub>2</sub>)

Chemical formula	TiO <sub>2</sub>
Atomic radius (nm)	O : 0.066 (covalent) Ti : 0.146 (metallic)
Crystal structure and lattice constant ( $\overset{\circ}{A}$ )	Tetragonal, $a=b=4.584$ and $c=2.953$
Density (g/cm <sup>3</sup> )	4.240
Melting point (°C)	≈1870
Thermal expansion coefficient (°C <sup>-1</sup> ) (Temperature range: 298-1883 K [183])	$\alpha_a = 8.9 \times 10^{-6}$ $\alpha_c = 11.1 \times 10^{-6}$
Hardness (Mohs)	6-6.5
Electrical resistivity ( $\Omega\text{m}$ )	$1.0 \times 10^{10}$ at temperature=298 K $3.0 \times 10^5$ at temperature=773 K $1.2 \times 10^2$ at temperature=1073 K
Refractive index at 1.55 $\mu\text{m}$ (wavelength)	$n_o = 2.452$ $n_e = 2.709$
Birefringence at 1.55 $\mu\text{m}$ (wavelength)	0.257

A more detailed compendium of bulk properties of rutile is given in [184].

The titanium-oxygen phase diagram exhibits many phases with a variety of crystal structures; see Fig. 2.2 [185]. Rutile can be reduced by heating bulk single crystals in either vacuum or a reducing atmosphere, leading to visible colour changes from transparent to light and, eventually, dark blue [180].

A systematic investigation by Diebold [180] and Li [186] demonstrated that the reduction of rutile single crystals, which is closely related to the crystal colour (the colour is correlated with heating temperature rather than time), changes the resistivity of the crystals from ~10  $\Omega\text{.cm}$  (blue crystals) to ~1000  $\Omega\text{.cm}$  (bright crystals) measured at 300 K. Electron paramagnetic resonance (EPR) also revealed that darker rutile crystals (i.e. oxygen deficient) exhibit higher concentrations of extended Ti<sup>3+</sup> with a decrease in substitutional defects (related to O vacancies) and Ti interstitials as compared to lighter coloured crystals [180].



**Fig.2.2.** Phase diagram of the Ti-O system. The region  $Ti_2O_3$ - $TiO_2$  contains  $Ti_2O_3$ ,  $Ti_3O_5$ , seven discrete phases of  $Ti_nO_{2n-1}$  (Magnelli phases: homologous series of shear structures in phase regions previously believed to be continuous solid solutions) and  $TiO_2$  [185]

Overall, the bulk structure of reduced  $TiO_{2-x}$  crystals is quite complex with various types of defects (such as charged oxygen vacancies,  $Ti^{3+}$  and  $Ti^{4+}$ ) and the defect structure varies with oxygen deficiency which depends on temperature, impurities, etc. Despite years of research, the question of which type of defect is dominant in which region of oxygen deficiency, is still subject to debate [181].

### 2.2.3. Bulk crystal growth of rutile ( $TiO_2$ )

Rutile crystals can be grown using a variety of techniques; for example, crystal growth was reported as long ago as 1962 using the Verneuil method, although the crystals so produced were reported to have high dislocation densities [187]. Over the past decade, the floating zone method (FZ) has become increasingly used for the preparation of single crystal rutile rods. Since rutile is not a conductor, infra red heating has been employed during FZ rather than the induction or electron beam heating methods that are



often associated with FZ. Generally, rutile crystals grown by this method have often not been of suitable quality for device applications, however, since typical defects have included low angle grain boundaries, bubble inclusions and colour changes from the pale yellow of stoichiometric  $\text{TiO}_2$  to blue colours characteristic of oxygen deficient Magnelli phases ( $\text{Ti}_n\text{O}_{2n-1}$ ).

Several publications have described studies aimed at increasing the perfection of rutile crystals produced using image furnaces [188-195]. Many of these studies have attempted to determine to what extent the crystal quality is dependent upon the oxygen pressure in the growth chamber and/or the crystal growth rate, but there appears to be little consistency within the literature as to the results. For example, Higuchi et al. [188] state that the formation of low angle grain boundaries was depressed by float zoning under low oxygen pressures (e.g.  $1 \times 10^3$  Pa), while Park et al. [193] reported that crystals grown under higher oxygen pressures ( $5 \times 10^5$  Pa) contained fewer low angle grain boundaries compared to crystals grown under a pressure of  $1 \times 10^5$  Pa.

Later work by Park et al. [194] concluded that FZ under an oxygen pressure of  $5 \times 10^5$  Pa also ‘produced bright and transparent crystals due to the concentration of interstitial  $\text{Ti}^{3+}$  ions’, whereas rutile grown at an oxygen partial pressure of  $1 \times 10^3$  Pa ‘exhibited a deep dark colour of the whole crystal due to their solid state growth behaviours’.

Alternative approaches to the problem of improving the quality of image furnace grown crystals have included studying the effects of doping  $\text{TiO}_2$  with small quantities of other oxides such as  $\text{ZrO}_2$ ,  $\text{Sc}_2\text{O}_3$  and  $\text{Al}_2\text{O}_3$  [189–191]. However, transparent and grain boundary free crystals still proved to be difficult to prepare.

Very recent work by Higuchi et al. [195] concluded that having a small crystal diameter of about 3 mm was the key to preparing high quality rutile crystals by the optical FZ method, stating that crystals grown at rates of up to 60 mm/h under oxygen partial pressures of  $1 \times 10^3$  Pa did not contain low angle grain boundaries. However, they also reported that use of growth rates above 40 mm/h led to the incorporation of a number of bubbles within the as grown crystals.

### 2.3. Cobalt-doped TiO<sub>2</sub> and its magnetic properties

#### 2.3.1. Introduction

In the quest for ways to make electronic devices smaller, cheaper, and faster, a promising new field of research is emerging in spintronics [198]. Spintronics is a new and more powerful branch of electronics in which the spin property of electrons, in addition to their charge, is utilized to achieve greater efficiency and functionality. The most common spintronics device is the spin-valve, which is the main component of computer hard-drive read heads. Future advances will rely on the integration of spintronics in conventional semiconductor technology, resulting in what has been dubbed: semiconductor spintronics. This new branch of electronics may lead to advances in the fields of optoelectronics, spin quantum devices, and quantum computing, but its ultimate success hinges on the resolution of several issues that can be stated broadly as spin generation, injection, transport, and detection.

Mn-doped GaAs is an example of the early and ongoing efforts with diluted magnetic impurities in III-V semiconductors which produced successful ferromagnetic semiconductors at low temperatures [199]. The search for ferromagnetism in a semiconductor at room temperature was accelerated with the predictions of Dietl et al. [200] who performed an exhaustive theoretical study of potential candidate materials in 2000. They notably predicted room temperature ferromagnetism for 5% Mn doped ZnO. An increased sense of enthusiasm for magnetically doped semiconductors arose with the discovery of room-temperature ferromagnetism in cobalt-doped anatase TiO<sub>2</sub> thin films by Matsumoto et al. in 2001 [201]. Here Ti<sub>1-x</sub>Co<sub>x</sub>O<sub>2</sub> films (0 ≤ x ≤ 0.08) were produced on LaAlO<sub>3</sub> (001) and SrTiO<sub>3</sub> (001) substrates by combinatorial laser molecular beam epitaxy (MBE) at oxygen partial pressures of 10<sup>-6</sup>-10<sup>-5</sup> Torr and temperatures of 677-727 °C. Although titanium dioxide itself is a diamagnetic material, these thin films were reported to be ferromagnetic even above 400 K with a magnetic moment of 0.32 μ<sub>B</sub>/Co (Bohr magneton per cobalt atom). More characterization of these films using XRD and TEM techniques indicated no sign of segregation of impurity phases in the Co/Ti compositional range of x < 0.08. Such films were reported to be optically transparent,

semiconducting and ferromagnetic at room temperature, and might be ideal candidates for spin-based electronic devices.

### 2.3.2. Current state of affairs

Since the discovery of ferromagnetic behaviour in Co-doped TiO<sub>2</sub>, the material has been studied extensively using a wide variety of thin film growth methods by several groups [202-223]. An ongoing controversy surrounding Co-doped TiO<sub>2</sub> is determining the mechanism giving rise to ferromagnetism. The observed ferromagnetism behaviour leads to the question of whether the cobalt atoms really incorporate into the TiO<sub>2</sub> (rutile or anatase) structure by substituting Ti atoms or form Co clusters.

Following Matsumoto's report [201], some studies supported the theory that cobalt is well incorporated (not clustered) in Co-doped anatase [202-205]. However, Kim et al. in 2003 [206] claimed that Co clusters in the host structure were responsible for the high temperature magnetic behavior in Co-doped anatase TiO<sub>2</sub> thin films, meaning that the ferromagnetism is due to a secondary phase, rather than being an intrinsic property of the host material. The formation of Co clusters was also supported in the other reports [207-212].

A possible factor influencing the Co distribution could be the presence of oxygen vacancies, as indicated by later work of Kim et al. [211], who investigated the influence of the oxygen partial pressure ( $P_{O_2}$ ) during growth on the Co distribution in epitaxial anatase films grown on SrTiO<sub>3</sub> substrates by pulsed laser deposition (PLD). They found an increasing tendency of Co to cluster, and with it an increasing magnetic moment per Co atom, with decreasing  $P_{O_2}$ ; these results were also supported by Murakami [213] and Stampe [210]. Although the presence of oxygen vacancies is reported to enhance the ferromagnetism [214-215], they also affect both the electronic and optical properties as reported by H. Weng [215].

The reported room temperature magnetic moments ( $\mu$ ) in Co-doped TiO<sub>2</sub> range from  $\sim 0.1 \mu_B/\text{Co}$  [206] to values as high as  $\sim 2.0 \mu_B/\text{Co}$  [212]. These contradictory results suggest that the magnetic properties of Co-doped TiO<sub>2</sub> films depend heavily on the method and conditions of sample preparation [216].

Overall, the thin film work on Co-doped  $\text{TiO}_2$  covers a wide range of techniques and the results are often contradictory. Appendix B attempts to collate the reported work in terms of technique, preparation conditions (i.e. substrate, temperature, type of atmosphere and gas pressure), structural characterization and magnetic characterizations, while any conclusions from the authors as to the origin of any ferromagnetic properties are also included.

Although the origin of the ferromagnetism observed in Co-doped  $\text{TiO}_2$  films, both anatase and rutile, is not clear at present, if the magnetism is intrinsic in nature, one should see similar behaviour in bulk samples, where effects on the microstructure and the magnetic interaction due to lattice mismatch between substrate and thin film are obviously eliminated.

Also, it is noted that the formation of  $\text{CoTiO}_3$  and  $\text{CoTi}_2\text{O}_5$  phases, which are known to exist in the bulk Co-Ti-O phase diagram, was not reported in thin films.

### 2.3.3. Magnetic properties of Co-doped $\text{TiO}_2$ bulk samples

A few research groups have used bulk samples to investigate magnetic properties of Co-doped  $\text{TiO}_2$ , for example polycrystalline powders prepared by solid state reaction [224] or sol-gel [225-226] methods, and cobalt implanted single crystalline rutile samples in which (100) and (001) faces were irradiated [227].

In the first work by Joh et al. [224], the structural and magnetic properties of  $\text{Ti}_{1-x}\text{Co}_x\text{O}_2$  powders were studied with various Co concentrations ( $x=0.01-0.10$ ) synthesized using a solid state reaction ( $900^\circ\text{C}$  for 24 h in an evacuated quartz tube under the pressure of  $<10^{-6}$  Torr). The magnetization measurements showed room temperature ferromagnetism in this material, but the magnetic moment per Co atom decreased significantly as the cobalt concentration was increased. This reduction of magnetization was attributed to the second phase formation of  $\text{CoTiO}_3$  for Co concentrations higher than  $x=0.02$  (magnetization measurements of pure  $\text{CoTiO}_3$  prepared using a solid state reaction showed paramagnetic behaviour with a magnetization much smaller than that of

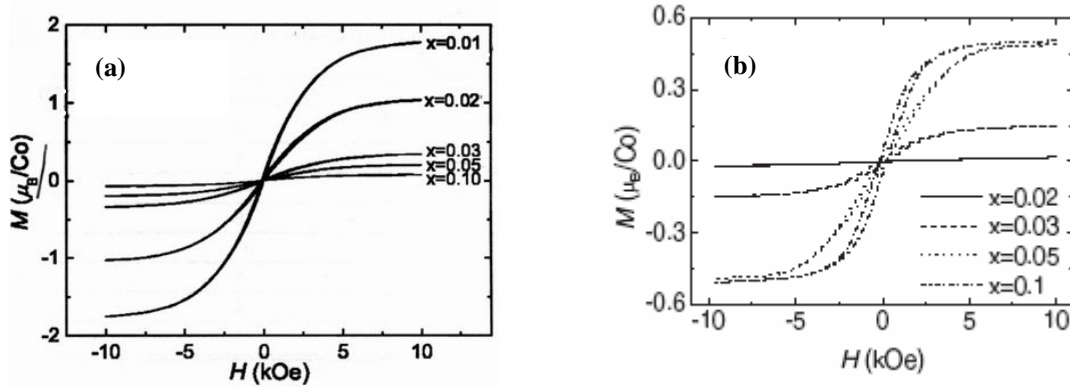
Co-doped  $\text{TiO}_2$ ). The reported room temperature magnetic moments in these powders ranged from  $\sim 1.8 \mu_B/\text{Co}$  for  $x=0.01$  to  $\sim 0.05 \mu_B/\text{Co}$  for  $x=0.10$  (Fig. 2.3.a).

Later work by Joh et al. [225] reported enhanced ferromagnetism in  $\text{Ti}_{1-x}\text{Co}_x\text{O}_2$  powder samples prepared using the sol-gel method and annealed in vacuum. In this report, the precursor annealed at 770 K for 5 h at a pressure of  $10^{-6}$  Torr, showed enhanced ferromagnetism at room temperature, but when the same precursor was annealed at 770 K for 5 h in air, only paramagnetic behaviour was observed. Structural studies showed dominant anatase and minor rutile phases in the vacuum-annealed samples, while the  $\text{CoTiO}_3$  phase was observed in air annealed samples. This led to the conclusion that the enhanced magnetization in the vacuum-annealed samples was due to oxygen deficiency which prevented the formation of  $\text{CoTiO}_3$ . It was also reported that a reduced oxygen environment can promote the clustering of Co-rich clusters as evidenced by transmission electron microscopy in samples where  $x=0.1$ , thus giving rise to an enhanced ferromagnetic behaviour. However, no direct observation of Co clusters in samples with  $x \leq 0.05$  was made.

Contrary to their earlier work [224], the values of magnetic moment for enhanced ferromagnetism samples [225] was reported to be  $\sim 0.45 \mu_B/\text{Co}$  for  $x=0.1$ , but almost zero for  $x=0.02$  (Fig. 2.3.b).

As shown in Fig. 2.3.a [224] and 2.3.b [225], not only were the magnetization values found to be of different magnitude between the two studies, but as the cobalt concentration increased, the magnetization decreased in Fig. 2.3.a, while in Fig. 2.3.b the magnetization increased.

Further work by Hui et al. [226] showed that  $\text{Ti}_{0.96}\text{Co}_{0.04}\text{O}_2$  powders fabricated by the sol-gel method (at  $450^\circ\text{C}$  for 1 h) exhibited a small magnetic moment of  $0.029 \mu_B$  per Co atom for the samples annealed in air, while the powders annealed in vacuum had strong room temperature ferromagnetism with a large magnetic moment of  $1.18 \mu_B$  per Co atom which is not consistent with the previous work of Joh et al. [225].



**Fig.2.3.** Magnetization vs. magnetic field curves at room temperature for  $\text{Ti}_{1-x}\text{Co}_x\text{O}_2$  powders, (a) ref. [224] and (b) ref. [225]

To find out more about the possible origins of ferromagnetism and magnetic anisotropy in Co-doped  $\text{TiO}_2$ , Akdogan et al. [227] used substrates of single crystalline rutile plates which were implanted with Co ions. Although they reported in-plane magnetic anisotropy of the (100) and (001) samples using hysteresis loops, they did not give details of the substrate conditions and preparation techniques. Two main mechanisms were suggested for the observed ferromagnetism; the first was the formation of a Co nanogranular layer within the irradiated region of rutile and the second one was that magnetic  $\text{Co}^{2+}$  ions occupying titanium lattice sites may be strongly exchange coupled via electrons trapped by charge-compensating oxygen vacancies.

Overall, it can be concluded from the literature that the origin of ferromagnetism in Co-doped  $\text{TiO}_2$  is not clear yet and more work needs to be carried out to understand the ferromagnetic interaction mechanism in this material.

It is also worth mentioning that based on XRD measurements, the reported solubility limit of Co ions in anatase and rutile *thin films* is different, as shown in Fig. 2.4 [228]. However, the solubility limit in films could be different from that of bulk because the non-equilibrium conditions pertaining in thin film preparation may make it possible to achieve more highly doped material than is possible under the equilibrium conditions represented in bulk growth.

Knowledge of the phase relations for the Ti-Co-O ternary system is also essential for study of bulk samples; Fig. 2.5 shows the phase relations in the  $\text{CoO-TiO}_2$  pseudo-binary system which was determined by the quenching technique [229]. As shown in the

diagram, three crystalline phases  $\text{TiO}_2$ ,  $\text{CoTi}_2\text{O}_5$  and  $\text{CoTiO}_3$  are stable at lower concentrations of  $\text{CoO}$ .

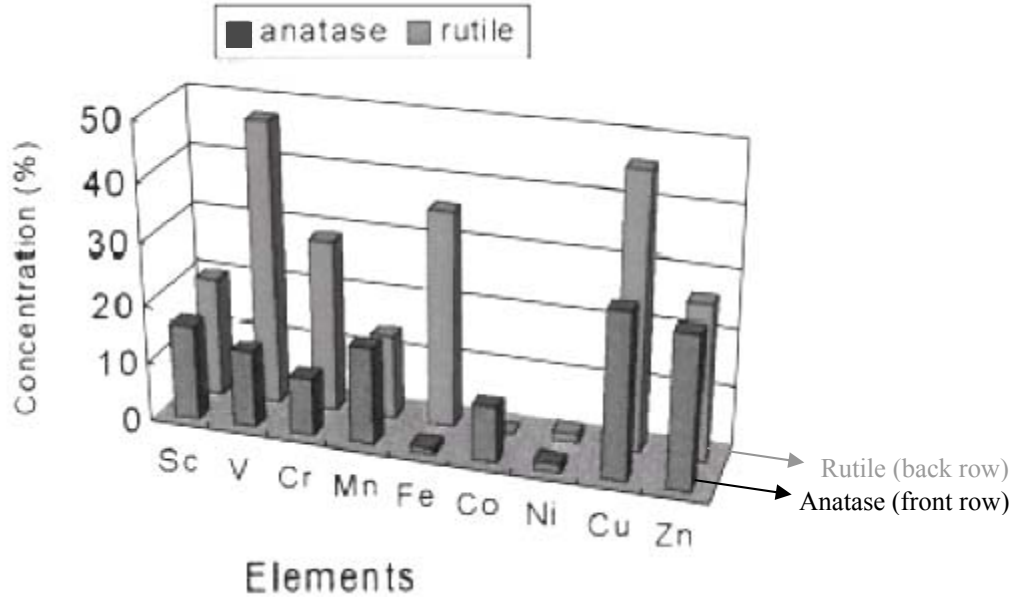


Fig.2.4. Solubility limits of different transition metal ions in anatase and rutile thin films [228]

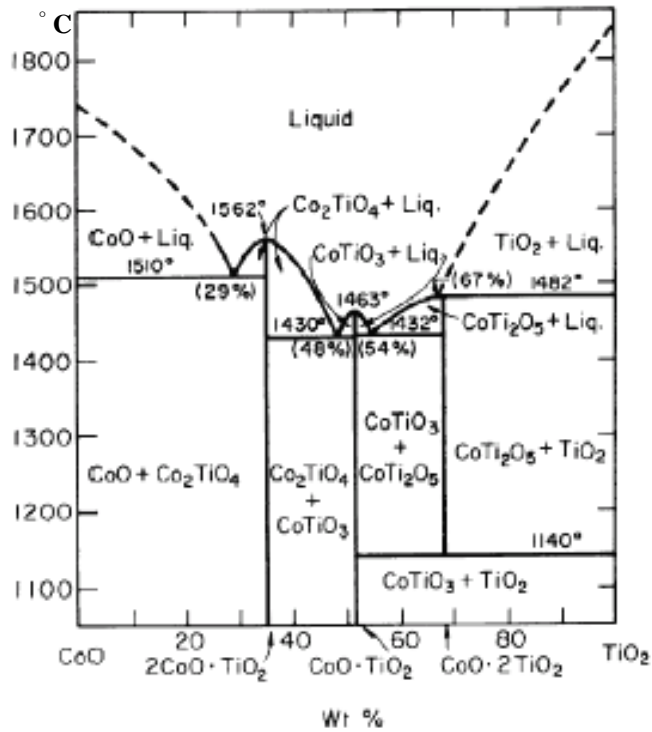


Fig.2.5. phase relations in the system  $\text{CoO-TiO}_2$  [229]

## 2.4. Rare earth orthoferrites

### 2.4.1. Introduction

Rare earth orthoferrites with the general formula  $R\text{FeO}_3$  (where  $R$  is a rare earth ion) belong to the widely studied family of transition metal oxides with an orthorhombically distorted perovskite structure. These materials have attracted interest since the 1950's due to their novel magnetic and magneto-optic properties and are still the subject of much research aimed at a better understanding of properties of the magnetic subsystems (one on the rare-earth ions and another on the iron ions) and how interactions between them depend on external parameters, such as temperature, field, pressure, etc., [230-233].

Along with fundamental property measurements, research into possible device applications of orthoferrites has also been undertaken by many groups; in particular, in the 1960's and 1970's, the magnetic domain behaviour in these materials led to a large number of investigations looking at potential applications for orthoferrites as memory or logic devices [234-236], as well as for pattern processing [237]. Although orthoferrites have since been overtaken by ferromagnetic garnets for magnetic bubble devices, interest in orthoferrites again took off in the 1990's, particularly from the viewpoint of their domain wall dynamics, for the velocity of the domain wall motion (at up to 20 km/s) is reported to be the highest known in any magnetically ordered media [238-240]. Recent investigations by Didosyan et al. [241-249], report that orthoferrites show much promise for use in various innovative micro-technological devices such as magnetic sensors, magneto-optical current sensors, light spot position measurers, magneto-optical rotational speed sensors and fast latching optical switches.

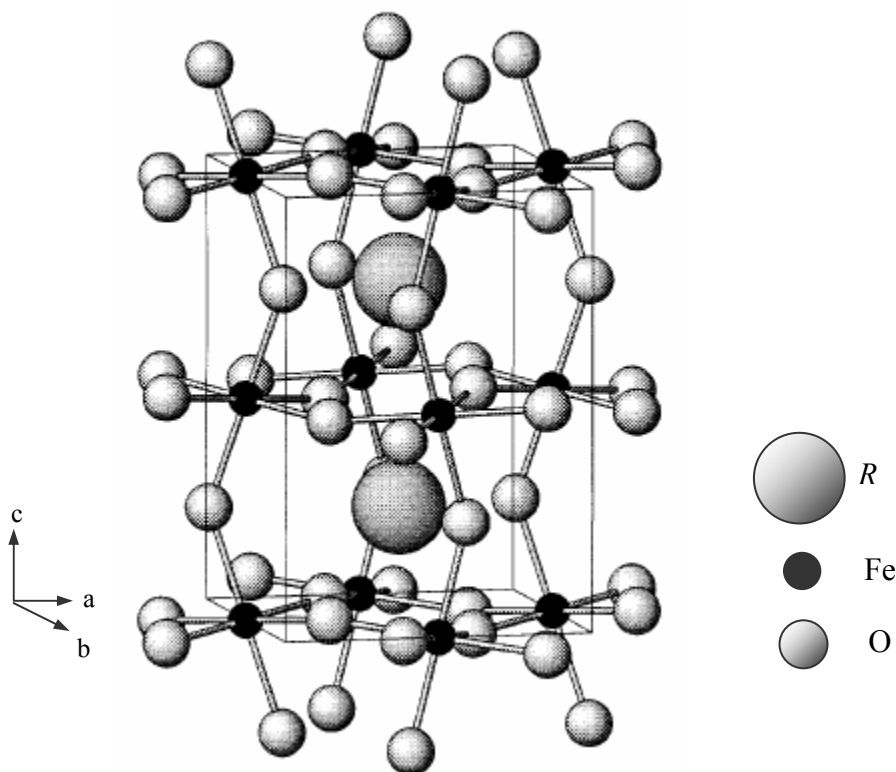
### 2.4.2. Features of orthoferrites

In the ideal perovskite structure ( $ABO_3$ ), which belongs to the cubic space group  $Pm\bar{3}m$ , the  $A$  cation is surrounded by 12 oxygen ions in a regular dodecahedral environment and the  $B$  cation is octahedrally coordinated by 6 oxygen ions, giving rise to a  $180^\circ$  B-O-B bond angle. Distortion from the ideal structure is largely related to a mismatch between  $A$ -O and B-O bond distances. If the  $A$  cation is replaced by a smaller one,  $BO_6$



octahedrons would rotate about the cubic crystallographic axis to release the structural stress. The cooperative rotation of the  $\text{BO}_6$  octahedron consequently leads to a decrease in the B-O-B bond angle and a reduction in the coordination number of  $A$  cations. Such distortions, controlled by different  $A$  cations for the same B cation, play crucial roles in metal-insulator transition, magnetoresistance, spin transition, etc., because the electronic structure in perovskite is strongly dependent upon the B-O-B bond angle [250].

The series of orthoferrites  $R\text{FeO}_3$ , where  $R$  is rare earth, crystallize in the orthorhombically distorted perovskite structure (space group:  $Pbnm$ ), which is a common arrangement for many  $\text{ABO}_3$  compounds. The crystallographic unit cell, shown in Fig. 2.6, contains four equivalent iron ions. The distortion of the perovskite structure is such that the iron environment remains essentially octahedral, however the axes of the four octahedral sites are in different directions (with increasing rare earth atomic number, the orthorhombic distortion increases) [251].



**Fig.2.6.** Crystal structure of orthoferrites ( $R\text{FeO}_3$ ) [250]

The lattice constants, volume per unit cell and density of some rare earth orthoferrites calculated from X-ray powder data are shown in table 2.2 [251]

**Table 2.2.** Crystallographic constants of orthoferrites ( $R\text{FeO}_3$ )

$R$	$a (\text{Å})$	$b (\text{Å})$	$c (\text{Å})$	Vol. per unit cell ( $\text{Å}^3$ )	X-ray density ( $\text{g/cm}^3$ )
Tb	5.326	5.602	7.635	227.8	7.66
Dy	5.302	5.598	7.623	225.6	7.84
<b>Y</b>	<b>5.283</b>	<b>5.592</b>	<b>7.603</b>	<b>224.6</b>	<b>5.70</b>
Ho	5.278	5.591	7.602	224.3	7.96
<b>Er</b>	<b>5.263</b>	<b>5.582</b>	<b>7.591</b>	<b>223.0</b>	<b>8.07</b>
Tm	5.251	5.576	7.584	222.1	8.16
Yb	5.233	5.557	7.570	220.1	8.35
Lu	5.213	5.547	7.565	218.8	8.46

The temperature dependence of the lattice parameters ( $a$ ,  $b$  and  $c$ ) has also been measured for some orthoferrites, such as  $\text{ErFeO}_3$  [252] and  $\text{YFeO}_3$  [253], and table 2.3 shows changes of lattice parameters (measured using X-ray diffraction) for  $\text{ErFeO}_3$  in the 10-300 K temperature range and (using neutron diffraction) for  $\text{YFeO}_3$  between 300 and 900 K. These results clearly indicate the anisotropic thermal expansion behaviour of these orthoferrites, particularly for  $\text{ErFeO}_3$  where  $\alpha_a/\alpha_b$  is about 2.125.

**Table 2.3.** Thermal expansion of  $\text{ErFeO}_3$  and  $\text{YFeO}_3$  lattice parameters

<b>ErFeO<sub>3</sub></b> 10-300 K	$\alpha_a = 8.875 \times 10^{-6} \text{ K}^{-1}$	$\alpha_b = 4.176 \times 10^{-6} \text{ K}^{-1}$	$\alpha_c = 9.672 \times 10^{-6} \text{ K}^{-1}$
<b>YFeO<sub>3</sub></b> 300-900 K	$\alpha_a = 8.130 \times 10^{-6} \text{ K}^{-1}$	$\alpha_b = 12.142 \times 10^{-6} \text{ K}^{-1}$	$\alpha_c = 12.747 \times 10^{-6} \text{ K}^{-1}$

The presence of two magnetic subsystems (one on the rare-earth ions and another on the iron ions) in the crystal structure of rare earth orthoferrites has made the magnetic properties of these materials very interesting, albeit complicated, since there is competition between Fe-Fe, R-Fe and R-R interactions. At ambient temperatures the magnetic properties of  $R\text{FeO}_3$  systems depend mainly on the Fe-Fe interactions which

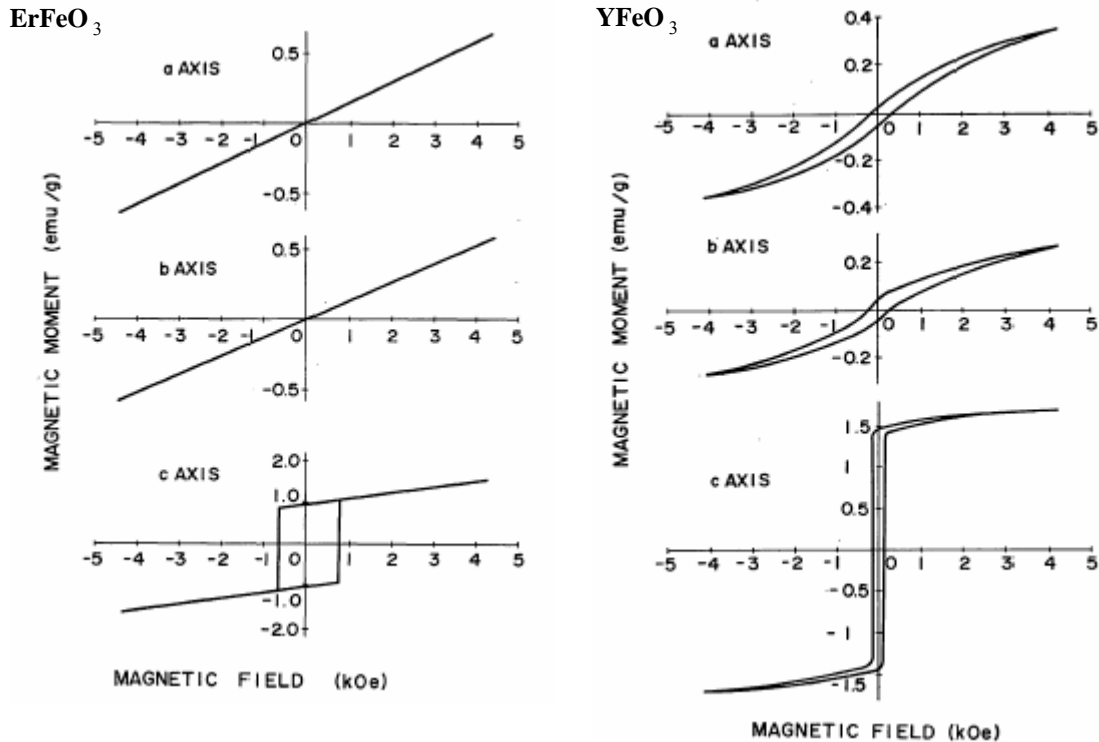
leads to antiferromagnetic type ordering with Neel temperatures ranging from 623 K (Lu) to 740 K (La) as shown in Table 2.4 [254].

Most members of the rare earth orthoferrite family are classed as canted antiferromagnets, for example in  $\text{ErFeO}_3$  and  $\text{YFeO}_3$  the atomic moments align at an angle to the c-axis such that the components of magnetisation perpendicular to the c-axis cancel out, whereas the components of atomic magnetisation parallel to the c-axis give a weak spontaneous magnetisation in the c-axis.

**Table 2.4.** The Neel temperature in rare earth orthoferrites

R	La	Pr	Nd	Sm	Eu	Gd	Tb	Dy	Y	Ho	Er	Tm	Yb	Lu
$T_N$ (K)	740	707	687	674	662	657	647	645	<b>640</b>	639	<b>636</b>	632	627	623

Fig. 2.7 shows magnetization curves indicating a strong uniaxial magnetic anisotropy measured at room temperature on single crystals of erbium and yttrium orthoferrites which were grown using the flux technique by Mikami [255].

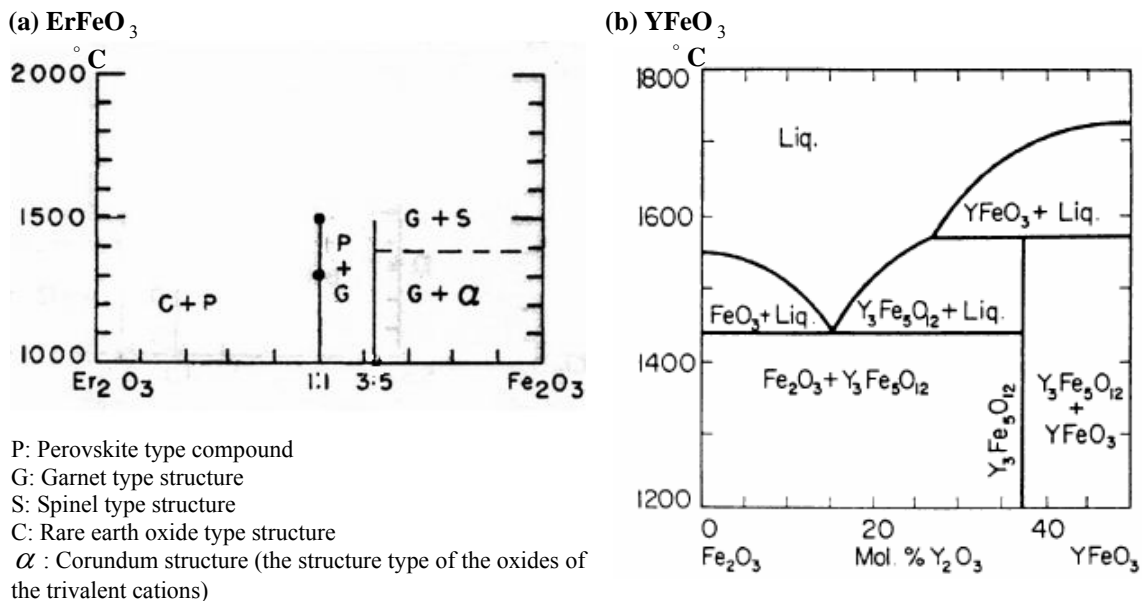


**Fig.2.7.** Magnetization curves of  $\text{ErFeO}_3$  (left) and  $\text{YFeO}_3$  (right) single crystals grown by the flux technique [255]

### 2.4.3. Bulk crystal growth of rare earth orthoferrites

#### 2.4.3.1. Phase diagram information for rare earth orthoferrites

Comprehensive constitutional information for R-Fe-O ternary systems is clearly desirable to explain the solidification behaviour of orthoferrites during bulk crystal growth. Unfortunately, such information is scarce, although not entirely absent. For example, Schneider et al. [256] performed phase equilibrium studies of several  $R_2O_3$ - $Fe_2O_3$  systems (where  $R$ =Nd, Sm, Eu, Dy, Ho, Er, Tm and Yb), and while the subsolidus binary phase diagrams reported did not specify any solidus and liquidus lines, they did predict that phases such as garnets (i.e.  $R_3Fe_5O_{12}$  type) and other rare earth oxide type structures would exist near to the  $RFeO_3$  composition, as shown in Fig. 2.8.a for  $ErFeO_3$ . Van Hook [257] gave a more complete phase diagram for the  $Y_2O_3$ - $Fe_2O_3$  system (Fig. 2.8.b), which shows a garnet phase as being stable up to 50 mole%  $Y_2O_3$  along with other phases such as orthoferrite, magnetite and hematite. Nielsen and Blank [258] confirmed this work, but reported that other systems (where  $R$ =Dy and Yb) behave differently since no stable region of  $Yb_3Fe_5O_{12}$  or  $Dy_3Fe_5O_{12}$  (i.e. similar to  $Y_3Fe_5O_{12}$  in the  $Y_2O_3$ - $Fe_2O_3$  system) formed.



**Fig.2.8.** Phase diagrams of (a)  $ErFeO_3$  [256] and (b)  $YFeO_3$  [257]

Also, rapidly quenched  $\text{Yb}_2\text{O}_3\text{-Fe}_2\text{O}_3$  melts prepared in air near the 50 mole%  $\text{Fe}_2\text{O}_3$  composition contained previously unreported, non-magnetic, oxides such as  $\text{Yb}_6\text{Fe}_6\text{O}_{17}$  or  $\text{Yb}_{1.05}\text{Fe}_{0.67}^{3+}\text{Fe}_{0.28}^{2+}\text{O}_{2.86}$  [258]. Recent studies of phase stability of  $R_2\text{O}_3\text{-Fe}_2\text{O}_3$  systems by Wu and Li [259] have also predicted the formation of both  $R\text{FeO}_3$  perovskites and other non-identified complex oxides in the  $\text{Er}_2\text{O}_3\text{-Fe}_2\text{O}_3$  and  $\text{Y}_2\text{O}_3\text{-Fe}_2\text{O}_3$  systems.

#### 2.4.3.2. Growth of rare earth orthoferrites by the flux method

The first technique used to grow rare earth orthoferrite crystals was the flux method, employed by Remeika in 1956 [260], with  $\text{PbO}$  as the flux. Several modifications to the technique were reported during the 1960s by Remeika et al. and other groups [261-265], but the crystals prepared always had  $\text{Pb}$  as a contaminant due to the flux constituents. For example, chemical analysis of  $\text{LaFeO}_3$  crystals grown using the system  $\text{PbO}(\text{B}_2\text{O}_3)_x$  as a flux [264], indicated that about 13.4 weight % of the rare earth was substituted by lead. While such substitution was most serious for rare earths with larger ionic radii, it was still detectable in compounds of the smaller rare earths leading to the authors' conclusion that any flux system containing lead would probably act in a similar manner. The as-grown crystals produced by Remeika and Kometani were typically  $10 \times 5 \times 2$  mm in size.

In 1969, Wanklyn [266] found that a flux consisting of  $\text{PbO-PbF}_2\text{-B}_2\text{O}_3$  was suitable for the preparation of some orthoferrites, but attempts to produce  $\text{YFeO}_3$  crystals with the same proportions of flux as for  $\text{ErFeO}_3$  were not successful. Also, she reported the formation of second phases such as oxyfluorides and garnets in the crystals with smaller rare earth ions. This tendency to form a second phase was reported to be related to the radius of the rare earth ion and to the ratio of  $\text{PbO/PbF}_2$ . The crystals so produced were up to 10 mm in size and back reflection Laue X-ray photographs taken over three faces of the largest crystal of  $\text{GdFeO}_3$  showed no indication of twinning.

Orthoferrite single crystal growth in  $\text{PbO-PbF}_2$  and  $\text{PbO-PbF}_2\text{-B}_2\text{O}_3$  fluxed melts were studied by Giess et al. in 1970 [267], with particular attention being given to crystal morphology and perfection. They reported that crystals from 2 to 10 mm in size were located, mostly at the melt surface, with  $\{110\}$  or  $\{001\}$  faces in the plane of the surface. A few crystals also formed in the melt, away from the surface on the crucible wall. The

single crystals so produced typically contained defects, such as dendritic structures (especially in regions of crystals formed during the early stages of growth), planar bands or striations (which were parallel to the growth interfaces), low angle grain boundaries and twins.

Second phase formation of rare earth oxyfluorides (ROF),  $\text{PbFe}_{12}\text{O}_{19}$  or  $\text{R}_3\text{Fe}_5\text{O}_{12}$ , in flux grown rare earth orthoferrites has been related to the growth dynamics and the volatilization loss of  $\text{PbF}_2$  in  $\text{PbO-PbF}_2\text{-B}_2\text{O}_3$  flux melts [268]. In this case, a study of orthoferrite crystals of Ytterbium, Yttrium and Samarium-Terbium showed that the orthoferrite phase was only obtained when the volatilization loss of  $\text{PbF}_2$  was sufficiently large and low  $\text{PbF}_2$  losses resulted in crystals of rare earth oxyfluoride,  $\text{PbFe}_{12}\text{O}_{19}$  or  $\text{R}_3\text{Fe}_5\text{O}_{12}$  being crystallized from the flux.

Damen [269, 271] used a specific time-temperature program to determine the nucleation temperature and growth rate of flux grown  $\text{YbFeO}_3$  with the aim of interpreting striation effects (the traces of earlier stages of solid-liquid interfaces of a crystal) in the as-grown crystals. From the results, he concluded that it is possible to estimate the nucleation temperature, size and shape of the crystals at various stages of growth. Although flux inclusions were not completely absent and the crystals were still in mm size, no evidence of dendritic growth and striations was observed.

Further studies of the growth mechanism of flux grown orthoferrite crystals were carried out by Akaba in 1974 [270], who found two types of growth spiral on the surfaces of the crystals which seemed to play an important role in the growth mechanism of the flux-grown  $\text{RFeO}_3$  single crystals. Flux growth of orthoferrites was also studied by Arai [272] and Barilo et al. [273-274], but large, high quality and defect free crystals still proved to be difficult to prepare due to pick up of impurities, either from the flux or from the crucible.

It is apparent from the literature, therefore, that flux grown orthoferrite crystals invariably suffer from inclusions, second phase formation and other defects, while only relatively small ( $\text{mm}^3$ -size) crystals have been obtained despite the amount of effort that has gone into investigating orthoferrite growth by this technique. It must be questioned, therefore, whether the single crystal property measurements performed on flux grown orthoferrites

have used samples in which some of the rare earth has been replaced by lead or other impurities.

#### **2.4.3.3. Growth of rare earth orthoferrites by the Czochralski and Bridgman techniques**

In 1972, Nielsen and Blank [275] attempted to study the crystal growth and phase equilibrium relationships in some rare earth orthoferrite systems. With this aim, three crystal growth techniques were examined: simple slow cooling, Czochralski and Bridgman methods. Many attempted growths employing the Czochralski method (which was also used by Balbashov [276]), yielded only small defective crystals of the orthoferrites of Dy, Sm, Tb, Tm, Y and Yb. In the cases of Dy and Yb, excessive  $\text{Fe}^{2+}$  content was a major problem. The phase studies revealed that simply slow cooling the melt might yield crystals of improved quality and some melts were cooled at 3 deg/h until solidification was complete. Crystals of Dy, Yb, Tm and  $\text{Sm}_{0.55}\text{Er}_{0.45}$  orthoferrite about  $0.5 \text{ cm}^3$  in volume were grown in this way, but inclusions high in  $\text{Fe}^{2+}$  were still present. Of the three techniques tried, the Bridgman method in an  $\text{O}_2$  atmosphere was selected as yielding the best results. However, only growths of  $\text{YFeO}_3$  and  $\text{YbFeO}_3$  were tried, although the authors reported that other orthoferrites could be grown in the same way provided that their melting points are sufficiently low to find suitable crucibles [275].

While the Bridgman technique was successfully used to grow large orthoferrite single crystals, some defects were still present in the as-grown crystals. The defects most often observed in crystals grown in air were small inclusions of an opaque phase, which were 2-3 microns in diameters and frequently arranged in rows, presumably decorating dislocations. Also, it was reported that during rapid Bridgman growth, bubbles were included along with the precipitates resulting in an inclusion pair. While other crystal defects such as twinning and striation were also observed, it was suggested that twinning could be avoided by preparing melts which were precisely 50 mole %  $\text{Fe}_2\text{O}_3$  and that striations were a result of temperature fluctuations caused by rapid growth rates.

#### **2.4.3.4. Growth of rare earth orthoferrites by the floating zone method**

In the early 1970s, Okada et al. [277] and Fairholme et al. [278-279] were the first groups to report encouraging results on the growth of orthoferrite crystals (up to 6 cm long and 1 cm diameter) by a floating zone method. They reported the advantages of this technique to be a shorter growth time and less contamination since no crucible or flux is used.

The floating zone apparatus used by Fairholme et al. was a furnace which utilized the focused radiation of a 2.5 KW Xenon arc lamp. Up to 12 twelve passes of the zone through the rod were performed at the growth rates between 3 and 100 mm/h. They found that crystals grown at growth rates above 20 mm/h had cracks in the centre of crystals and although no second phases were present, the crystals included low angle grain boundaries and laminar twins. The incidence of twinning was reported to be dependent on the growth procedure and the size of the rare earth ions in the orthoferrites; here, the density of twins was found to increase with the size of the rare earth ion, reflecting the degree of distortion in the orthoferrite lattice.

Regions of non-uniform optical transparency (circular striations near to the edge) about 0.1 mm wide were also observed in the crystals, these being attributed to fluctuations in divalent iron concentrations of between 0.3 and 0.5 % of the total iron content. An increase in  $\text{Fe}^{2+}$  was also found in crystals grown using a large number of passes, even when 1 atmosphere of oxygen was applied during the growth.

A number of orthoferrite crystals grown by the floating zone method have also been reported in papers that have focused on the magnetic or optical characterization of the materials [280, 281, 282, 233] orthoferrites] or the growth apparatus [283], but these have not given details of the actual growth conditions or the qualities of the crystals.



## **2.5. Summary of conclusions reached from the literature review**

### **2.5.1. Image furnace characterization**

The experimental factors revealed as being of most importance during image furnace crystal growth are the feed rod preparation, the growth rate, the growth atmosphere and gas pressure, the temperature gradient within the sample, the molten zone temperature and the rotation rate. The evidence from the literature indicates that these parameters need to be closely tailored to the material being grown in order to prepare defect-free crystals. This matching of growth conditions to the material in question seems generally to have been carried out on an empirical basis for, although certain trends are present, relatively few papers seek to explain scientifically why a particular combination of experimental parameters has been chosen.

### **2.5.2. TiO<sub>2</sub>**

Rutile is the most stable form of titania and finds use, in single crystal form, in applications such as polarizers and optical isolators. Rutile is easily reduced and when oxygen deficient changes colour from the pale yellow characteristic of the stoichiometric material to blue. Image furnace grown rutile crystals are often not suitable for device applications due to the presence of defects such as low angle grain boundaries, bubble inclusions and colour changes. There is little consistency in the literature, however, as to the experimental conditions needed to obtain high quality crystals during FZ growth. For example, it is not clear what effect, if any, the gas pressure has on sub grain boundary formation or colour changes, or whether bubble formation is linked to high growth rates.

### **2.5.3. Co-doped TiO<sub>2</sub>**

Doping rutile with Co is generally accepted to induce ferromagnetic behaviour in thin films, making the material a candidate for spin based electronic devices. There is little consistency in opinion, however, as to whether Co is truly incorporated into the rutile lattice (i.e. substituting for Ti), or whether the observed ferromagnetism is due to Co clustering. Furthermore, even if Co does substitute for Ti in rutile films, it is not clear

whether this is due to the non-equilibrium conditions inherent with film preparation. If this is the case, it might not be possible to replicate such conditions in bulk growth.

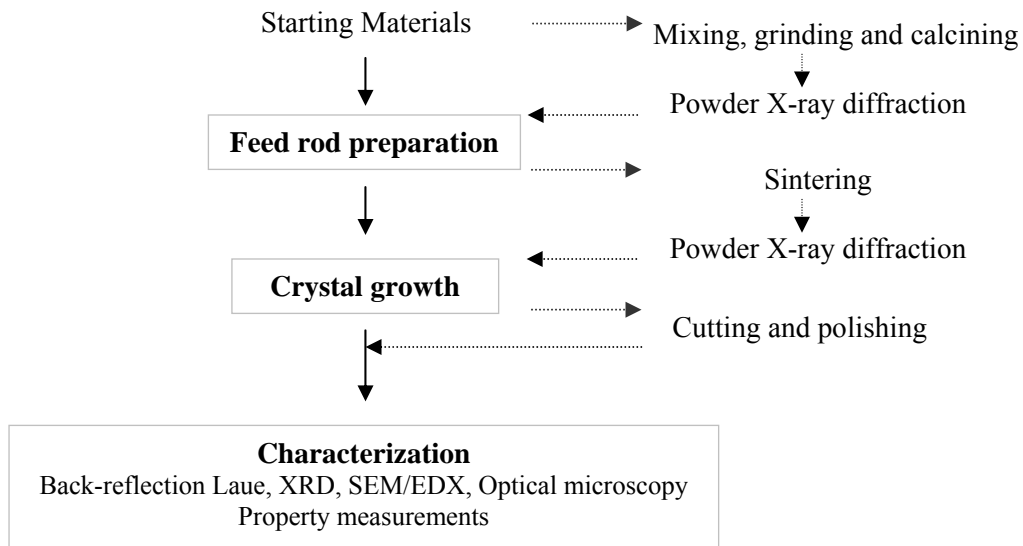
#### **2.5.4. Rare earth orthoferrites**

Rare earth orthoferrites with orthorhombically distorted perovskite structures are antiferromagnetic materials with relatively high Neel temperatures.  $\text{ErFeO}_3$  and  $\text{YFeO}_3$ , the compounds studied in this work, are canted antiferromagnets that exhibit weak spontaneous magnetization in the 'c' axis together with rapid domain wall velocities that make them candidates for use as magnetic or magneto-optical sensors or optical switches. Traditionally rare earth orthoferrite crystals have been grown by flux techniques, but this is invariably reported to result in crystals contaminated by flux inclusions (e.g. Pb); some doubt must be cast, therefore, on the value of physical property measurements obtained from such crystals. Rare earth orthoferrite crystals have been grown using image furnaces, but have tended to suffer from cracking and second phase inclusions for reasons that have not been positively identified. Certainly, no publication to date has reported the experimental conditions that will consistently give high quality crystals during image furnace growth.

# CHAPTER 3: EXPERIMENTAL PROCEDURES

## 3.1. Introduction

The experimental procedures described in this thesis principally divide into three stages, namely feed rod preparation, crystal growth and sample characterization. Fig. 3.1 depicts a schematic of the experimental processes followed in this project, while the actual procedures along with the equipment used in this study are described below.



**Fig.3.1.** Experimental layout of the present investigation

## 3.2. Materials and feed rod preparation

### 3.2.1. Rutile (TiO<sub>2</sub>) feed rods

Fine rutile (TiO<sub>2</sub>) powder with a stated purity of 99.6%, purchased from Goodfellow Cambridge Limited (UK), was used as starting material. It should be noted that the same grade of powder was used for all the work described in this study, so any effects that impurities in the starting material may have had upon the crystal growth processes should be the same in all runs. To make starting rods for float zoning, approximately 7 g of powder was packed into a thin rubber tube and sealed in the tube while being evacuated using a vacuum pump. The powder was then compacted into a rod, typically 6 mm in

diameter and 100 mm long, by placing the sealed tube containing the powder in a hydraulic press (Fig. 3.2.a) under an isostatic pressure of  $70 \times 10^6$  Pa. Upon removal from the tube, the compacted rod was drilled at one end and hung from a Pt wire in a vertical tube furnace (Fig. 3.2.b) and sintered at  $1600^\circ\text{C}$  for 8 h in air.

### 3.2.2. Co-doped $\text{TiO}_2$ (rutile) powders and feed rods

For reasons explained in the results and discussion section, two starting material combinations were used to make Co-doped  $\text{TiO}_2$  powders and feed rods for crystal growth, namely  $\text{CoO}+\text{TiO}_2$  and  $\text{Co}+\text{TiO}_2$ . They were mixed in a stoichiometric ratio and the Co content was varied from 2 to 8 % with respect to titanium. The first mixture ( $\text{CoO}+\text{TiO}_2$ ) was calcined at  $1100^\circ\text{C}$  for 8 h in oxygen using a horizontal tube furnace (Fig. 3.2.c), while the second mixture ( $\text{Co}+\text{TiO}_2$ ) was additionally calcined at  $1100^\circ\text{C}$  for 8 h in vacuum ( $10^{-6}$  mbar). After grinding and phase identification using XRD, calcined powders were used for both magnetic measurements and feed rod preparation. The same feed rod preparation method as described for the pure rutile was followed, except the sintering temperature was selected to be  $1100^\circ\text{C}$  for 8 h in either oxygen (for the powders calcined in oxygen) or vacuum (for the powder calcined in vacuum). Higher sintering temperatures were found not appropriate due to evaporation of phases including cobalt which led to departures from the stoichiometric composition.

### 3.2.3. Orthoferrite ( $R\text{FeO}_3$ , $R= \text{Y}$ and $\text{Er}$ ) feed rods

The starting materials used for the preparation of feed rods for  $\text{ErFeO}_3$  were  $\text{Er}_2\text{O}_3$  (99.9% purity) +  $\text{Fe}_2\text{O}_3$  ( $\geq 99.0$  % purity), and for  $\text{YFeO}_3$  were  $\text{Y}_2\text{O}_3$  (99.9% purity) +  $\text{Fe}_2\text{O}_3$  ( $\geq 99.0$  % purity) obtained from the Aldrich Chemical Company. Stoichiometric amounts of the raw materials were thoroughly ground together and then synthesized in either a horizontal or box furnace (Fig. 3.2.c and 3.2.d) at  $1200^\circ\text{C}$  for 20 h in air with an intermediate grinding after 10 h. After confirmation by X-ray diffraction that the constituents had converted to the orthoferrite structures, the powders were packed and sealed into a rubber tube, then compacted into a rod (following the same procedure as

that described for the rutile feed rods). After removal from the rubber tube, the rods were sintered in a vertical tube furnace (Fig. 3.2.b) at 1600 °C and 1700 °C for 8 h in air for  $\text{ErFeO}_3$  and  $\text{YFeO}_3$  respectively.



(a) Hydraulic press used for compacting starting powders into rods.



(b) Vertical tube furnace used for sintering compacted rods (<1750 °C).



(c) Horizontal tube furnace used for calcining powders and sintering compacted rods (<1200 °C) in oxygen or air.



(d) Box furnace used for calcining powders and sintering compacted rods (<1700 °C) in air.

**Fig.3.2.** Photographs of the hydraulic press and furnaces used to prepare feed rods

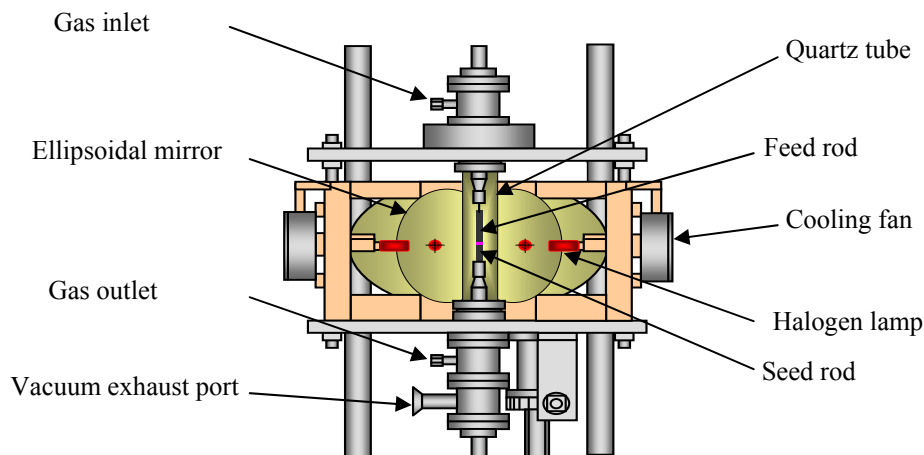
### 3.3. Crystal growth

#### 3.3.1. The optical floating zone furnace (image furnace)

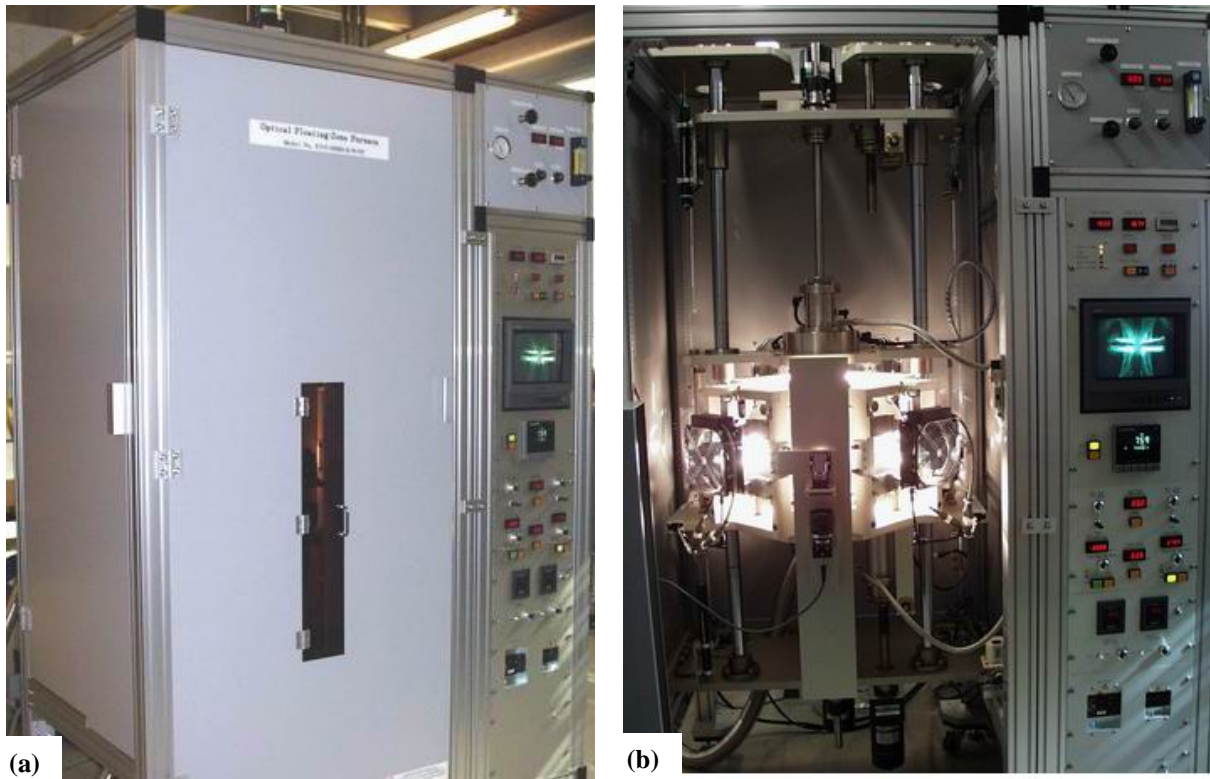
The apparatus employed for the floating zone crystal growth was a Crystal System Inc. infrared convergence type image furnace (model FZ-T-10000-H-VI-VP) with four ellipsoidal mirrors. In this system, four halogen lamps (rather than two as used in some image furnaces) are used to create uniform temperature conditions around the sample to minimize radial thermal stresses. The maximum operating temperature is 2200 °C. Within the growth chamber, gas pressures of up to 10 bar (1.0 MPa) can be used. The specifications and capabilities of the image furnace as reported by the manufacturers are as follows:

- |  |   |
|--|---|
| • Maximum operating temperature                      | 2200 °C   |
| • Typical (average) operating temperature            | 1800 °C   |
| • Temperature uniformity around the horizontal plane | ≤ 50 °C   |
| • Growth speed range                                 | 0.05 to 27 mm/h                                     |
| • Rotation rate range                                | 0 to 57 rpm   |
| • Ultimate vacuum                                    | $5 \times 10^{-5}$ torr ( $6.66 \times 10^{-3}$ Pa) |
| • Maximum pressure                                   | 1 MPa (10 bar)                                      |
| • Number of mirrors/lamps                            | 4 sets  |
| • Monitoring system                                  | CCD camera and CRT monitor system                   |

Fig. 3.3 shows a schematic of the four mirror image furnace, while Fig. 3.4.a and 3.4.b are pictures taken of the furnace while operating with the safety door both closed and open.



**Fig.3.3.** Schematic of the four mirror image furnace



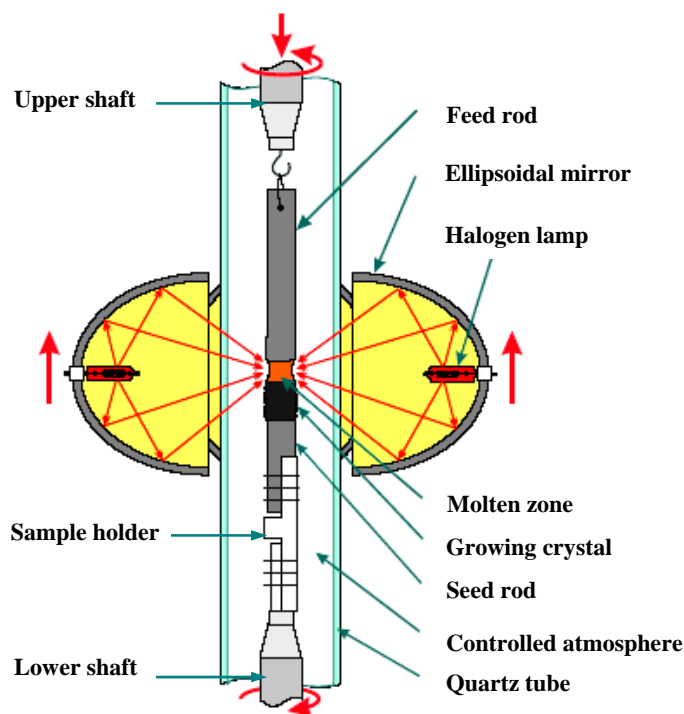
**Fig.3.4.** Four mirror image furnace in two views, (a) outside and (b) and inside

The sample feed and seed rods were loaded into the image furnace by affixing them to the upper and lower shafts as shown in Fig. 3.5. Usually, the feed rod was hung from the upper shaft and the seed rod was fastened to the lower shaft. Both the upper and lower shafts could be rotated in opposite directions (i.e. clockwise and counterclockwise) to ensure uniform mixing and temperature in the molten zone, while the upper shaft also had independent upward and downward movement; this was used for connecting and disconnecting the feed rod to/from the seed rod when initiating the molten zone, when finishing the growth respectively, and also to control the feeding rate into the molten zone.

To move the molten zone along the sample, all four ellipsoidal mirrors (along with their halogen lamps) were moved up or down with respect to the sample.

The enveloping gas was contained using quartz tubes around the sample (a thicker quartz tube was used when growing crystals under higher pressures between 3-10 bar).

In this study, atmospheres of oxygen, argon and helium were used with gas pressures in the range of 1-8.5 bar, as well as vacuum. Growth conditions (i.e. growth rate, rotation rate, etc.) for all crystals will be mentioned individually in the next chapter.



**Fig.3.5.** Schematic of the optical FZ technique with more attention to the shafts, sample holders and movements

### 3.4. Sample characterization techniques

#### 3.4.1. Back-reflection X-ray Laue technique

To prepare as-grown single crystals for subsequent characterization, crystal cutting (in a particular crystallographic direction) and polishing procedures were necessary. Prior to cutting, the as grown crystals were aligned using the back-reflection X-ray technique. In this technique, the conditions for diffraction are met by using "white" X-rays, i.e., a continuous spectrum. Thus, although the specimen is a fixed single crystal, the variable necessary to ensure that the Bragg law is satisfied for different sets of planes in the crystal, is provided by the range of wavelengths in the beam. Thus each set of crystal planes 'chooses' the appropriate  $\lambda$ , from the 'white' spectrum to give a reflection according to Bragg's law,  $n\lambda = 2d\sin\theta$

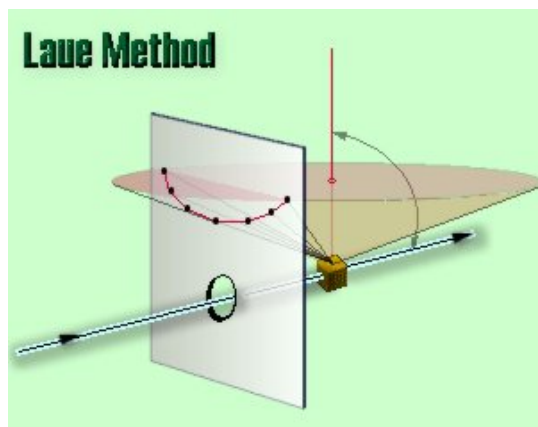


where  $n$  is an integer,  $\lambda$  is the wavelength of the X-rays,  $d$  is the interplanar spacing generating the diffraction and  $\theta$  is the diffraction angle.

Depending upon the sample characteristics, the Laue technique can be used in either transmission or back reflection geometries (Fig. 3.6). In the back-reflection method as used in this study, the film is placed between the X-ray source and the crystal, and the beams which are diffracted in a backward direction are recorded on a film.

The diffracted beams forms an array of spots that lie on curves on the film, the spots lying on any one curve being reflections from planes belonging to one zone (i.e. where all the lattice planes are parallel to a common direction, the zone axis). Consequently, the Laue pattern is able to indicate the symmetry of the crystal. For example, if the beam is directed along a [111] or [100] direction in a cubic crystal, the Laue pattern will show three- or fourfold symmetry, respectively.

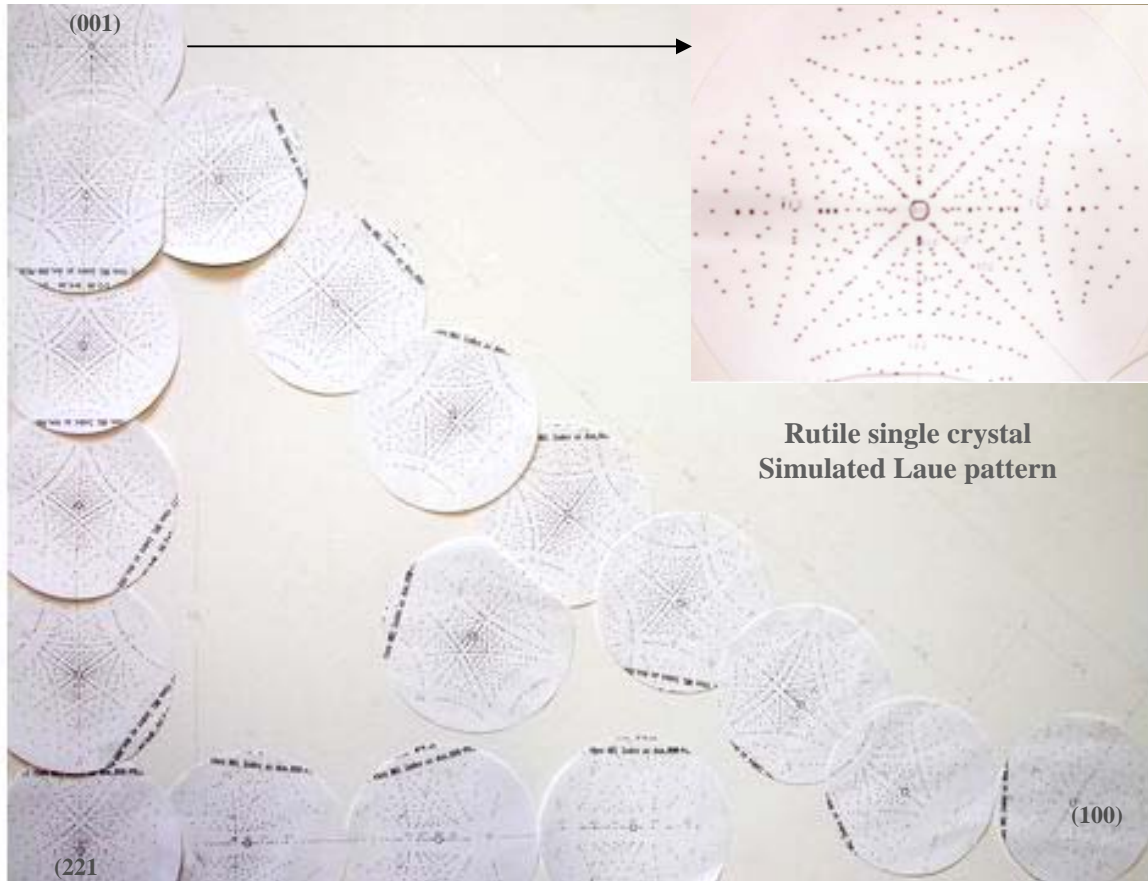
Crystal orientation is determined from the position of the spots which can be indexed (i.e. attributed to a particular plane) by measuring the angles between them using special charts, the Greninger chart being used for back-reflection patterns.



**Fig.3.6.** Scheme of the Laue technique in the back-reflection geometry

Despite the simplicity of the technique, orientation work, particularly for complex crystal structures, can be a time consuming process; thus, it is a great advantage to be able to simulate Laue patterns for different crystal orientations of different structures. Commercial software is available to permit this, although in the present work, programs developed 'in house' were used to print out a series of 'maps' to allow rapid

interpretation of film patterns. Fig. 3.7 shows one of the maps prepared for the tetragonal rutile ( $\text{TiO}_2$ ) structure.



**Fig.3.7.** A typical map including simulated Laue patterns prepared for rutile crystals

The Laue technique was also used to study imperfections in crystals resulting from crystal growth or deformation, since the Laue spots on films from perfect crystals are sharp, while those from deformed crystals are elongated or split. This elongated appearance or splitting of the diffraction spots is known as asterism and arises in an analogous way to the reflection of light from curved or cracked mirrors. Therefore, the Laue technique can also be used to assess crystal perfection from the size and shape of the spots. If the crystal has been deformed in anyway, the spots become distorted, while split spots indicate the presence of sub-grain boundaries.

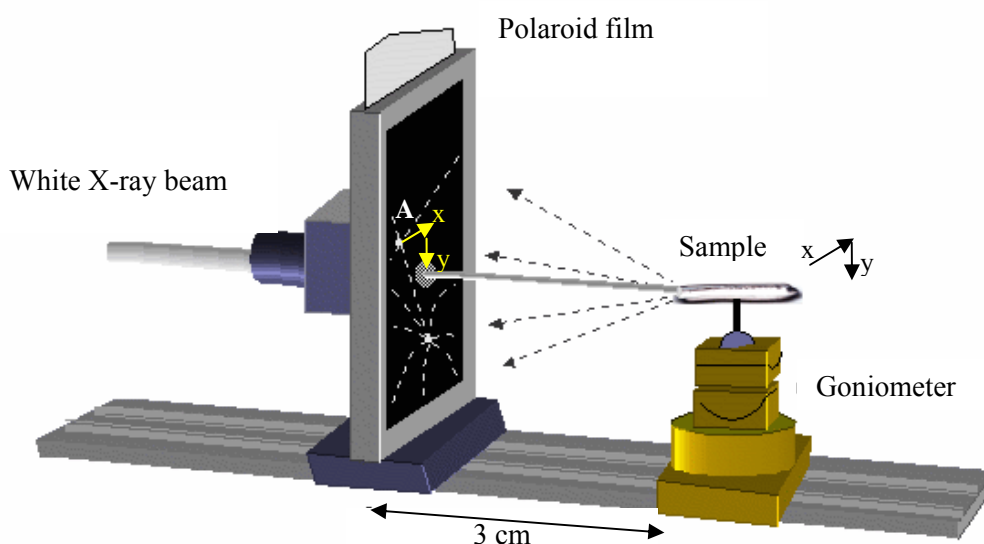
In this study, the crystal faces were invariably much larger than the area of the X-ray beam, so several photographs were taken from different positions along the crystal to

ensure that the symmetry and quality of the crystal were consistent throughout its length or cross section.

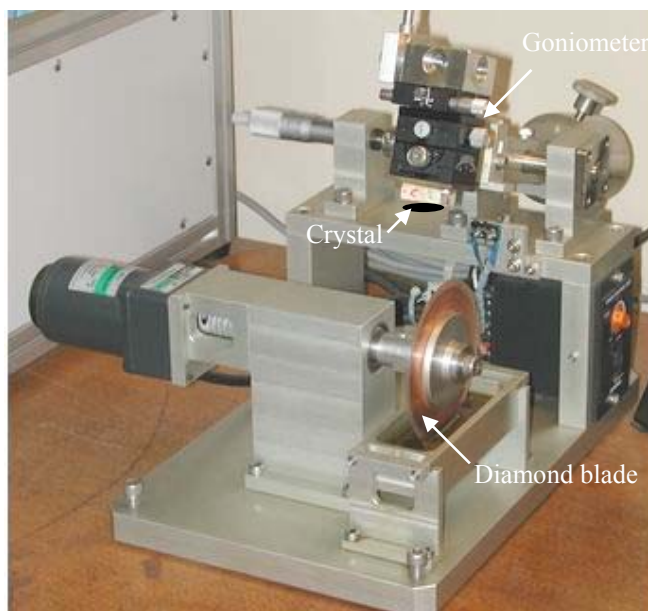
An unfiltered tungsten X-ray source was employed to take the X-ray Laue back-reflection photographs, while the working distance between the Polaroid film and sample was set at 3 cm. Samples were mounted on goniometers that allowed both linear and rotary movement (about two axes). These goniometers could be used to transfer aligned samples onto cutting wheels, as explained in the next section.

#### 3.4.1.1. Cutting aligned single crystals

Before cutting a single crystal in a specific direction or plane, the sample was first fixed on a goniometer to find the desired plane by the Laue technique. As an example, if it was found that the marked spot A on the Laue picture was the reflection from the desired plane to cut (as it is shown in Fig. 3.8), the goniometer was shifted until spot A was in the centre of the film by moving it through angles  $x$  and  $y$  as determined from the Greninger chart. When the A spot was at the centre of the film (as confirmed by another Laue photograph), the goniometer (with the sample still attached), was transferred to the cutter in such a way that the cutter blade was parallel to the desired plane. The cutter used in this study had a diamond tipped blade and is shown in Fig. 3.9.



**Fig.3.8.** Schematic of a goniometer on the X-ray Laue set. Once aligned the crystal, still on the goniometer, was transferred to the cutter.



**Fig.3.9.** Photograph of the diamond blade cutter, used to prepare oriented samples from as-grown single crystals.

### 3.4.2. X-ray diffractometry

X-ray powder diffraction is a technique widely applied for the characterization of crystalline materials such as phase identification and the determination of crystal structures. In this technique, interaction of X-rays with the sample (a randomly oriented powder) creates secondary “diffracted” beams of X-rays related to interplanar spacings in the crystalline powder according to Bragg’s Law.

Diffractometers come in two basic varieties:  $\theta$ - $\theta$  in which the X-ray tube and detector move simultaneously or a  $\theta$ - $2\theta$  in which the X-ray tube is fixed, and the specimen moves at 1/2 the rate of the detector to maintain the  $\theta$ - $2\theta$  geometry. The angles and intensities of the diffracted beams are recorded electronically using a detector and specialized software resulting in a plot of  $2\theta$  (horizontal axis) vs. intensity (vertical axis) for the specimen.

Phase identification is accomplished by comparing the data (peak positions and relative intensities) from the specimen with peak positions and relative intensities from sets of “standard” data provided by sources such as the International Center for Diffraction Data (ICDD).

A Siemens X-ray diffractometer (a  $\theta$ - $2\theta$  system) using a tube with copper  $K_{\alpha}$  radiation ( $\lambda = 1.54$  Angstrom) at room temperature was used for powder X-ray diffraction patterns. The scanning rate was 1 degree per minute at increments of  $0.05^{\circ}$ .

X-ray rocking curves were also measured to check the crystal quality using the diffractometer. To perform the technique, a conventional theta- $2\theta$  scan of the peak of interest is firstly made and the  $2\theta$  position is measured accurately. Then, the detector is moved to that position, and during the rest of the measurement the detector remains stationary. Finally, a conventional theta- $2\theta$  scan is performed, and the start and the finish values determine the length of the rocking curve. (Due to limitations of the software, the x-axis is labeled as  $2\theta$ , rather than  $\theta$ , and the values are all twice as big as they really are). The width of the rocking curve is a direct measure of the range of orientation on mosaic spread present in the irradiated area of the crystal.

### 3.4.3. Optical microscopy

The light microscope provides two-dimensional representation of structure over a magnification range of up to roughly 1000X. Examination of samples in the as-polished condition (which is generally necessary), can reveal structural features such as shrinkage or gas porosity, cracks and inclusions of foreign matter.

The selected microscopical technique used for the rutile crystals in this study, was polarized-light transmission microscopy. The only requirements of this technique are that the incident light through the specimen is plane-polarized and that the reflected light is analyzed by a polarizing unit in a crossed relation with respect to the polarizer, i.e. the plane of polarization of the analyzer is perpendicular to that of the polarizer.

One of the main uses of polarized light is to distinguish between areas of varying orientation, since these can be revealed as differences of intensity under crossed polars. The technique is, therefore, very useful for information on cleavage faces, twin bands and sub-grain boundaries.

Low angle grain boundaries and bubble inclusions in thin plates (thickness  $\approx 1.5$  mm) of rutile crystals were investigated using the polarized-light technique. Samples used for optical microscopy were cold mounted and mechanically polished using diamond paste of various grades down to  $1 \mu\text{m}$ .

#### 3.4.4. Scanning electron microscopy (SEM)

Scanning electron microscopes use a beam of highly energetic electrons to examine objects on a very fine scale. This examination can yield the information such as topography (the surface features of an object or "how it looks"), morphology (the shape and size of the particles making up the object), composition (the elements and compounds that the object is composed of and the relative amounts of them) and crystallographic information (how the atoms are arranged in the object). The combination of high magnification, large depth of focus, good resolution, and ease of sample observation makes the SEM one of the most widely used instruments.

In a SEM, when an electron beam strikes a sample, a large number of signals are generated. Secondary electrons (SE) are produced when an incident electron excites an electron in the sample and loses some of its energy in the process. The excited electron moves towards the surface of the sample and, if it still has sufficient energy, it exits the surface and is called secondary electron (non-conductive specimens can be coated with a conductive material to increase the number of secondary electrons that will be emitted from the sample). Secondary electrons, by convention, are those emitted with energies less than 50 eV.

Alternatively, when the electron beam strikes the sample, some of the electrons are scattered (deflected from their original path) by atoms in the specimen in an elastic fashion (no loss of energy). These essentially elastically scattered primary electrons (high-energy electrons) that rebound from the sample surface are called backscattered electrons (BSE).

The mean free path length of secondary electrons in many materials is approximately 10 Å. Thus, although electrons are generated throughout the region excited by the incident beam, only those electrons that originate less than 10 Å deep in the sample escape to be detected as secondary. This volume of production is very small compared with BSE and X-rays. Therefore, the resolution using SE is better than either of these and is effectively the same as the electron beam size. The shallow depth of production of detected secondary electrons makes them ideal for examining topography. The secondary electron yield depends on many factors, and is generally higher for high atomic number targets, and at higher angles of incidence.

BSE can be used to generate an image in the microscope that shows the different elements present in a sample. All elements have different sized nuclei and as the size of the atom nucleus increases, the number of BSE increases; therefore, the backscattered electron image contains two types of information: one on specimen composition and the other on specimen topography. BSE emission intensity is a function of the specimen's atomic number, therefore, the higher the atomic number, the brighter is the signal. For example, minerals with  $^{26}\text{Fe}$  will appear brighter than those containing  $^{12}\text{Mg}$ .

The generation region of backscattered electrons is larger than that of secondary electrons, namely, several tens of nm; therefore, backscattered electrons give poorer special resolution than secondary electrons. However, because they have a larger energy than secondary electrons, they are less influenced by charge-up.

In conjunction with scanning electron microscopy, energy dispersive X-ray spectroscopy (EDS or EDX) is a technique that utilizes X-rays emitted from the sample during bombardment by the electron beam to characterize the elemental composition of materials imaged in a SEM. When the sample is bombarded by the electron beam of the SEM, electrons are ejected from the atoms comprising the sample's surface. A resulting electron vacancy is filled by an electron from a higher shell, and an X-ray is emitted to balance the energy difference between the two electrons. The EDS X-ray detector measures the number of emitted X-rays versus their energy. The energy of the X-ray is characteristic of the element from which the X-ray was emitted. A spectrum of the energy versus relative counts of the detected X-rays is obtained and evaluated for qualitative and quantitative determinations of the elements present in the sampled volume.

In this study, a scanning electron Microscopy (JEOL 6060, Fig. 3.10) equipped with an energy dispersive X-ray (EDX) analysis was employed to obtain images using both secondary electrons and backscattered electrons. According to the microscope specifications, resolutions up to 3.5 nm (in high vacuum mode) and 4.0 nm (in low vacuum mode) are guaranteed, while the magnification is reported to be in the range of 8X-300,000X; however, these data can be changed depending on the sample characteristics. Although an overall accuracy of compositional analysis is not given by the manufactures, it can vary depending on the sample components; for example, much more accurate analysis is obtained from samples with heavier elements.

Images were obtained with the microscope operating at 20 kV and the working distance of 10 mm for EDX analysis carried out using polished crystals.



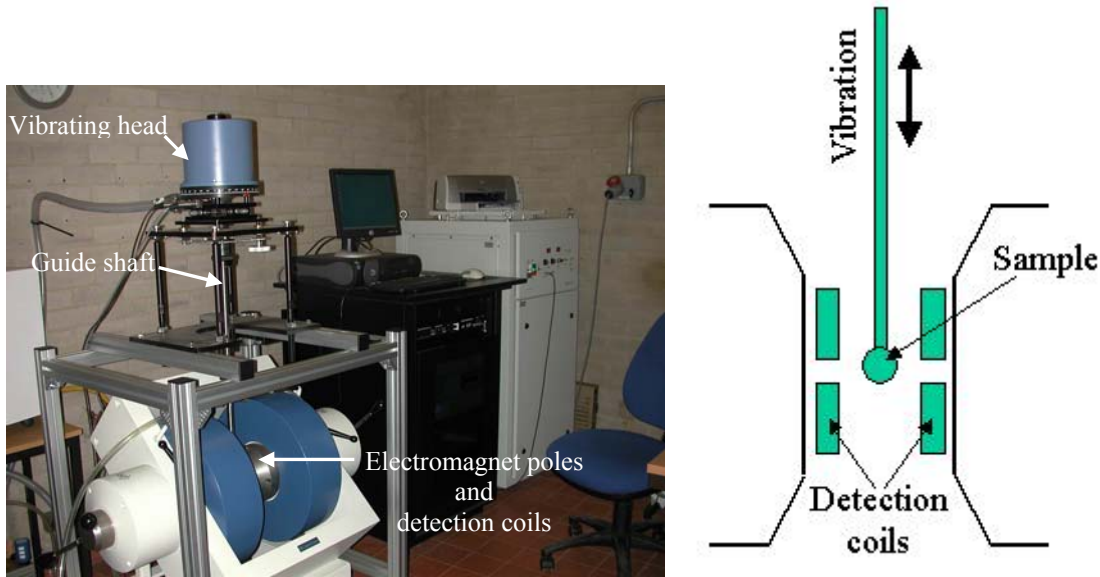
**Fig.3.10.** Scanning electron microscopy used in this study

#### **3.4.5. Magnetization measurements**

The VSM technique, devised by Foner in 1936, is suited to measure either powders or crystals as the sample is suspended and vibrated between the poles of an electromagnet. Sensing coils attached to the poles of the electromagnet detect the magnetic moment from the vibrating sample as the sample's field lines cut the detection coils in a uniform magnetic field (provided by the electromagnet). The AC voltage on the detection coils is read through a lock-in amplifier which is in phase with the sample vibration.

A vibrating sample magnetometer (VSM) manufactured by LakeShore (model 7300) was used for magnetization measurements and a schematic of the VSM is shown in Fig. 3.11. To obtain accurate data, the sample size should be  $\leq 3 \times 3 \times 3$  mm for both compacted powders (using cylindrical sample holders) and crystals (which are stuck on the flat sample holders). The operating temperature range is between room temperature to  $\leq 1000^\circ\text{C}$ , and the maximum applied field is  $\pm 2.5$  Tesla.





**Fig.3.11.** VSM and detection coil set-up

### 3.4.6. Density measurements

Density measurements based on the Archimedes' principle involves weighing a sample both in air and under a liquid of known density. The density of the sample is then calculated using the equation:

$$\rho_{Sample} = \frac{W_{air} \times \rho_{liq}}{W_{air} - W_{liq}} \quad (\text{Eq. 3.1})$$

Where

$W_{air}$  = weight of sample in air

$W_{liq}$  = weight of sample submerged in liquid

$\rho_{liq}$  = density of liquid

$\rho_{sample}$  = density of sample

The liquid used was Diethyl-Pthalate ( $C_6H_4(CO_2C_2H_5)_2$ ) with a measured density of  $1.125 \text{ g/cm}^3$  at  $10.5 \text{ }^\circ\text{C}$  (calculated using a copper standard). The liquid was kept at constant temperature during measurements by containing it in a water cooled bucket. The accuracy of the technique depends very much upon the sample size, larger samples giving much more accurate results. For a typical sample size of  $0.1 \text{ cm}^3$ , the accuracy was calculated to be  $\sim \pm 0.015 \text{ g/cm}^3$ .

# CHAPTER 4: FZ SYSTEM CHARACTERIZATION (RESULTS AND DISCUSSION)

## 4. FZ system (image furnace) characterization

### 4.1. Introduction

The literature review indicated that the principal growth parameters (feed rod characteristics, growth rate, the growth atmosphere and its pressure, temperature gradient and rotation rate) play key roles during growth of single crystals using image furnaces since crystal quality, growth stability and materials properties can all be affected by changing these parameters. The evidence from the literature also demonstrated that these parameters need to be closely tailored to the material being grown in order to prepare defect-free crystals. This matching of growth conditions to the material in question seems generally to have been carried out on an empirical basis for, although certain trends are present, relatively few papers seek to explain scientifically why a particular combination of experimental parameters has been chosen.

The aim of this part of the thesis, therefore, was to study the effects of growth parameters when using a four mirror image furnace, in order to find possible explanations for their influences during crystal growth.

### 4.2. Temperature

Temperature has been chosen as the first factor investigated as this is the primary parameter in FZ crystal growth. Heat is initially applied to a sample to produce a molten zone, a by-product of which is a temperature distribution along the sample. Once a molten zone has been established, the temperature of which can be estimated by reference to the phase diagram for a sample with a specific composition, the secondary parameters (such as growth rate, gas pressure, type of atmosphere and rotation rate) come into play to grow a crystal.

Since the image furnace differs from most conventional furnaces as the controls do not enable the operator to set a 'temperature', rather just a 'lamp power', preliminary

experiments were carried out to get a feel for the relationship between the lamp power setting and the actual sample temperatures attained. Because the heating system in the image furnace is provided using the radiation from an optical source, the temperature attained in the sample should depend on sample characteristics such as surface condition, light absorption, colour, etc., so it was suspected that the lamp power/temperature relationship may be complicated.

The first experiment performed was to measure the lamp power required to melt samples of various materials. It soon became evident that increasing the melting temperature of the sample does not necessarily increase the required lamp power to melt the sample; for example, it was found that 90% of the total lamp power was required to melt a copper ( $T_m \approx 1084^\circ\text{C}$ ) rod with a diameter of  $\sim 6$  mm, while for  $\text{YFeO}_3$  feed rods with a melting point of  $>1700^\circ\text{C}$  and the same diameter as the copper rod, only 60% of the total lamp power was needed. Also, for a material such as silica ( $T_m \approx 1610^\circ\text{C}$ , diameter  $\approx 2\text{-}5$  mm), it was found that the material had not melted even after using the total lamp power (100%) which would be presumed to give a temperature of over  $2000^\circ\text{C}$  according to the furnace specifications.

Further experiments were carried out to melt copper rods of different diameters and surface conditions as shown in Table 4.1.

**Table 4.1** Lamp power required to melt different copper rods

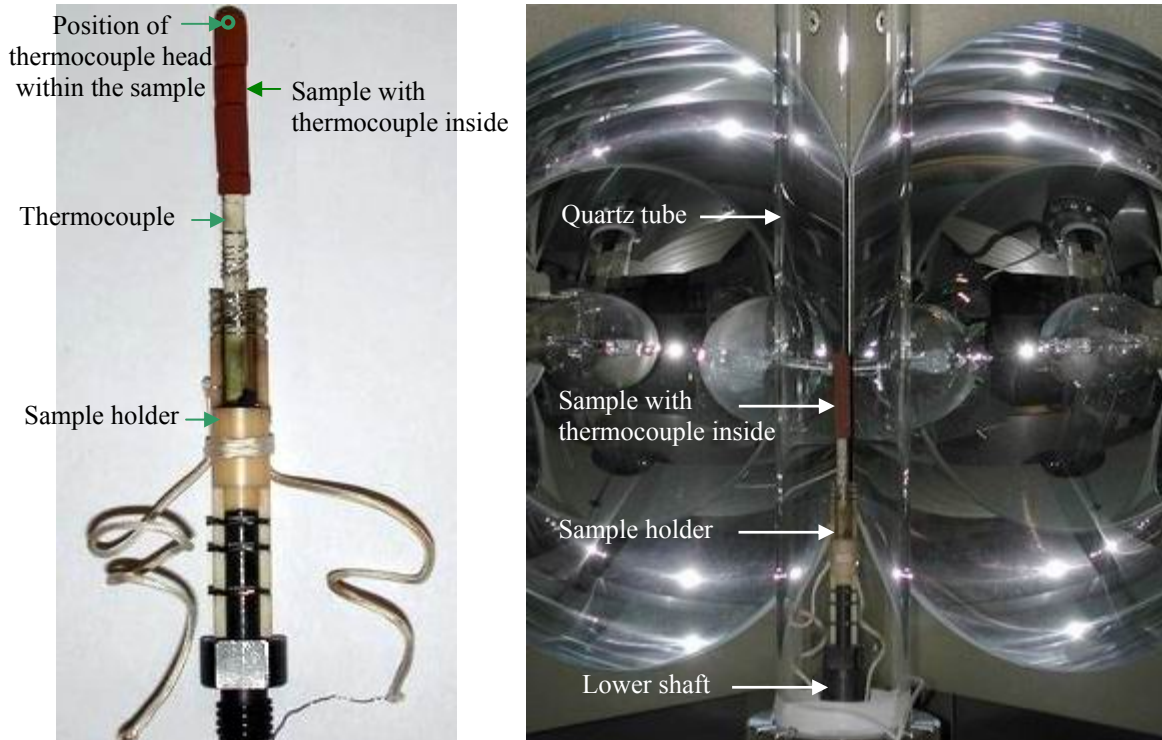
Diameter (mm)	0.3	1.1	6.1	6.1
Surface condition	Shiny	Shiny	Shiny	Black and oxidized surface
Lamp power used to melt the Cu rod (%)	60.6	66.4	90.5	69

From the table, it is obvious that higher lamp powers are required to melt larger diameter copper rods with the same surface condition (i.e. shiny and reflective), but considerably less power is needed to melt a sample of the same diameter with a black and oxidized surface.

Overall, it was concluded that the temperature attained in/along the sample depends crucially on the ‘material characteristics’, since a particular lamp power setting (e.g.

60%) would create a temperature of  $1700^{\circ}\text{C}$  in a sample of one material, while in another sample it could be several hundred degrees lower.

To obtain more detailed information on the temperature trends in the image furnace, a Pt-13%Rh thermocouple was placed within a hollowed out  $\text{YFeO}_3$  polycrystalline feed rod (Fig. 4.1) and passed for 30 mm within the rod along the growth axis.



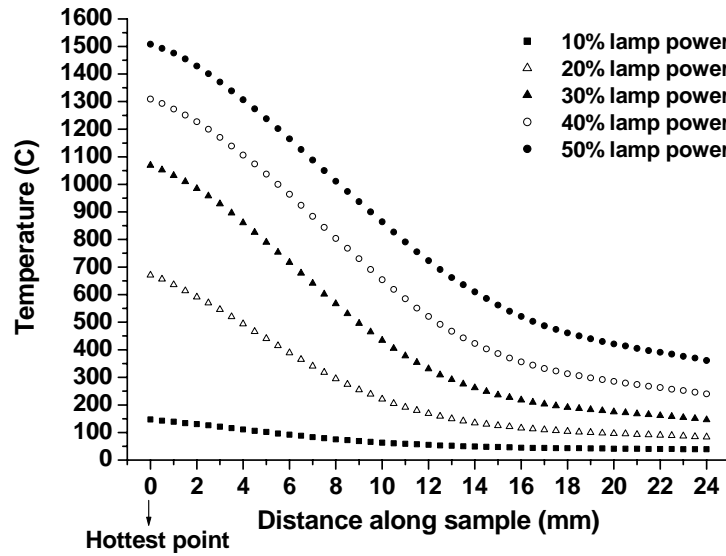
**Fig.4.1.** Pt-13%Rh thermocouple set up for temperature measurements

Temperature gradients along the sample were measured by moving the mirrors at a constant rate with respect to the sample so that the thermocouple position within the rod moved towards the position of maximum temperature.

Systematic temperature measurements were then performed at various lamp powers, types of gas, growth rates and gas pressures to measure temperature profiles at all conditions. It should be noted that, of necessity, these experiments were carried out at temperatures below the melting point of the  $\text{YFeO}_3$  feed rod, therefore, the temperature profiles do not give the actual temperatures that would be obtained during a growth procedure on this material.

### 4.3. Effect of lamp power on the temperature distribution

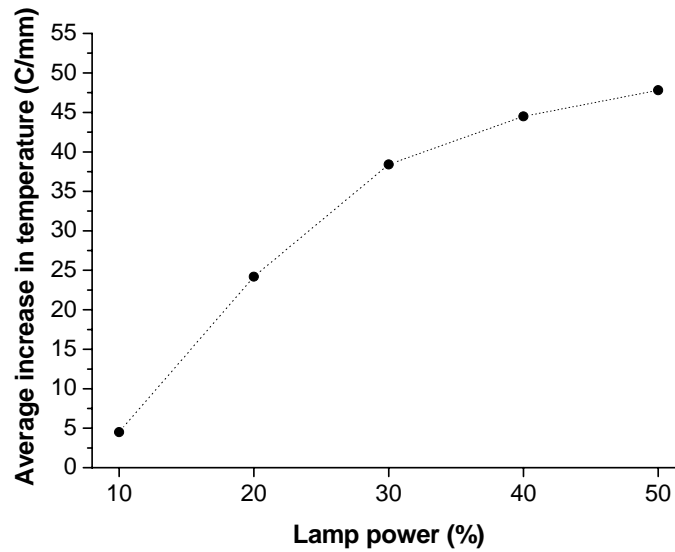
To study the effect of lamp power on the temperature gradient along a growing crystal, temperature profiles were measured at different lamp powers ranging from 10 to 50%, as shown in Fig. 4.2. All these experiments were performed at a zoning rate of 20 mm/h (the travelling speed of  $\text{YFeO}_3$  rod) and an oxygen pressure of 1 bar.



**Fig.4.2.** Temperature vs. distance plots measured from the position of maximum temperature down the  $\text{YFeO}_3$  sample at different lamp powers (10, 20, 30, 40 and 50%). Increasing the lamp power increases the temperature nonlinearly along the sample. All measurements were performed at zoning rate of 20 mm/h under 1 bar oxygen pressure.

These results clearly indicate that increasing the lamp power both increases the temperature and, in consequence, produces sharper temperature profiles along the sample. The average increase in temperature per millimeter was measured for each temperature profile from Fig. 4.2, and plotted versus the applied lamp power, as shown in Fig. 4.3. This plot demonstrates that increasing the power increases the temperature gradient along the sample.

In general, materials with higher melting points will exhibit larger temperature gradients along the growing crystal during FZ, although the thermal conductivity of the material will alter the gradient to some extent.



**Fig.4.3.** Average increase in temperature vs. lamp power; the higher is the applied power the larger is the temperature gradient along the sample.

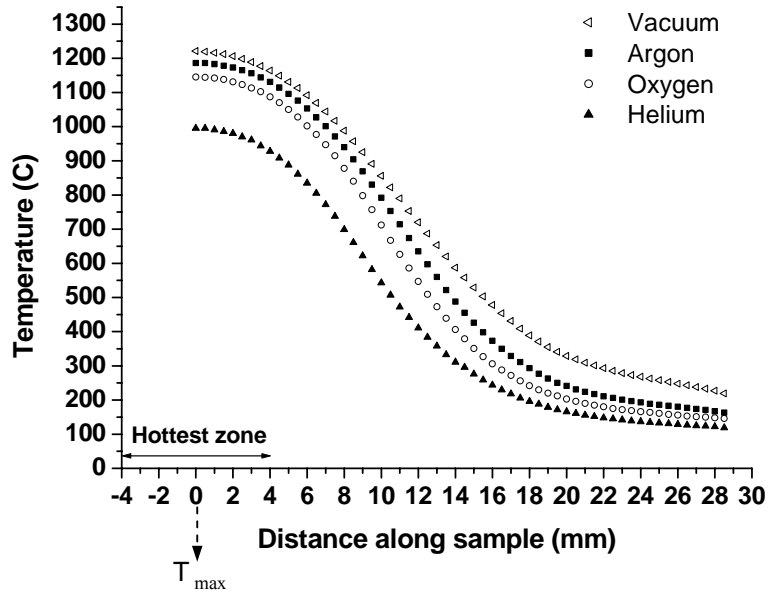
#### 4.4. Effect of gas type on the temperature distribution

To investigate the effect of using different gases on the temperature distribution along the growth axis, argon, oxygen and helium (at an equal pressure of 1 bar) as well as vacuum conditions ( $1.3 \times 10^{-2}$  mbar) were employed and temperature profiles were measured (Fig. 4.4). In all these experiments the applied power and zoning rate were 30% and 20 mm/h respectively.

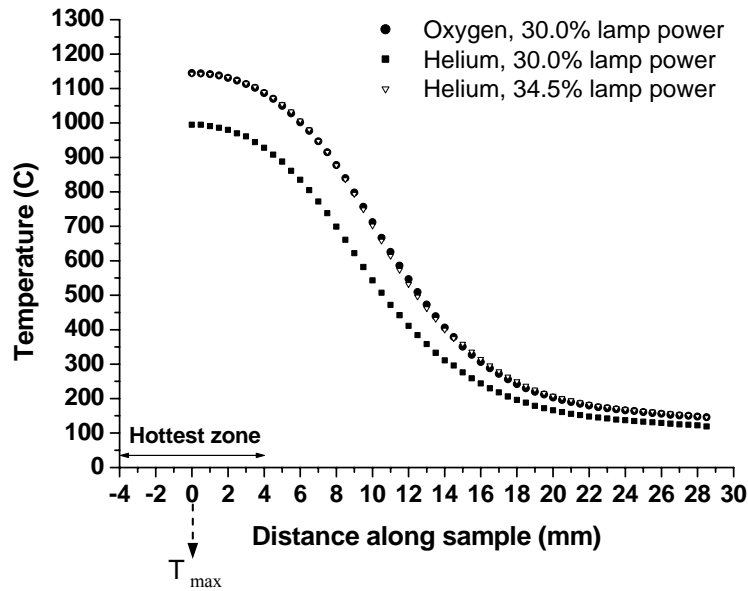
Fig. 4.4 indicates that different maximum temperatures and temperature distributions along the sample were produced using different growth atmospheres for the same lamp power and zoning rate (i.e. the sample was coolest when helium was the growth atmosphere, meaning that a higher lamp power would be required to melt the sample). These results are consistent with the fact that thermal conductivity of helium ( $0.1513 \text{ /W m}^{-1} \text{ K}^{-1}$ ) is higher than that for oxygen ( $0.02658 \text{ /W m}^{-1} \text{ K}^{-1}$ ) and argon ( $0.01772 \text{ /W m}^{-1} \text{ K}^{-1}$ ).

Experimentally, it was found that the lamp power in helium needed to be increased to 34.5% to give a maximum temperature equivalent to that obtained for oxygen at 30% power ( $\sim 1150^\circ \text{C}$ ). The temperature profile with helium at 34.5% of the power is compared with the profile for oxygen at 30% power in Fig. 4.5. As can be seen, the

profiles are very similar once the power settings are adjusted to give the same maximum temperature.



**Fig.4.4.** Temperature profiles at different atmospheres. All measurements were performed at zoning rate of 20 mm/h and lamp power of 30%. The pressure was 1 bar for oxygen, helium and argon, while the pressure in vacuum condition was  $1.3 \times 10^{-5}$  bar.



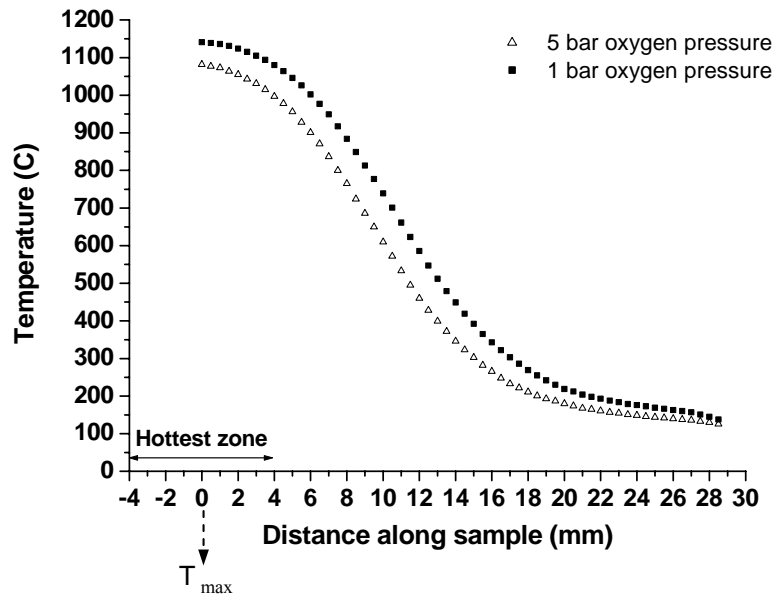
**Fig.4.5.** Effect of increasing the lamp power (from 30.0 to 34.5%) on the temperature profile for helium. All measurements were performed at zoning rate of 20 mm/h and the pressure of 1 bar.

#### 4.5. Effect of gas pressure on the temperature distribution

Two oxygen pressures of 1 and 5 bar were selected to examine the effect of gas pressure on the temperature profile when applying the same lamp power of 30% and zoning rate of 10 mm/h during temperature measurements. As shown in Fig. 4.6, increasing the oxygen pressure, from 1 to 5 bar, decreased the temperature along the sample.

*This is a very important observation as it explains why higher lamp powers are needed to melt samples under higher gas pressures.* This decrease in temperature at higher pressures can be explained by a larger heat exchange between the sample and the higher number of oxygen molecules at higher pressures. Although the increased number of gas particles at higher pressures may also lead to extra scattering of the light with a consequent reduction of the temperature attained, this is not thought to be the dominant cause of the decrease in temperature since such an effect would be expected to give a wider temperature distribution, which was not found experimentally.

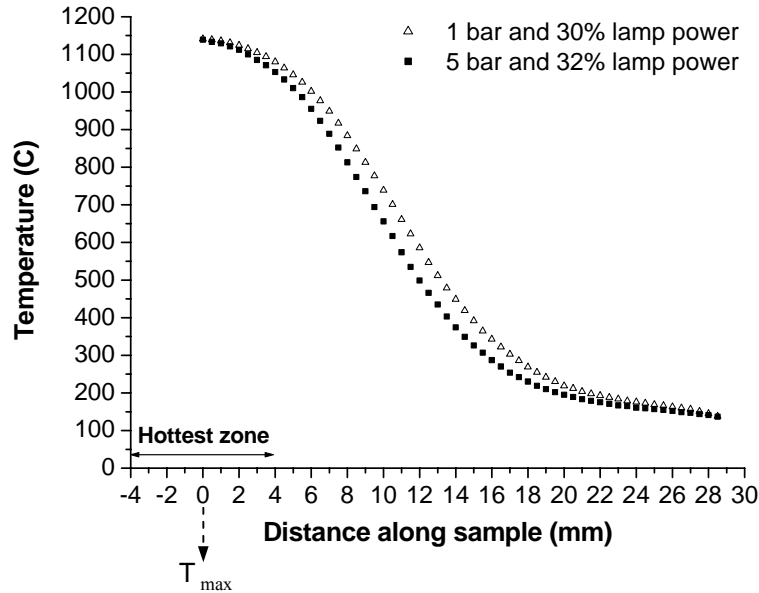
The implication of higher gas pressures reducing the sample temperature will be discussed more fully later with reference to several points raised in the literature review.



**Fig.4.6.** Temperature distributions along the growth axis at two different oxygen pressures of 1 and 5 bar. These experiments were performed at the same zoning rate of 10 mm/h and 30% of lamp power. Increasing the oxygen pressure in the growth chamber decreases the temperature along the sample.

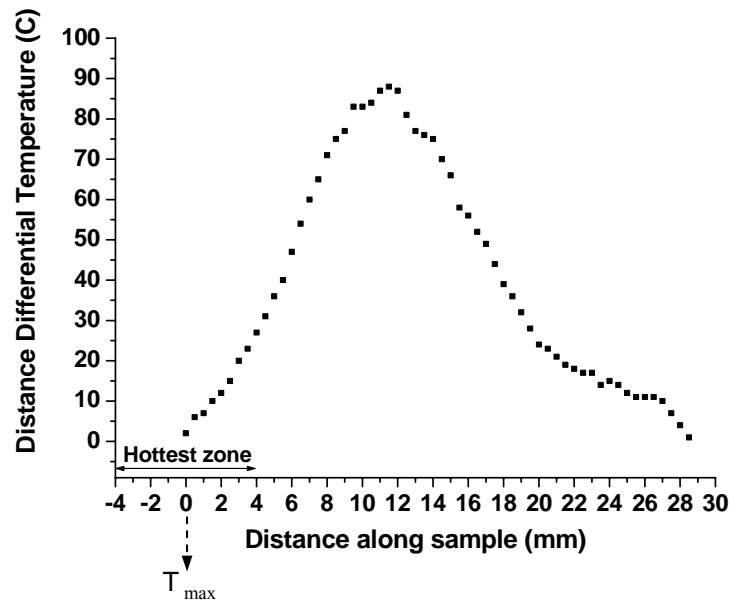


Experimentally, it was found that it was necessary to increase the lamp power to 32% under 5 bar oxygen pressure to achieve the same maximum temperature of 1141 °C, as was attained under 1 bar oxygen pressure at 30% lamp power, as shown in Fig. 4.7. (At 30% power and 5 bar pressure, the maximum temperature was only 1082 °C).



**Fig.4.7.** Temperature distribution curves along the growth axis under two oxygen pressures of 1 bar (at 30% lamp power) and 5 bar (at 32% lamp power). Increasing the lamp power by 2% under 5 bar oxygen pressure equalizes the maximum temperature, but it does not match the temperature distribution along the sample for the run under 1 bar and 30% lamp power. These experiments were performed at zoning rate of 10 mm/h.

The temperature differential between these two graphs (i.e. 32% power at 5 bar oxygen and 30% power at 1 bar oxygen) is plotted in Fig. 4.8, where it is evident that the difference in temperature increases as the distance increases from the hottest zone to a maximum ( $\Delta T = \sim 90^\circ\text{C}$ ) after 8 mm growth length, before decreasing with further distance along the sample.



**Fig.4.8.** Differential temperature curve measured from the temperature profiles for two oxygen pressures of 1 bar (at 30% lamp power) and 5 bar (at 32% lamp power). Although increasing the lamp power by 2% equalizes the hottest zone temperature, a differential temperature between the profiles of up to 90 °C is still observed at distances a few millimeters from the hottest zone.

Overall, increasing the gas pressure during optical float-zone crystal growth can have a number of possible effects related to temperature variations. Firstly, increasing the gas pressure decreases the temperature of sample; therefore, a higher ‘*lamp power*’ is required to melt the sample under higher gas pressures; however, it is noted that higher gas pressures can also affect the phase relations of some materials which could change both the melting point of the material (this would not happen to all materials and changes are likely to be small) and ‘*composition*’ of the material.

Secondly, increasing the gas pressure creates a sharper temperature gradient along the growing crystal so, ‘*cracks*’ may be more likely to occur due to larger thermal stresses. The possible occurrence of ‘*second phase formation or inclusions*’ could also be affected due to decreases in temperature along the growing crystal, while ‘*vapourization of volatile components*’ from the sample could be limited at higher pressures both due to the suppression effects and because the feed rod and growing crystal run at lower temperatures during growth. However, ‘*bubble formation*’ in the molten zone and growing crystal may be more likely (particularly for feed rods which are not well compacted) because the feed rod, close to the molten zone, would run at lower

temperatures so would not be sintered so well prior to melting. Any bubble formation could also affect the ‘*molten zone stability*’.

Overall, it is evident that the effects of varying gas pressure during optical FZ melting can be complicated and affect the growth process and eventual crystal quality in several different ways.

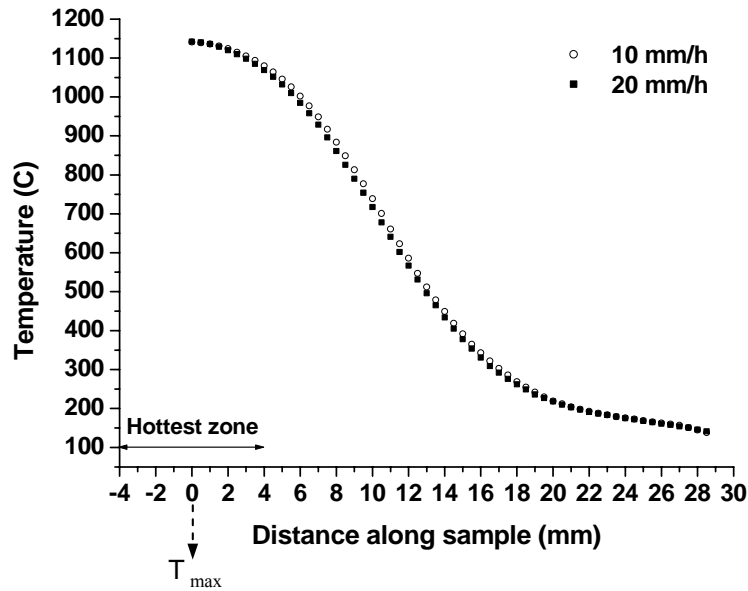
#### **4.6. Effect of zoning rate on the temperature distribution**

To investigate the effect of zoning speed on the temperature distribution, two zoning rates of 10 and 20 mm/h were selected. Experiments were performed under oxygen pressure of 1 and 5 bar, while the lamp power in all experiments was 30%. Temperature profiles were measured as shown in Fig. 4.9 and 4.10.

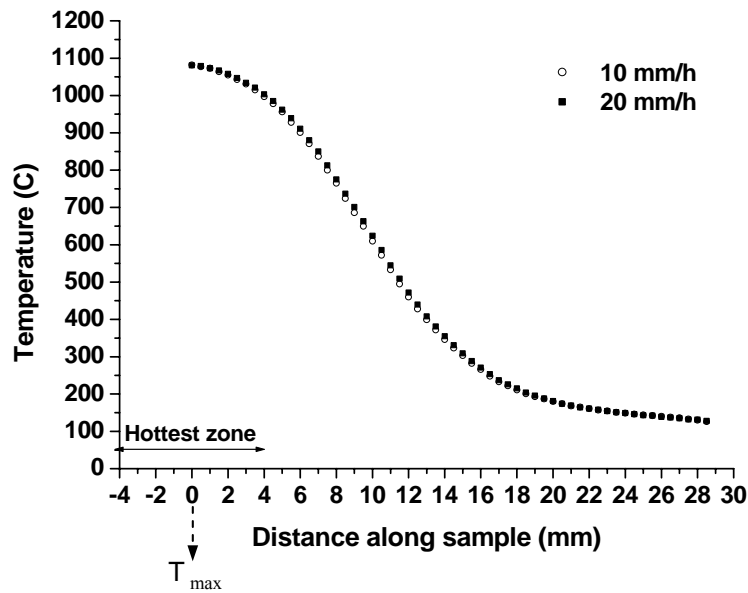
The temperature profiles at zoning rates of 10 and 20 mm/h in Fig. 4.9 and 4.10, clearly indicate that varying the speed, independent of gas pressure, does not in itself change the temperature distribution along the sample; however, using a higher zoning speed causes a higher cooling rate because the sample has to pass through the temperature distribution more quickly (e.g. during a crystal growth at 20 mm/h compared to a growth at 10mm/h, the sample is passed twice as quickly through the temperature distribution, so the cooling rate is twice as fast).

Therefore, increasing the zoning rate would be expected to increase the cooling rate in the growing crystal; this could have several possible consequences for the growing crystal. A higher cooling rate causes larger thermal stresses, and as a result, ‘*cracking*’ is more likely to happen and smaller size crystals may be produced. In addition, depending on the material and its phase stability, a higher cooling rate at higher growth speeds could affect both the occurrence of ‘*second phases or inclusions*’ and the ‘*stability of a molten zone*’.

Therefore, the zoning rate during optical FZ melting is also a determining factor which can affect growth process and crystal quality in different ways related to cooling rate.



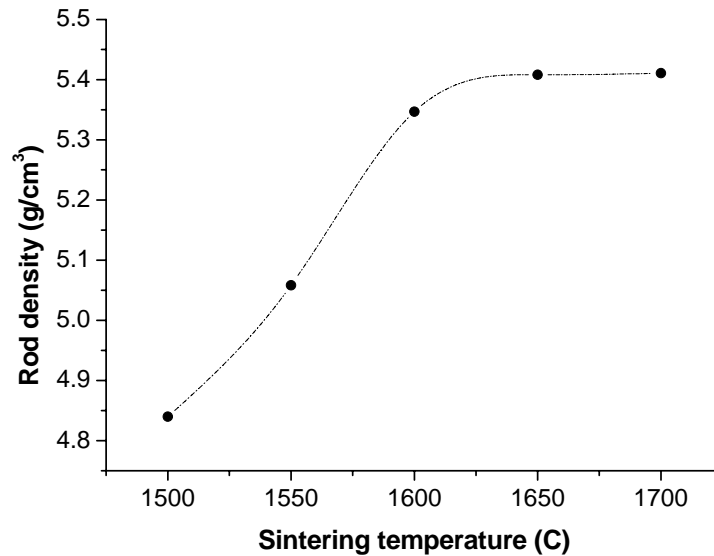
**Fig.4.9.** Temperature distribution along the growth axis at two different zoning rates of 10 and 20 mm/h. These experiments were performed under 1 bar oxygen pressure and 30% lamp power.



**Fig.4.10.** Temperature distribution along the growth axis at two different zoning rates of 10 and 20 mm/h. These experiments were performed under 5 bar oxygen pressure and 30% lamp power.

#### 4.7. Temperature characterization of the FZ system using density measurements

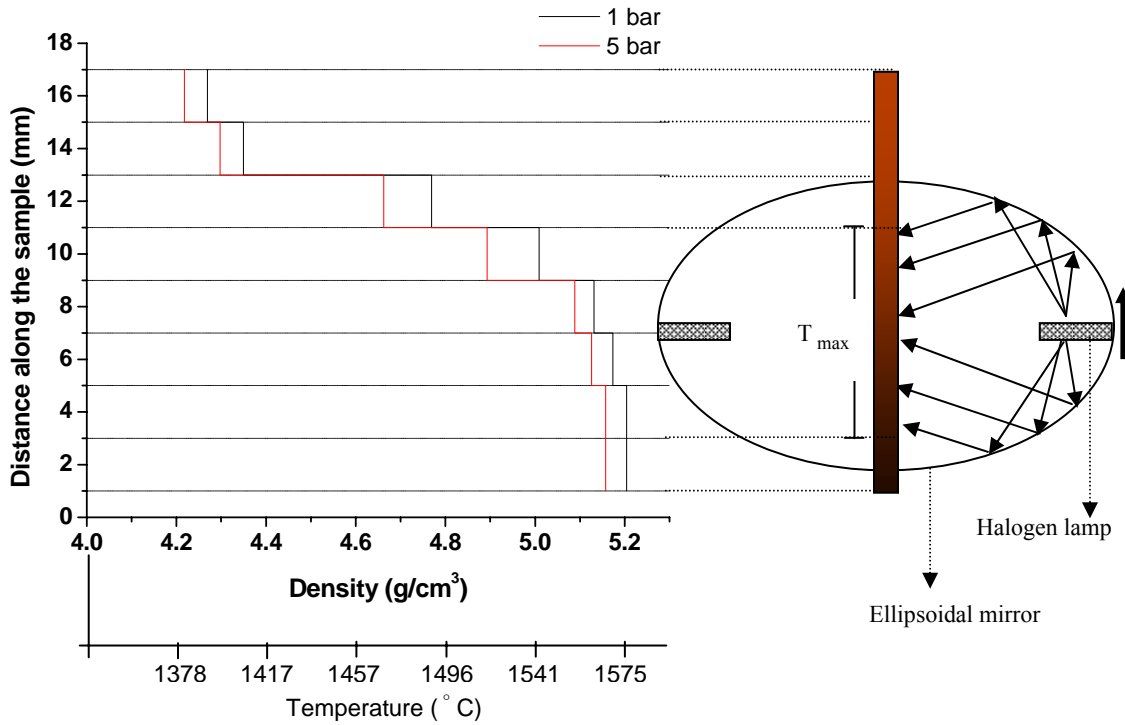
In addition to the experiments described above for directly measuring temperature profiles at higher gas pressures using a Pt-13%Rh thermocouple, attempts were also made to utilize a materials property (density) to indirectly measure temperature gradients. For this purpose, several short polycrystalline  $\text{YFeO}_3$  rods, each with an initial density of  $\sim 4.15 \text{ g/cm}^3$  (prepared by pressing its powder using a hydraulic press under an isostatic pressure of  $70 \times 10^6 \text{ Pa}$  and heating at  $1300^\circ \text{C}$  for 1h), were initially sintered by heating them at temperatures ranging from  $1500$  to  $1700^\circ \text{C}$  for 0.8 h in air using a tube furnace. Their densities were then measured and plotted to give a density vs. sintering temperature calibration as shown in Fig. 4.11. (For these experiments only one furnace was used and all samples were placed in the same place in centre of the furnace to reduce experimental errors).



**Fig.4.11.** Density of  $\text{YFeO}_3$  polycrystalline rods sintered at different temperatures

Two longer polycrystalline rods of  $\text{YFeO}_3$  ( $\rho = \sim 4.15 \text{ g/cm}^3$ ) with the same diameter of  $\sim 5 \text{ mm}$ , were then heated in the image furnace at 55% of the total lamp power (i.e.  $< 60\%$  at which the sample melts) under oxygen pressures of 1 and 5 bar respectively. Both

samples were moved at a zoning rate of 10 mm/h over a distance of 10 mm as indicated in Fig. 4.12. (This zoning rate of 10 mm/h for 8 mm distance in  $T_{max}$  was chosen to give a total time of 0.8 h, equal to the duration that samples were placed in the tube furnace for calibration measurements in Fig. 4.11). Samples were then cut into 2 mm slices and density of each piece was measured and plotted versus distance (Fig. 4.12).



**Fig.4.12.** Changes in density along  $YFeO_3$  polycrystalline rods heated at 55% of the lamp power at two oxygen pressures of 1 and 5 bar. Increasing the gas pressure gives lower density rods as a result of decreasing the temperature in the sample (temperature data were obtained from Fig.4.11).

As shown in Fig. 4.12, the density of the rod heated under 5 bar oxygen pressure is lower at all points than the equivalent part of the rod which was heated under 1 bar oxygen pressure, confirming that higher temperatures were obtained in the sample heated under the lower gas pressure. (The temperatures quoted for different densities along the sample in Fig. 4.12, were obtained by interpolation and extrapolation of the data in Fig. 4.11).

While such density measurements confirmed the data acquired using the thermocouple experiments, the technique is clearly not suited to very accurate estimation of sample temperatures. However, density measurements could be useful to obtain information about very high temperatures in the image furnace, in particular, when a suitable thermocouple is not available.

#### 4.8. Effect of gas pressure on sample temperatures

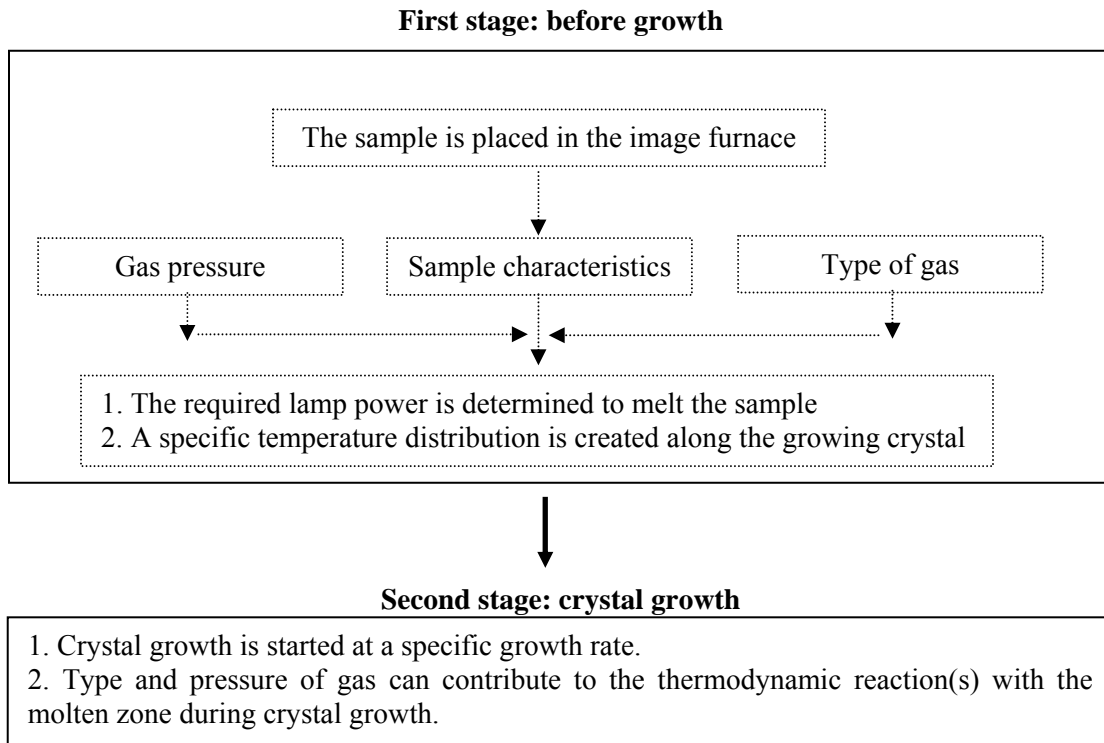
As has been clearly shown in the previous sections, increasing the gas pressure in the image furnace reduces the temperature attained by the sample. However, it has been variously reported in the literature that use of higher gas pressures during FZ increases the melting point of some materials, as reported for  $\text{Bi}_2\text{Sr}_2\text{CaCu}_2\text{O}_{8+x}$  [24,101,112],  $\text{La}_{2-x}\text{Sr}_x\text{CuO}_{4-\delta}$  [26],  $\text{Bi}_{2+x}\text{Sr}_{2-y}\text{CuO}_{6+\delta}$  [100],  $\text{CuO}$  [173] and  $(\text{La}_{1-x}\text{Sr}_x)_2\text{CaCu}_2\text{O}_{6+\delta}$  [176]. Presumably this assumption has been made because higher lamp powers have been necessary to melt the material at higher pressures. *The results presented here, both direct temperature measurement and density, clearly indicate that this assumption is incorrect, however, since the need for higher lamp powers comes from the extra cooling effect of higher gas pressures, rather than any change in the melting point.*

The important link between higher gas pressures and sharper temperature gradients along growing crystals does not appear to have been reported before either. Indeed, once these two effects are taken into account, there is a complete consistency between the reported effects of gas pressure for several papers covering FZ of different materials in the literature review. Invariably no reason has been given in these papers to explain the experimental changes found as a result of varying pressure.

#### 4.9. Summary of FZ system characterization and likely influences of growth parameters related to ‘temperature’ profiles

From these investigations of temperature effects during FZ, it can be concluded that the combination of three parameters, namely ‘*material characteristics*’ (such as diameter, melting point, light absorption, etc.), ‘*gas pressures*’ and ‘*type of gas atmosphere*’,

determine the required lamp power to melt the sample and to produce a specific temperature distribution along the growing crystal. During crystal growth at a particular growth rate, the type and pressure of the growth atmosphere also contribute to the thermodynamic reaction(s) within the molten zone. Fig. 4.13 depicts a schematic of two stages of the technique, before growth and during growth.



**Fig.4.13.** A schematic of the optical FZ technique in two stages, before growth and during growth

The possible influences of the investigated FZ parameters (lamp power, growth atmosphere, gas pressure and growth rate) as related to the parameter of ‘*temperature*’ can be summarized as follows:

**Lamp power**

- **Maximum temperature and temperature gradient**

Increasing the lamp power increases the maximum temperature in the sample (where the molten zone is located) in such a way that sharper temperature gradients are created along the growing crystal.



### **Type of growth atmosphere**

- **Maximum temperature, temperature gradient and lamp power**

Different growth atmospheres (oxygen, argon, helium, etc.) change both the maximum temperature attained and the temperature distribution along the growth axis (i.e. a higher lamp power is required to produce a molten zone under higher thermal conductivity atmospheres such as helium).

### **Gas pressure**

- **Maximum temperature, temperature gradient and lamp power**

Increasing the gas pressure decreases the maximum temperature attained and creates a sharper temperature gradient along the sample; therefore, a higher lamp power is required to produce a molten zone at higher gas pressures. Although using a higher lamp power increases the maximum temperature, a sharper temperature gradient still remains along the growing crystal at higher gas pressures.

- **Cracks**

The sharper temperature gradients along the growing crystal associated with the use of higher gas pressures may cause cracking in some materials due to larger thermal stresses.

- **Second phase formation or inclusions**

Depending on the phase diagram of the material, the sharper temperature gradients at higher gas pressures may affect possible formation of second phases or inclusions in the growing crystal as a result of faster cooling rates.

- **Vapourization of volatile components**

Vapourization of volatile materials from both the feed rod and the growing crystal could be limited under higher gas pressures. This is not just because higher pressures inhibit volatilization, but also because the sharper temperature gradients mean the as-grown crystal and feed rod spend less time at elevated temperatures.

- **Bubble formation**

With poorly compacted feed rods, the sharper temperature gradients associated with the use of higher gas pressures may increase bubble formation in the molten zone and growing crystal, since the feed rod will be less well sintered before melting. Such bubble formation could also affect the molten zone stability.

### **Growth rate**

- **Cooling rate**

Increasing the growth speed increases the cooling rate in the growing crystal.

- **Cracks and crystal size**

Increasing the cooling rate at higher growth speeds, may lead to cracking due to larger thermal stresses.

- **Second phases or inclusions**

Depending on the material and its phase stability, a higher cooling rate may give crystals with second phases or inclusions.

- **Molten zone stability**

A higher cooling rate may change the composition of the molten zone and affect the stability of the molten zone.

All of these possible effects of increasing the growth rate have been mentioned in the literature, but usually without any explanations as to their origin.

# CHAPTER 5: RUTILE

## (RESULTS AND DISCUSSION)

### 5. TiO<sub>2</sub> (Rutile)

#### 5.1. Introduction

Initial runs on the image furnace using rutile as a test material proved disappointing as the resulting crystals were of poor quality and variable colour. A comprehensive review of the literature indicated that several studies aimed at increasing the perfection of rutile crystals produced using image furnaces had attempted to determine to what extent the crystal quality is dependent upon the oxygen pressure in the growth chamber and/or crystal growth rate, but there appeared to be little consistency within the literature as to the results.

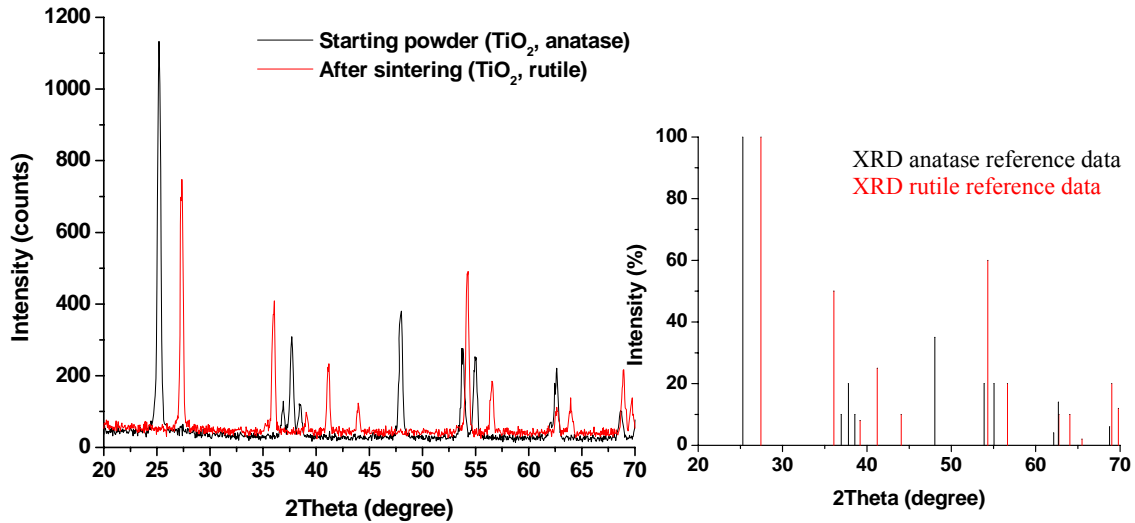
Gas pressure and growth rate are not the only variables in FZ growth, however, since the rotation rate and the zone temperature are other operator controlled parameters. However, little, if any, of the published work on the growth of rutile crystals, appeared to have investigated whether either of these variables has any effect upon the eventual crystal quality.

In this study, therefore, attempts have been made to investigate systematically the influence of *all* of the growth parameters on the quality of undoped rutile crystals prepared using the optical floating zone method. Thus, the effects of varying growth rates, rotation rates, oxygen pressures and molten zone temperatures have all been assessed, rather than just the dual factors of growth rate and oxygen pressure that have been the subjects of most previous investigations.

#### 5.2. Feed rod preparation

Compacted feed rods were prepared using the starting titanium dioxide powder (TiO<sub>2</sub>, purity 99.6%), as explained in section 3.2.1. Then, feed rods were sintered directly, without any calcination procedure, at 1600°C for 8h in air. Fig. 5.1 shows X-ray

diffraction patterns taken at room temperature from both the starting (as purchased) powder and the feed rod after the sintering procedure.



**Fig.5.1.** XRD patterns from the starting TiO<sub>2</sub> powder (in anatase structure) and after sintering at 1600° C for 8h in air, which changed it to the rutile structure.

The XRD pattern from the starting material shows that the anatase structure of titanium dioxide transformed to the rutile structure after sintering at 1600° C (this phase transformation of TiO<sub>2</sub> at high temperature is clearly established in the literature).

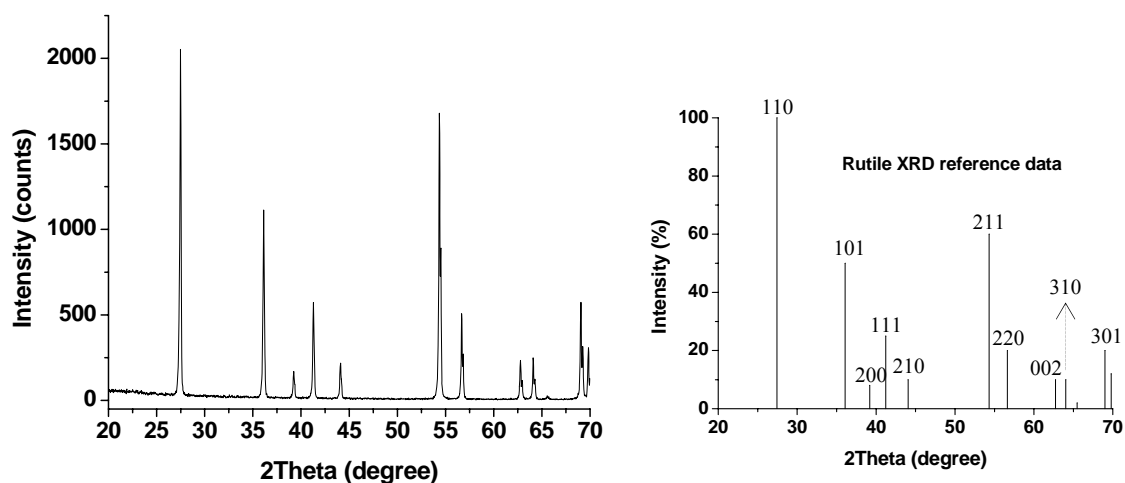
### 5.3. Crystal growth

Sintered feed rods of TiO<sub>2</sub> (rutile) were used for crystal growth at different growth conditions, as discussed in detail in the following sections. Typical examples of an as-grown crystal and a polished longitudinal section of crystal with a thickness of approximately 1.5 mm are shown in Fig. 5.2. The transparency of the crystal is evident since the background letters on the surface below the crystal are clearly readable.



**Fig.5.2.** A typical as-grown rutile single crystal (left) and a view through a longitudinal section cut from such a crystal (right) to illustrate its transparency (the writing is below the crystal).

An XRD pattern from the as-grown  $\text{TiO}_2$  crystal (taken after crushing the crystal) indicated that the rutile structure is the stable phase after growth, as shown in Fig. 5.3.



**Fig.5.3.** XRD from a crushed rutile single crystal

## 5.4. Influence of growth parameters

### 5.4.1. Effect of growth rate

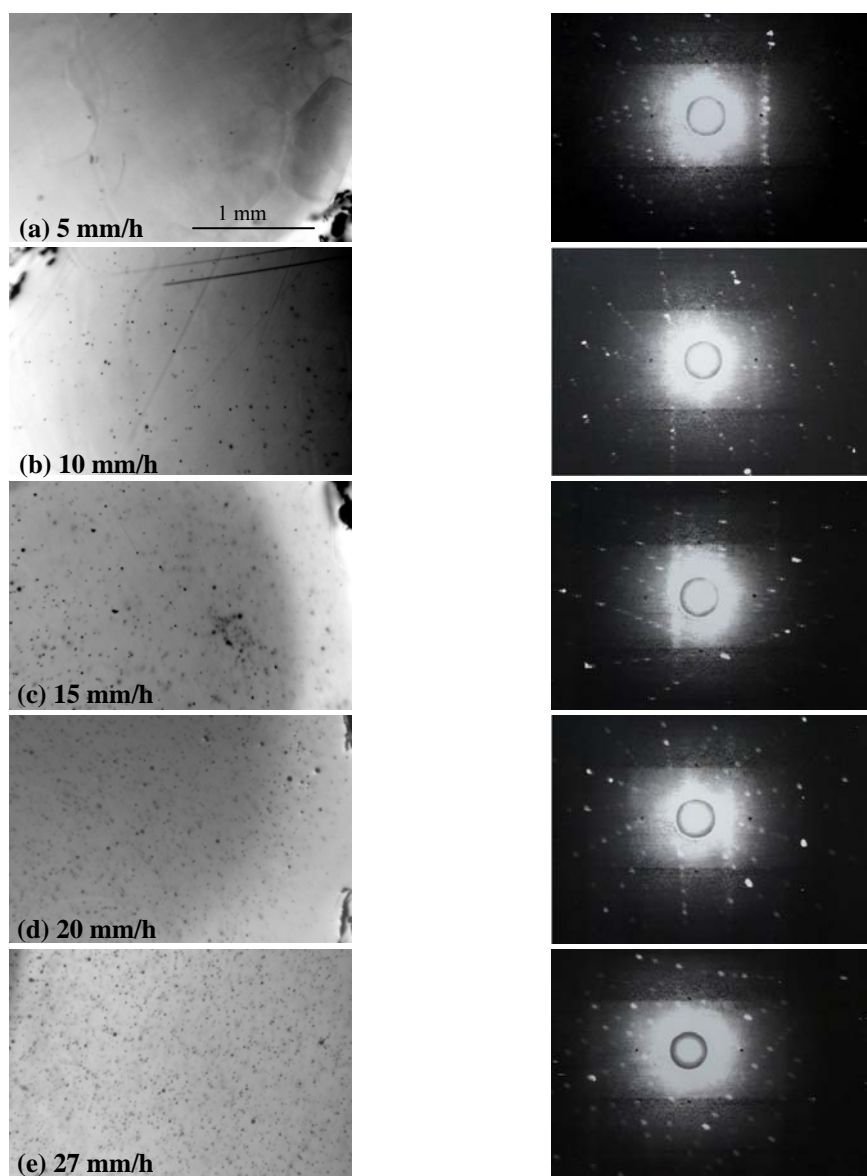
To determine the effect of growth rate on eventual crystal quality, crystals were grown at rates of 5, 10, 15, 20 and 27 mm/h, but a consistent rotation rate of 30 rpm, and oxygen pressure of  $5 \times 10^5$  Pa. Fig. 5.4 shows polarized light photographs of polished cross sections taken from all of these crystals. It was found that when the growth rate

was below 10 mm/h, crystals tended to contain a number of low angle grain boundaries, particularly in the peripheral area, as illustrated in Fig. 5.4a. The use of higher growth rates of 15, 20 or 27 mm/h, however, appeared to suppress the formation of low angle grain boundaries, although crystals grown at these higher rates contained an increasing number of bubbles trapped within them (Figs. 5.4c-e). These bubble inclusions are discussed in detail in a following section in which the investigation of rotation rate is described.

X-ray Laue pictures were also taken from the outer surface of as-grown crystals and typical examples are also shown in Fig. 5.4. Since the typical subgrain size revealed by the polarised light metallography was less than the X-ray beam size (1 mm diameter) the amount of splitting in the 'Laue spots' gives an indication of the misalignment of neighbouring subgrains. Thus in Fig. 5.4a, the spots are split by approximately 2 to 3 degrees, while in Fig. 5.4e, no splitting was detectable.

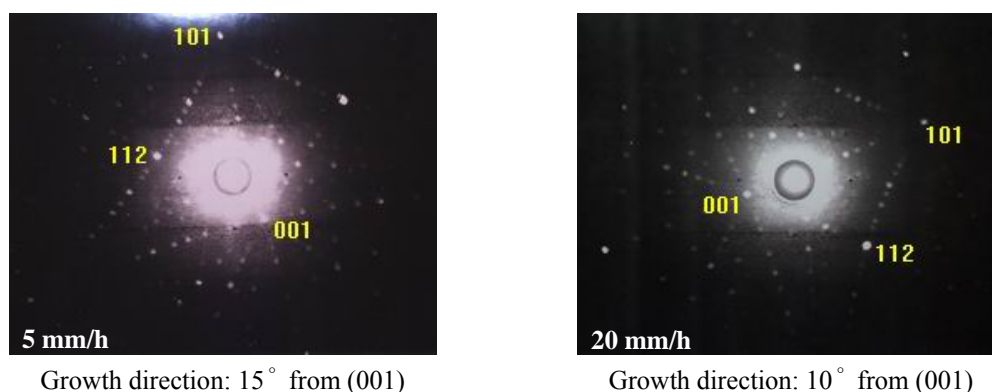
The appearance of spot splitting on the Laue pictures taken from samples grown at lower rates, together with the absence of spot splitting at higher rates, supports the observation from the optical microscopy that crystals grown at higher growth rates had significantly fewer low angle grain boundaries, but increasing numbers of bubble inclusions.

Electron backscattered diffraction (EBSD) (a technique which allows crystallographic information to be obtained from samples in the scanning electron microscope) was also used in an attempt to measure low angle grain boundary misorientations. However, the conducting layer of gold on the polished cross section of TiO<sub>2</sub> crystals, which was deposited upon the sample to eliminate charging, prevented diffraction patterns being obtained from crystals. This is probably because the gold layer was too thick (the deposited layer must be very thin, approximately 2-3 nm, in order to obtain satisfactory patterns).



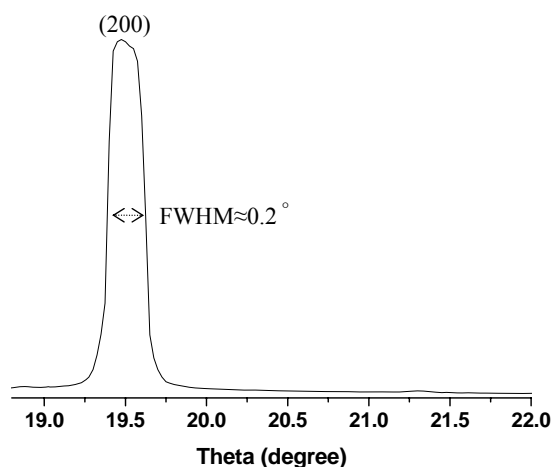
**Fig.5.4.** Polarised light photographs (taken in transmission mode) of polished cross sections of as-grown rutile crystals prepared using different growth rates (left) with corresponding back reflection Laue pictures taken from the crystals (right). The growth rates used were 5, 10, 15, 20 and 27 mm/h. For all of these growths, the oxygen pressure was  $5 \times 10^5$  Pa and the rotation rate was 30 rpm. At lower growth rates, subgrain boundaries are evident together with spot splitting on the Laue photographs. Higher growth rates gave better quality pictures, but the samples contain bubbles.

X-ray Laue diffraction data, taken from the cross section of rutile crystals grown at different growth rates, indicated that the growth speed affected the growth direction to some extent, and crystals close to the 'c' orientation of the seed were usually obtained. Fig. 5.5 shows two typical Laue diffractions taken from crystals grown at 5 and 20 mm/h.



**Fig.5.5.** Growth direction of rutile crystals grown at growth rates of 5 and 20 mm/h.

An X-ray rocking curve of across the (200) Bragg diffraction peak with a full-width at half maximum (FWHM) spread of about 0.2°, measured on the rutile single crystal grown at 27 mm/h, confirmed the high quality of this crystal, as shown in Fig. 5.6.

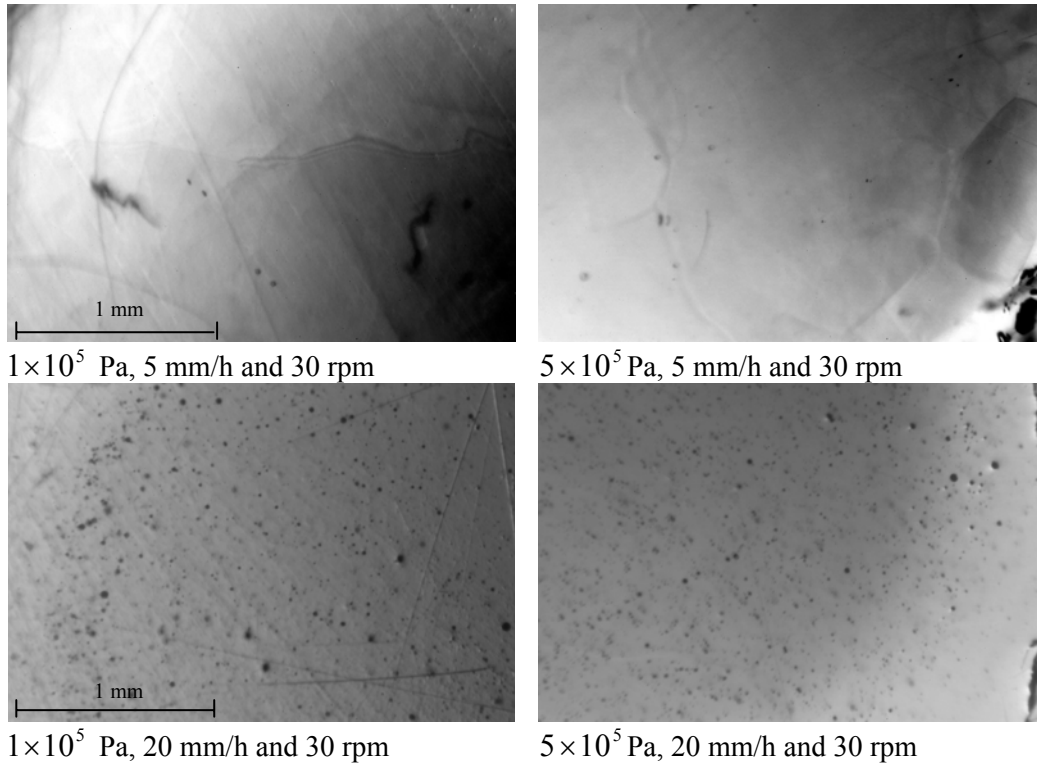


**Fig.5.6.** X-ray rocking curve of the (200) Bragg diffraction peak measured on the rutile single crystal grown at 27 mm/h (Fig. 5.4e).



### 5.4.2. Effect of oxygen pressure

In order to evaluate the effect of oxygen pressure during FZ of rutile, crystals were grown at 5 mm/h and 30 rpm rotation rate under an oxygen pressure of  $1 \times 10^5$  Pa and also under a higher oxygen pressure of  $5 \times 10^5$  Pa. This experiment was then repeated at the higher growth speed of 20 mm/h. The cross sections of crystals grown are shown in Fig. 5.7.



**Fig.5.7.** Polarised light transmission micrographs of rutile crystals illustrating the effect of changing the oxygen pressure during growth at two different pull rates. The upper two micrographs were from crystals grown at 5 mm/h under an oxygen pressure of  $1 \times 10^5$  Pa (left) and  $5 \times 10^5$  Pa (right). The lower micrographs were from crystals grown at 20 mm/h under an oxygen pressure of  $1 \times 10^5$  Pa (left) and  $5 \times 10^5$  Pa (right). For all four growths, the rotation rate was 30 rpm.

It is apparent from this figure that variation of oxygen pressure within this range did not have significant effect on either the occurrence of low angle grain boundaries seen at the lower growth rate or the number of bubbles evident at the higher rate. The change in

oxygen pressure also had no apparent effect on the colours of the crystals. These results appear to be contrary to the observations of Park [193], who reported that crystals grown under oxygen pressures of  $5 \times 10^5$  Pa. contained fewer low angle grain boundaries than crystals grown at and  $1 \times 10^5$  Pa, for growth rates of 3 mm/h and rotation rates for the upper and lower shafts of 10 and 50 rpm respectively.

It should be noted, however, that changing the gas pressure can also change the molten zone temperature as explained in the previous chapter. The extent of this effect was not fully realised when the experiments described in this section were performed, while this factor seems not to have been considered by previous workers. The whole topic of molten zone temperature in rutile is discussed in detail in section 5.4.4.

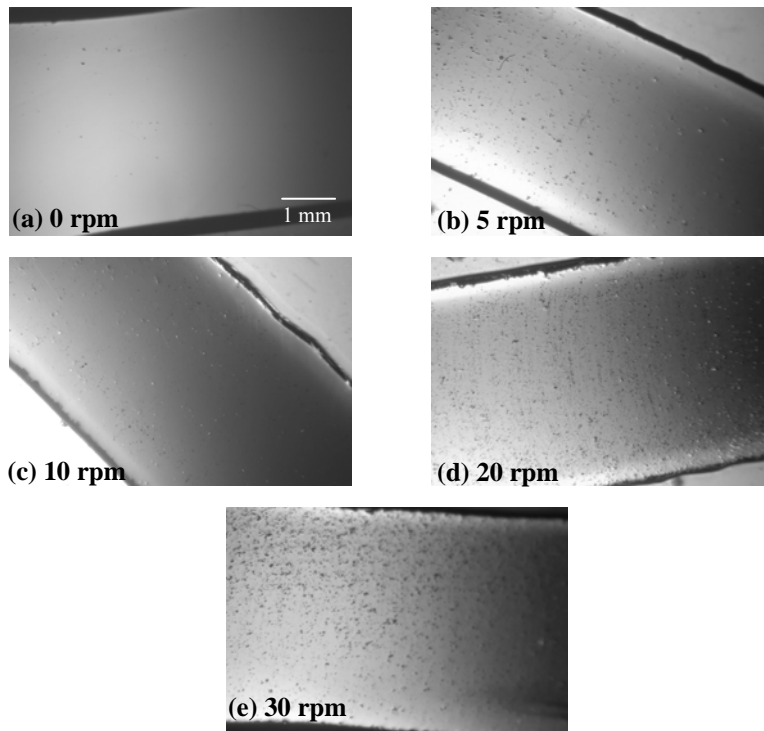
### **5.4.3. Effect of rotation rate**

Rotation appears to have been applied in all of the previously reported image furnace work on rutile, the rotation rates during growth generally being in the range 10 to 50 rpm. Indeed, the study of the literature presented in chapter 2 indicates that rotation seems to have been applied for the vast majority, if not all, of the crystal growths of various materials using image furnaces. The usually accepted reasons for such rotation are to provide an even temperature distribution within the molten zone, so giving a stable solid-liquid interface, and to achieve a uniform shape in the as-grown crystal. Also, for some materials the phase diagram may indicate that there is a constitutional need for the sort of thorough mixing of the melt that rotation provides. However, it is not uncommon during FZ growth of metallic samples (albeit using induction or electron beam rather than infra red heating) to neither rotate the feed rod nor the growing crystal [196]. This lack of rotation was not reported to have a significantly detrimental effect on the uniformity of as grown crystals so long as the feed rods were of fairly uniform diameter.

To investigate whether the rate of rotation of the growing crystal and feed rod had any effect upon eventual crystal quality for image furnace grown rutile, crystals were grown at a constant pull rate of 27 mm/h, but different rotation rates of 0, 5, 10, 20 and 30 rpm.

The oxygen pressure within the chamber was set at  $1 \times 10^5$  Pa for all of these growths. The longitudinal sections of these crystals are shown in Fig. 5.8.

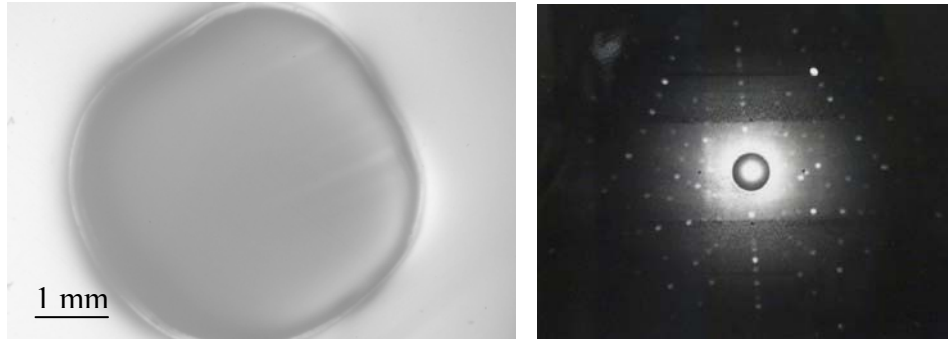
It is apparent from this figure that, at this growth rate of 27 mm/h, variation of the rate of rotation had a pronounced effect on the number of bubble defects in the final crystal. In this respect, increasing the rotation rate increased the number of bubbles, while crystals grown without rotation were essentially bubble-free.



**Fig.5.8.** Polarised light transmission micrographs of longitudinal sections from rutile crystals grown at rotation rates of 0, 5, 10, 20 and 30 rpm. The same growth rate of 27 mm/h and oxygen pressure of  $1 \times 10^5$  pa was used for all these crystals. Increasing the rotation rate clearly increased the number of bubbles within the crystals.

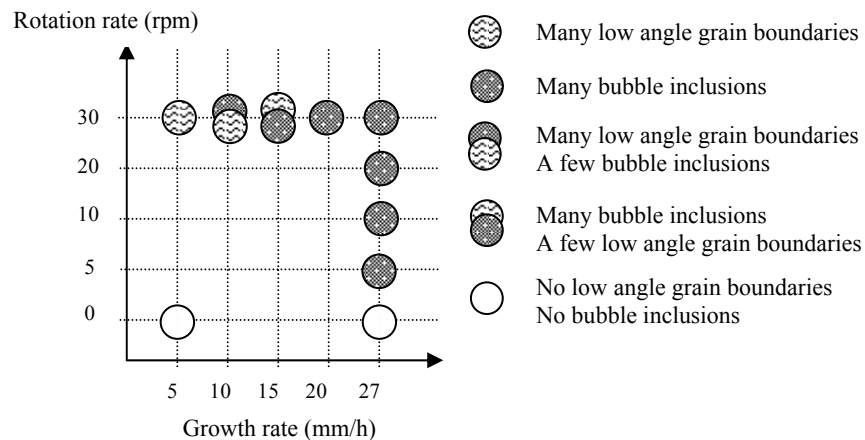
A further growth was performed using zero rotation, but with a lower zoning rate of 5 mm/h. At this growth rate, crystals grown using a rotation rate of 30 rpm were bubble free, but contained sub-grain boundaries (Fig. 5.4a). However, the crystal grown without rotation was found to be free from both sub-grain boundaries and bubbles,

while X-ray Laue photographs from the crystal exhibited sharp, unsplit spots (Fig. 5.9), similar to the crystal grown without rotation at the higher rate of 27 mm/h.



**Fig.5.9.** Polarised light transmission micrograph from a cross section (left) and X-ray Laue picture from the surface (right) of an as-grown rutile crystal prepared at a rate of 5 mm/h with zero rotation, under  $1 \times 10^5$  Pa oxygen.

It would seem clear from these results that there is an interrelationship between the growth rate, the rotation rate and the defects found in image furnace grown rutile crystals. This is illustrated in Fig. 5.10, which summarizes the results from several of the crystal growths performed in this study.



**Fig.5.10.** Diagram illustrating the interrelationship between the growth and rotation rates and the defects found in rutile crystals grown using the image furnace.

Two possible explanations considered for the origin of the bubbles found in some of the rutile crystals include their being a result of reduction of the samples during zoning (i.e. oxygen evolved from the bulk) or that they were created from voids within the sintered feed rod, which were not 100% dense. However, in neither of these cases would lowering the rotation rate be expected to affect the number of bubbles formed. Rather, the absence of either sub-grain boundaries or bubbles in crystals that were grown at zero rotation rates for both high and low growth rates would appear to indicate that these defects originate from the effects of rotation. Although the exact mechanism by which this could happen is open to question, internal friction within the molten zone when rotation is applied must be considered as a probable factor. A complicating aspect in any explanation of these phenomena is that the phase diagram does not indicate unambiguously whether  $\text{TiO}_2$  melts congruently [185], so the exact nature of the interface between the growing crystal and the molten zone is not clear. However, it is possible that material in the molten zone could separate slightly from the growing crystal under the stresses imparted by rotation and thereby introduce voids that become assimilated into the solidifying crystal as bubbles. The absence of bubbles (albeit counterbalanced by the presence of subgrain boundaries) in crystals grown when rotation was employed at low (linear) zoning rates, could be explained if the slower growth gave time for any bubbles introduced by the effects of rotation to escape, possibly through coalescence.

Although the exact mechanism of bubble and sub-grain boundary formation in image furnace grown rutile crystals is not fully resolved, *the experimental evidence strongly suggests that both of these defects originate from the effects of rotation during growth* and that good quality crystals can be grown over a range of growth rates if rotation of the seed crystal and feed rod is avoided.

As noted earlier, it would appear from the comprehensive search of the literature that this is the first time that image furnace growth of  $\text{TiO}_2$  has been reported with no rotation of either the growing crystal or feed rod. Contrary to the generally accepted wisdom, the as-grown crystals were uniform in shape while no problems were encountered in stability of the molten zone during zoning. One possible reason why rotation seems to have been universally employed in the previous reports of optical float

zoning of rutile may be that early image furnaces generally had only two or three mirrors. Such equipment may not have produced as homogeneous a molten zone in a relatively poor thermal conductor such as rutile without rotation as more modern image furnaces, which typically have four mirrors.

#### **5.4.4. Effect of molten zone temperature**

While samples of good crystalline quality were eventually achieved by reducing the rotation rates to zero, the colours of the crystals so produced were not always the pale yellow characteristic of stoichiometric rutile. Rather, some crystals assumed the blue colour typical of oxygen deficient rutile [189-191], while others varied from yellow to blue along their length; this indicates that the colour of rutile is very sensitive to minor changes in some facet of the float zone processing. Since the molten zone temperature is the main experimental variable that could not be set absolutely during a run, it was considered possible that variations in this temperature could be the origin of these colour variations. (While the exact form of the Ti-O phase diagram is not clear at elevated temperatures, the colour of rutile is generally accepted [181,185,197] to be sensitive to oxygen content).

The actual temperature attained in the molten zone during optical float zoning (along with the related molten zone length) is rarely mentioned in publications describing rutile crystal growth. This may be because it is presumed that knowledge of the actual temperature is not important so long as it is sufficiently high to melt the sample and not so high that the molten zone becomes too long and falls out.

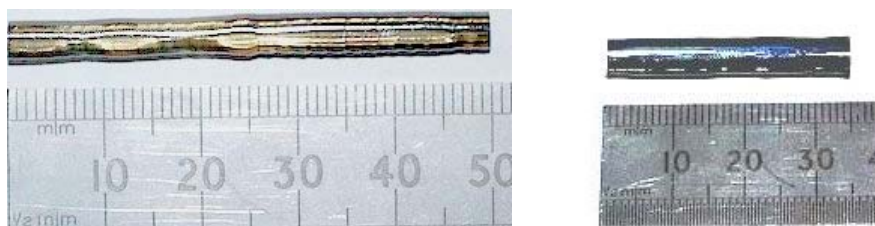
Unfortunately, it is extremely difficult to accurately measure the temperature attained in the molten zone during optical FZ, so the usual indicator used to gauge sample temperature is lamp power. Naturally, this only gives a very crude measure of temperature, although when runs are performed on samples of a particular material of similar dimensions and identical lamp alignments, similar lamp powers may be assumed to yield broadly similar molten zone temperatures for any given gas pressure. The lamp power influences not only the temperature, of course, but also the length of the molten zone. During FZ, too wide a molten zone may result in the zone becoming unstable and falling out, while too narrow a zone can lead to the formation of a bridge of solid (or

partially solid) material between the growing crystal and the feed rod. While this may not necessarily prevent crystal growth in all materials [196], it can lead to strain being imparted into the growing crystal, especially if rotation is employed. With relatively low density materials such as rutile, fairly long molten zones can be tolerated before they become unstable and ‘drop out’, so it is natural to err on the side of using a wider zone (i.e. higher molten zone temperatures) rather than risk using narrow zones that could result in premature solidification. This contrasts with the situation when float zoning metallic samples, where sample densities are usually higher, meaning that molten zone lengths (and temperatures) often need to be reduced to a minimum to maintain zone stability.

In the previous sections of this study that described the effects of pulling and rotation rates and oxygen pressures, the lamp power for all of the runs described was set at a value of ~75% (at 5 bar) or ~73.5% (at 1 bar) of the full power available. To investigate the effect of varying the molten zone temperature, some of the previous experiments were repeated using a lower lamp power setting of 71%, while keeping the gas pressure constant at 5 bar to prevent any influence on zone temperature from pressure effects. From a simple linear extrapolation of power versus temperature, this reduction in power was estimated to lower the temperature attained in the molten zone by approximately 80 °C compared with the previously used setting of 75%. With this lower lamp power setting, all of the samples so prepared had a consistent pale yellow colour along their whole length, while crystal qualities were still found to be consistently high when a pulling rate of 25 mm/h and zero rotation rates were used (Fig. 5.11), samples exhibiting no spot splitting on X-ray Laue photographs.

*These results would appear to indicate that the reason for a blue colouration of image furnace grown rutile crystals is the use of a too high molten zone temperature leading to oxygen loss.* This would be consistent with the fact that rutile is very sensitive to the exact oxygen content and can be reduced easily at high temperatures to become dark blue [189-191]. If this interpretation is correct, then the colour gradient sometimes found along image furnace grown rutile crystals could be due to changes in the molten zone temperature that inevitably take place when zoning using a constant lamp power setting. (In this respect, a constant power setting does not imply an exactly constant

temperature within the molten zone throughout a whole crystal growth run, for the actual temperature attained will depend upon several factors including the precise dimensions of the sample and the position of the zone within the sample).



**Fig.5.11.** Rutile crystal grown at a lower temperature using 71 % of the available halogen lamp power (left) showing a pale yellow colour and a similar crystal grown at a higher temperature using 75 % of the available halogen lamp power (right), which is blue in colour.

Although EDX analysis of light elements (such as oxygen in rutile crystals) using scanning electron microscopy does not give precise compositional values, the atomic percentage of Ti and O measured from a typical dark blue rutile crystal and a yellow crystal, confirmed a higher oxygen content in the yellow sample, as shown in Table 5.1.

**Table 5.1.** EDX analysis of yellow and blue rutile single crystals

Element	Atomic%	Atomic%
	Dark blue TiO <sub>2</sub> crystals	Yellow TiO <sub>2</sub> crystals
O	61.71	62.95
Ti	38.29	37.05
Totals	100	100

Before leaving the topic of molten zone temperature during FZ of rutile, it is perhaps worth speculating that some of the contradictory results from previous workers [188,193] regarding the effects of gas pressure on the quality of rutile crystals could in some part be due to temperature effects. Clearly, the colour of rutile crystals are very sensitive to the zoning temperature, while it was demonstrated in chapter 4 that varying the gas pressure can change the molten zone temperature by an amount similar to that needed to cause colour changes in rutile during float zoning.



### 5.5. Summary

- The experimental parameters that have most influence on the quality of rutile crystals grown by the image furnace technique are the rotation rate and the molten zone temperature.
- Good quality crystals can be grown if no rotation is employed at both low and high zoning rates. With rotation, crystals grown at low rates tend to have many sub-grains, while crystals grown at high rates contain bubble inclusions.
- Increasing the molten zone temperature leads to the preparation of blue (oxygen deficient) crystals, while lower zone temperatures yield pale yellow crystals.
- Changes in the oxygen pressure during FZ within the range 1-5 bar, has no effect upon eventual crystal quality.
- The suggestions in the literature that the zoning rate and gas pressure are the main factors that determine the quality of FZ rutile crystals are erroneous.

## CHAPTER 6: COBALT-DOPED RUTILE (RESULTS AND DISCUSSION)

### 6. Co-doped TiO<sub>2</sub> (rutile)

#### 6.1. Introduction

Doping titanium dioxide with cobalt is generally accepted to induce ferromagnetism, making the material a potential candidate for use in spin based electronic devices. Co-doped TiO<sub>2</sub> thin films have been prepared using a wide variety of techniques; however, there is some debate as to whether Co is truly incorporated into the TiO<sub>2</sub> lattice (i.e. substituting for Ti), or whether the observed ferromagnetism is due to Co clustering in an otherwise diamagnetic TiO<sub>2</sub> matrix. Thus, despite research using both Co-doped TiO<sub>2</sub> thin films and bulk samples (in the form of anatase and rutile powders and single crystals implanted with Co ions) to investigate the magnetic properties, the origin of the ferromagnetism is not fully resolved at present. However, the evidence from the literature (section 2.3.2) indicates that the oxygen pressure and type of atmosphere used during sample preparation are two of the factors that determine whether room temperature ferromagnetism is observed.

The aim of this part of the project, therefore, was to prepare bulk crystalline samples of Co-doped TiO<sub>2</sub> (rutile) in both powder form (using a solid state reaction) and in single crystal form (using the optical FZ technique for the first time) in order to better understand the magnetic properties of the material. Furthermore, to investigate the effect of oxygen content on the magnetic behaviour, two starting material combinations were used, namely 'CoO+TiO<sub>2</sub>' with subsequent procedures performed in oxygen, and 'Co+TiO<sub>2</sub>' with subsequent experiments in either vacuum (for powder and feed rod preparation) or argon (for FZ crystal growth).

It should be noted this work on bulk crystals should more closely reflect equilibrium conditions than earlier work on thin films. When comparing the results, therefore, these differences should be borne mind.

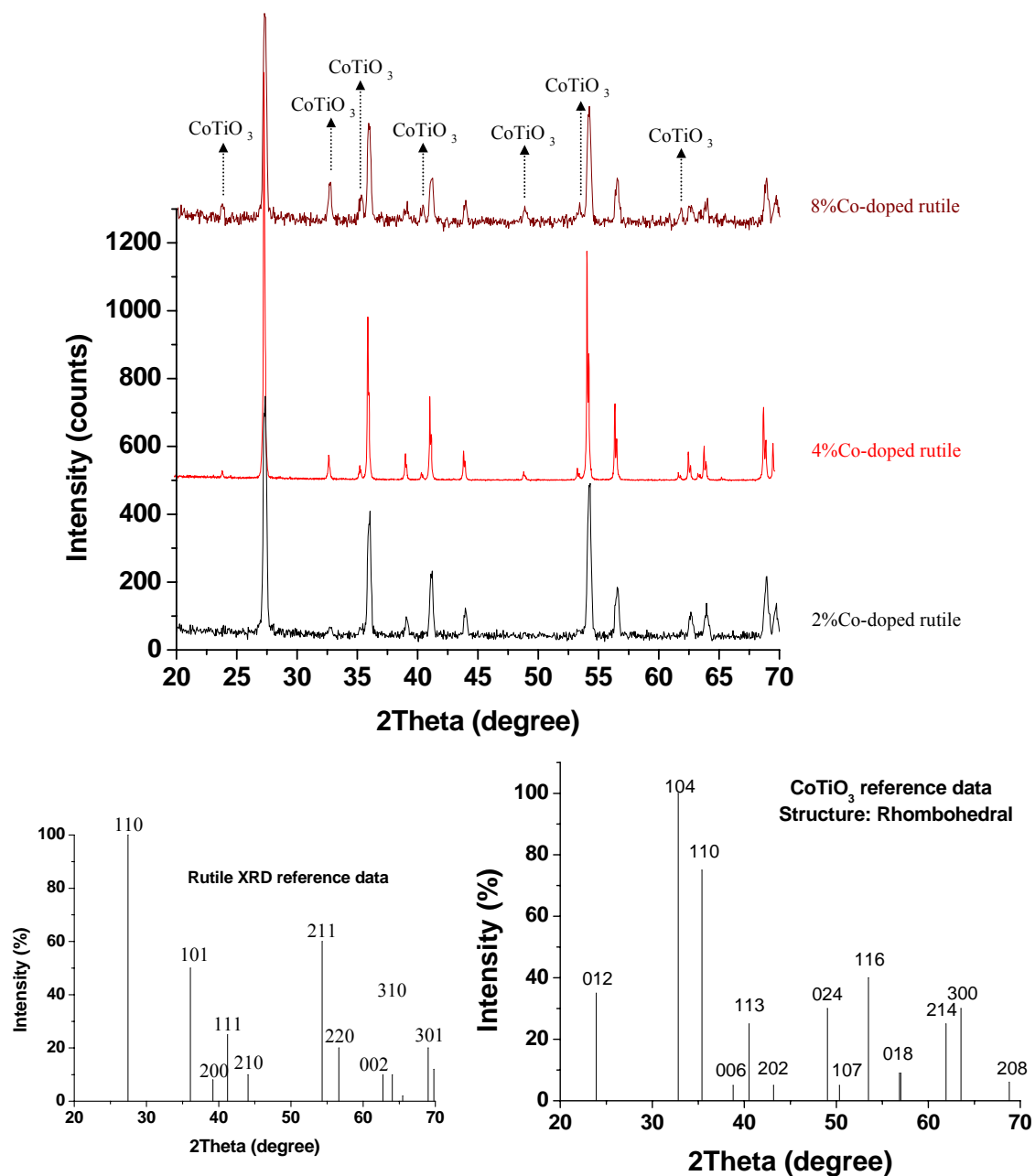
## 6.2. Co-doped TiO<sub>2</sub> powders

### 6.2.1. Preparation of Co-doped TiO<sub>2</sub> powders

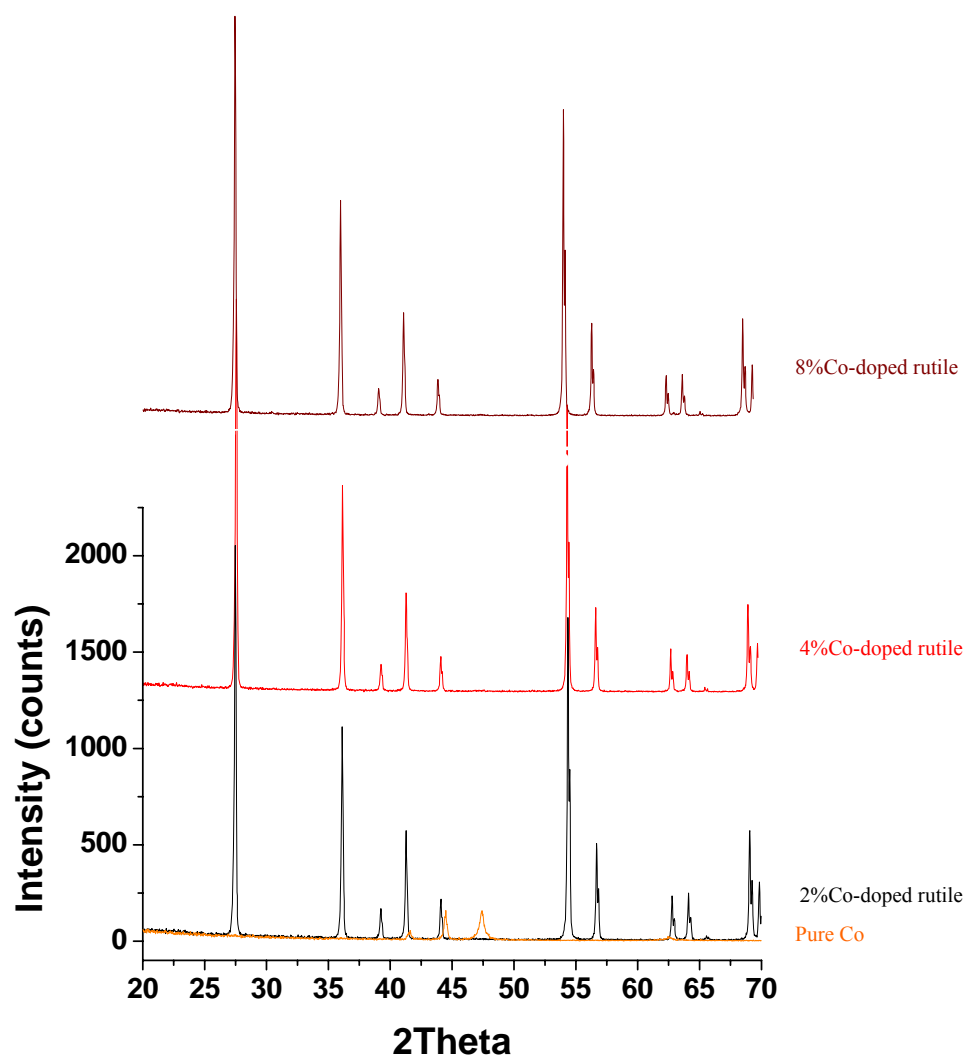
Starting material combinations of both CoO+TiO<sub>2</sub> (anatase) and Co+TiO<sub>2</sub> (anatase) powders were separately well mixed in the desired ratio and the Co content was varied from 2 to 8 atomic % substitution with respect to titanium. These mixtures were calcined at 1100 °C for 8 h in oxygen (for CoO+TiO<sub>2</sub>) or vacuum at 10<sup>-9</sup> bar (for Co+TiO<sub>2</sub>). One apparent difference between powders after calcining was that powders synthesized in oxygen were greenish, while powders synthesized in vacuum were greyish in colour. Phase identification using X-ray diffraction indicated that the combination of CoO+TiO<sub>2</sub> (anatase) synthesized in oxygen was converted mainly to the rutile structure with some weak second phase reflections consistent with CoTiO<sub>3</sub>, as shown in Fig. 6.1, where XRD reference patterns for rutile and CoTiO<sub>3</sub> are also given. Here the CoTiO<sub>3</sub> peak intensities for different contents of Co indicate that increasing the Co content from 2 to 8% increased the amount of the CoTiO<sub>3</sub> phase. These results are consistent with the phase relations in the TiO<sub>2</sub>-CoO pseudo-binary system shown in Fig. 2.5 [229].

XRD patterns taken from Co+TiO<sub>2</sub> (anatase) mixture synthesized in vacuum showed only the rutile structure (Fig. 6.2). No clear evidence for the formation of any second phases (e.g. CoO, Co<sub>3</sub>O<sub>4</sub>, CoTiO<sub>3</sub> or CoTi<sub>2</sub>O<sub>5</sub>) was observed in XRD patterns for these powders calcined in vacuum, although the formation of some small amounts of second phases (below the detection limit of the XRD technique) is possible because a perfect vacuum is not achievable in practice and titanium dioxide itself provides Ti and O atoms around Co particles. Also, while no peaks were detected from pure Co, this is possibly due to the relatively weak peak intensities expected for this element.

The starting material combination of Co+TiO<sub>2</sub> (anatase) powder (%Co=2-8) was also calcined in oxygen at 1100 °C for 8 h. XRD from the resulting powders indicated the rutile structure with extra peaks consistent with CoTiO<sub>3</sub>, i.e. similar to powders prepared using CoO:TiO<sub>2</sub> mixtures synthesized in oxygen.



**Fig.6.1.** XRD patterns taken from  $\text{CoO}+\text{TiO}_2$  (anatase) powder synthesized at  $1100^\circ\text{C}$  for 8 h in oxygen. The Co content varied from 2 to 8% with respect to titanium. XRD reference data for rutile and  $\text{CoTiO}_3$  are also given. These patterns show that synthesized powders mainly comprise the rutile structure with small amounts of  $\text{CoTiO}_3$  second phase.



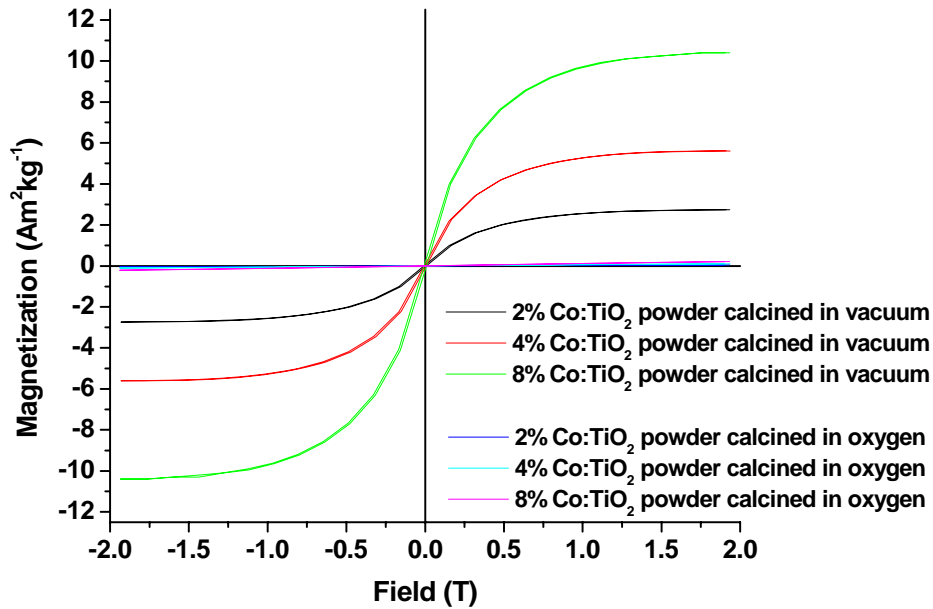
**Fig.6.2.** XRD patterns taken from  $\text{Co}+\text{TiO}_2$  (anatase) powder synthesized at  $1100^\circ\text{C}$  for 8 h in vacuum. The Co content varied from 2 to 8% with respect to titanium. These patterns show that the material has the rutile structure with no detectable segregation of other phases such as Co, cobalt oxides,  $\text{CoTiO}_3$  and  $\text{CoTi}_2\text{O}_5$ .

### 6.2.2. Magnetic properties of Co-doped rutile powders

The magnetic properties of the as-synthesized powders described in section 6.2.1 were measured at room temperature. Magnetization measurements performed on initially CoO:TiO<sub>2</sub> mixtures synthesized in oxygen (which gave the rutile structure with some second phase CoTiO<sub>3</sub>) showed that the powders were paramagnetic (Fig. 6.3). This is consistent with fact that CoTiO<sub>3</sub> is a paramagnetic phase at room temperature (CoTiO<sub>3</sub> is antiferromagnetic at low temperature with a Neel temperature of ~35.6 K); thus, the magnetization values for these powders would be expected to be relatively small at room temperature due to the presence of diamagnetic rutile with paramagnetic CoTiO<sub>3</sub>.

On the other hand, magnetization vs. field plots measured from initially Co:TiO<sub>2</sub> mixtures synthesized in vacuum (which led to the formation of the rutile structure with no obvious evidence of other phases on the XRD patterns shown in Fig. 6.2) showed room temperature ferromagnetism for all powders (Fig. 6.3). While increasing the Co content from 2 to 8% increased the magnetic moment per kilogram, no significant difference was observed in the calculated magnetization values *per Co atom* (~1.8-1.9 μ<sub>B</sub>/Co atom) for Co contents between 2 and 8%. These magnetization values per Co atom are comparable to the average magnetic moment per atom of 1.7 Bohr magneton for pure Co; therefore, it can be concluded that the electronic structure of Co did not change in the local environment (TiO<sub>2</sub>) during the solid state reaction when prepared under vacuum. (These magnetization values per Co atom are two orders of magnitude higher than those measured from powders synthesized in oxygen).

Since the magnetic moment values per Co atom in vacuum-prepared powders are equivalent to pure cobalt and no clear evidence of second phases such as cobalt oxides, CoTiO<sub>3</sub> and CoTi<sub>2</sub>O<sub>5</sub> were seen from XRD patterns, the enhanced magnetization in these powders could be attributed to the presence of Co particles which were too small to be detected by the X-ray diffraction technique. This observation of room temperature FM in Co-doped TiO<sub>2</sub> powders prepared in a reduced oxygen environment is consistent with the reported work by Cho et al. [225], where the presence of Co metal clusters was observed in vacuum-annealed powders (synthesized by the sol-gel method) using a high resolution TEM.



**Fig.6.3.** Magnetization measurements performed on powders synthesized in oxygen and vacuum for Co contents between 2 and 8% shown in Fig. 6.1 and Fig. 6.2 respectively.

Overall, it can be concluded that an oxygen deficient environment during the preparation of Co-doped TiO<sub>2</sub> powders using a solid state reaction was crucial for the observation of room temperature ferromagnetism, while preparation in oxygen rich conditions destroyed the ferromagnetism and led to the formation of the paramagnetic second phase CoTiO<sub>3</sub>. The topic of the exact origin of the ferromagnetism seen in vacuum prepared powders is returned to in a later section on single crystals.

### 6.3. Co-doped rutile single crystals

#### 6.3.1. Feed rod preparation

Both powder combinations described in section 6.2.1 were used to prepare feed rods for FZ using the same method as explained for the pure rutile, except that the sintering temperature was selected to be 1100 °C for 8 h in either oxygen (for the powder calcined in oxygen) or vacuum (for the powder calcined in vacuum). Higher sintering temperatures (for example, 1600 °C in oxygen) were found to be inappropriate due to

evaporation of phases including cobalt, leading to departures from the stoichiometric composition.

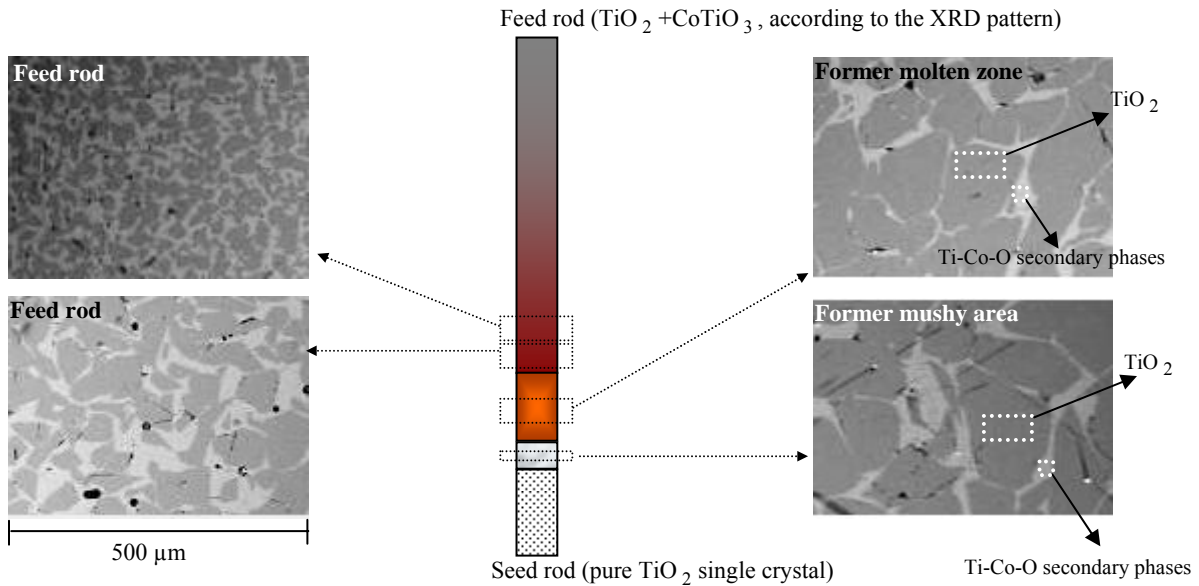
### 6.3.2. Crystal growth

Since detection of the formation of any second phases (using both the X-ray diffraction and SEM/EDX techniques) would be more likely at higher cobalt contents, crystal growths were only attempted with Co contents of 4 and 8%, rather than 2%.

However, growths using feed rods synthesized in oxygen (i.e.  $\text{TiO}_2 + \text{CoTiO}_3$ ) with a Co content of 8% were not successful due to the formation of a mushy (liquid+solid) region below the molten zone, which led to the zone falling out. (These unsuccessful runs were performed under 1 bar oxygen pressure using ~66.0% of the total lamp power). SEM studies of this area around the melt zone (performed on a sample after an unsuccessful growth) indicated that, once solidified, this region contains  $\text{TiO}_2$  (darker area) and second phases of Ti-Co-O (lighter area) as shown in Fig. 6.4. This non-congruent melting behaviour of the material is consistent with the phase relations of CoO- $\text{TiO}_2$  system (Fig. 2.5) in which the first solid to form as liquid with a concentration of 8%CoO+92% $\text{TiO}_2$  is cooled should be  $\text{TiO}_2$ . The phase diagram further indicates that the liquid composition (Co-Ti-O phase) changes as the solidification goes to completion. EDX analysis was not sufficiently accurate to find the exact composition of any Co-Ti-O phases in the present samples, however, because the phases contain the light element oxygen.

In an attempt to narrow the mushy area during FZ and to make a more clearly defined liquid (molten zone)/solid (growing crystal) interface, the oxygen pressure was increased to 5 bar. While this created a sharper temperature gradient along the sample, it did not sufficiently increase the stability of the molten zone to allow controllable FZ. (70% lamp power was required to melt the sample at 5 bar compared to 66% needed to melt the material under 1 bar oxygen pressure; this is consistent with the temperature characterization of the FZ system described in chapter 4, which showed that higher lamp powers are required to melt samples at higher gas pressures due to the cooling effects of the gas).

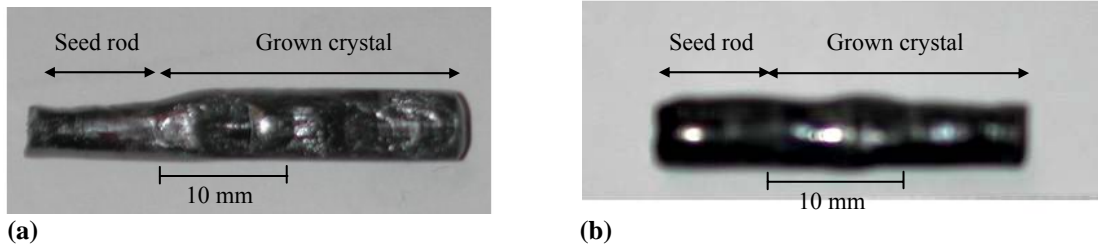




**Fig.6.4.** Backscattered images taken from the cross sections of the feed rod ( $\text{TiO}_2 + \text{CoTiO}_3$ ) with the Co content of 8% near to the molten zone, the molten zone and growing crystal at the beginning of growth procedure.

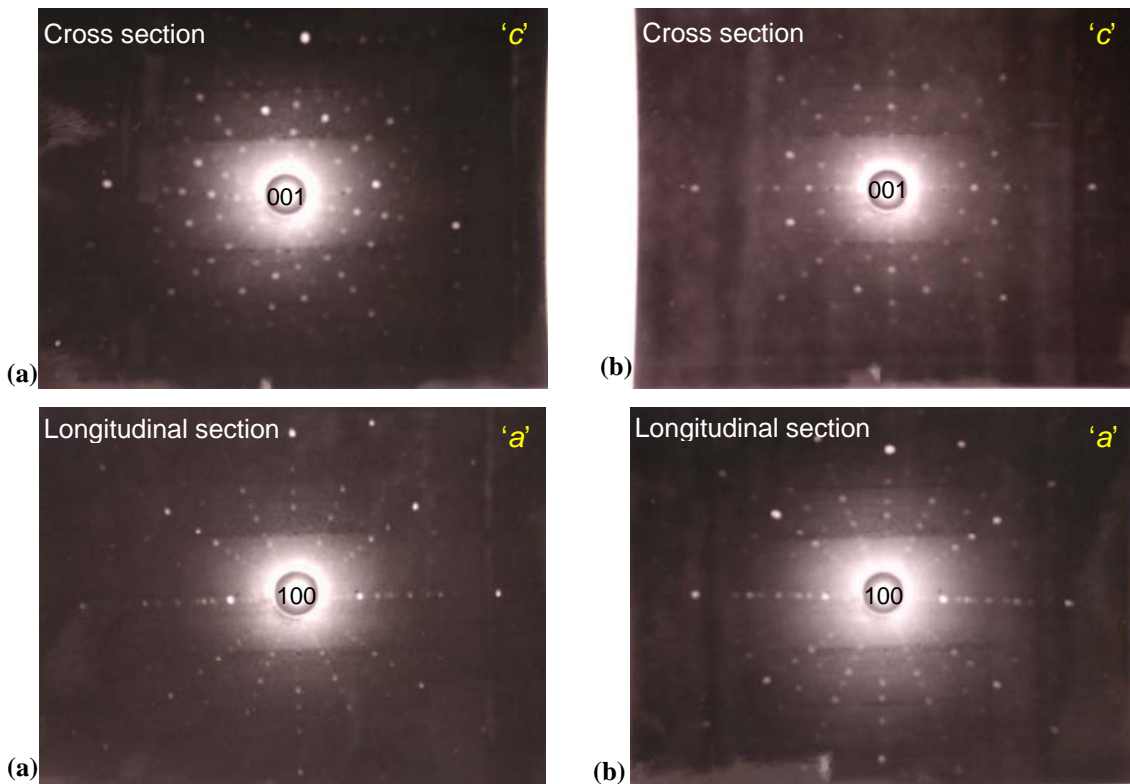
However, by both reducing the Co content to 4% and increasing the gas pressure to 5 bar it proved possible to perform successful growths due to the formation of a more solid region below the melt zone and, consequently, a more stable molten zone. The formation of a more solid region below the molten zone at a Co content of 4% is again consistent with the reported phase relations (Fig. 2.5) in which the solidification process at this composition starts with a lesser amount of liquid compared to 8% Co content. Growths using feed rods synthesized in vacuum also exhibited stable molten zones during growth under 5 bar argon for the 4%Co composition.

Fig. 6.5 shows 4%Co: $\text{TiO}_2$  crystals grown in *both* oxygen and argon using feed rods calcined in oxygen and vacuum respectively. These growths were performed under 5 bar gas pressure at a growth rate of 5 mm/h, with rotation rates of 15 rpm for the growing crystal (lower shaft) and 0 rpm for the feed rod (upper shaft). Although both crystals appear black in these pictures, cutting and polishing revealed that the crystal grown in oxygen (Fig. 6.5.a) was actually red, while the crystal grown in argon shown in Fig. 6.5.b, was black.



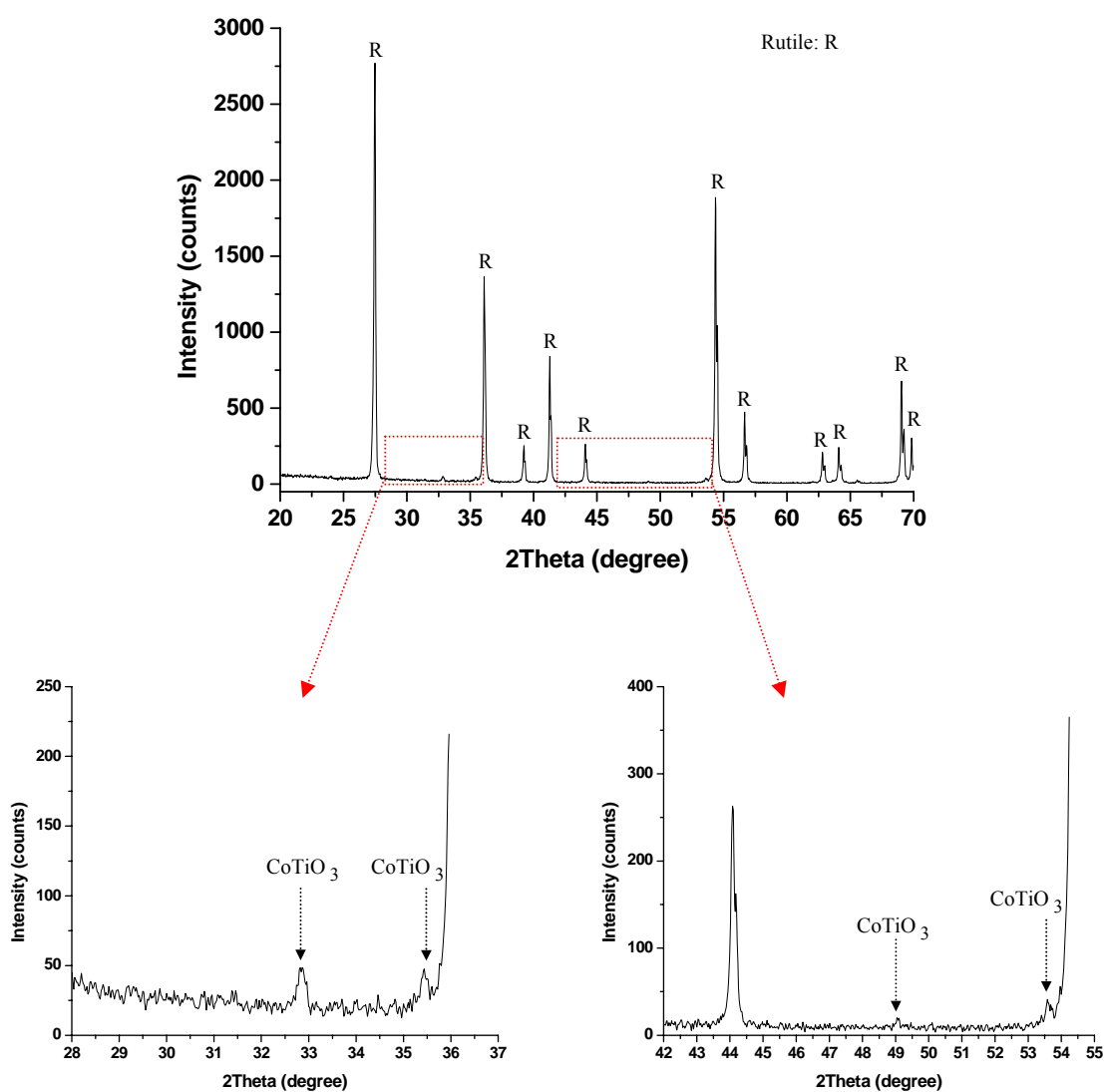
**Fig.6.5.** Typical 4%Co:TiO<sub>2</sub> single crystals grown in oxygen (a) and argon (b). These growths were carried out under 5 bar gas pressure at a growth rate of 5 mm/h, with rotation rates of 15 rpm for the growing crystal and 0 rpm for the feed rod.

X-ray Laue diffraction photographs taken along the lengths and cross sections of the crystals (Fig. 6.6) indicated that both crystals exhibited an equally high crystalline quality, and that the crystals had adopted the orientation of the seed crystal, which was a pure TiO<sub>2</sub> single crystal oriented with the 'c'-axis along its length.

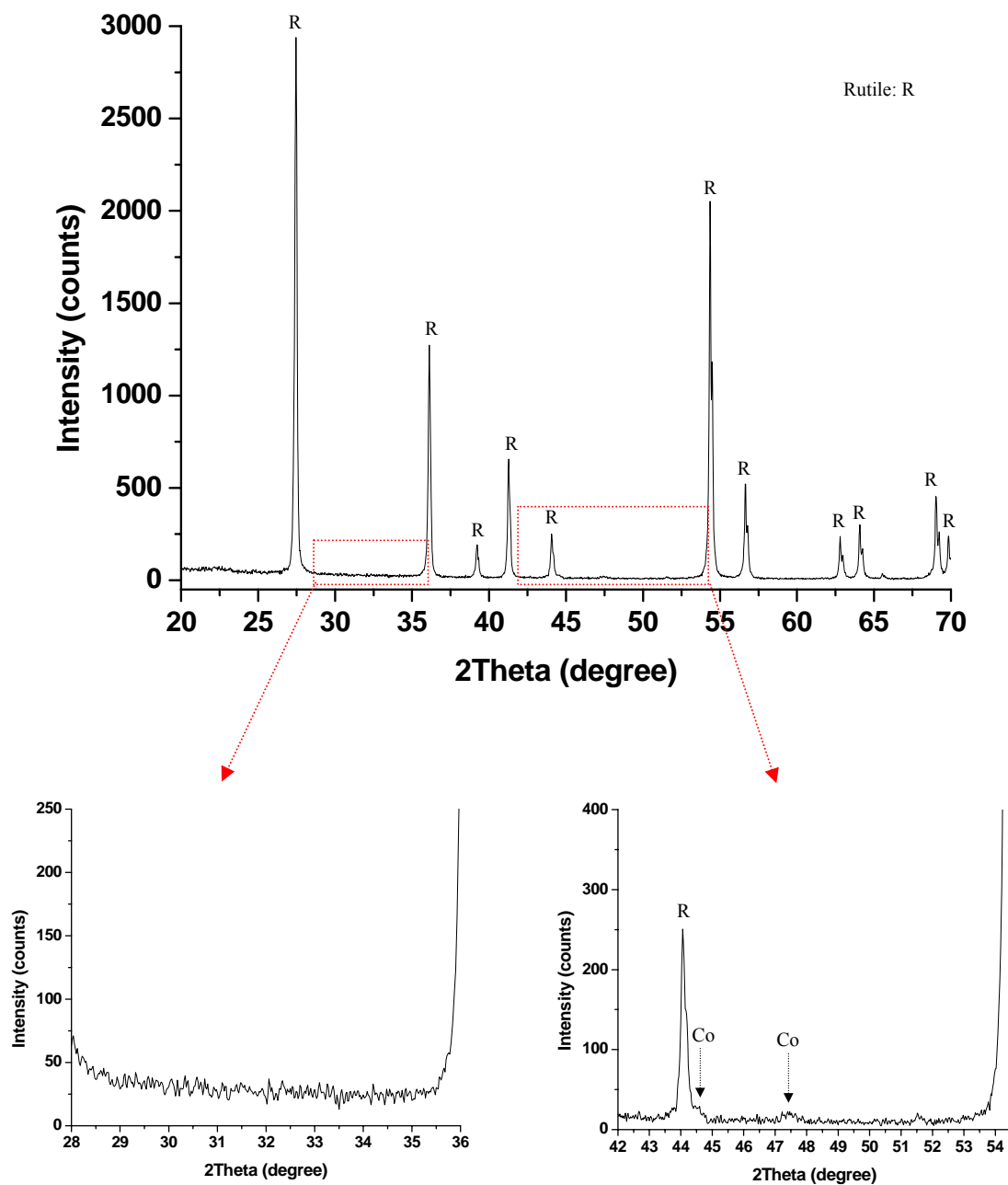


**Fig.6.6.** Laue diffraction photographs taken from the cross and longitudinal sections of the crystals grown in oxygen (a) and in argon (b). These X-ray Laue pictures indicated that both crystals exhibited an equally high crystalline quality, and the growth direction was [001].

X-ray diffraction patterns of the crushed as-grown *crystals* indicated that the crystal grown in oxygen had the rutile structure with second phase  $\text{CoTiO}_3$  (Fig. 6.7) similar to the starting powder. However, the crystal grown in argon showed the rutile structure with very weak and broad extra peaks consistent with the 002 and 101 [hcp] reflections for pure Co at  $2\theta$  values of  $44.7^\circ$  and  $47.5^\circ$  respectively (Fig. 6.8). This contrasts with the *starting powder* in which no extra reflections beyond those expected for rutile were evident. The broadening of these peaks could indicate strain within the Co clusters, and/or that they were not pure Co, but contained some Ti or O.



**Fig.6.7.** The XRD pattern taken from the crushed 4%Co-doped  $\text{TiO}_2$  single crystal grown under 5 bar oxygen pressure



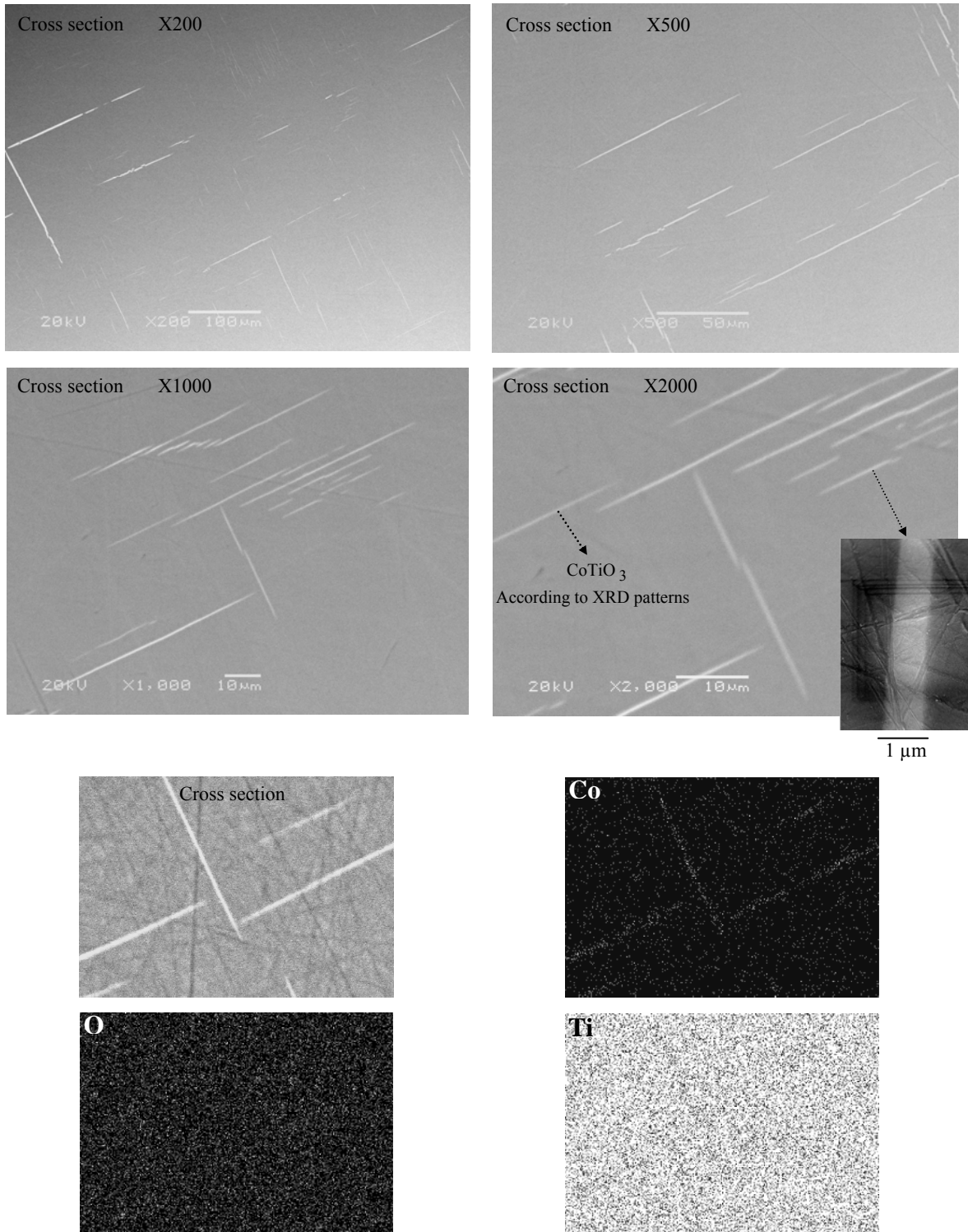
**Fig.6.8.** The XRD pattern taken from the crushed 4%Co-doped TiO<sub>2</sub> single crystal grown under 5 bar argon pressure

For further characterization, back scattered SEM micrographs were taken from polished cross and longitudinal sections of crystals grown in oxygen (Fig. 6.9 and Fig. 6.10) and in argon (Fig. 6.11 and Fig. 6.12) along with chemical mapping figures obtained by EDX to demonstrate the distribution of elements. The formation of second phases in both crystals is clearly shown in back scattered images, although the inclusions were differently shaped.

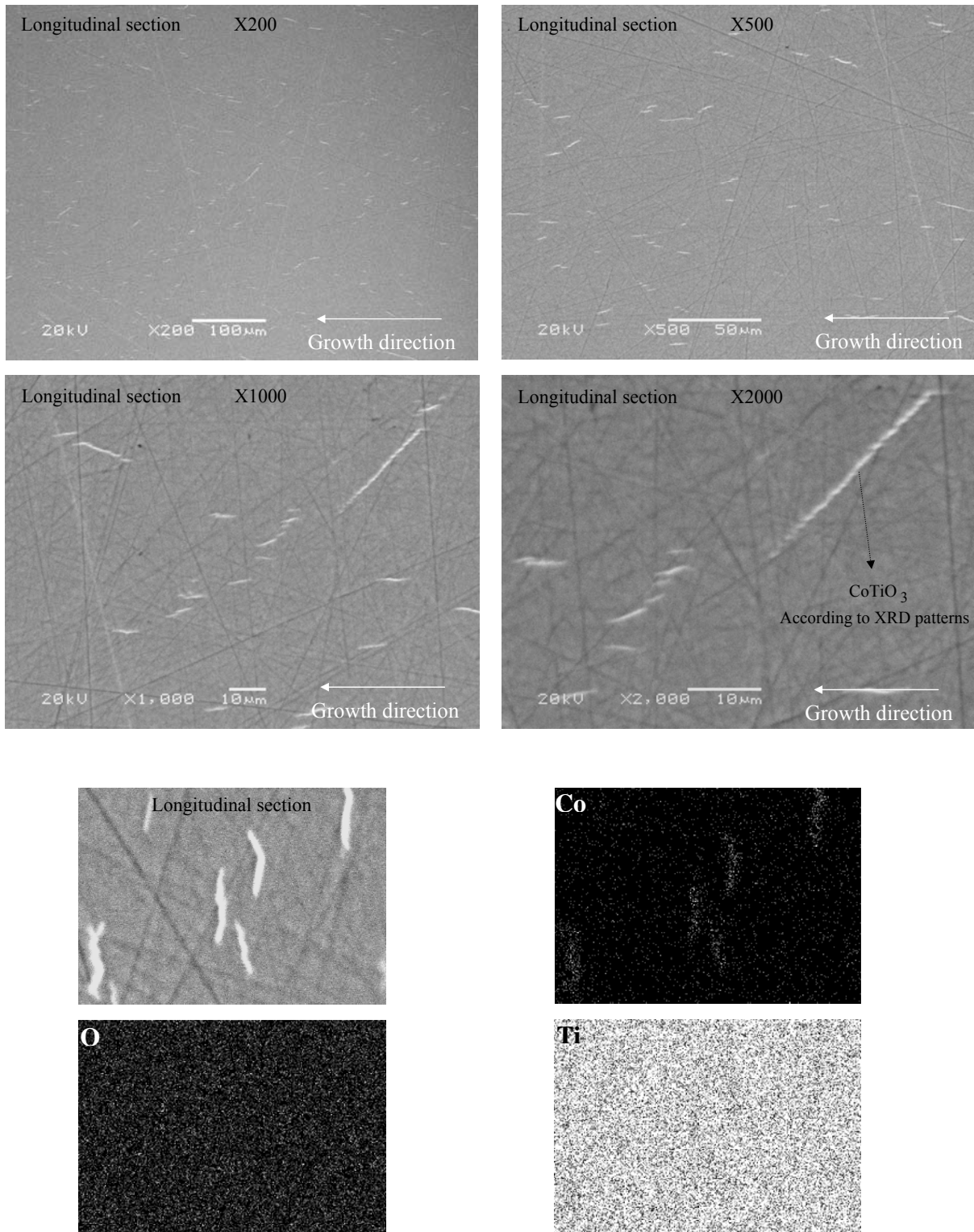
Chemical mapping figures taken from the *crystal grown in oxygen* revealed that Ti and O were uniformly distributed throughout the whole area, while the secondary phase particles also contain Co; this is consistent with the conclusion that these secondary precipitants are a Ti-Co-O phase. Conversely, the EDX maps in Figs. 6.11 and 6.12 taken from the *crystal grown in argon* clearly shows a significant drop in Ti and O signal intensities in the precipitates indicating the secondary phase is either Co metal or very rich in Co.

While the EDX technique is not particularly suited to examining light elements such as oxygen, analyses performed on both crystals (i.e. grown in oxygen and argon) indicated that the matrix was very close to  $\text{TiO}_2$  with no clear evidence of Co incorporation, while all second phases consistently included Co atoms. Although the technique was found not to be sufficiently accurate to identify the *exact* Co-Ti-O second phase in the sample grown in oxygen, results are consistent with the XRD data that indicated the second phase is  $\text{CoTiO}_3$ . For the crystal grown in argon, the EDX results showed that second phases were Co rich with the average atomic percentage of more than 90% (with the atomic percentage of Ti varying between 3.72-10%), which again agrees with the XRD data from the as-crushed crystal that showed broad peaks consistent with Co. Since these Co rich clusters consistently have a square shape in cross section and are elongated along the 'c' direction of the matrix (growth direction) it can be surmised that they are either single crystal or polycrystalline with a preferential crystalline orientation.

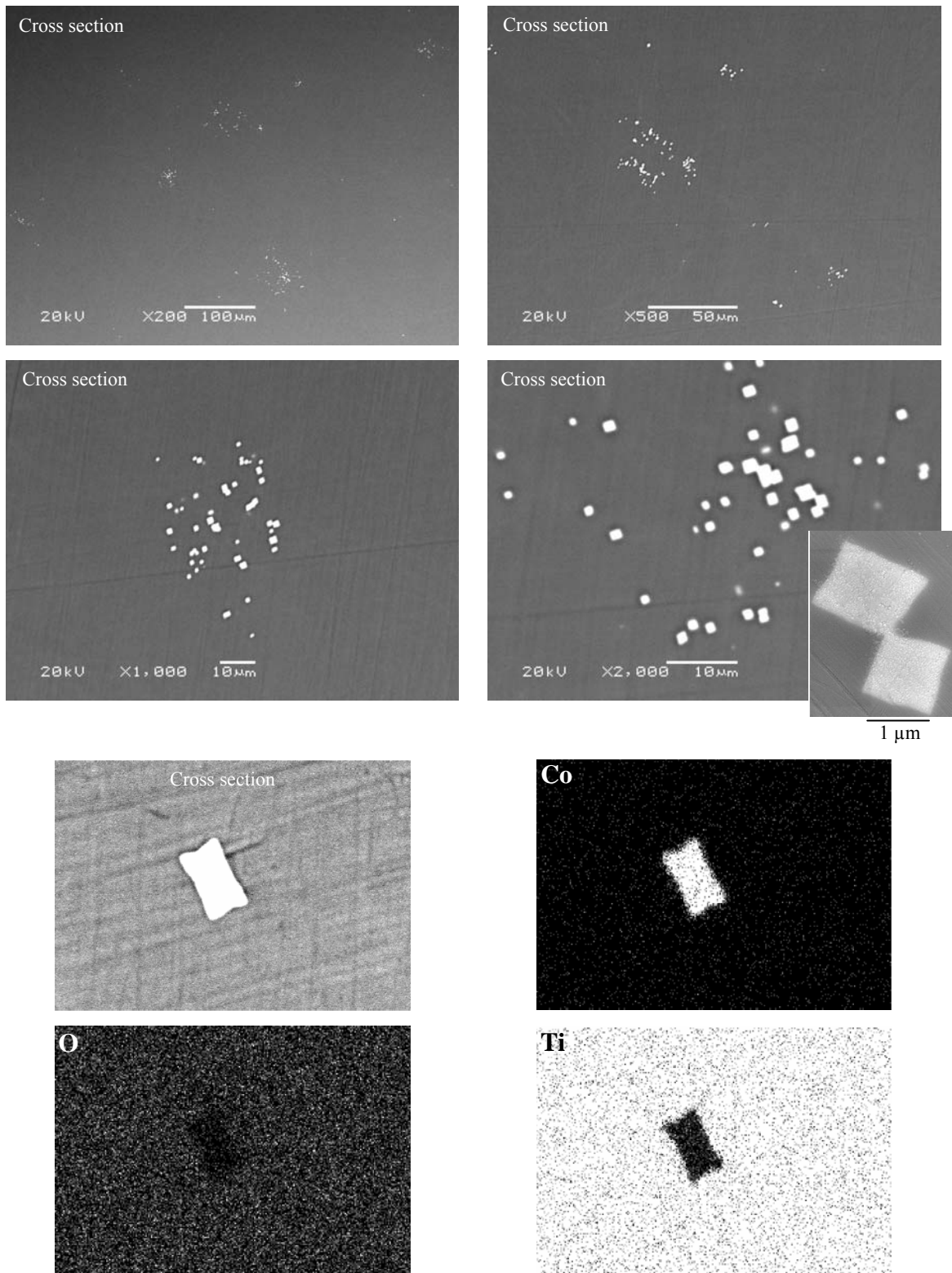
Overall, the above results clearly indicate that in neither crystals Co had dissolved into the rutile matrix during equilibrium preparation from its melt using the FZ technique. Furthermore, it is evident that the type of atmosphere used during crystal growth affects the type of cobalt-based second phases; crystals grown in oxygen had  $\text{CoTiO}_3$  precipitants, while the crystal grown in argon had Co-rich particles as the second phase.



**Fig.6.9.** SEM back scattered micrographs of a *cross section* cut from a 4%Co:TiO<sub>2</sub> single crystal grown at 5 mm/h in oxygen. Growth in oxygen led to the formation Co-Ti-O phases which were identified as CoTiO<sub>3</sub> by XRD (Fig. 6.8). EDX chemical mapping images are also given.

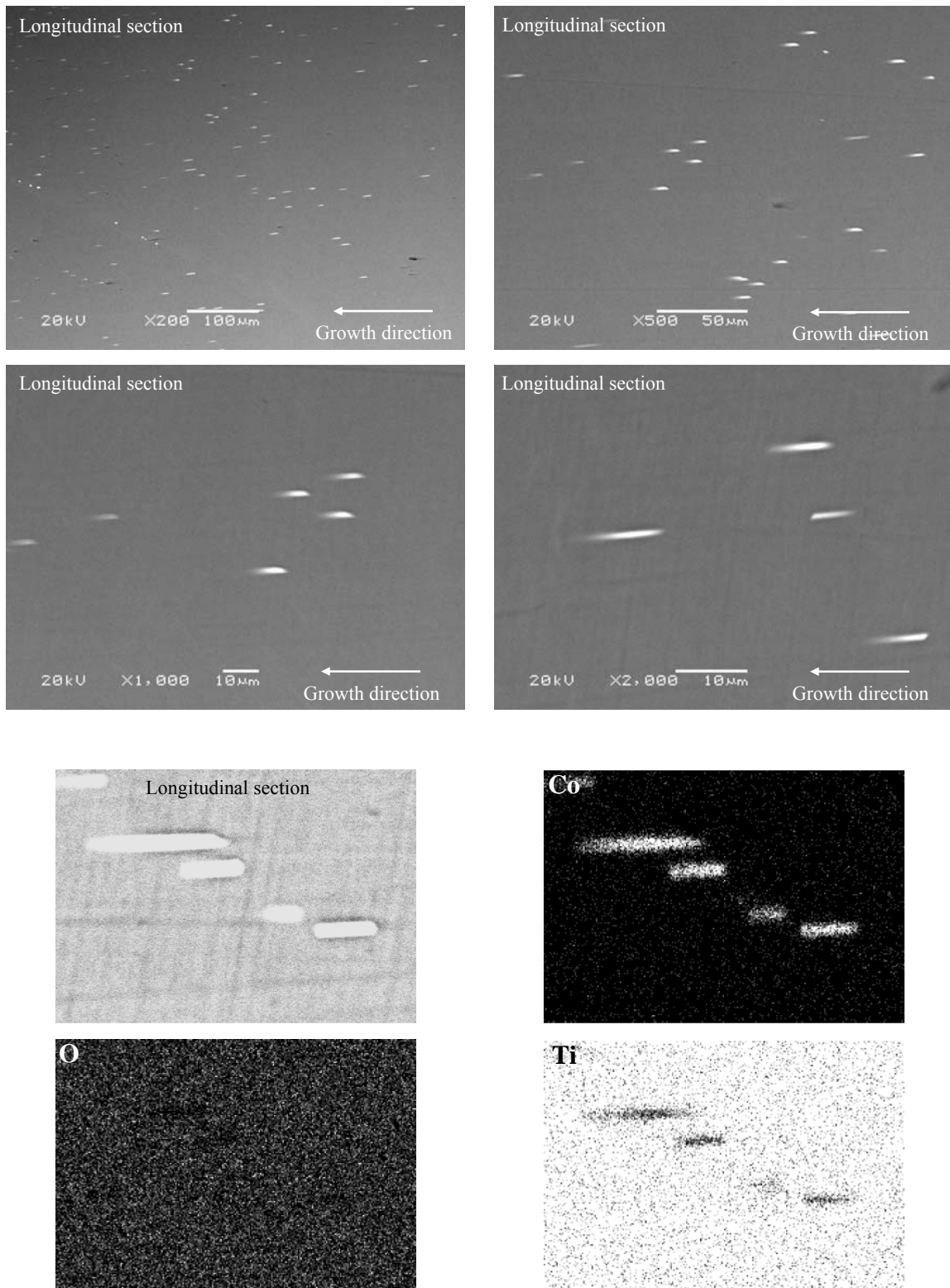


**Fig.6.10.** SEM back scattered micrographs of a *longitudinal section* cut from a 4%Co:TiO<sub>2</sub> single crystal grown at 5 mm/h in *oxygen*. Growth in oxygen led to the formation Co-Ti-O phases which were identified as CoTiO<sub>3</sub> by XRD. EDX chemical mapping images are also given.



**Fig.6.11.** SEM back scattered micrographs of a *cross section* cut from a 4%Co:TiO<sub>2</sub> single crystal grown at 5 mm/h in *argon*. Growth in *argon* led to the formation Co rich particles. EDX chemical mapping images are also given.

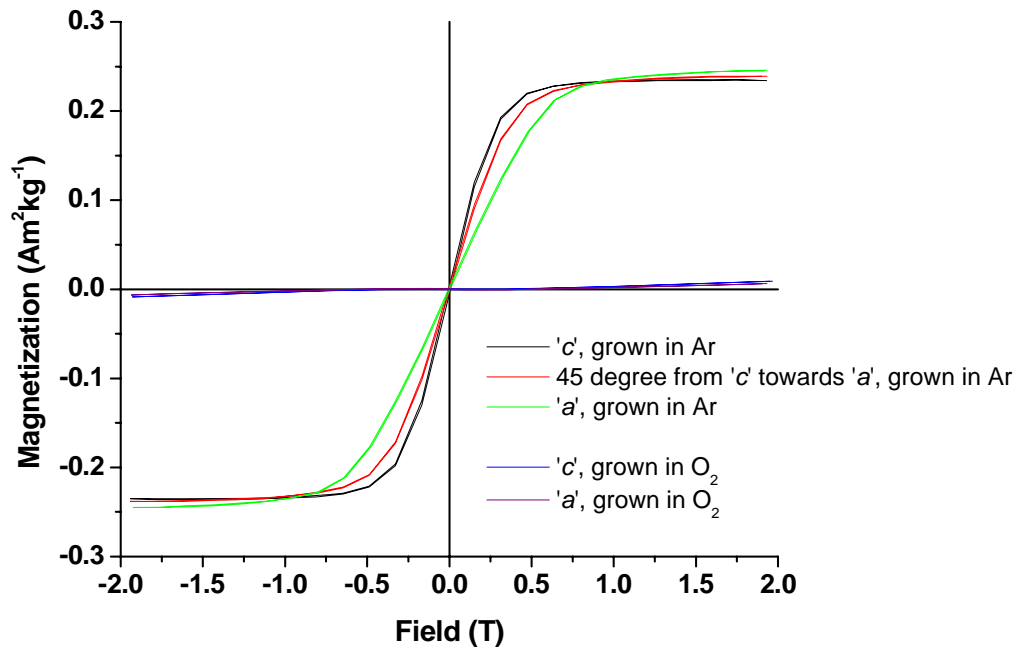




**Fig.6.12.** SEM back scattered micrographs of a *longitudinal section* cut from a 4%Co:TiO<sub>2</sub> single crystal grown at 5 mm/h in *argon*. Growth in *argon* led to the formation Co rich particles oriented along the growth direction. EDX chemical mapping images are also given.

### 6.3.3. Magnetic properties of Co-doped rutile single crystals

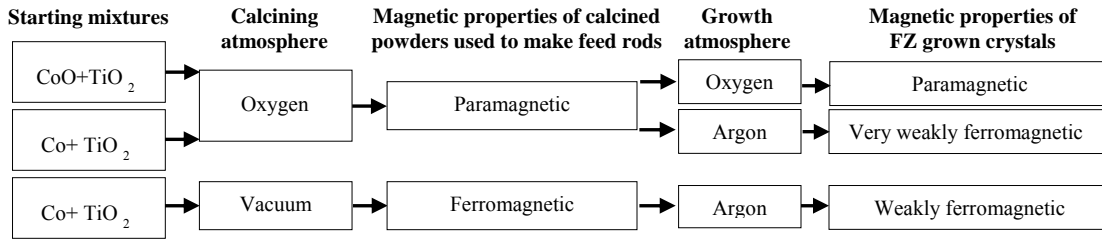
The magnetic response from the 4%Co:TiO<sub>2</sub> single crystal samples was measured as a function of magnetic field along the 'c', 'a' and 45 degree from 'c' towards 'a' directions for the sample grown in argon, and along 'c' as well as 'a' for the sample grown in oxygen, as shown in Fig. 6.13. These measurements clearly indicate that room temperature ferromagnetism was observed only in the crystal grown in argon. This had a saturation magnetization about 0.24 Am<sup>2</sup>kg<sup>-1</sup> (~0.083 μ<sub>B</sub>/Co atom), with the easy magnetization direction along 'c' and the hard direction of magnetization along 'a'. Crystals grown in oxygen, however, only showed a weak paramagnetic behaviour.



**Fig.6.13.** M-H curves measured at room temperature for 4%Co:TiO<sub>2</sub> (rutile) crystals grown in oxygen and argon. Room temperature ferromagnetism with magnetization 0.24 Am<sup>2</sup>kg<sup>-1</sup> (~0.083 μ<sub>B</sub>/Co atom) was observed in crystals grown in argon, while a weak paramagnetic behaviour was obtained from crystals grown in oxygen.

A single FZ experiment under *argon* was also performed with a CoO:TiO<sub>2</sub> (%Co=4) mixture initially calcined in *oxygen*, which gave a weakly ferromagnetic sample with a saturation magnetization about 0.017 μ<sub>B</sub> /Co atom along the 'c' direction. The various

routes used to prepare the crystals from starting mixes to final FZ growth are summarized in Fig. 6.14.



**Fig.6.14.** Preparation routes and magnetic properties of Co-doped rutile powders and single crystals

The differences of the magnetic properties of the two main crystal types (i.e. grown in oxygen or argon), as shown in Fig. 6.13, can be explained from the results of the microstructural studies carried out using XRD and SEM. In this regard, the room temperature ferromagnetism observed in crystals grown in argon is almost certainly due to the formation of ferromagnetic Co rich clusters. However, the saturation magnetization of these crystals ( $0.24 \text{ Am}^2 \text{ kg}^{-1}$  which equates to  $\sim 0.083 \mu_B/\text{Co}$  atom if the Co content in the crystal is assumed to be 4%), is significantly lower than the magnetization of the feed rod/starting material (4%Co:TiO<sub>2</sub> powders prepared in vacuum) which had values about  $5.61 \text{ Am}^2 \text{ kg}^{-1}$  or  $\sim 1.9 \mu_B/\text{Co}$  atom (close to the magnetic moment of pure cobalt,  $1.7 \mu_B/\text{Co}$  atom). Since this significant decrease in magnetization values occurred as a result of the FZ crystal growth process (i.e. increasing the temperature to the melting point,  $\sim 1800^\circ \text{C}$ , and then solidification of the molten zone) it could possibly be caused by either a reduced amount of Co in the final crystal compared to the start material and/or a reduction in the magnetization of the Co atoms present. These possible scenarios are discussed below.

#### (1) *Evaporation of Co during FZ*

Co losses of about 1.5-2.0 %Co were reported [285] during melting and crystal growth of CoTi crystals ( $T_m \approx 1325^\circ \text{C}$ ). However, the loss of more Co during FZ growth of

4%Co:TiO<sub>2</sub> crystals is likely since the melting temperature of the material, ~1800 °C, is much higher.

(2) *Segregation of Co during FZ*

A reduced amount of Co in the as-grown crystal could result if Co is “pushed” along by the molten zone. Since the back scattered images taken from the crystal (Figs. 6.11 and 6.12) point to a very low solubility of Co into the TiO<sub>2</sub> matrix, some transport of Co particles could take place during FZ. (Such transport of Co to give a composition about 1% richer at the top portion of FZ grown CoTi crystals is reported by Zhang et al. [285]). Some strength to this argument was given by a magnetization measurement taken from the final (solidified) molten zone section after crystal growth which showed enhanced magnetization values (~2.3 Am<sup>2</sup> kg<sup>-1</sup>) compared to the as-grown crystal.

(3) *Changes in the electronic structure of Co*

Any reaction of Co with Ti or O will decrease its magnetization values due to changes in magnetic/electronic structure of Co. In this regard, several studies have indicated that the Co between Ti layers (as the local environment) has very small magnetic moments (down to 0.07 μ<sub>B</sub>) [286], while increasing the Ti concentration significantly decreased the magnetic moment of Co in Co<sub>100-x</sub>Ti<sub>x</sub> thin films [287-289]. While the X-ray data from the crushed crystal indicated that the Co-rich inclusions still had the Co structure, it should be noted that the solubility limit for Ti dissolved in Co has a maximum of 15% at 1190 °C.

Further work, however, is needed to discover which of the reasons suggested to explain why the crystal had a lower than expected magnetization value is correct. It is also noted that the saturation magnetization value measured from the crystal grown in argon is close to the lowest room temperature magnetic moment (~0.1 μ<sub>B</sub>/Co) reported for Co-doped TiO<sub>2</sub> thin films [206].

One more magnetization measurement was performed on the single crystal grown in argon *after powdering* to see whether the differences in magnetic properties between the start materials (powders) for FZ and the final crystal could be due to the form of the sample. The measured saturation magnetization value (0.204 Am<sup>2</sup> kg<sup>-1</sup>), however, was close to the value obtained from the crystal before powdering (0.24 Am<sup>2</sup> kg<sup>-1</sup>), thereby

showing that the act of powdering did not have a significant effect on the magnetic properties.

The dependence of the magnetic properties of the single crystal on a preferred direction (i.e. easy and hard magnetization directions along 'c' and 'a' directions respectively) shows that this material exhibits some magnetic anisotropy. Since the matrix, rutile, is a diamagnetic material, this apparent anisotropy must come from the Co rich clusters and probably arises either from the shape anisotropy of the individual precipitates (due to magnetostatic effects, i.e. the demagnetizing field was less when measuring magnetization along the long axis of these needle shaped clusters) and/or from the intrinsic magnetocrystalline anisotropy of Co (if these clusters are single crystals or preferentially aligned). However, since these clusters are small in size, shape anisotropy could be more dominant than magnetocrystalline anisotropy.

The room temperature paramagnetic behaviour of crystals grown in oxygen can be explained by the formation of paramagnetic second phases of  $\text{CoTiO}_3$ , as described earlier for the powder samples.

Overall, it can be concluded that the magnetic properties of Co-doped rutile bulk samples (both single crystals prepared using the FZ technique and polycrystalline powders prepared using a solid state reaction) clearly depend on the material preparation conditions. In the case of single crystals, Co-rich clusters form after processing  $\text{Co}:\text{TiO}_2$  mixtures in vacuum/argon which lead to ferromagnetism, while paramagnetic (at room temperature)  $\text{CoTiO}_3$  forms after processing  $\text{CoO}:\text{TiO}_2$  mixtures under oxygen. The same explanations probably hold for as-calcined powders, although no evidence could be found from XRD for Co-rich clusters in samples prepared in vacuum, so incorporation of Co into the  $\text{TiO}_2$  lattice, giving the observed ferromagnetism, can not be ruled out from the present results. However, a much more likely explanation is that the XRD peaks from Co clusters were too broad to be detected.

Concerning the ongoing controversy of whether Co atoms really incorporate into the  $\text{TiO}_2$  structure or form clusters in *thin films*, it would appear likely from the evidence of the present work that if any Co *incorporation* does occur, it is a non-equilibrium effect. Also, it is suggested that the present research would indicate that study of the Co-based

second phases, which appear to be the source of the ferromagnetic properties in Co-doped  $\text{TiO}_2$ , is best achieved using bulk samples.

#### 6.4. Summary

- The magnetic properties of Co-doped rutile bulk samples (both single crystals prepared using the FZ technique and polycrystalline powders prepared using a solid state reaction) depend upon both the material preparation conditions.
- An oxygen deficient environment during the preparation of Co-doped  $\text{TiO}_2$  powders using a solid state reaction was crucial for the observation of room temperature ferromagnetism, while preparation in oxygen rich conditions led to the formation of paramagnetic material that included second phase  $\text{CoTiO}_3$ .
- The preparation of  $\text{Co}:\text{TiO}_2$  single crystals from the melt using the FZ technique indicated that Co does not dissolve into the rutile matrix, and that the type of atmosphere during FZ affects on the type of cobalt-based second phases.
- Crystals grown in oxygen had  $\text{CoTiO}_3$  precipitants and showed weak paramagnetic behaviour, while crystals grown in argon had Co-rich particles as the second phase and showed ferromagnetism at room temperature.

# CHAPTER 7: RARE EARTH ORTHOFERRITES (RESULTS AND DISCUSSION)

## 7. Rare earth orthoferrites, $R\text{FeO}_3$ ( $R=\text{Er}$ and $\text{Y}$ )

### 7.1. Introduction

High quality single crystals of orthoferrites are indispensable for providing a better understanding of the magnetic properties and potential applications of these materials; however, despite the current popularity of image furnaces for crystal growth of oxide materials no comprehensive studies seem to have been reported on the growth and characterization of orthoferrite single crystals. Furthermore, given the amount of effort that has been expended upon both physical property determination and crystal growth of rare earth orthoferrites, few publications appear to have investigated the relationship between crystal quality and properties. For example, it is not known in any detail how responsive are the magnetic properties of these materials to factors such as impurity concentration, second phase distribution, crystallinity or other defects that may be produced during the preparation of crystals.

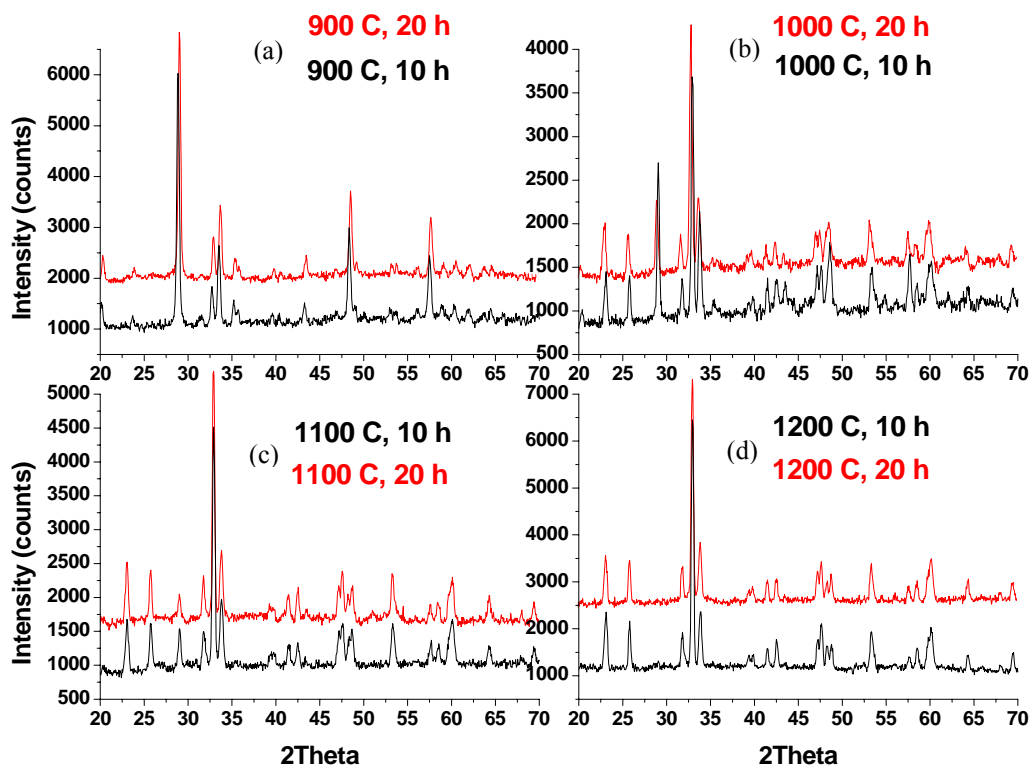
The aim of this part of the project, therefore, was to attempt to grow high quality orthoferrite crystals ( $R\text{FeO}_3$ ,  $R=\text{Er}$  and  $\text{Y}$ ) using the optical FZ technique, and also to investigate the effects of growth parameters, such as growth rate, oxygen pressure and rotation rate on both the quality of crystals and their subsequent magnetic properties.

### 7.2. Erbium orthoferrite ( $\text{ErFeO}_3$ )

#### 7.2.1. Feed rod preparation of $\text{ErFeO}_3$

Stoichiometric amounts of the starting materials,  $\text{Er}_2\text{O}_3$  (99.9% purity) +  $\text{Fe}_2\text{O}_3$  ( $\geq 99.0\%$  purity), were thoroughly ground/mixed together (for 2 h by hand) and then synthesized at 900-1200° C for either 10 or 20 h in air to find the appropriate calcination procedure at which the constituents were converted to the orthoferrite structure. Fig. 7.1a-d shows

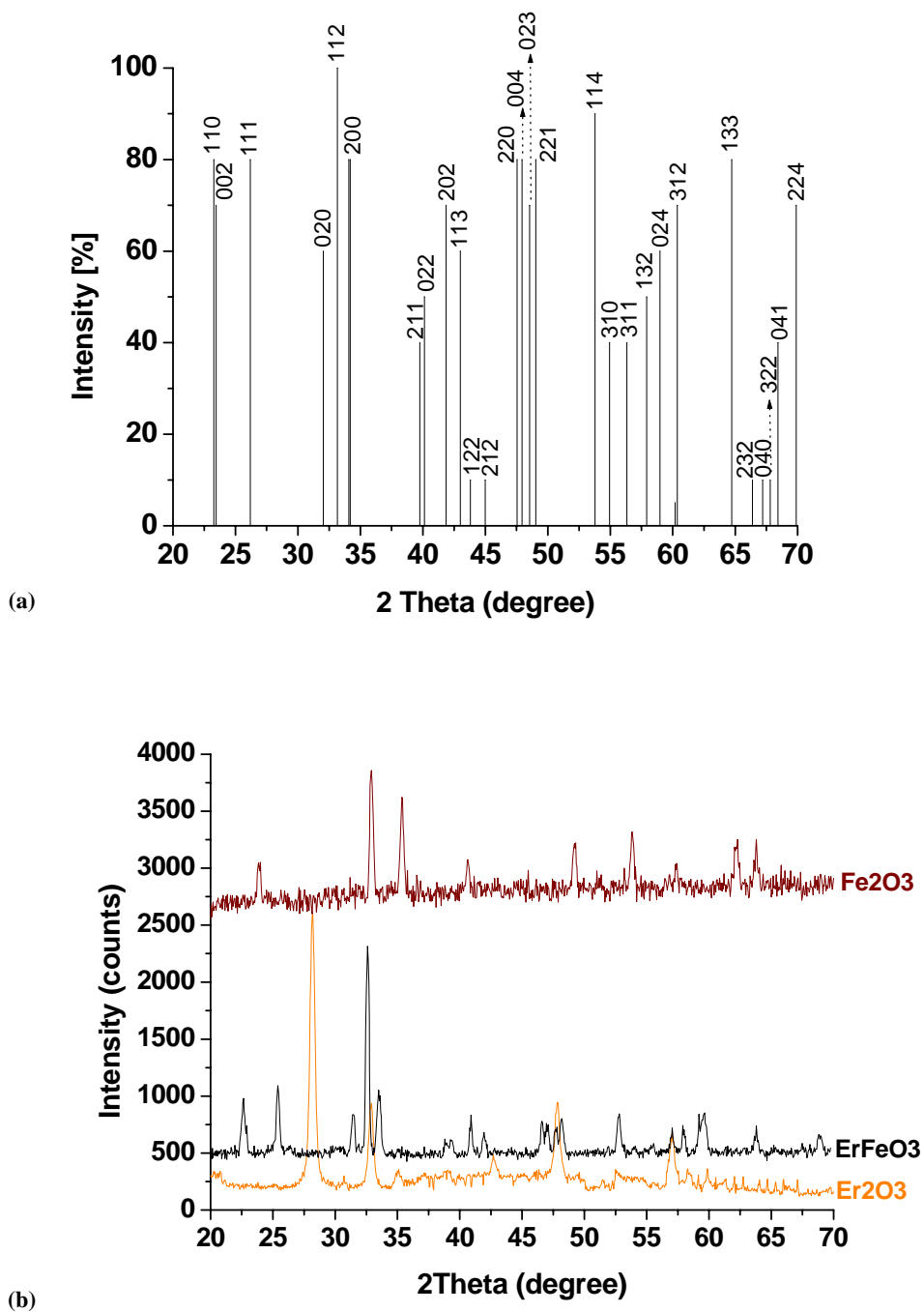
XRD patterns taken from powders after calcining at temperatures ranging from 900 to 1200 °C for 10 and 20 h (with an intermediate grinding after 10 h).



**Fig.7.1.** Effect of calcining temperature and time for converting the constituents to the  $\text{ErFeO}_3$  structure. The starting materials were thoroughly ground and mixed for 2 h by hand.

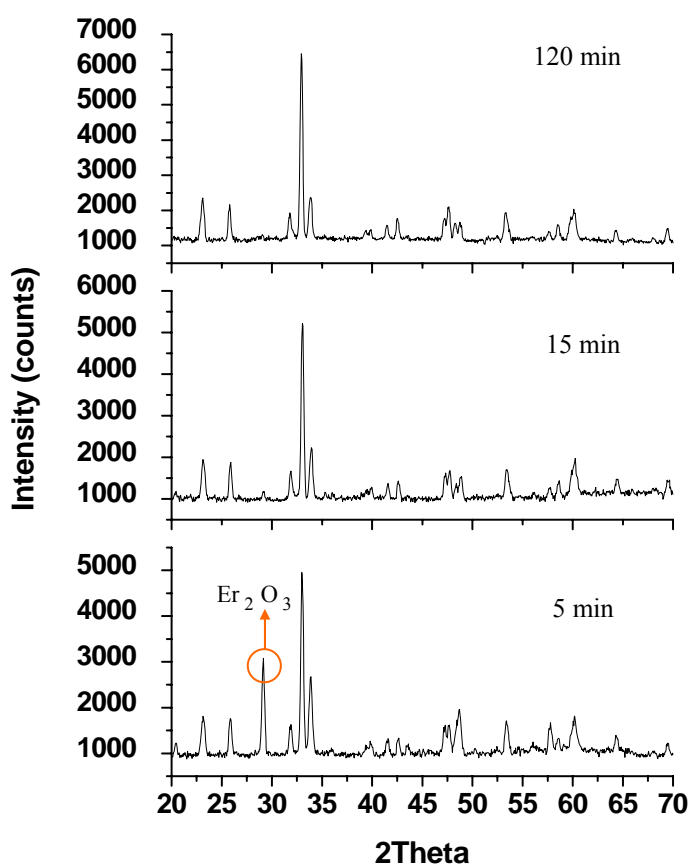
Comparison with the XRD reference data for  $\text{ErFeO}_3$  (Fig. 7.2.a), indicates that the XRD patterns taken from powders synthesized at 1200 °C for 10 or 20 h gave the appropriate orthoferrite structure, while at lower temperatures ( $\leq 1100$  °C) XRD patterns showed peaks from the starting materials, i.e. either  $\text{Er}_2\text{O}_3$  or  $\text{Fe}_2\text{O}_3$ . (XRD patterns taken from  $\text{Er}_2\text{O}_3$  and  $\text{Fe}_2\text{O}_3$ , and erbium orthoferrite synthesized at 1200 °C for 20 h, are shown together for comparison in Fig 7.2.b). Varying the calcination *time* between 10 and 20 h did not significantly affect the structure obtained, as indicated in Figs. 7.1a-d.





**Fig.7.2.** (a) XRD reference data for  $\text{ErFeO}_3$ , and (b) XRD patterns taken from the starting materials,  $\text{Er}_2\text{O}_3$  and  $\text{Fe}_2\text{O}_3$ , and  $\text{ErFeO}_3$  synthesized at  $1200^\circ\text{C}$  for 20h.

It is also worth mentioning that the starting materials needed to be mixed and ground well before calcining; otherwise, the orthoferrite structure was not achieved even after calcining at  $1200^{\circ}\text{C}$ . This is illustrated in Fig. 7.3 where XRD patterns are shown as a function of *mixing times* between 5 and 120 min. (Since the mixing/grinding procedure was performed manually, the times quoted are only approximate). The XRD pattern taken from the powder mixed for 5 min clearly shows a strong peak from  $\text{Er}_2\text{O}_3$ , while the pattern taken from the powder mixed and ground for 120 min (2h) shows only the appropriate orthoferrite structure.



**Fig.7.3.** XRD patterns taken from  $\text{ErFeO}_3$  powders synthesized at  $1200^{\circ}\text{C}$  for 20 h, as a function of different mixing times for the starting materials.

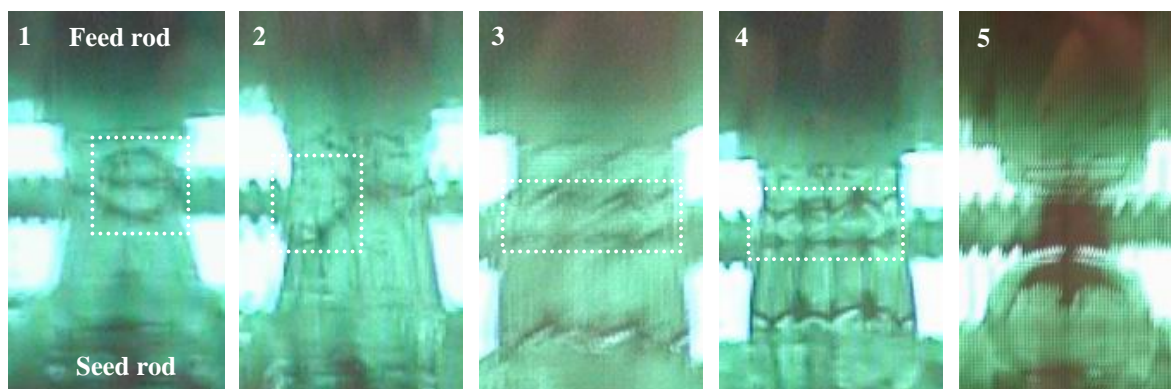
After confirmation by X-ray diffraction that the constituents had converted to the orthoferrite structure, the powders were packed and sealed into a rubber tube, then

compacted into a rod (as described in the experimental procedure section 3.2.3). After removal from the rubber tube, the rods were sintered at either 1500 °C or 1600 °C for 8 h in air. Powder X-ray diffraction taken from feed rods after sintering at both temperatures indicated the orthoferrite structure of  $\text{ErFeO}_3$ .

### 7.2.2. Crystal growth

Because  $\text{ErFeO}_3$  is a relatively high density material ( $\rho=8.09 \text{ g/cm}^3$ ), finding zoning conditions that gave a stable molten zone was an important initial step for the growth procedure.

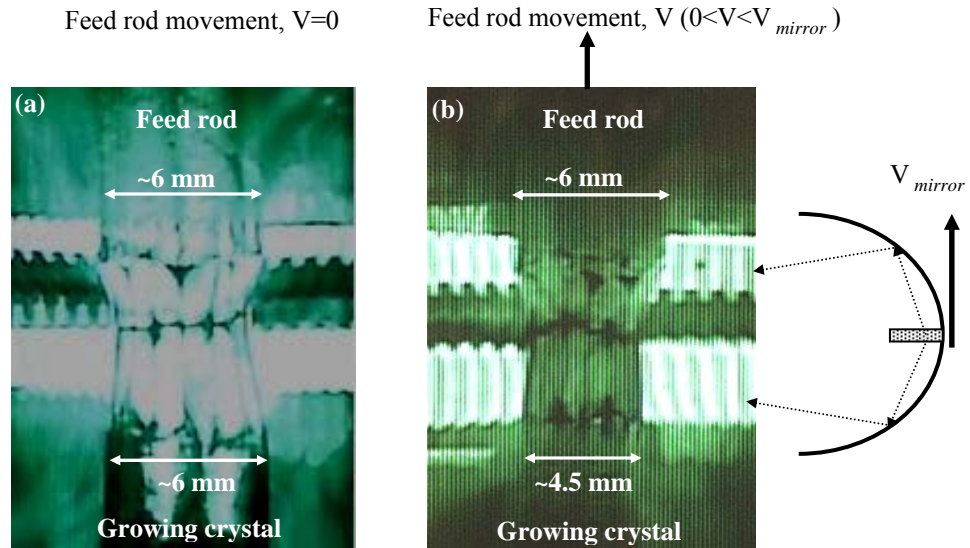
Although the feed rods sintered at 1500 °C were of the correct structure, they were not well compacted ( $\rho=7.34 \text{ g/cm}^3$ ) and crystal growth was not successful due to the formation of a large bubble in the molten zone after every a few millimeters growth, leading to collapse of the zone. Stills taken from the monitor of the image furnace in Fig. 7.4 show the formation of a typical large bubble in the molten zone, which finally led to the zone falling down. However, when using feed rods sintered at 1600 °C ( $\rho=7.66 \text{ g/cm}^3$ , closer to the density of as-grown crystals) growths were more successful.



**Fig.7.4.** The formation of a large bubble which was led to collapse the molten zone during crystal growth of  $\text{ErFeO}_3$  using low compacted feed rods sintered at 1500 °C.

The actual zone shape was also found to have a bearing on zone stability. In this regard, when growth was performed by moving only the mirror (Fig. 7.5a) the shape of molten zone (when seen from the side) was close to rectangular and some trouble was still

experienced with zone instability. However, it was found that a more stable zone configuration resulted by reducing the feeding rate into molten zone by moving the feed rod with respect to the mirror movement (i.e. the growing crystal is withdrawn from the molten zone more quickly than new feed material is fed into the zone). This is shown in Fig. 7.5b, where the shape of the molten zone is relatively trapezoidal since the growing crystal is narrower than the feed rod.



**Fig.7.5.** Molten zone shapes during crystal growth of  $\text{ErFeO}_3$ , (a) when only the mirror moves, and (b) when both the feed rod and mirror move at the same direction

The higher stability of a molten zone with such a trapezoidal shape (Fig. 7.5b) is possibly due to its *higher gravity centre* compared to the conventional molten zone shape (Fig. 7.5a) in which the gravity centre is in the middle of the molten zone.

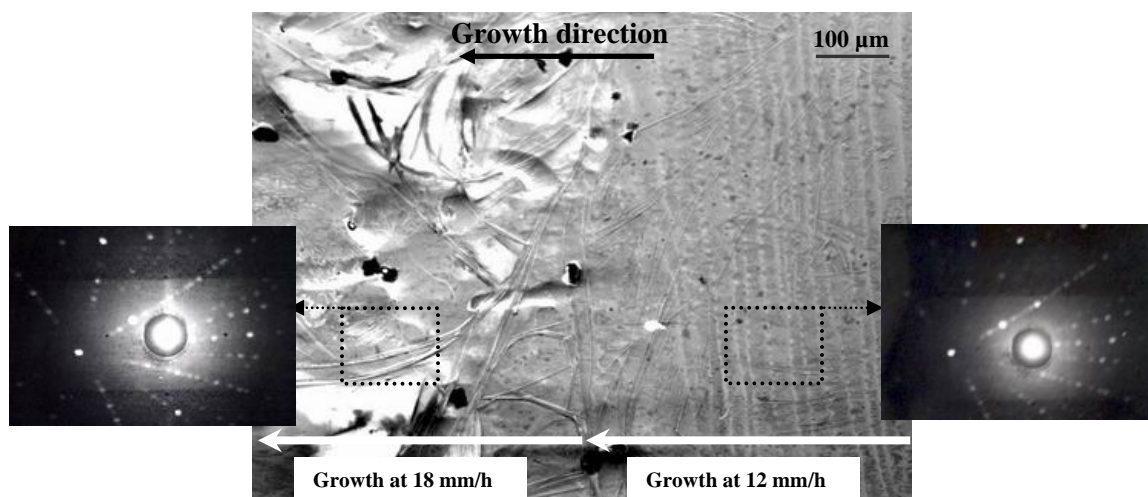
An initial unseeded run was performed to produce a crystal that was used as a seed for all subsequent growths. X-ray Laue analysis indicated that this seed crystal had had an orientation with the  $[391]$  direction (which is  $20^\circ$  from the ' $b$ ' direction) along its length. Fig. 7.6 shows a typical as-grown  $\text{ErFeO}_3$  single crystal along with a Laue photograph taken from its cross section, confirming that it had adopted the  $[391]$  orientation of the seed. During all of the growths, the molten zone was moved upwards during the run with the seed crystal being at the bottom and the feed rod above it and only one zone pass was performed.



**Fig.7.6.** A typical  $\text{ErFeO}_3$  single crystal grown using the four mirror image furnace (left), and a Laue diffraction taken from the cross section of the crystal (right) showing the high quality of the crystal with  $[391]$  as the growth direction.

### 7.2.2.1. Effect of growth rate on the microstructure of $\text{ErFeO}_3$

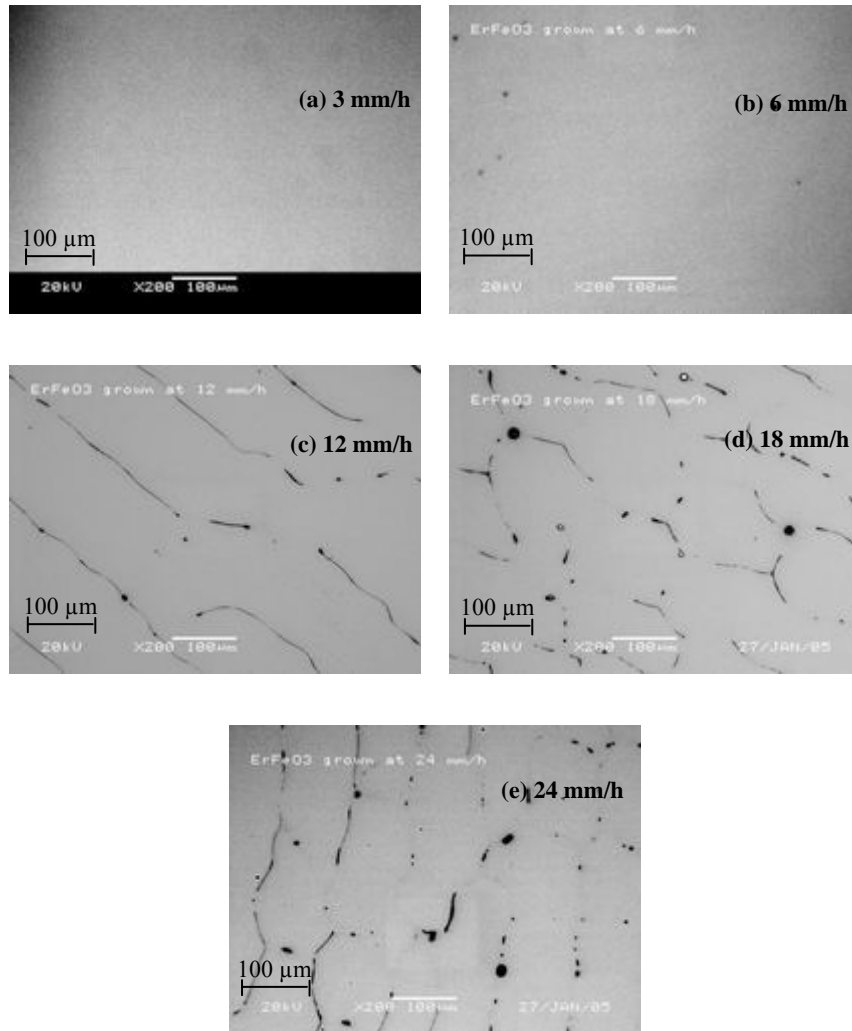
Crystals were grown at zoning rates of 3, 6, 12, 18 and 24 mm/h under 1 bar oxygen pressure, with rotation rates of 15 rpm for the growing crystal (lower shaft) and 0 rpm for the feed rod (upper shaft). X-ray Laue analysis showed all of the crystals to have adopted the orientation of the seed crystal in spite of using different growth rates. One apparent difference between crystals, which could be clearly seen by the naked eye, was that when growth rates of 3 and 6 mm/h were applied, the surfaces of the crystals produced were shiny and smooth whereas the use of growth speeds of 18 and 24 mm/h gave crystals with rough and non uniform surfaces. The crystal grown at 12 mm/h had a generally smooth finish, although not quite as shiny as the 3 and 6 mm/h crystals. The SEM image reproduced in Fig. 7.7 clearly demonstrates how the crystal surface morphology changed as the growth speed was increased from 12 to 18 mm/h during a growth. Despite the marked variations in surface finish of the crystals, X-ray Laue pictures taken at regular intervals along the lengths and cross sections of the crystals indicated that they all exhibited an equally high crystalline quality with no detectable variation of the orientation between pictures and no evidence of spot splitting or distortion (the X-ray beam used had a diameter of 1 mm and allowed orientation variations of less than 1 deg to be detected).



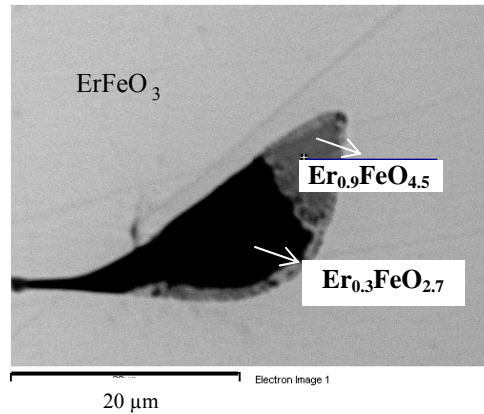
**Fig.7.7.** SEM image taken from the surface of  $\text{ErFeO}_3$  crystal where the growth rate has been changed from 12 mm/h to 18 mm/h. As the growth rate increases the surface becomes rough and non uniform.

Back scattered SEM micrographs were taken from polished cross sections of the crystals and Fig. 7.8 shows typical images taken from the samples grown at 3, 6, 12, 18 and 24 mm/h. The main feature of these micrographs is the formation of second phase inclusions in crystals grown at rates of 12 mm/h and above. At higher magnification, some of the inclusions could be seen to have an internal structure; this is illustrated in Fig. 7.9, which shows an inclusion in the crystal grown at 24 mm/h that clearly comprises both lighter and darker areas. EDX analysis was performed on this inclusion, with analysis data being taken from several points within each of the lighter and darker areas. The results are tabulated in Table 7.1 where the analysis data is presented both in terms of the atomic percentages of the constituents as well as by means of a formula ( $\text{Er}_x\text{Fe}_y\text{O}_z$ ) in which the Fe value,  $y$ , is normalized to unity.

Although the EDX technique used is not particularly suited to light element analysis (so the O contents quoted should be treated with some caution), these results indicate that the darker part of the inclusion had a composition that was essentially Er deficient compared to the  $\text{ErFeO}_3$  matrix, (with  $x$  being 0.3), while the lighter area of the inclusion was principally O rich (with  $z$  in the range 4.3 to 4.6). Further EDX data taken from two other randomly chosen inclusions within this crystal and one inclusion each from the crystals grown at 18 and 12 mm/h yielded broadly similar results.



**Fig.7.8.** SEM back scattered micrographs of cross sections cut from ErFeO<sub>3</sub> crystals grown at (a) 3 mm/h, (b) 6 mm/h, (c) 12 mm/h, (d) 18 mm/h and (e) 24 mm/h. Increasing the growth speed resulted in the formation of second phase inclusions in the crystals. All these experiments were performed under 1 bar oxygen pressure, with rotation rates of 15 rpm for the growing crystal and 0 rpm for the feed rod.



**Fig.7.9.** A typical back scattered SEM micrograph taken from  $\text{ErFeO}_3$  crystal grown at a higher zoning rate (24 mm/h) showing in greater detail one of the inclusions within the  $\text{ErFeO}_3$  matrix. This inclusion has two areas (lighter and darker) of different compositions as measured by EDX.

**Table 7.1.** EDX analysis results from the inclusion shown in Fig. 7.9. The results are given in terms of both atomic % and as a formula normalized to give a Fe value of unity.

	% Er	% Fe	% O	Formula
Darker area	6.5	25.3	68.2	$\text{Er}_{0.3}\text{FeO}_{2.7}$
	6.6	25.2	68.3	$\text{Er}_{0.3}\text{FeO}_{2.7}$
	6.9	25.6	67.5	$\text{Er}_{0.3}\text{FeO}_{2.6}$
	6.8	25.8	67.4	$\text{Er}_{0.3}\text{FeO}_{2.6}$
Lighter area	13.9	15.5	70.6	$\text{Er}_{0.9}\text{FeO}_{4.6}$
	14.1	15.9	70.1	$\text{Er}_{0.9}\text{FeO}_{4.4}$
	14.0	16.2	69.8	$\text{Er}_{0.9}\text{FeO}_{4.3}$
	13.9	15.8	70.4	$\text{Er}_{0.9}\text{FeO}_{4.5}$

To ascertain exactly what these second phases might be, how they formed and why they are only present in crystals grown at higher speeds, comprehensive constitutional information for the Er-Fe-O ternary system (or the  $\text{Er}_2\text{O}_3$ - $\text{Fe}_2\text{O}_3$  pseudo binary system), is clearly desirable. Unfortunately, such information is scarce, although not entirely absent. For example, Schneider et al. [256] performed phase equilibrium studies of several  $R_2\text{O}_3$ - $\text{Fe}_2\text{O}_3$  systems (where  $R=\text{Nd, Sm, Eu, Dy, Ho, Er, Tm}$  and  $\text{Yb}$ ), and while



the subsolidus binary phase diagrams reported did not specify any solidus and liquidus lines, they did predict that phases such as garnets (i.e.  $R_3Fe_5O_{12}$  type) and other rare earth oxide type structures would exist near to the  $RFeO_3$  composition. Van Hook [257] gave a more complete phase diagram for the  $Y_2O_3$ - $Fe_2O_3$  system, which shows a garnet phase as being stable up to 50 mole%  $Y_2O_3$  along with other phases such as orthoferrite, magnetite and hematite. Nielsen and Blank [258] confirmed this work, but reported that other systems (where  $R=Dy$  and  $Yb$ ) behave differently since no stable region of  $Yb_3Fe_5O_{12}$  or  $Dy_3Fe_5O_{12}$  (i.e. similar to  $Y_3Fe_5O_{12}$  in the  $Y_2O_3$ - $Fe_2O_3$  system) formed. Also, rapidly quenched  $Yb_2O_3$ - $Fe_2O_3$  melts prepared in air near the 50 mole%  $Fe_2O_3$  composition contained previously unreported, non-magnetic, oxides such as  $Yb_6Fe_6O_{17}$  or  $Yb_{1.05}Fe_{0.67}^{3+}Fe_{0.28}^{2+}O_{2.86}$  [258]. Recent studies of phase stability of  $R_2O_3$ - $Fe_2O_3$  systems by Wu and Li [259] have also predicted the formation of both  $ErFeO_3$  perovskites and other non-identified complex oxides in the  $Er_2O_3$ - $Fe_2O_3$  system.

While the above information would point to the  $Er_3Fe_5O_{12}$  garnet structure as a likely contender for second phase inclusions in  $ErFeO_3$ , the analysis data presented in Table 7.1 would indicate that neither part of the inclusion shown in Fig. 7.9 exhibited the ideal  $Er_3Fe_5O_{12}$  garnet composition (which would equate to  $Er_{0.6}FeO_{2.4}$  in the notation used in the table). Although the composition of the darker area was closer to the garnet composition than the lighter part, the balance of evidence from the analyses performed on both this and other inclusions would suggest that they were not true garnets, but other more complex oxides.

As far as deciding how and why the inclusions formed, the most obvious explanation is that stoichiometric  $ErFeO_3$  does not form congruently from the melt. This could explain both why a slower growth rate gives inclusion-free crystals (i.e. the reduced speed and associated lower cooling rate give more time for any reactions that may occur during solidification to go to completion) and why the inclusions have a range of compositions. If, indeed,  $ErFeO_3$  does not melt congruently, it is also possible that the 'molten' zone was not completely liquid during the current float zoning operations. This raises the question of whether the zone temperature, as well as the zoning rate, could have a bearing upon the quality of the  $ErFeO_3$  crystals grown. Attempts were made, therefore, to determine whether varying the zone temperature would influence the solidification

process in such a way that it affected the eventual crystalline perfection and the occurrence of inclusions. However, it was found to be impossible to increase the temperature of the zone by any significant degree beyond the minimum required for processing before the zone became unstable and fell out (this was not altogether surprising given that  $\text{ErFeO}_3$  is a relatively dense material compared with many metal oxides). Overall, therefore, all that could be concluded is that phase relationships in the Er-Fe-O system are complicated and that it is found empirically that slower growth rates are needed during float zoning if  $\text{ErFeO}_3$  crystals are to be free from second phase inclusions, while the attainable molten zone temperature is intrinsically limited by the properties of the material.

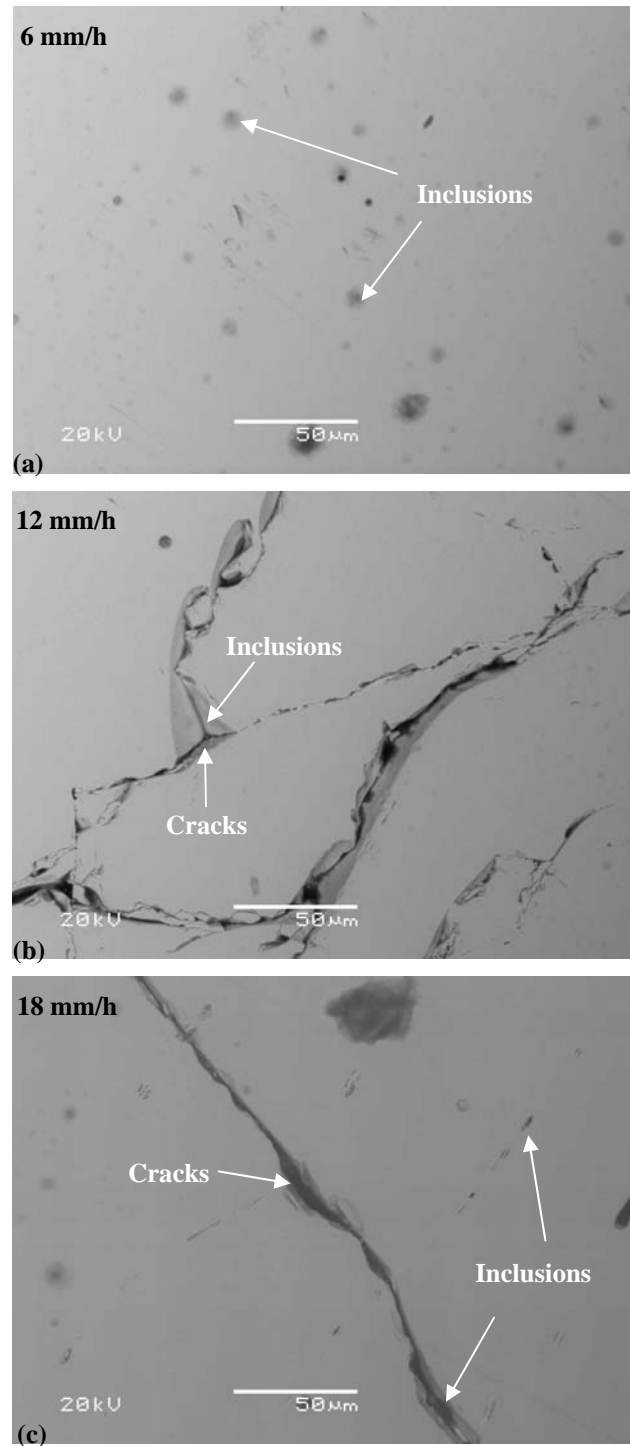
**7.2.2.2. Effect on crystal quality of increasing oxygen pressure to 5 bar**

To investigate the effect of oxygen pressure during crystal growth of  $\text{ErFeO}_3$ , the pressure was increased from 1 to 5 bar. The first effect of increasing the gas pressure to be observed was that the lamp power required to melt the sample increased from ~60.3% at 1 bar to ~62.6% at 5 bar oxygen pressure. This observation is again consistent with the temperature characterization of the system (chapter 4) which indicated that higher lamp powers are required to melt samples at higher gas pressures due to the cooling effects of the gas.

Fig. 7.10 shows the effect of increasing the gas pressure to 5 bar on the microstructure of  $\text{ErFeO}_3$  crystals grown at 6, 12 and 18 mm/h, and these results are compared to the growths performed under 1 bar oxygen pressure (Fig. 7.8) in Table 7.2.

**Table 7.2.** Summary of the defects produced at different growth conditions in  $\text{ErFeO}_3$

Pressure	Growth rate		
	6 mm/h	12 mm/h	18 mm/h
1 bar	No cracks	No cracks	No cracks
	No second phases	<b>Second phases</b>	<b>Second phases</b>
5 bar	No cracks	<b>Cracks</b>	<b>Cracks</b>
	<b>Limited second phases</b>	<b>Second phases</b>	<b>Second phases</b>



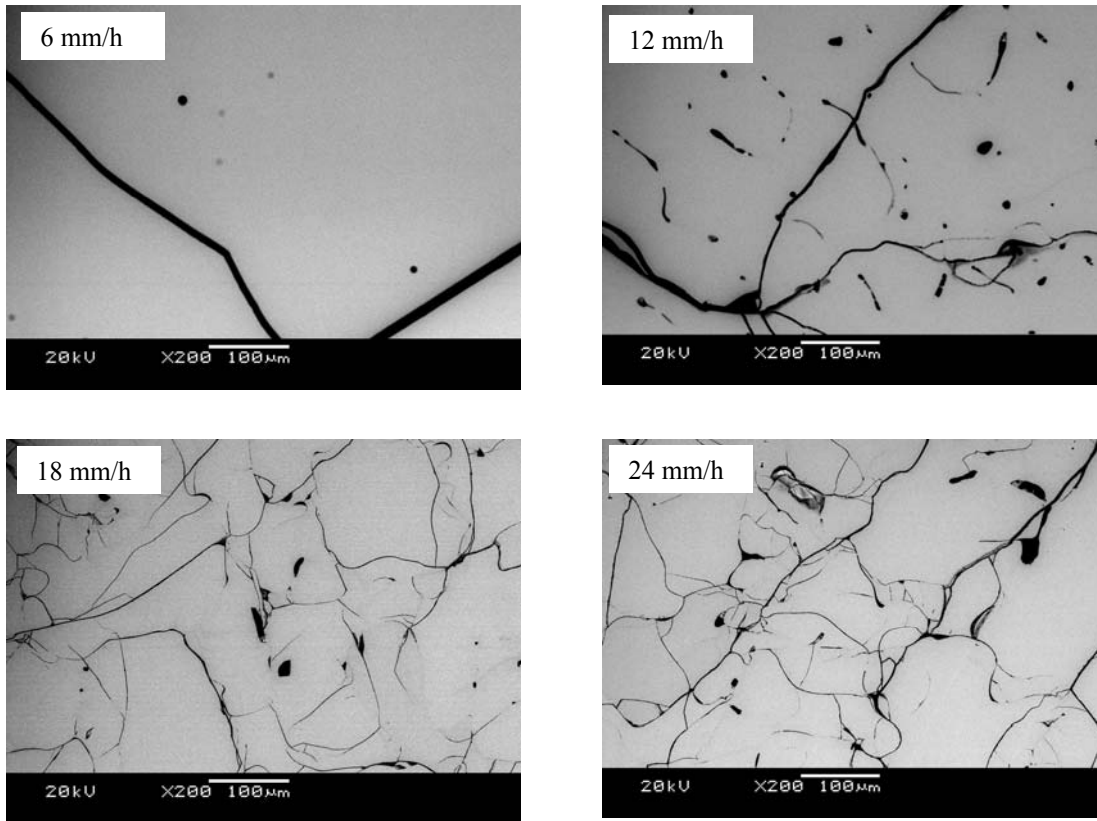
**Fig.7.10.** Back scattered images of cross sections cut from  $\text{ErFeO}_3$  crystals grown under 5 bar oxygen pressure at 6, 12 and 18 mm/h. Increasing the gas pressure added defects such as second phases (in the crystal grown at 6 mm/h) and cracks (in crystals grown at 12 and 18 mm/h). Rotation rates of 15 rpm for the growing crystal and 0 rpm for the feed rod were applied during these experiments.

As shown in table 7.2, increasing the gas pressure to 5 bar led to cracking (in samples grown at 12 and 18 mm/h) and second phases (in samples grown at 6 mm/h) compared to those crystals grown at 1 bar gas pressure. These results are also consistent with the temperature characterization of the furnace (as described in chapter 4) pointing to sharper temperature gradients along the growing crystal at higher gas pressures.

Thus in  $\text{ErFeO}_3$ , a sharper temperature gradient was found to lead to the formation of small inclusions in the sample grown at 5 bar and 6 mm/h, while in samples grown at 12 and 18 mm/h, the higher cooling rate (resulting from the higher growth rate) together with the sharper temperature gradient (due to the higher gas pressure) led to the formation of both cracks and second phases.

### 7.2.2.3. Effect of reducing the rotation rate of growing crystal to zero

In an attempt to examine the effect of reducing the rotation rate of the growing crystal to zero, a series of crystals were grown at rates between 6 and 24 mm/h (under 1 bar oxygen pressure). All of these crystals were found to have cracks, as shown in Fig. 7.11. These cracks are most probably due to radial thermal stresses which are likely to be more intense when the growing crystal is not rotated (although the maximum light focus from the bulbs in the image furnace is in the molten zone, some light from each of the four bulbs also hits the growing crystal). With many materials, such as  $\text{TiO}_2$ , this is not a problem, but  $\text{ErFeO}_3$  would be expected to crack easily in relatively small thermal gradients as it exhibits highly anisotropic thermal expansion behaviour where  $\alpha_a / \alpha_b \approx 2.125$  [252].



**Fig.7.11.** Back scattered images of cross sections cut from  $\text{ErFeO}_3$  crystals grown with rotation rate of zero for both the growing crystal and the feed rod. These experiments were performed under 1 bar oxygen pressure at 6, 12, 18 and 24 mm/h. Reducing the rotation rate to zero led to cracks in all crystals.

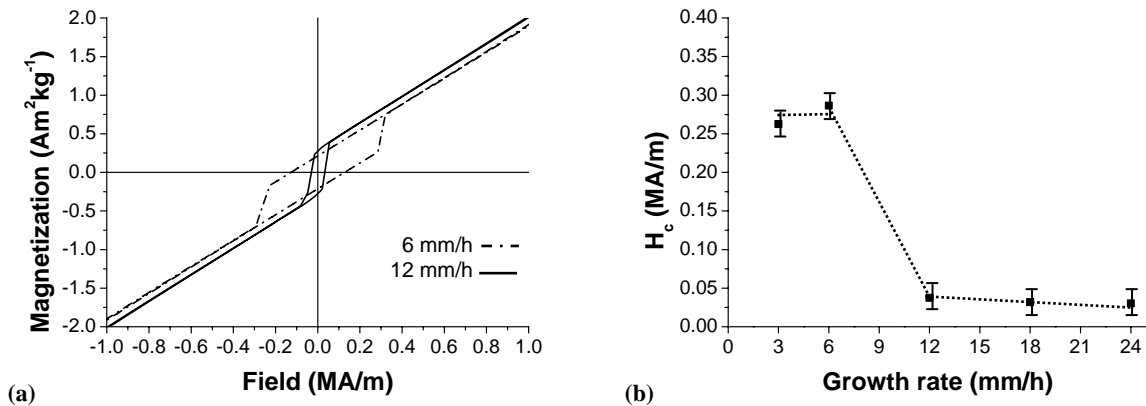
### 7.2.3. Magnetic properties of $\text{ErFeO}_3$ crystals

The above results have indicated that a variety of defects can form in FZ grown  $\text{ErFeO}_3$  crystals depending upon the exact growth conditions. In this section, the effects that these defects have upon magnetic properties are investigated.

As noted in the literature review,  $\text{ErFeO}_3$  is a canted antiferromagnet meaning that the atomic moments align at an angle to the c-axis such that the components of magnetisation perpendicular to the c-axis cancel out, whereas the components of atomic magnetisation parallel to the c-axis give a spontaneous magnetisation in the c-axis.

### 7.2.3.1. Effect of growth rate on magnetic properties

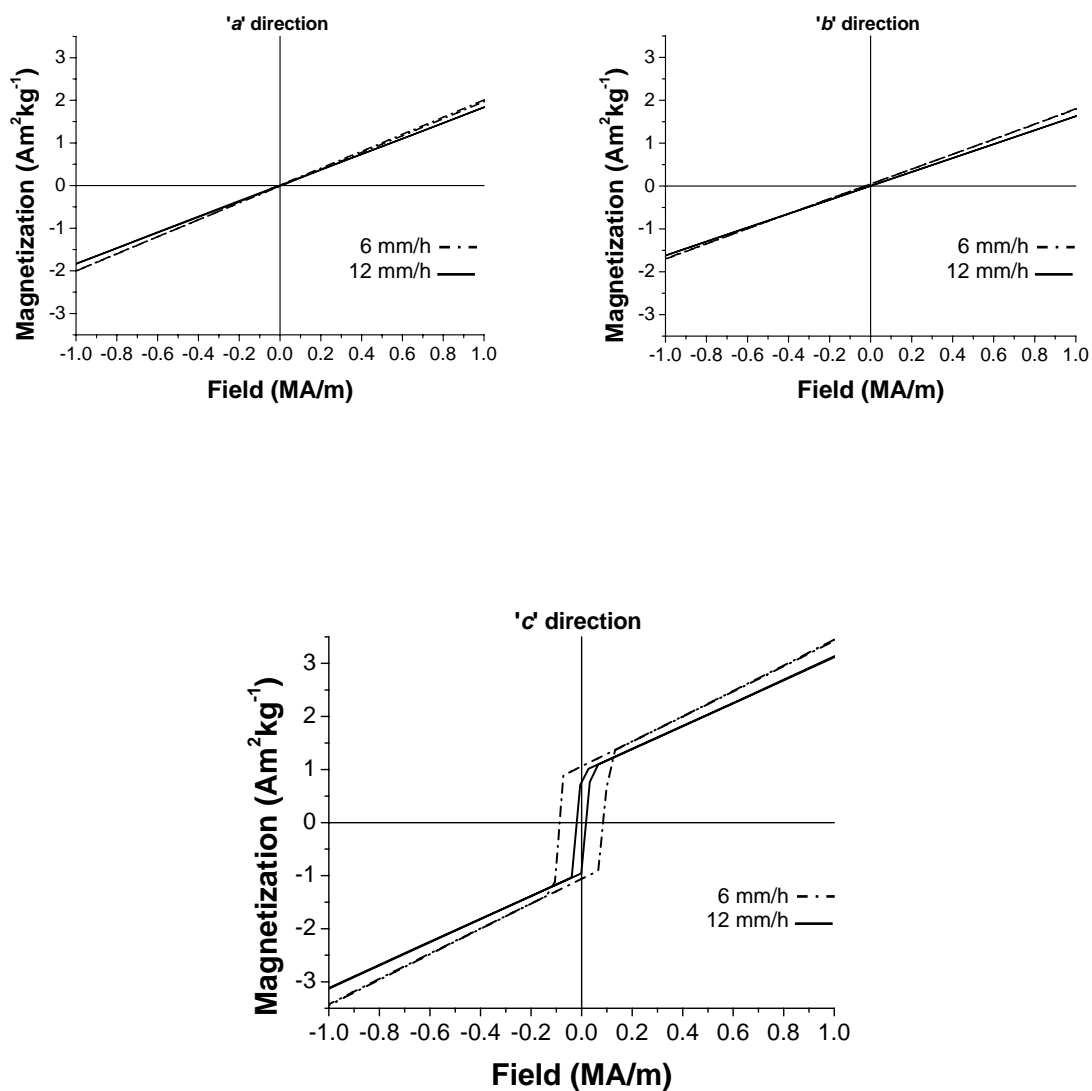
Magnetisation vs. field plots were initially measured at room temperature on disk shaped samples cut directly from the cross section of crystals grown at 6 and 12 mm/h at 1 bar oxygen pressure using rotation (see Fig. 7.8). These samples had the [391] growth direction parallel to the field during measurements. The results show a clear distinction between the slower (inclusion free) and more quickly grown crystals, with the former having significantly wider hysteresis loops than the latter. This effect is illustrated in Fig. 7.12a, which shows the magnetisation curves for the crystals grown at 6 and 12 mm/h, while the magnetisation results from all of the crystals grown at 1 bar using rotation are summarized in Fig. 7.12b, where the coercivity of these samples  $H_{cj}$  (after removal of the field independent component) is plotted against growth rate.



**Fig.7.12.** (a) Magnetization curves and (b) coercivity measurements for disk shaped samples cut directly from the cross sections of  $\text{ErFeO}_3$  crystals grown at different rates. During these measurements, the [391] direction within the disk was parallel to the field. The errors indicated in the coercivity values are due to sample alignment uncertainties during the magnetization measurements.

To quantify more accurately the magnetic properties of the crystals, crystallographically aligned specimens (rectangular specimens, approximately  $3 \times 2 \times 1$  mm along the 'c', 'b' and 'a' directions respectively) were cut using a diamond wheel from the crystals for more detailed study. Thus, Fig. 7.13 shows magnetization vs. field plots at room

temperature along the three principal crystallographic directions for samples from the crystals grown at 6 and 12 mm/h.



**Fig.7.13.** Magnetization vs. field plots along the principal crystallographic directions for  $\text{ErFeO}_3$  single crystals grown at 6 and 12 mm/h. When the field is along the 'c' direction, the slower grown crystal shows a significantly wider hysteresis loop compared to the faster grown crystal.

It is immediately obvious that the major effect of growth speed on the magnetic properties was to change the width of the hysteresis loop when the field is applied along the 'c' direction. (Note that the coercivity values are lower than those indicated in Fig. 7.12 as the applied field is now parallel to the c-axis). Here the faster grown crystals (i.e. those containing second phase inclusions) had very narrow hysteresis loops whereas the sample grown at 6 mm/h (i.e. free from inclusions) had a significantly wider loop. This is consistent with the second phase inclusions acting as nucleation sites for domain reversal. In this respect, the faster grown samples may actually be better suited to use in optical switching devices as the presence of the second phase inclusions lowers the coercivity, speeding domain reversal. However, it is likely that scattering of light would be reduced in inclusion-free crystals.

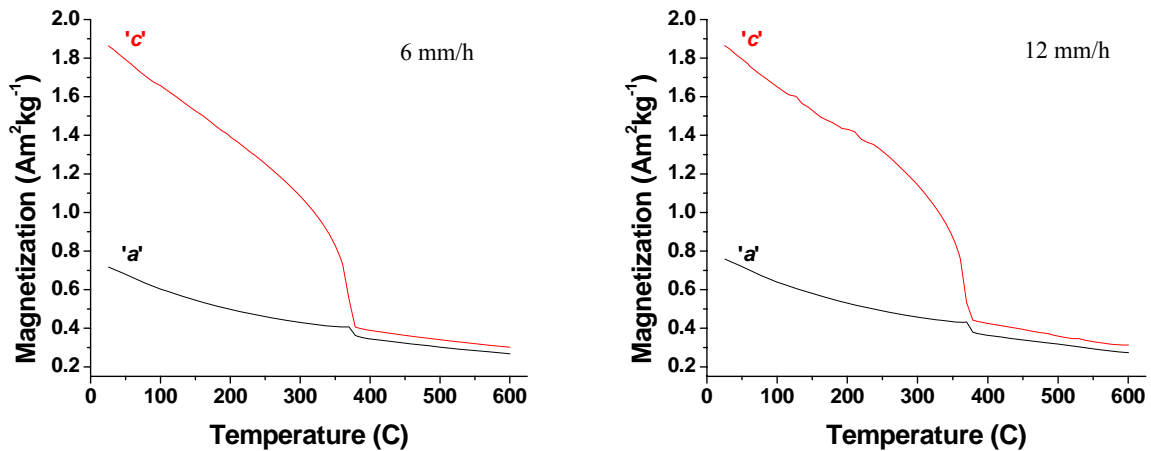
It is worth noting that magnetization measurements on a flux grown  $\text{ErFeO}_3$  single crystal, as reported by Mikami et al. [255], showed a coercivity (with the c-axis parallel to the field) intermediate between the values measured here for 'slowly' and 'quickly' grown crystals, although the remanence was similar. This is reasonable as the remanence is an intrinsic property of the orthoferrite phase, whereas the coercivity is an extrinsic property related to the microstructure. Therefore a different coercivity for the flux grown crystals is indicative of a microstructure that is different due to the very different growth conditions.

The magnetisation plots in Fig. 7.13 suggest that the second phase inclusions found in the crystal grown at 12 mm/h are not ferromagnetic at room temperature since there are no significant differences in the total magnetisation between this sample and the inclusion free crystal grown at 6 mm/h. To determine whether the inclusions could be antiferromagnetic, magnetisation vs. temperature plots were performed for both types of samples (i.e. slowly and quickly grown crystals) between room temperature and 600 °C at 0.4 MA/m (Fig. 7.14). Since only one 'feature' in these plots was apparent at 363 °C, consistent with the reported [254] Neel temperature of  $\text{ErFeO}_3$ , it was concluded that the inclusions are probably either diamagnetic or paramagnetic at room temperature.

While recently published work on the magnetic properties of  $\text{ErFeO}_3$  [284] has indicated that the room temperature axis of magnetisation changed after swift heavy ion irradiation (a similar flipping of the easy axis upon cooling below approximately 90 K is well



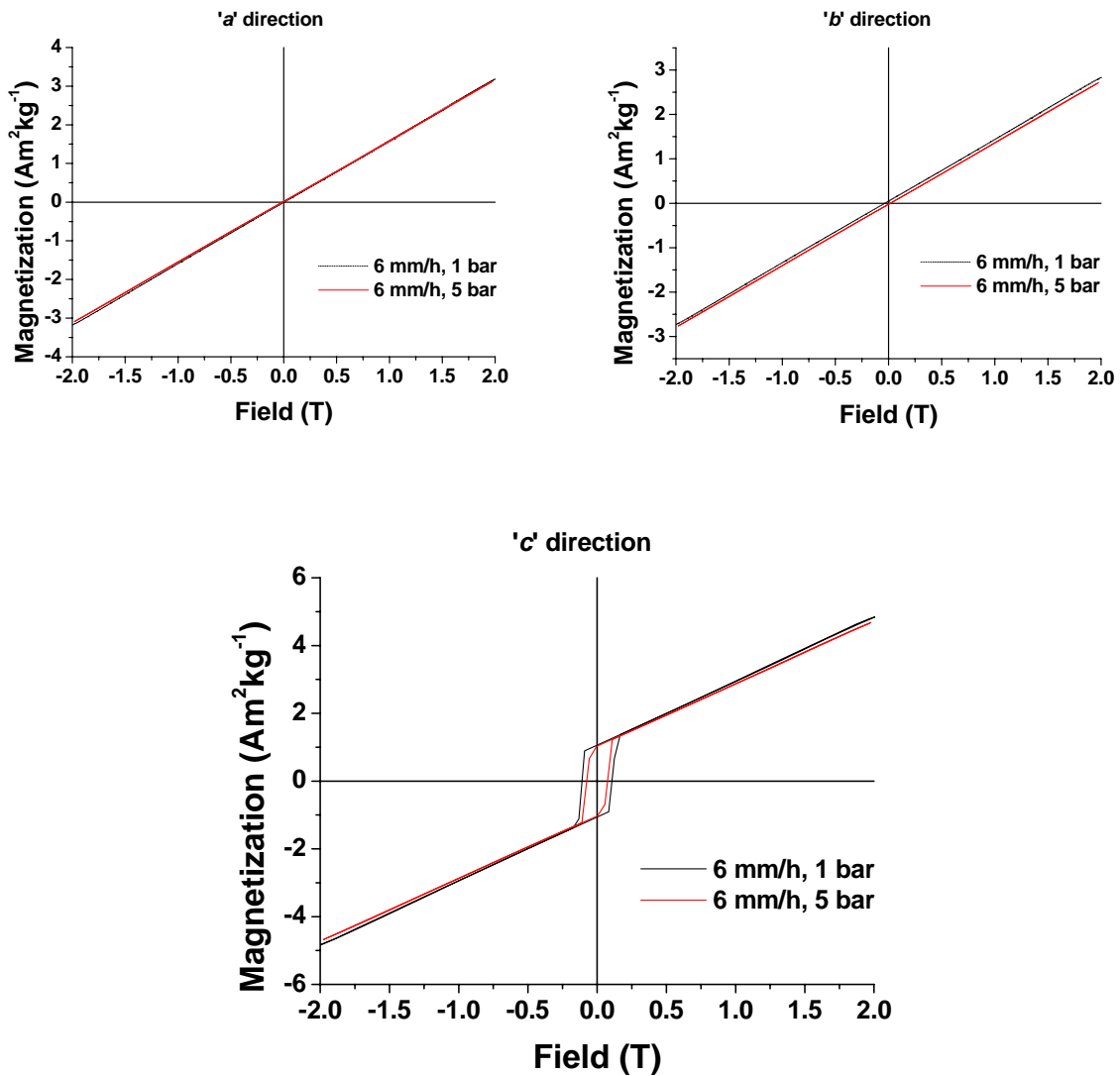
documented [233]), no such effect was found in the present work between ‘good’ crystals and those containing second phase inclusions. It should be noted, however, that the damage caused to the lattice by such irradiation is significantly greater than any effects associated with the presence of inclusions, which do not influence the crystallinity of the orthoferrite matrix.



**Fig.7.14.** Magnetization measurements at 0.4 MA/m between room temperature and 600 °C from crystals grown at 6 mm/h and 12 mm/h

### 7.2.3.2. Effect of increasing the oxygen pressure during FZ growth on magnetic properties

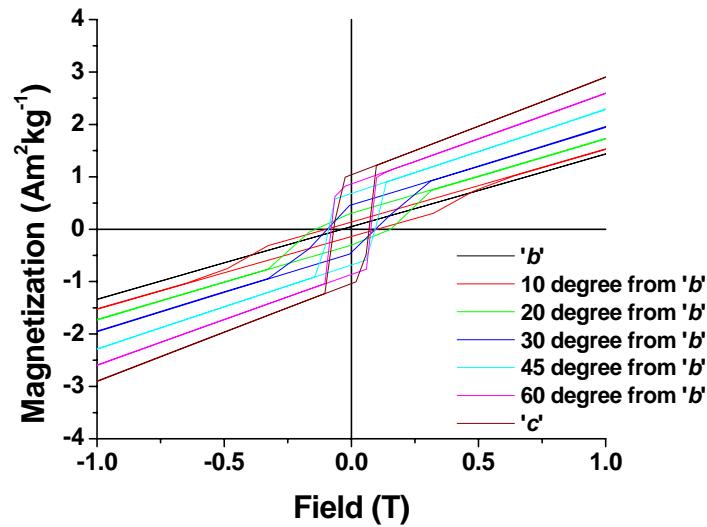
Because the crystals grown at 12 and 18 mm/h under 5 bar oxygen (Fig. 7.10b-c) contained cracks, sample preparation for magnetic measurements was not successful. However, the crystal grown at 6 mm/h (Fig. 7.10a) was used to investigate the effect on magnetic properties of increasing the oxygen pressure to 5 bar (which led to crystals with small inclusions). As shown in Fig. 7.15, the hysteresis loop (with the field along the ‘c’ direction) for the sample grown at 5 bar with inclusions is smaller than for the crystal grown at 1 bar. These results clearly show the high sensitivity of magnetic properties to the microstructure in  $\text{ErFeO}_3$  crystals.



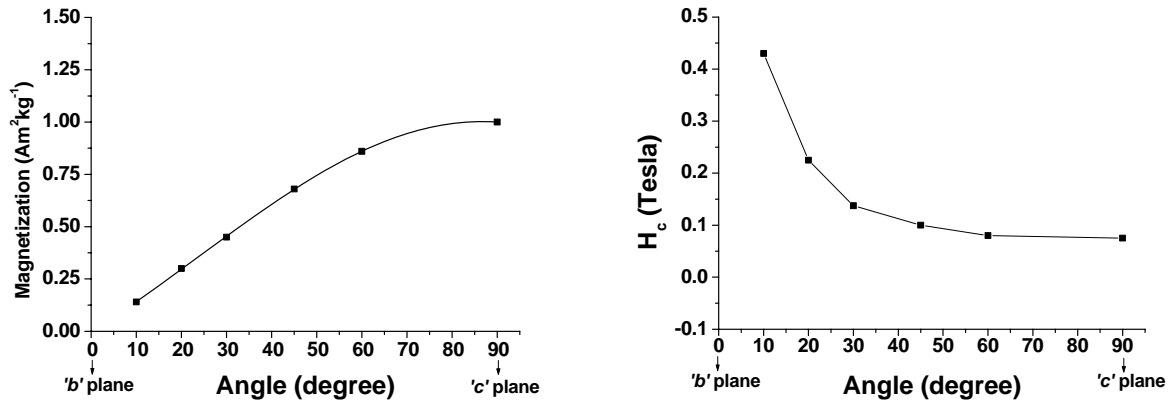
**Fig.7.15.** Magnetization vs. field plots along the principal crystallographic directions for  $\text{ErFeO}_3$  single crystals grown at 6 mm/h under two oxygen pressures of 1 and 5 bar

### 7.2.3.3. Magnetocrystalline anisotropy measurements of $\text{ErFeO}_3$ single crystals

Magnetocrystalline anisotropy measurements of  $\text{ErFeO}_3$  were performed from 'b' direction towards 'c' (Fig. 7.16) using a high quality crystal (i.e. without inclusions or cracks) grown at 6 mm/h under 1 bar oxygen pressure with a rotation rate of 15 rpm for the growing crystal and 0 rpm for the feed rod. Magnetization and coercivity values measured from Fig. 7.16 are shown in Fig. 7.17 which shows how these parameters change at different angles between two principal crystallographic directions.



**Fig.7.16.** Magnetocrystalline anisotropy of high quality  $\text{ErFeO}_3$  crystals grown at 6 mm/h under 1 bar oxygen pressure with rotation rate of 15 rpm for the growing crystal



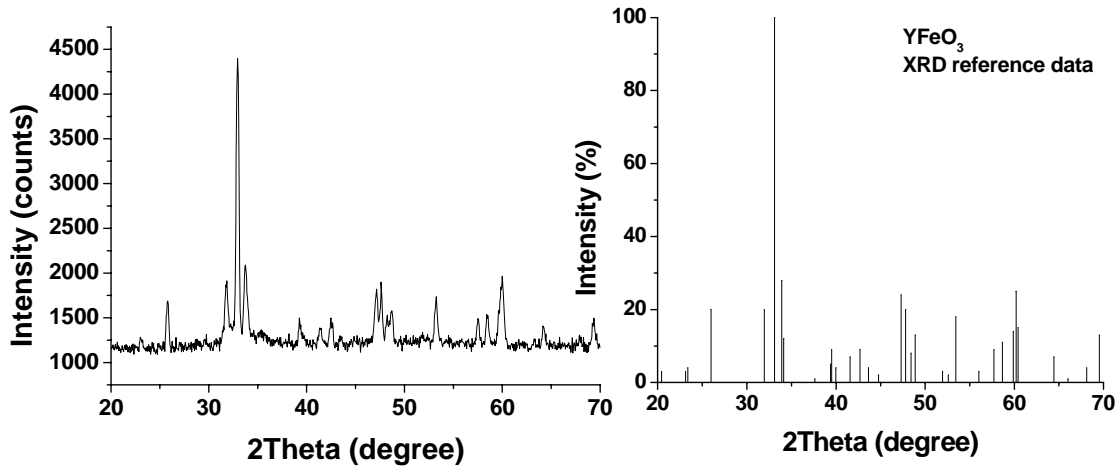
**Fig.7.17.** Magnetization and coercivity values for  $\text{ErFeO}_3$  crystals measured from Fig. 7.16

These measurements, showing the magnitude of the magnetic anisotropy along different crystallographic directions, could be of importance in determining the suitability of orthoferrite crystals for particular applications. Moreover, these experimental measurements performed on high quality single crystals could be used for comparison with data obtained from theoretical predictions of non-linear behaviour of ferromagnetic materials which are still a challenge in many fields of technical science.

### 7.3. Yttrium orthoferrite ( $\text{YFeO}_3$ )

#### 7.3.1. Feed rod preparation

Stoichiometric amounts of the starting materials,  $\text{Y}_2\text{O}_3$  (99.9% purity) +  $\text{Fe}_2\text{O}_3$  ( $\geq 99.0\%$  purity), were thoroughly ground and mixed together (for  $\sim 2$  h) and then synthesized at  $1200^\circ\text{C}$  for 20 h in air with an intermediate grinding after 10 h (i.e. the same calcining procedure as was used for  $\text{ErFeO}_3$ ). Fig. 7.18 shows the XRD pattern taken from the powder after calcining which indicates the appropriate orthoferrite structure of  $\text{YFeO}_3$ .



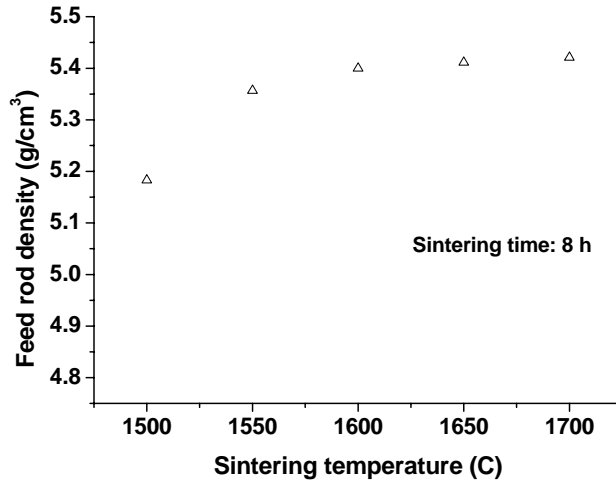
**Fig.7.18.** XRD pattern taken from  $\text{YFeO}_3$  powder after calcining at  $1200^\circ\text{C}$  for 20 h (left), and XRD reference data for  $\text{YFeO}_3$  (right)

The powder was then compacted into rods, typically 6 mm in diameter and 80 mm long, and sintered at temperatures between  $1500$  and  $1700^\circ\text{C}$  for 8 h in air.

#### 7.3.2. Crystal growth

As was found with  $\text{ErFeO}_3$ , growths using  $\text{YFeO}_3$  feed rods sintered at low temperatures were not successful due to the formation of a large bubble in the molten zone, although successful growths were performed using feed rods sintered at  $1700^\circ\text{C}$ . Fig. 7.19 shows

density values for  $\text{YFeO}_3$  feed rods sintered at temperatures between 1500 and 1700 °C (at which the highest density,  $\sim 5.42 \text{ g/cm}^3$ , was obtained).



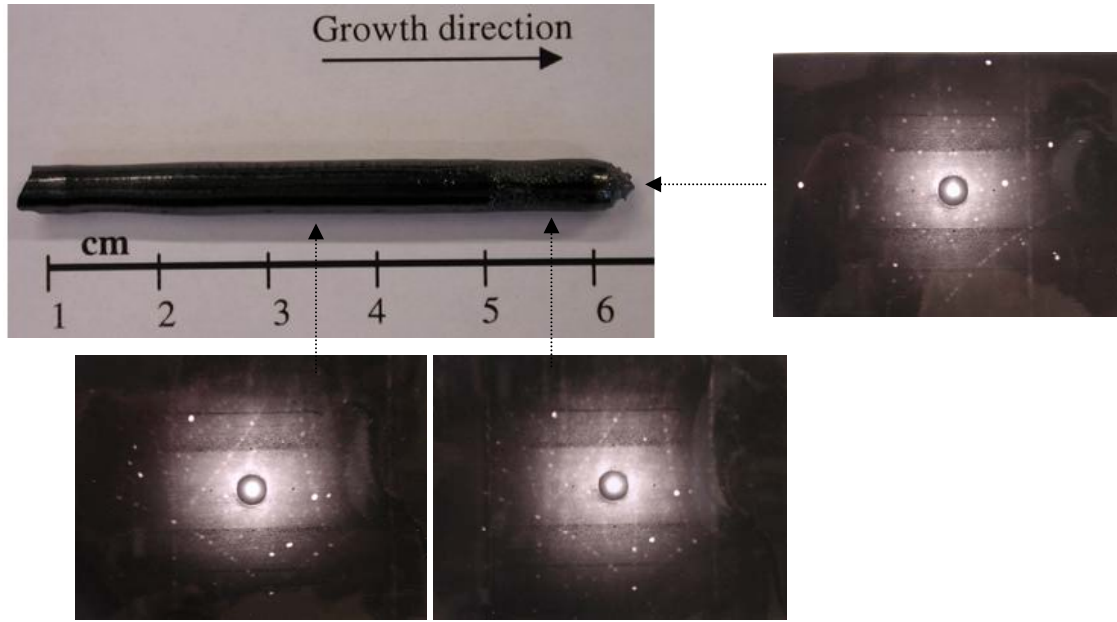
**Fig.7.19.** Density values for  $\text{YFeO}_3$  feed rods sintered at 1500-1700 °C

At  $\rho=5.7 \text{ g/cm}^3$ ,  $\text{YFeO}_3$  has a significantly lower density than  $\text{ErFeO}_3$  and a stable molten zone was achieved more easily during FZ. A typical molten zone shape obtained during crystal growth is shown in Fig. 7.20.



**Fig.7.20.** A typical molten zone obtained during crystal growth of  $\text{YFeO}_3$

Fig. 7.21 shows an as-grown  $\text{YFeO}_3$  crystal with X-ray Laue diffraction patterns taken from the cross section and along the crystal indicating the high quality of this crystal.

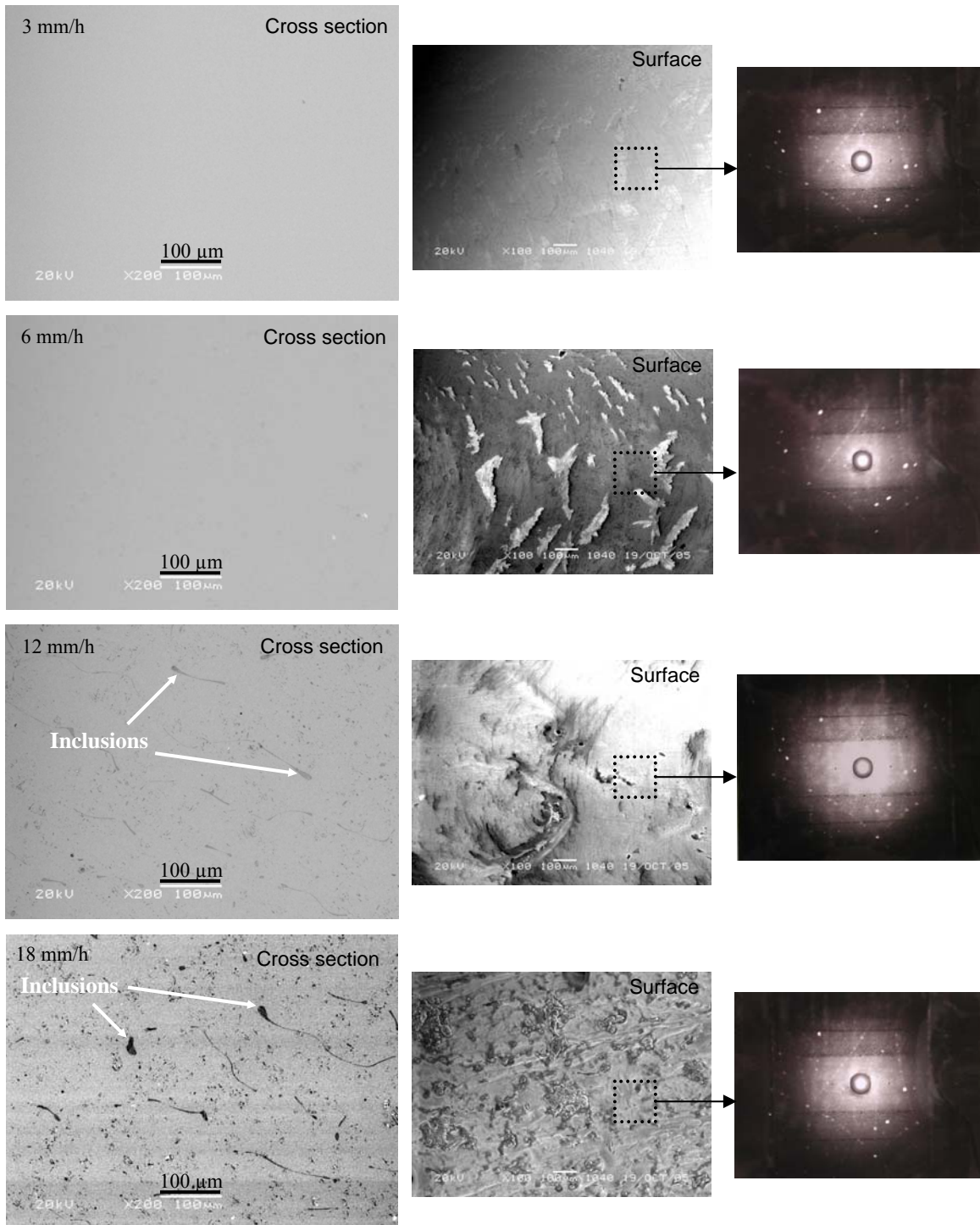


**Fig.7.21.** A typical as grown  $\text{YFeO}_3$  single crystal together with X-ray Laue diffraction patterns, taken from the surface and cross section, indicating the high quality of this crystal

### 7.3.2.1. Effect of growth rate on the microstructure of $\text{YFeO}_3$ crystals

Yttrium orthoferrite crystals were grown at rates between 3 and 18 mm/h to investigate the effect of growth rate on the microstructural and magnetic properties. Fig. 7.22 shows back scattered SEM images taken from polished cross sections of the crystals. The main feature of these micrographs is the formation of second phase inclusions in crystals grown at rates of 12 and 18 mm/h (similar to the growth of  $\text{ErFeO}_3$  crystals as described in the previous pages). EDX analysis was performed on randomly chosen inclusions within the crystals grown at 12 and 18 mm/h, and the results indicated that these inclusions are iron rich with the average atomic percentage ratio of  $\text{Fe}/\text{Y} \approx 1.25\text{-}2.02$  (the same explanation as given in section 7.2.2.1 for the formation of inclusions in  $\text{ErFeO}_3$  can be repeated here to explain why and how these inclusions are formed).

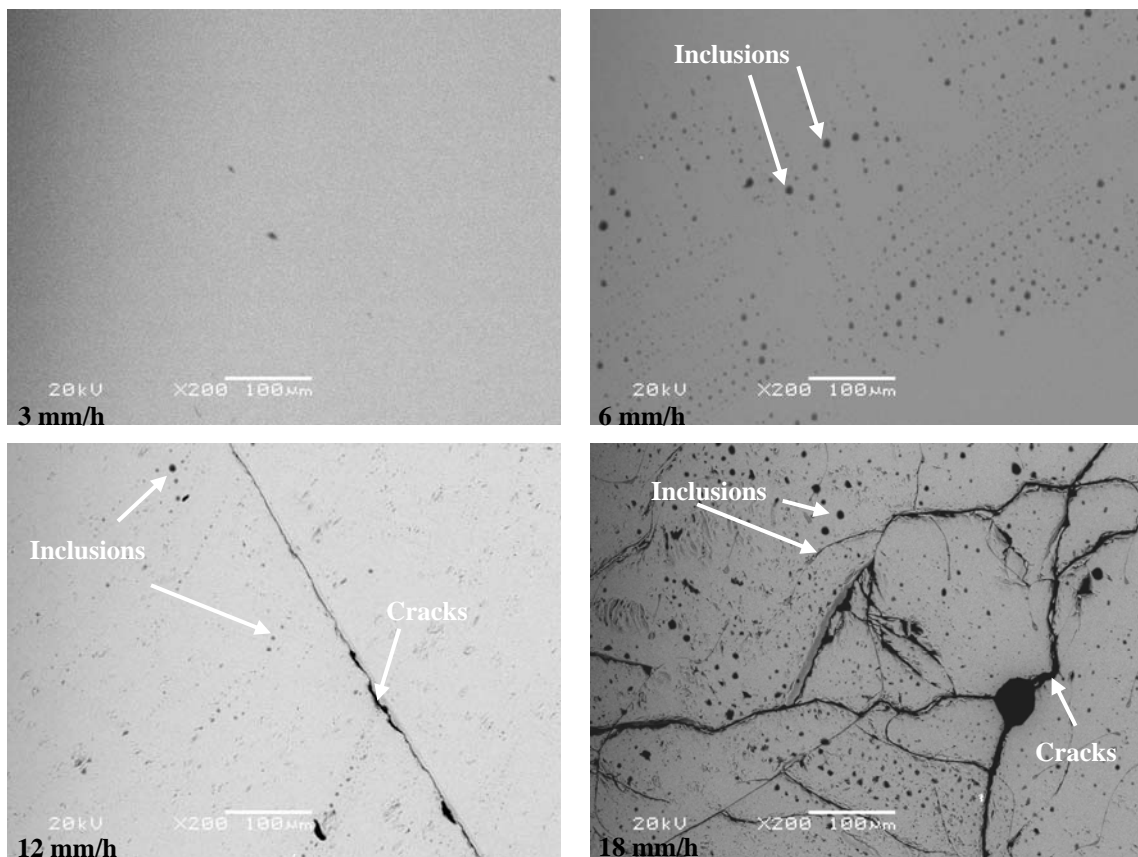
X-ray Laue photographs taken along the crystals (Fig. 7.22) indicated that all crystals had similar quality; however, SEM images taken from the surface of these crystals indicated that when growth rates of 3 and 6 mm/h were applied, the surfaces of the crystals were shiny and smooth, whereas the use of growth rates of 12 and 18 mm/h gave crystals with a rough and non-uniform surface.



**Fig.7.22.** Back scattered SEM images taken from the polished cross sections of  $\text{YFeO}_3$  crystals (left) grown at 3, 6, 12 and 18 mm/h. SEM pictures taken from the surface of each crystal (middle images) along with X-ray Laue diffraction patterns (right) are also shown. All these experiments were performed under 1 bar oxygen pressure with rotation rate of 15 rpm for the growing crystal and 0 rpm for the feed rod.

### 7.3.2.2. Effect of increasing the oxygen pressure to 5 bar during FZ

The effect of increasing the gas pressure to 5 bar was to increase the lamp power required to melt the sample from ~60.0% (the power required at 1 bar) to ~63.3%. The observation of this effect is again entirely consistent with the temperature characterization of the system (chapter 4) indicating that higher lamp powers are required to melt samples at higher gas pressures. Back scattered SEM micrographs (Fig. 7.23) show the effect of increasing the gas pressure to 5 bar on the microstructure of  $\text{YFeO}_3$  crystals grown at 3, 6, 12 and 18 mm/h.



**Fig.7.23.** Backscattered SEM images of cross sections cut from  $\text{YFeO}_3$  crystals grown under 5 bar oxygen pressure at 3, 6, 12 and 18 mm/h. Increasing the gas pressure caused the formation of defects such as second phases (crystal grown at 6 mm/h) and cracks (crystals grown at 12 and 18 mm/h). Rotation rates of 15 rpm for the growing crystal and 0 rpm for the feed rod were applied during these experiments.



As can be seen, increasing the gas pressure to 5 bar induced defects such as cracks to form (in samples grown at 12 and 18 mm/h) and second phases (in samples grown at 6 mm/h) when compared to 1 bar gas pressure (Fig. 7.22). Again, these results are consistent with the temperature characterization of the image furnace which showed that sharper temperature gradients exist along a growing crystal at higher gas pressures. It is evident, therefore, that, like  $\text{ErFeO}_3$ , the quality of  $\text{YFeO}_3$  crystals is extremely sensitive to the cooling rate of the growing crystal. Cooling too quickly, due to either increasing the gas pressure and/or the growth rate, can lead to crystals containing inclusions and possibly cracks.

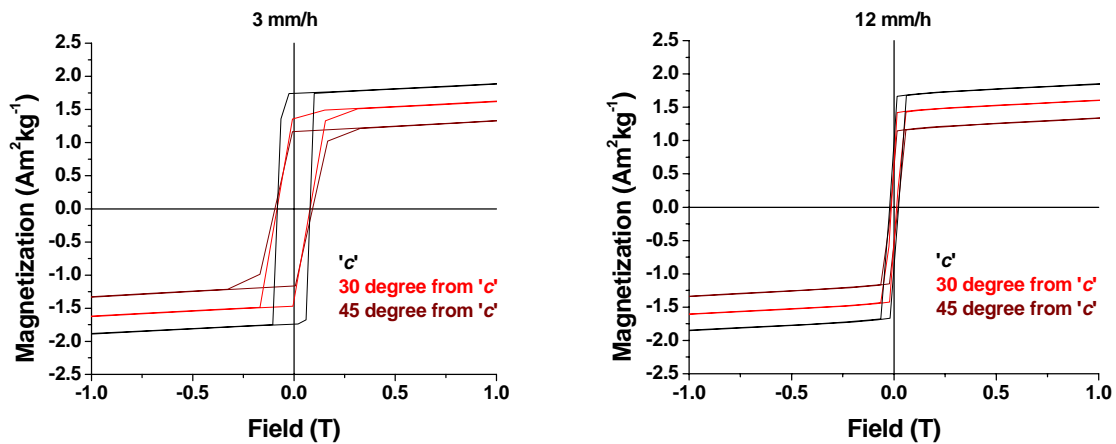
### 7.3.2.3. Effect of reducing the rotation rate of the growing crystal to zero

Reducing the rotation rate of the growing crystal to zero did not affect on the quality of crystals grown at 3-18 mm/h (under 1 bar oxygen pressure), and defects such cracks (as were observed in  $\text{ErFeO}_3$ ) were not observed in  $\text{YFeO}_3$  crystals, most probably due to a smaller anisotropic thermal expansion behaviour in yttrium orthoferrite. Here  $\alpha_a = 8.130 \times 10^{-6} \text{ }^\circ\text{K}^{-1}$ ,  $\alpha_b = 12.142 \times 10^{-6} \text{ }^\circ\text{K}^{-1}$  (giving an  $\alpha_b/\alpha_a$  value of 1.493) and  $\alpha_c = 12.747 \times 10^{-6} \text{ }^\circ\text{K}^{-1}$  [253], compared to  $\text{ErFeO}_3$  where  $\alpha_a/\alpha_b \approx 2.125$  [252].

### 7.3.3. Magnetic properties of $\text{YFeO}_3$ crystals

#### 7.3.3.1. Effect of growth rate on magnetic properties

Magnetization measurements were performed with the field applied along the 'c' direction, and also at 30° and 45° degrees from 'c' towards 'b' for crystals grown at 3 and 12 mm/h as shown in Fig. 7.24. These results clearly show that the effect of inclusions in the crystal grown at the faster rate was to lower the coercivity field (as was observed and explained for the  $\text{ErFeO}_3$  crystals).



**Fig.7.24.** Magnetization vs. field plots measured from  $\text{YFeO}_3$  crystals grown at 3 and 12 mm/h. The slower grown crystal shows a wider hysteresis loop compared to the faster grown crystal.

#### 7.3.3.2. Magnetocrystalline anisotropy measurements of $\text{YFeO}_3$ single crystals

Magnetocrystalline anisotropy measurements of  $\text{YFeO}_3$  were performed with the field moving from parallel to the 'b' direction towards 'c' (Fig. 7.25) using a high quality crystal (i.e. without inclusions and cracks) grown at 3 mm/h under 1 bar oxygen pressure with rotation rate of 15 rpm for the growing crystal and 0 rpm for the feed rod. Magnetization and coercivity values are shown in Fig. 7.26. Again, such data could be used to tailor the properties of a single crystal sample to a specific application.

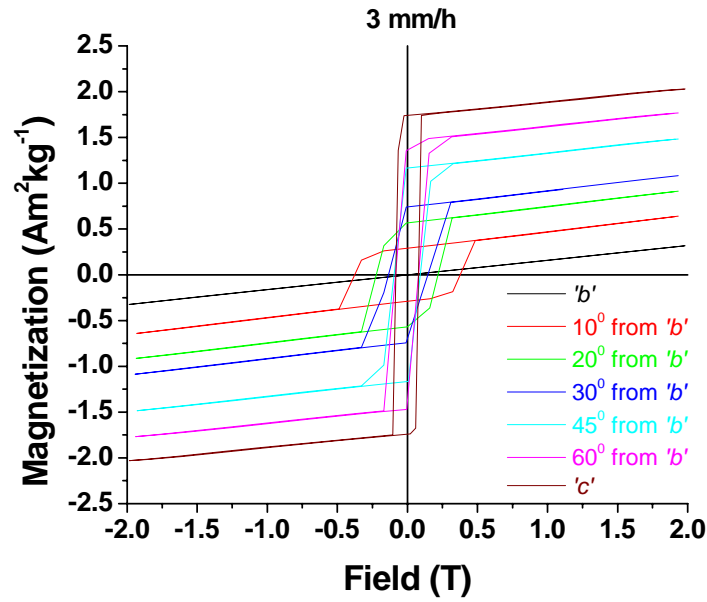


Fig.7.25. Magnetocrystalline anisotropy of high quality YFeO<sub>3</sub> crystals grown at 3 mm/h under 1 bar oxygen pressure with rotation rate of 15 rpm for the growing crystal

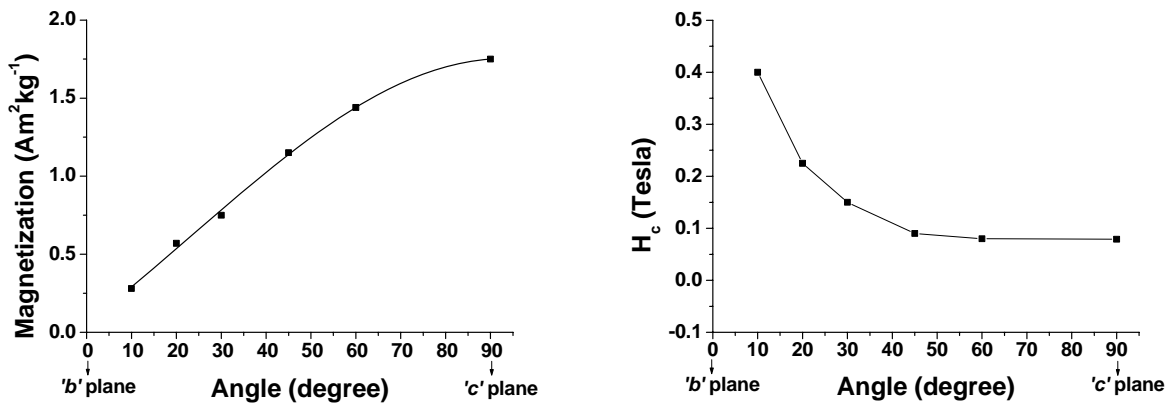


Fig.7.26. Magnetization and coercivity values for YFeO<sub>3</sub> crystals measured from Fig. 7.25

#### 7.4. Summary

- A trapezoidally shaped molten zone (with a wider feed rod above and a narrower crystal below) was found to give a significantly more stable molten zone in  $\text{ErFeO}_3$ .
- The growth rate used during floating zone growth of  $\text{ErFeO}_3$  and  $\text{YFeO}_3$  crystals was found to have a significant effect upon both the microstructure and magnetic properties of the crystals.
- $\text{ErFeO}_3$  and  $\text{YFeO}_3$  crystals grown at rates of 3 and 6 mm/h were of good crystalline quality and inclusion free.
- Crystals grown at 12 and 18 mm/h were of good crystalline quality, but contained second phase inclusions.
- Increasing the gas pressure from 1 to 5 bar led to cracking (in  $\text{ErFeO}_3$  and  $\text{YFeO}_3$  crystals grown at 12 and 18 mm/h) and formation of second phases (in samples grown at 6 mm/h).
- Reducing the rotation rate of the growing crystal to zero led to cracking in  $\text{ErFeO}_3$ , but it did not affect on the quality of  $\text{YFeO}_3$  crystals.
- Thermomagnetic analysis performed on  $\text{ErFeO}_3$  crystals indicated that the second phase inclusions were probably either diamagnetic or paramagnetic in behavior, although EDX analysis did not allow definitive identification of the phases present.
- The effect of the inclusions in  $\text{ErFeO}_3$  and  $\text{YFeO}_3$  crystals was to lower the coercivity (i.e. narrow the hysteresis loop found in the magnetization vs. field plots); this was attributed to their nucleating reverse magnetic domains and so aiding the demagnetization process.

## CHAPTER 8: CONCLUSIONS AND FUTURE WORK

### 8. Conclusions and future work

The findings of the research presented in this thesis have been listed at the end of the relevant chapters, but are repeated here for completeness together with suggestions for future work.

#### 8.1. Conclusions

##### 8.1.1. Image furnace characterization

The variations of temperature induced along the growth axis of a sample during optical float-zoning as a result of altering the lamp power, gas pressure, type of atmosphere and zoning rate have been studied for a four mirror image furnace. The temperature characterization results were discussed with a view to indicating how varying the growth parameters can affect crystal quality and growth stability in different ways during optical float-zoning. Temperature profiles measured under different growth parameters revealed that:

- The combination of three parameters, namely ‘material characteristics’ (such as sample diameter, melting point, light absorption, etc.), ‘gas pressures’ and ‘type of gas atmosphere’, determine the required lamp power to melt the sample and to produce a specific temperature distribution along the growing crystal.
- Increasing the lamp power increases the maximum temperature (where the molten zone is located) in such a way that sharper temperature gradients are created along the growing crystal.
- Different growth atmospheres (oxygen, argon, helium, etc.) change both the maximum temperature attained and the temperature distribution along the growth axis (i.e. a higher lamp power is required to produce a molten zone under higher thermal conductivity atmospheres such as helium).
- Increasing the gas pressure decreases the maximum temperature attained for a given lamp power and creates a sharper temperature gradient along the sample;

therefore, a higher lamp power is required to produce a molten zone at higher gas pressures.

- The sharper temperature gradients along the growing crystal associated with the use of higher gas pressures may cause cracking due to increased thermal stresses in some materials.
- Depending on the phase diagram of the material, the sharper temperature gradients at higher gas pressures may affect possible formation of second phases or inclusions in the growing crystal as a result of faster cooling rates.
- Vapourization of volatile materials from both the feed rod and the growing crystal could be limited under higher gas pressures. This is not just because higher pressures inhibit volatilization, but also because the sharper temperature gradients mean the as-grown crystal and feed rod spend less time at elevated temperatures.
- With poorly compacted feed rods, the sharper temperature gradients associated with the use of higher gas pressures may increase bubble formation in the molten zone and growing crystal, since the feed rod will be less well sintered before melting. Such bubble formation could affect the molten zone stability.
- Because increasing the growth speed increases the cooling rate in the growing crystal, this may lead to cracking in some materials due to larger thermal stresses.
- Depending on the material and its phase stability, a higher cooling rate may lead to either the formation or elimination of second phases or inclusions in as-grown crystals.
- A higher cooling rate may change the composition of the molten zone and affect the stability of the molten zone.

### **8.1.2. Rutile ( $\text{TiO}_2$ )**

Rutile single crystal rods of approximately 5 mm diameter and up to 60 mm in length have been grown by the optical floating zone method using a variety of growth rates, rotation rates, oxygen pressures and molten zone temperatures. The crystals were characterized using both polarized optical microscopy and X-ray Laue techniques. The results indicate that:

- The experimental parameters that have most influence on the quality of rutile crystals grown by the image furnace technique are the rotation rate during growth and the molten zone temperature.
- Good quality crystals can be grown at both low and high zoning rates if no rotation is employed. With rotation, crystals grown at low rates tend to have many sub-grains, while crystals grown at high rates contain bubble inclusions.
- Increasing the molten zone temperature leads to the preparation of blue (oxygen deficient) crystals, while lower zone temperatures yield pale yellow crystals characteristic of stoichiometric rutile.
- Changes in the oxygen pressure during FZ within the range 1-5 bar, has no effect upon eventual crystal quality. Thus, the previously reported dependence of crystal colour on oxygen pressure during FZ is erroneous, as is the suggestion that the zoning rate is the major factor governing crystal quality.

### 8.1.3. Co-doped TiO<sub>2</sub>

Co-doped rutile samples in the form of both powders and bulk single crystals have been studied with particular emphasis on the dependence of their magnetic, compositional and structural properties upon the type of atmosphere used during their preparation. Both powders and single crystals were characterized using X-ray diffractometry and vibrating sample magnetometry, while the crystals were also studied using the X-ray Laue technique, scanning electron microscopy and energy dispersive X-ray analysis. The results indicate that:

- The magnetic properties of Co-doped rutile bulk samples (both single crystals prepared using the FZ technique and polycrystalline powders prepared using a solid state reaction) depend upon the material preparation conditions.
- An oxygen deficient environment during the preparation of Co-doped TiO<sub>2</sub> powders using a solid state reaction was crucial for the observation of room temperature ferromagnetism, while preparation in oxygen rich conditions led to the formation of paramagnetic material that included second phase CoTiO<sub>3</sub>.

- The preparation of Co:TiO<sub>2</sub> single crystals from the melt using the FZ technique indicated that Co does not dissolve into the rutile matrix, and that the type of atmosphere during FZ affects on the type of cobalt-based second phases.
- Crystals grown in oxygen had CoTiO<sub>3</sub> precipitants and showed weak paramagnetic behaviour, while crystals grown in argon had Co-rich particles as the second phase and showed ferromagnetism at room temperature.

#### 8.1.4. Rare earth orthoferrites (RFeO<sub>3</sub>, R=Er and Y)

Erbium and Yttrium orthoferrite (ErFeO<sub>3</sub> and YFeO<sub>3</sub>) single crystals have been successfully grown by the floating zone technique using a four-mirror image furnace. Particular attention was given to the influence of the growth rate on the microstructural and magnetic properties of the crystals. The as-grown crystals were characterized using the X-ray Laue technique, scanning electron microscopy, energy dispersive X-ray analysis and vibrating sample magnetometry. The results indicate that:

- A trapezoidally shaped molten zone (with a wider feed rod above and a narrower crystal below) was found to give a significantly more stable molten zone in ErFeO<sub>3</sub>.
- The growth rate used during floating zone growth of ErFeO<sub>3</sub> and YFeO<sub>3</sub> crystals was found to have a significant effect upon both the microstructure and magnetic properties of the crystals.
- ErFeO<sub>3</sub> and YFeO<sub>3</sub> crystals grown at rates of 3 and 6 mm/h were of good crystalline quality and inclusion free.
- Crystals grown at 12 and 18 mm/h were of good crystalline quality, but contained second phase inclusions.
- Increasing the gas pressure from 1 to 5 bar led to cracking (in ErFeO<sub>3</sub> and YFeO<sub>3</sub> crystals grown at 12 and 18 mm/h) and formation of second phases (in samples grown at 6 mm/h).
- Reducing the rotation rate of the growing crystal to zero led to cracking in ErFeO<sub>3</sub>, but it did not affect on the quality of YFeO<sub>3</sub> crystals.



- Thermomagnetic analysis performed on  $\text{ErFeO}_3$  crystals indicated that the second phase inclusions were probably either diamagnetic or paramagnetic in behavior, although EDX analysis did not allow definitive identification of the phases present.
- The effect of the inclusions in  $\text{ErFeO}_3$  and  $\text{YFeO}_3$  crystals was to lower the coercivity (i.e. narrow the hysteresis loop found in the magnetization vs. field plots); this was attributed to their nucleating reverse magnetic domains and so aiding the demagnetization process.

## 8.2. Suggestions for future work

Based upon the research work presented here, the following suggestions are given for future work:

### 8.2.1. FZ system characterization

- Investigate the effect of using a trapezoidal molten zone shape during growth (as used for  $\text{ErFeO}_3$ ) for FZ growth of higher density metallic samples.
- Since silica did not melt even after using the total lamp power (which would be presumed to give a temperature of up to  $2000^\circ\text{C}$  in some materials), growth of a highly volatile material may be possible if it is sealed in a closed tubular transparent silica container, provided that the material does not react with the silica tube and has a lower melting point than silica.
- When performing crystal growths using the optical FZ method, temperature characterization of the system, as performed in this study, could be valuable in order to optimize crystal quality.

### 8.2.2. Rutile

- Optical property measurements (such as transparency measurements, etc.) should be performed to investigate the possible effects of defects (bubble inclusions, low angle grain boundaries and oxygen deficiency) on the optical properties of rutile crystals.

- Dielectric measurements could also be performed using both oxygen deficient (blue crystals) and stoichiometric (pale yellow crystals) crystals to investigate the effect of oxygen content on these measurements.
- More experiments could be performed to determine precisely how the rotation rate is linked to the formation of defects such as bubbles and low angle grain boundaries.

### 8.2.3. Co-doped $\text{TiO}_2$

- Since both the spin and charge properties of electrons are important in  $\text{Co:TiO}_2$ , room temperature conductivity measurements of 4% $\text{Co:TiO}_2$  crystals are suggested to find the exact effect that oxygen content (or growth atmosphere) has on the electronic properties.
- The effect of growth parameters such as growth rate and atmosphere pressure needs to be fully assessed.
- More characterization of  $\text{Co:TiO}_2$  single crystals is suggested using TEM to determine whether the Co-rich clusters (found in crystals grown in argon) are single crystal and if so, along which crystalline direction they are aligned.
- Possible room temperature ferromagnetism could be investigated by doping  $\text{TiO}_2$  with other ferromagnetic elements such as Fe and Ni. Depending on their phase relations with  $\text{TiO}_2$ , the solubility of one of these elements into the rutile structure during equilibrium preparation using FZ melting technique could provide more information regarding the origin of magnetic properties.

### 8.2.4. Rare earth orthoferrites ( $R\text{FeO}_3$ , $R=\text{Er}$ and $\text{Y}$ )

- FZ growth of other rare earth orthoferrites is suggested to investigate/find their growth behaviour compared to  $\text{ErFeO}_3$  and  $\text{YFeO}_3$ . The preparation of high quality crystals could provide more reliable physical property measurements compared to crystals grown using other techniques such as flux growth.

- More physical characterizations such as magnetic and magneto-optic measurements could be performed using high quality crystals grown by the FZ technique.

**Appendix A. Summary of the crystals grown by the FZ method using image furnaces since 1990 with particular reference to the growth conditions**

Material	Growth Conditions				Results		Ref. / year
	Growth Rate (mm/h)	Rotation rate (rpm) FR: feed rod SR: seed rod or growing crystal	Atmosphere (Related Pressure, bar)	No. of mirrors	Size (mm) D: Diameter L: Length	Quality	
Bi-Sr-Ca-Cu-O	1, 2, 6	-	Air (-)	2	D : 6	-Aligned polycrystalline structure was obtained. -Slower growth rates yielded larger crystals with better alignment. - A wide range of compositions and inclusions	[6]
LuFe <sub>2</sub> O <sub>4</sub> LuFeCoO <sub>4</sub> YbFeMgO <sub>4</sub>	1	-	CO <sub>2</sub> + CO (-) Air (-) Air (-)	1	3 × 2 × 15 1 × 5 × 10 5 × 3 × 20	-Cracks along the all single crystal boules	[7]
Y <sub>2</sub> O <sub>3</sub> -doped SrZrO <sub>3</sub> Y <sub>2</sub> O <sub>3</sub> -doped SrCeO <sub>3</sub>	-	-	-	-	D : 2 L: 30	-	[8]
R <sub>2</sub> Fe <sub>14</sub> B R=Nd, Y	-	-	-	-	-	-	[9]
TiO <sub>2</sub>	5	FR: 25 SR: 30	O <sub>2</sub> (1, 0.01)	2	D : 6	-Low angle grain boundaries -Oxygen deficiency	[10]
Ni-doped Bi-Sr-Ca-Cu-O	0.35-0.45	FR: 30-38 SR: 38	Air (1)	2	15 × 4 × 0.12	-Single crystals with different compositions were obtained. -Second phase inclusions	[11]
Bi <sub>2</sub> Sr <sub>2</sub> Ca <sub>1-x</sub> Y <sub>x</sub> Cu <sub>2</sub> O <sub>y</sub>	-	-	-	-	0.5 × 2 × 0.01	-	[12]
Nd <sub>2-x</sub> Ce <sub>x</sub> CuO <sub>4</sub>	-	-	-	-	D : 6 L : 50	-Inclusion and crack free, but crystals were not superconductive.	[13]
Bi <sub>2</sub> Sr <sub>2</sub> CuO <sub>6</sub>	-	-	-	-	40 × 6 × 1	-	[14]
CaSi <sub>2</sub>	10	-	Ar (-)	-	D : 10 L : 100	-Low angle grain boundaries	[15]
ZrO <sub>2</sub> -doped TiO <sub>2</sub>	5	FR: 30 SR: 30	O <sub>2</sub> (-)	2	-	-Low angle grain boundaries -Oxygen deficiency	[16]

$\text{Sc}_2\text{O}_3$ -doped $\text{TiO}_2$	5	FR: 30 SR: 30	$\text{O}_2$ (-)	2	D: ~6 L: ~30	-Low angle grain boundaries and cracks -Oxygen deficiency	[17]
$\text{Bi}_2\text{Sr}_2\text{CaCu}_2\text{O}_{8+\delta}$	1-2	FR: 40 SR: 40	Air (2)	2	$10 \times 3 \times 0.3$	-	[18]
$\text{Bi}_2\text{Sr}_2\text{CaCu}_2\text{O}_x$	0.5	FR: 20 SR: 20	Air (1)	-	-	-	[19]
Bi-(Sr,La)-Cu-O	0.8-4	FR: 60 SR: 60	Air (2)	2	$2 \times 0.5 \times 0.1$	-Cracks -The crystals were not superconducting.	[20]
Bi-Sr-Ca-Cu-O	0.2-1	FR: 36 SR: 30	Air (-)	2	$20 \times 5.5 \times 1.5$	-Microcracks -Small crystals and cellular liquid/solid interface were obtained at higher growth rate ( $\geq 0.2\text{mm/h}$ )	[21]
$\text{Bi}_2\text{Sr}_2\text{CaCu}_2\text{O}_8$	-	-	-	2	-	-Large and high quality crystals	[22]
$\text{La}_{2-x}\text{Ba}_x\text{CuO}_4$	-	-	-	-	D: 5 L: 25	-	[23]
$\text{Bi}_2\text{Sr}_2\text{CaCu}_2\text{O}_{8+x}$	~0.26	FR: 30 SR: 30	Air (-) $\text{O}_2$ (2, 3)	2	D: 6 L: 60-80	-Higher Sr/Ca ratio and different <i>c</i> -axis parameters at higher oxygen pressures. -Different magnetic AC susceptibilities at different oxygen pressures.	[24]
$\text{Bi}_{2.1}\text{Sr}_{1.9}\text{Ca}(\text{Cu}_{1-y}\text{Fe}_y)_2\text{O}_x$ $y \leq 0.03$	0.2	FR: 36 SR: 30	Air (-)	2	A few mm	-Multiphase grains when $y > 0.01$ -Microcracks and smaller crystals with an increase of <i>y</i>	[25]
$\text{La}_{2-x}\text{Sr}_x\text{CuO}_{4-\delta}$	0.4- 0.5, 1.8	FR: 25 SR: 25	Air (-) $\text{O}_2$ (2-5)	2	D: 5 L: 25	-Second phase inclusions at higher oxygen pressures and a higher growth rate (1.8 mm/h) -Crack and non-uniform distribution of Sr	[26]
$\text{Li}_3\text{VO}_4$	0.5-1	-	Ar (-) $\text{O}_2$ (-) Ar+ $\text{O}_2$ (-) Dry air (-) and Wet air (-)	1	D: 5 L: 5	-Cracks, low angle grain boundaries and bubble formation in the molten zone and crystals -Colouration of crystals (oxygen deficiency)	[27]
$\text{NiAl}_2\text{O}_4$	2.5, 5, 10	FR: 5-40 SR: 5-40	$\text{O}_2$ (1-3)	1	D: 5 Length: 5	-No significant differences in compositions for different growth rates and oxygen pressures. -Stable growth at a lower temperature gradient and using a growth rate of 5 mm/h -Cracks	[28]

$\text{NiTa}_2\text{O}_6$	5	FR: 30 SR: 30	Ar (-) $\text{O}_2$ (-)	2	D: ~6 L: ~30	-Colouration -The stream of oxygen was more effective in suppressing the evaporation of NiO compared to Ar stream. -Cracks and low angle grain boundaries	[29]
$\text{Y}_3\text{Fe}_5\text{O}_{12}$	1-4	FR: 30 SR: 30	Air (-) $\text{O}_2$ (~1)	2	D: 6-8 L: 80	-Repeated zone travelling was used to obtain crystals without voids and second phases.	[30]
$\text{Ca}_{2-x}\text{Nd}_x\text{Al}_{2+x}\text{Si}_{1-x}\text{O}_7$ $0 < x < 0.3$	0.5-1	FR: 20-25 SR: 20-25	-	2	D: 5 L: 20-30	-Cracks due to the thermal shock	[31]
$\text{Ba}_{1-x}\text{Sr}_x\text{TiO}_3$	1-2	-	$\text{O}_2$ (-)	2	D: 8 L: 4	-Cracks due to the temperature gradient -More cracks in larger diameter crystals	[32]
$\text{Bi}_2\text{Sr}_2\text{CaCu}_2\text{O}_x$	0.2-1	FR: 12 SR: 12	Ar+ $\text{O}_2$ (1)	2	$0.5 \times 2$	-Larger and inclusion free crystals at lower growth rates	[33]
$\text{Ca}_2\text{CuO}_3$	1	FR: 30 SR: 30	$\text{O}_2$ (1)	-	$7 \times 3 \times 3$	-Range of compositions, impurity phases and bubble formation in the molten zone	[34]
Cr-doped $\text{Mg}_2\text{SiO}_4$	2	FR: 50 SR: 50	$\text{O}_2$ (ambient pressure)	1	D: ~6 L: ~30	-Cracks and impurities	[35]
$\text{CuFeO}_2$	1, 2	-	Ar (-)	-	D: 5-8 L: 10-30	-The as-grown crystals are almost homogeneous.	[36]
$\text{La}_2\text{NiO}_{4+\delta}$ $0.19 \geq \delta \geq 0.12$	3.5-4.0	FR: 45 SR: 45	Air (-) Ar (-) $\text{O}_2$ (1, 3, 5)	2	D: 7 L: 20	-Large and homogeneous single crystals -Second phases in crystals grown in Ar	[37]
$\text{R}_2\text{X}_3$ R=Rare earth element X=S, Se, Te	-	-	-	2	D: ~6	-	[38]
$\text{Fe}_2\text{SiO}_4$	1.5	FR: 30-40 SR: 30-40	CO-CO <sub>2</sub> -Ar (-)	1	D: 10 L: 40-60	-Bubbles, impurities and low angle grain boundaries	[39]
$(\text{Fe}_x\text{Mg}_{1-x})_2\text{SiO}_4$	~1	FR: 30-40 SR: 30-40	CO-CO <sub>2</sub> -Ar (-)	1	D: ~6 L: 20-60	-Cracks, bubbles, low angle grain boundaries and inclusions	[40]
$\text{CuGeO}_3$ Zn-doped $\text{CuGeO}_3$	2	-	$\text{O}_2$ (-)	2	D: 5 L: 30	-Crack free -Inhomogeneous distribution of Zn	[41]
$\text{RNi}_2\text{B}_2\text{C}$ R=Y, Ho	1.5	FR: 15 SR: 15	Ar (-)	2	D: 6 L: 60-110	-No second phase or cracks	[42]

$\text{La}_{2-x}\text{Sr}_x\text{CuO}_4$ $x=0.15, 0.20$	1, 5	FR: 30 SR: 30	$\text{O}_2$ (2)	2	$3 \times 3$	-Cracks, second phase and grain boundaries -Larger grains at the lower growth rates	[43]
$\text{La}_{1-x}\text{A}_x\text{MnO}_3$ A=Ca, Sr $x=0-0.33$	10-20	FR: 30 SR: 60	Air (-)	-	D : 7 L : 60	-Colouration, striations on the surface, inhomogeneous composition	[44]
GaAs Te-doped GaAs	12, 60, 120, 240	FR: - SR: 1-4	-	2	D : 6-7 L : 20	-	[45]
$\text{CuFeO}_2$	0.5-3.0	FR: 15-30 SR: 15	Ar (-)	-	D : 5-8 L : 10-30	-Inclusions -Almost homogeneous in composition	[46]
$\text{RTaO}_4$ R=Nd, Ho, Er	-	-	-	2	D : 8 L : 70	-	[47]
Cr-doped $\text{Mg}_2\text{SiO}_4$	-	-	Ar (-) Ar+ $\text{O}_2$ (-) $\text{O}_2$ (-)	1	D : 5-6 L : 25	-Different Cr concentrations at different growth atmospheres	[48]
$\text{Al}_2\text{O}_3$ -doped $\text{TiO}_2$	10	FR: 30 SR: 30	$\text{O}_2$ (-)	2	D : ~6	-Cracks and low angle grain boundaries	[49]
$\text{La}_{2-x}\text{Ca}_x\text{CuO}_4$ $0 \leq x \leq 0.1$	1	-	$\text{O}_2$ (2)	1	D : 5 L : 30	-Homogeneous in composition and inclusion free	[50]
$\text{YNi}_2\text{B}_2\text{C}$	1, 2, 3	FR: 15 SR: 12	Ar (-)	2	D : 5 L : ~60	-No second phase -Cracks	[51]
Bi-Sr-Ca-Cu-O	0.2-1	FR: 36 SR: 30	-	2	$20 \times 5.5 \times 1.5$	-Different transition temperatures under different growth rates -Smaller crystals at higher growth rates	[52]
Nd-doped $\text{YVO}_4$	3-10	-	$\text{O}_2$ (-)	2	-	-No inclusions, voids and growth striations -Cracks at the growth rate above 10 mm/h	[53]
$\beta_{II}$ - $\text{Li}_3\text{VO}_4$	0.2-0.5	FR: 30 SR: 30	Ar (-)	1	D : ~4 L : ~25	-Less impurities, a few cracks and larger crystals at the growth rate of 0.2 mm/h -No impurities, low angle grain boundaries or cracks using a heat reservoir	[54]
$\text{La}_{1.85}\text{Sr}_{0.15}\text{CuO}_4$ $\text{Nd}_{1.85}\text{Ce}_{0.15}\text{CuO}_4$	0.5-0.7	-	$\text{O}_2$ (8)	-	D : 7 L : 30	-The as-grown crystals displayed superconductivity better than crystals grown by the other methods.	[55]
$\text{Bi}_{12}\text{SiO}_{20}$	Up to 200	-	-	-	D : 1-6	-	[56]

La <sub>2-x</sub> M <sub>x</sub> CuO <sub>4</sub> M=Ca, Sr and Ba	0.8, 1	-	O <sub>2</sub> (2)	-	D : 5 L : 40	-Sub-grain and inclusion free -Formation of sub-grains was prevented by decreasing the growth rate to 0.8	[57]
La <sub>0.85</sub> Sr <sub>0.15</sub> MnO <sub>3</sub>	7	FR: 30 SR: 30	-	-	D : 4 L : 100	- Stoichiometric crystals were obtained.	[58]
Bi <sub>1.8</sub> Pb <sub>0.38</sub> Sr <sub>2.01</sub> CuO <sub>6+δ</sub>	0.3-5	FR: 30 SR: 30	Air (-)	-	6×3×0.03	-The best crystals were grown at 1 mm/h. -Free of low angle grain boundaries and any structural modulation	[59]
CuFeO <sub>2+δ</sub>	-	-	CO <sub>2</sub> (-) Ar (-) Ar+O <sub>2</sub> (-)	-	-	-Lattice parameters and oxygen content changed at different oxygen partial pressures.	[60]
YB <sub>44</sub> Si <sub>1.0</sub>	10	FR: 30 SR: 30	Ar (-)	-	D : 8 L : 50	-Sub-grains, impurities and cracks	[61]
RB <sub>6</sub> R=Tb, Dy, Ho, Y	4	-	Ar (1, 10)	-	L : 100	-Higher quality crystals at 10 bar pressure	[62]
Tb-Dy-Fe	5-200	FR or SR: 10-60	-	-	-	-Less twinning at lower growth rates	[63]
Bi <sub>2</sub> Sr <sub>2</sub> CaCu <sub>2</sub> O <sub>8+δ</sub>	0.5	-	Air (-)	-	-	-High quality	[64]
PrBa <sub>2</sub> Cu <sub>3</sub> O <sub>7-y</sub>	0.4-0.5	-	Ar+O <sub>2</sub> (0.001)	-	D : 4-5 L : 60-120	-No superconductivity in the crystals	[65]
Bi-Sr-Ca-Cu-O	0.2-1	-	-	2	2 mm along <i>c</i>	-Larger crystals and planar S/L interface at a growth rate of 0.2 mm/h	[66]
A-doped CuGeO <sub>3</sub> A=Al, Mg, Ni, Si, Zn	1	FR: 30 SR: 30	O <sub>2</sub> (2)	-	D : 7 L : 100	-High quality and large crystals -Use of higher oxygen pressure to prevent vapourization of CuO	[67]
NdBa <sub>2</sub> Cu <sub>3</sub> O <sub>7-δ</sub>	0.46	FR: 28 SR: 28	Ar+O <sub>2</sub> (-)	-	D : 3-4 L : 43	-Sharp temperature gradient was used to prevent the falling down of the solvent.	[68]
Sr <sub>2</sub> CuO <sub>2</sub> Cl <sub>2</sub>	5	FR: 30 SR: 30	Ar (1.2)+O <sub>2</sub> (0.2) Ar (1.2)	2	15×6×4	-High pressure was applied to suppress the evaporation of copper oxide -Poor quality crystal in Ar -Different lattice parameters at different growth atmospheres	[69]
Sr <sub>2.5</sub> Ca <sub>11.5</sub> Cu <sub>24</sub> O <sub>41</sub>	-	-	O <sub>2</sub> (10)	-	-	-	[70]
Nd <sub>0.7</sub> Sr <sub>0.3</sub> MnO <sub>3</sub> La <sub>0.5</sub> Ca <sub>0.5</sub> MnO <sub>3</sub>	2.5-10	-	O <sub>2</sub> (-)	2	D : ~8 L : ~50	-Cracks and inhomogeneous in composition -More defects at higher growth rates and sharp temperature gradient	[71]



$\text{PrBa}_2\text{Cu}_3\text{O}_{7-y}$	0.4-0.5	-	$\text{Ar}+\text{O}_2$ (-)	4	$\sim 1 \times 1 \times 1$	-Impurities, low crystalline quality, cracks and non-superconductive	[72]
(Eu, Dy)-doped $\text{SrAl}_2\text{O}_4$ (Eu, Nd)-doped $\text{CaAl}_2\text{O}_4$	4	FR: 21 SR: 21	$\text{Ar}+\text{O}_2$ (-) $\text{Ar}$ (-) $\text{Ar}+\text{H}_2$ (-)	4	$3 \times 4 \times 3$	-Formation of bubbles and instability of molten zone -Different properties at different growth atmospheres	[73]
$\text{Sr}_{14-x}\text{Ca}_x\text{Cu}_{24}\text{O}_{41}$ $0 \leq x \leq 12$	0.8-2.0, 3	FR: 30 SR: 30	$\text{O}_2$ (13)	2	D: $\sim 5$ L: 40-70	-Impurities at growth rate of 3 mm/h -Higher oxygen pressure of 13 gave more Ca incorporation into the structure	[74]
$\text{SrCuO}_2$	0.5-2	-	$\text{O}_2$ (-)	2	D: 3-4 L: $\sim 10$	-Unstable molten zone at the growth rates higher than 0.5 mm/h	[75]
$\text{Tb}_2\text{Ti}_2\text{O}_7$	5-20	FR: 10-20 SR: 10-20	$\text{O}_2$ (-) $\text{Ar}$ (-)	2	D: 3-5 L: $\sim 20$	-Large and high quality crystals -No noticeable difference in properties at different growth atmospheres -Colouration	[76]
$\text{YbB}_{12}$	-	-	-	4	D: 6 L: 50	-	[77]
$\text{Nd}_{9.33}(\text{SiO}_4)_6\text{O}_2$	2-5	FR: 50-80 SR: 50-80	$\text{N}_2$ (-)	2	D: 5 L: 20-40	-No low angle grain boundaries, twin structures and cracks -Lower growth rates and higher sintering temperature reduced bubbles in crystals.	[78]
$(\text{La}_{1-x}\text{A}_x)_y\text{MnO}_3$ A=Sr, Ca $x=0-0.3$	10-20	FR: 1 SR: 50	$\text{Ar}$ (3-5) $\text{Air}$ (-)	-	-	-Mn evaporation and formation of $\text{La}_2\text{O}_3$ inclusions in the crystals	[79]
$\text{La}_{1.92}\text{Sr}_{0.08}\text{CuO}_{4+\delta}$	0.5	FR: 30 SR: 30	$\text{O}_2$ (2)	2	D: 5.8 L: 87	-No grain boundaries or second phases	[80]
$\text{CuGeO}_3$	1	-	$\text{O}_2$ (1)	-	D: $\sim 5$ L: $\sim 120$	-	[81]
$\text{La}_{2-x}\text{Sr}_x\text{CuO}_4$	-	-	-	-	D: $\sim 5$ L: $\sim 120$	-	[81]
$\text{SrCuO}_2$ $\text{Sr}_2\text{CuO}_3$	1	-	-	-	D: 5-6	-	[81]
$\text{Sr}_{14}\text{Cu}_{24}\text{O}_{41}$	0.8-2	-	$\text{O}_2$ (1-13)	-	-	-Higher oxygen pressure of 13 gave more Ca incorporation into the structure	[81]
$\text{SrCu}_2(\text{BO}_3)_2$	0.3-1	FR: 10 SR: 10	$\text{O}_2$ (1)	4	D: 6 L: 43	-No imperfections	[82]

$Y_2 Cu_2 O_5$	0.1-1	FR: 40 SR: 40	$O_2$ (1) Ar+ $O_2$ (-)	1	D: 6 L: 40	-Cracks and second phases	[83]
$La_{2-x} Sr_x CuO_4$ $x=0.0, 0.09, 0.13$	1	FR: 25 SR: 15	$O_2$ (2)	1	D: ~5 L: ~30	-High quality, subgrain and inclusion free	[84]
$Ba(B_{1-x} Al_x)_2 O_4$ $x=0.0, 0.05$	5-20	-	-	-	D: 1 L: 20	-Transparent crystals were obtained.	[85]
Bi-Sr-Cu-O	0.2	FR: 30 SR: 30	$O_2$ (1-7)	4	$22 \times 6 \times 1.3$	-Higher oxygen pressures increased solubility of Sr and oxygen content of grown crystals, and also changed the crystal structure.	[86]
$B_{18} Si$	2	FR: 15 SR: 15	Ar (-)	-	D: ~7 L: ~30	-Impurities	[87]
$Cr^{4+}$ -doped $LiAlGeO_4$	-	-	Air (-)	-	-	-	[88]
$DyMnO_3$	5	FR: 20 SR: 20	Air (-)	2	-	-	[89]
Er:YVO <sub>4</sub>	7-10	FR: 20-30 SR: 20-30	-	2	$4.2 \times 4.8 \times 48$	-Inclusions at higher growth rates -No cracks or sub-grain boundaries	[90]
$La_{1.2} Sr_{1.8-y} Ca_y Mn_2 O_7$ $0.0 \leq y \leq 0.2$	7.2	FR: 35 SR: 45	Air (-)	2	D: ~4.5 L: ~100	-High quality -Mn volatilization and second phases	[91]
Nd-doped YVO <sub>4</sub>	10	FR: 30 SR: 30	$O_2$ (-)	2	D: 0.8-3 L: ~50	-No low angle grain boundaries, cracks or strains for any crystals up to 3 mm in diameter -Inclusions at the growth rates less than 10 mm/h	[92]
$Pr_{9.33} (SiO_4)_6 O_2$ $Sm_{9.33} (SiO_4)_6 O_2$	5	FR: 30 SR: 30	$N_2$ (-)	2	D: ~5 L: ~30	-No inclusions, low angle grain boundaries or twin structure -A few cracks	[93]
$(Mn_{1-x} Mg_x)GeO_3$ $x=0.06, 0.10, 0.20$	1	FR: 30 SR: 30	Air (-)	4	D: ~7 L: 40-50	-Almost free from twins, sub-grains and inclusions	[94]
TiO <sub>2</sub>	5-10	FR: 30 SR: 30	$CO_2 + O_2$ (-)	2	D: ~6	-No low angle grain boundaries at the higher growth rate of 10 mm/h, but bubbles introduced into the crystal	[95]
$Sr_2 RuO_4$	16.5-60	FR: 33 SR: 33	$O_2 + Ar$ (2-10)	2	~ $80 \times 4 \times 3$	-Lower superconducting transition temperature at higher growth rates -Impurities	[96]

Tm and Ho-doped $YVO_4$	5-10	FR: 20-30 SR: 20-30	-	2	$\sim 4 \times 4.8 \times 36$	-Sharper temperature gradient suppressed the formation of cracks, inclusions and sub-grain boundaries.	[97]
Tm <sup>3+</sup> -doped $CaYAlO_4$	3-8	FR: 10-20 SR: 10-20	$N_2$ (-), Ar (-), $O_2$ (-), Air (-), $N_2 + O_2$ (-)	2	$\sim 5 \times 5 \times 30$	-High quality crystals were obtained in a growth atmosphere of $N_2 + O_2$ . -Cracks	[98]
$Bi_2 Sr_2 Ca_2 Cu_3 O_{10+\delta}$	0.05	FR: 10.5 SR: 10.0	Ar+ $O_2$ (-)	2	$4 \times 2 \times 0.1$	-High quality and large crystals	[99]
$Bi_{2+x} Sr_{2-y} CuO_{6+\delta}$	0.5-1.0	FR: 12-20 SR: 12-20	$O_2$ (1-10)	4	$28 \times 6 \times 2.5$	-Large and high quality crystals - With increasing oxygen pressure the 'c'-axis decreases and the molten zone becomes unstable.	[100]
$Bi_2 Sr_2 CaCu_2 O_{8+\delta}$	0.2-0.4	FR: 20-30 SR: 20-30	$O_2$ (2-10)	4	mm size	-Impurities -More stoichiometric composition with increase of growth rate from 0.2 to 0.35	[101]
$Ca_{2+x} Y_{2-x} Cu_5 O_{10}$ $x=0, 0.5, 1.0, 1.5, 1.8$	0.5	FR: 15 SR: 15	$O_2$ (1-8) Air (-)	4	D : 6 L : 80	-More voids on the surface at the growth rates higher than 0.6 mm/h -Less impurities at higher oxygen pressures	[102]
$Ge_{1-x} Si_x$ $x \leq 10\%$	0.5-2	FR: 0-2 SR: 0-2	Ar (0.7)+ $H_2$ (0.1)	1	L : 44	-	[103]
Nd-doped $YVO_4$ Nd: 2-8.5%	5-25	FR: 10-30 SR: 10-30	$O_2$ (-)	2	D : 3-4 L : $\sim 70$	-Impurities at the growth rate of 5 mm/h -No macroscopic defects -Lower rotation rate of 15 rpm to stabilize the molten zone	[104]
$Nd_{0.67} Sr_{0.33} Mn_{1-x} Fe_x O_3$ $x=0.0, 0.1, 0.2$	-	-	-	4	-	-	[105]
$RFe_{1-x} Mn_x O_3$ R=Pr, Gd, Dy $0 < x < 0.6$	-	-	-	-	-	-	[106]
Rh-doped $Ru_2 Si_3$	-	-	Ar (-)	2	D : 1.5-2.5 L : 10-20	-	[107]
$(Sr_x Ba_{1-x})_{1-y} (Nb_2 O_5)_y$ $0.75 \geq x \geq 0.40$ $0.5050 > y > 0.4975$	1-5	FR: 15 SR: 15	Air (-)	-	D : 5 L : 70	-Compositional fluctuation, a few secondary phases, cracks and colouration	[108]
$ScB_{19+x} Si_y$	5-7	FR: 35	Ar (-)	4	D : 8	-Many irregular ridges on the crystal surface,	[109]

		SR: 35			L : 50	crack and grain boundaries	
SmLa <sub>0.8</sub> Sr <sub>0.2</sub> CuO <sub>4</sub>	0.25	FR: 25 SR: 30	Ar+O <sub>2</sub> (2)	4	D : 6 L : 100	-High quality crystals	[110]
Bi <sub>2</sub> Sr <sub>2</sub> Ca <sub>2</sub> Cu <sub>3</sub> O <sub>10+δ</sub>	0.04-0.2	FR: 25 SR: 15	Ar+O <sub>2</sub> (-)	4	10×6×0.5	-Impurities even at lower growth rates	[111]
Bi <sub>2</sub> Sr <sub>2</sub> CaCu <sub>2</sub> O <sub>8+δ</sub>	0.2	FR: 30 SR: 30	O <sub>2</sub> (0.0005, 0.001, 0.05, 0.1, 0.5, 0.8, 1)	4	15×5×1	-Impurities, phase decomposition, <i>c</i> -axis expansion and lower superconducting transition temperature at lower oxygen pressures.	[112]
CeSi <sub>2</sub> R <sub>2</sub> TMSi <sub>3</sub> R=Ce, Tb, Dy TM=Pd, Co, Ni	10-20	-	Ar (-)	4	D : 6 L : 40	-Element segregation	[113]
Ca <sub>12</sub> Al <sub>14</sub> O <sub>33</sub>	0.3-2	-	Air (-) O <sub>2</sub> (-)	4	D : ~5 L : ~50	-Bubbles, cracks and grain boundaries -Amorphous phase on the surface -Less bubbles and cracks at lower growth rates	[114]
La <sub>2</sub> CuO <sub>4</sub> La <sub>2-x</sub> Ba <sub>x</sub> CuO <sub>4</sub>	0.5-0.7	FR: 25-30 SR: 25-30	Air (<1) O <sub>2</sub> (<1, 1.5-2) Ar+O <sub>2</sub> (1.5)	2	D : ~3-3.5 L : ~20-30	-Impurities at higher oxygen pressures -High quality crystals obtained at the lower growth of 0.5 mm/h	[115]
La <sub>1-x</sub> Sr <sub>x</sub> MnO <sub>3</sub> X=0.0-0.3	6-8	FR: 40 SR: 40	Ar+O <sub>2</sub> (6-8)	4	D : 8 L : 70	-Micro-cracks in the outer surface at growth rates of 3-5 mm/h, and macro-cracks at higher growth rates of 12-15 mm/h. -Lower evaporation of Mn at higher pressures of argon and oxygen	[116]
La <sub>2-x</sub> Sr <sub>x</sub> NiO <sub>4+δ</sub> X=0.0-0.5	3-3.5	FR: 40 SR: 40	Ar+O <sub>2</sub> (5-7)	4	D : ~6 L : ~60	-Crack free and homogeneous -Evaporation and second phase formation at lower gas pressures	[117]
RMnO <sub>3</sub> R=Nd, Sm, Eu, Gd	4	FR: 20 SR: 20	Air (-)	2	-	-Single phase crystals	[118]
Mo <sub>5</sub> SiB <sub>2</sub>	4	-	Ar (-)	-	-	-	[119]
Nd-doped GdVO <sub>4</sub> Nd: 2-15%	5-55	FR: 10-30 SR: 10-30	O <sub>2</sub> (-)	2	D : ~3 L : ~80	-No second phases, cellular growth or cracks -Growth rates <30 mm/h was favourable to reduce the dislocations density	[120]

$\text{Ru}_2\text{Si}_3$	10	FR: 10 SR: 45	Ar (-)	2	D : ~7 L : ~40	-Cracks and inclusions -No twinning	[121]
$\text{SrZrO}_3$	5-65	FR: 3-25 SR: 3-100	Air (-)	2	D : 5 L : 40	-Colourless and transparent -Inclusions at the outer surface and cracks -Increasing the growth rate up to 60 mm/h improves the molten zone stability.	[122]
$\text{Sr}_3\text{Ru}_2\text{O}_7$	40	FR: 30 SR: 30	$\text{O}_2$ (1)	2, 4	~mm size	-	[123]
$\text{TiO}_2$	3	FR: 10 SR: 50	$\text{O}_2$ (3-8)	4	D : ~6 L : ~50	-Oxygen deficiency -A few low angle grain boundaries at higher oxygen pressures -Transparent and crack free	[124]
$\text{YbCoGaO}_4$	1.7	FR: 30 SR: 30	Air (-)	4	D : ~5 L : ~20	-No impurities	[125]
$\text{YCuO}_2$	<0.2	FR: 30 SR: 30	$\text{N}_2 + \text{O}_2$ (-)	2	~mm size	-	[126]
$\text{ANb}_2\text{O}_6$ A=Ni, Co, Fe, Mn	1-3	FR: 30-40 SR: 30-40	Air (-) $\text{O}_2$ (-) Ar+ $\text{O}_2$ (ambient)	4	D : 12 L : 80	-Small secondary grains on the surface -Bubble formation in the molten zone in a flow of air -Crack free -Precipitate layers on the crystal surface under high pressure atmosphere	[127]
$\text{BaGd}_2\text{Mn}_2\text{O}_7$	5	FR or SR: 1	Ar (-)	2	-	-	[128]
$\text{Ca}_2\text{Fe}_2\text{O}_5$	1-2	FR: 15-20 SR: 15-20	$\text{O}_2$ (1-2)	4	D : 6 L : 40	-Crack free, no inclusions or sub-grains -Homogeneous in composition	[129]
$\text{La}_{1-x}\text{Sr}_{1+x}\text{MnO}_4$ $0 \leq x \leq 0.6$	5-20	FR: ~30 SR: ~30	$\text{CO}_2$ (-) $\text{O}_2$ (2.5, 3.5)	2	D : ~4 L : 80-160	-Large and high quality crystals and chemically homogeneous -Best results were achieved at 5 mm/h	[130]
$\text{La}_{2-x}\text{Ba}_x\text{CuO}_4$	0.5, 0.7, 1.2	FR or SR: 30-35	$\text{O}_2$ (-)	2	D : 5 L : 20	-At higher growth rates (>0.5mm/h) inclusions, compositional non-homogeneity and lower superconducting transition temperatures were observed.	[131]
$\text{La}_{2-x}\text{Ce}_x\text{CuO}_4$	0.5	FR: 15 SR: 15	Ar (-) Ar+ $\text{O}_2$ (-) Air (-) and $\text{O}_2$ (-)	4	D : 4-5 L : 40-60	-No superconducting properties after growth -Higher Stability of the molten zone in oxygen mixed argon gas.	[132]

$\text{Nd}_{1-x}\text{Ce}_x\text{Ba}_2\text{Cu}_3\text{O}_y$	0.3-0.4	-	$\text{Ar} + \text{O}_2$ (-)	-	$1 \times 1 \times 0.5$	-	[133]
$\text{RB}_6$ R=La, Ce, Pr, Nd	10-18	FR: 30 SR: 30	Ar (-)	4	D : 5 L : 50-60	-Large and high quality	[134]
$\text{Nd}_2\text{CuO}_4$ $\text{Nd}_{1.85}\text{Ce}_{0.15}\text{CuO}_{4-\delta}$	0.5-0.6	FR: 30 SR: 30	$\text{O}_2$ (-) $\text{Ar} + \text{O}_2$ (-)	2	D : 5 L : 25	-High quality	[135]
$\text{SrFeO}_x$	1-8	FR: 15-20 SR: 15-20	$\text{O}_2$ (2-8)	4	-	-High quality and inclusion free crystals -Fewer cracks at the growth rates <2 mm/h	[136]
$\text{SrTiO}_3$	7-8	FR: 50-80 SR: 2-5	Ar (-) Air (-)	2	D : 15-20 L : 40-80	-Crack free	[137]
CaO-doped $\text{YVO}_4$	5	FR: 30 SR: 30	$\text{N}_2$ (-) $\text{O}_2$ (-)	-	-	-Higher transmittance when grown in atmosphere of oxygen	[138]
Zn-doped CuO	1-5	FR: 30 SR: 30	$\text{Ar} + \text{O}_2$ (4-8)	4	D : 8-9 L : 50-70	-Large and high quality crystals -Higher pressures of oxygen (6-8 bar) allowed successful growth without impurities	[139]
$\text{Bi}_2\text{Sr}_{2-x}\text{La}_x\text{CuO}_{6+\delta}$ $0 \leq x \leq 0.64$	0.3-1.5	FR: 30 SR: 15	$\text{O}_2$ (1-5)	4	$\sim 20 \times 5 \times 1$	-Inclusions -Smaller crystals were obtained at higher growth rates.	[140]
$\text{Bi}_2(\text{Sr}_x\text{Ca}_{3-x})\text{Cu}_2\text{O}_y$ $x=1.5-2$	0.1-0.2	FR: 12, 30, 39 SR: 12, 30, 39	$\text{Ar} + \text{O}_2$ (1, <1)	2	$6 \times 3 \times 0.2$	-	[141]
$\text{Bi}_2\text{Sr}_2\text{Ca}_{1-x}\text{Pr}_x\text{Cu}_2\text{O}_y$ $x=0.0-1.0$	0.2	-	$\text{Ar} + \text{O}_2$ (1, <1)	2	$5-10 \times 3 \times 0.2$	-Large, no impurities and homogeneous in composition	[142]
$\text{Ca}_2\text{Co}_{1-x}\text{Zn}_x\text{Si}_2\text{O}_7$ $0 \leq x \leq 1$	0.5-1.2	FR relative to SR: 40	Air (-)	2	-	-High quality crystals, free of inclusions -Cracks, bubbles and inclusions were found at higher growth rates	[143]
$\text{CeSi}_x$ $x=1.79-1.85$	2-15	FR: 5-20 SR: 30-60	-	2	D : 6-7 L : 50-70	-Segregation of Si and inclusions for $x > 1.82$ and $x < 1.80$ -Phase precipitations at higher growth rate	[144]
$\text{Nd}_2\text{CuO}_4$ $\text{Nd}_{1.815}\text{Ce}_{0.185}\text{CuO}_4$	0.5	FR: 30-35 SR: 30-35	$\text{Ar} + \text{O}_2$ (-)	2	D : $\sim 5$ L : 30-40	-Cracks specially at higher growth rates, inclusions, gas bubbles and uneven distribution of Ce	[145]

Bi <sub>2</sub> Sr <sub>2</sub> CaCu <sub>2</sub> O <sub>y</sub> Bi <sub>2</sub> Sr <sub>2</sub> PrCu <sub>2</sub> O <sub>y</sub> Bi <sub>2</sub> Sr <sub>2</sub> GdCu <sub>2</sub> O <sub>y</sub>	0.15-0.2	FR: 20-30 SR: 20-30	Ar+ O <sub>2</sub> (1, <1)	2	6×2×0.2	-High quality crystals	[146]
Na <sub>x</sub> CoO <sub>2</sub> x=0.5-1.0	2-10	FR: 40 SR: 40	Air (-) O <sub>2</sub> ( up to 2 bar) Ar (-) Ar rich+O <sub>2</sub> (7.5) Ar +O <sub>2</sub> rich (10)	4	-	-A reduction in Na loss when using a high pressure growth atmosphere -Impurities and Na loss	[147]
Nd-doped GdVO <sub>4</sub> Nd: 0.5-5%	10-20	FR: 5 SR: 40-60	O <sub>2</sub> (-)	2	D : 8 L : ~40	-No cracks, inclusions, low angle grain boundaries or growth striations	[148]
Pr <sub>5</sub> Si <sub>3</sub>	1.5-3	FR: 10 SR: 50	Ar +O <sub>2</sub> (2-10)	2	D : 6 L : 40-60	-Cracks in a small peripheral region -Inclusions	[149]
RB <sub>6</sub> R=La, Ce, Pr, Nd	10-18	FR: 30 SR: 30	Ar (-)	4	D : 6 L : 40-70	-Crack free	[150]
R <sub>9.33</sub> (SiO <sub>4</sub> ) <sub>6</sub> O <sub>2</sub> R=Pr, Nd, Sm	2-5	FR or SR: 80	N <sub>2</sub> (-)	2	D : ~6-7 L : ~20-40	-Cracks -No inclusions, low angle-grain boundaries or twin structures	[151]
TiO <sub>2</sub>	20-80	FR: 20 SR: 40	O <sub>2</sub> (0.001-0.1)	2	D : 3-5 L : ~70	-No grain boundaries in small diameter crystals -Bubbles and low angle grain boundaries	[152]
TiO <sub>2</sub>	2	FR: 20 SR: 30	O <sub>2</sub> (0.01, 5)	-	D : ~10 L : ~55	-Colouration, but subgrain-boundary free -Lower transmittance for the crystal grown at the lower oxygen pressure	[153]
Sr <sub>3</sub> Ru <sub>2</sub> O <sub>7</sub>	15, 20, 45	-	Ar+O <sub>2</sub> (3, 10)	-	D : 2.4-5 L : ~15-25	-	[154]
Sr <sub>3</sub> Fe <sub>2</sub> O <sub>7-x</sub>	1-5	FR: 10-15 SR: 10-15	O <sub>2</sub> (0.2-3)	4	D : 6 L : 40	-Inclusion free -High quality and large crystals were obtained at the lower growth rate of 1-2 mm/h	[155]
Tm-doped GdVO <sub>4</sub> Tm: 5-20%	10-20	FR: 5 SR: 30-45	O <sub>2</sub> (-)	2	D : ~5 L : ~60	-No cracks and inclusions, but a few low angle grain boundaries and bubbles	[156]

$\text{Ca}(\text{Cu}_{1-x}\text{Zn}_x)_2\text{O}_3$ $x=0,0.035,0.07,0.14$	1	FR: 30 SR: 30	$\text{O}_2$ (5)	4	D: 5-6 L: 90	-Cracks and second phases	[157]
$\text{CaMn}_{1-x}\text{Mo}_x\text{O}_3$ $0 \leq x \leq 0.15$	1-5	FR: 20 SR: 20	Air (0.2, 0.5, 2)	4	D: ~5 L: ~30	-Micro-cracks -High quality crystals obtained at the lower growth rate of 1mm/h	[158]
$\text{TiO}_2$	5-27	FR: 0-30 SR: 0-30	$\text{O}_2$ (1, 5)	4	D: ~5 L: ~50	-High quality crystals without bubbles, cracks and low angle grain boundaries	[159]
$\text{NiFe}_2\text{O}_4, \text{CoFe}_2\text{O}_4$ $\text{Ni}_x\text{Co}_{1-x}\text{Fe}_2\text{O}_4, x=0.2-0.8$ $\text{Ni}_{1-x}\text{Zn}_x\text{Fe}_2\text{O}_4, x=0.1-0.4$ $\text{Co}_{1-x}\text{Zn}_x\text{Fe}_2\text{O}_4, x=0.1-0.4$	10	FR: 40 SR: 40	$\text{O}_2$ (30-70)	2	D: 8-10 L: 50-70	-	[160]
$\text{Er}_2\text{PdSi}_3$	3-10	FR: 9 SR: 30	Ar (1)	2	D: ~6 L: ~25-50	-Homogeneous element distribution -No additional phase constituent	[161]
$\text{Gd}_{3-x}\text{Y}_x\text{Fe}_5\text{O}_{12}$	0.5-3	FR: 30 SR: 30	Air (-) $\text{O}_2$ (1)	2	D: 7 L: 20	-Fewer voids with decreasing growth rate	[162]
$\text{GeNi}_2\text{O}_4$ $\text{GeCo}_2\text{O}_4$	15-40	-	Air (1) Ar+ $\text{O}_2$ (5, 10) $\text{O}_2$ (10)	2,4	D: ~4 L: ~20	-No impurities or twins	[163]
$\text{La}_{1-x}\text{Sr}_x\text{CoO}_{3+\delta}$ $x=0, 0.33$	2-10	FR: 35 SR: 35	Ar (7-9) Ar+ $\text{O}_2$ (7-9)	4	D: 10 L: 100	-No micro-cracks or segregation -Large and crack free	[164]
$\text{LiFePO}_4$	2-4	FR: 15 SR: 15	Ar (-)	4	D: 5 L: 70	-No cracks, inclusions or grain boundaries in the inner area, but several grains were found in the periphery area	[165]
Nb-doped $\text{YB}_{66}$	7-10	FR: 6-20 SR: 6-20	Ar (-)	4	D: ~10 L: ~60	-Low quality for practical applications	[166]
R-doped $\text{LuVO}_4$ R=Nd, Tm, Yb	40	FR: 5 SR: 30	$\text{O}_2$ (-)	2	D: ~5 L: ~30	-No cracks or inclusions -Striation for the Nd-doped crystals	[167]
$\text{RNi}_2\text{B}_2\text{C}$ R=Y, Ho, Tb	1-3	FR: 10-30 SR: 20-60	Ar (1.5-2.5)	2	D: 6 L: 20-40	-Crack free and single phase -No twinning or stress distortions	[168]



$\text{Sr}_2 \text{RuO}_4$	20-40	FR: 10 SR: 10	Ar+ O <sub>2</sub> (ambient)	2	D : 4.5 L : 70	-Large with homogeneous properties -High superconductivity temperature at a growth rate of 4 mm/h	[169]
$\text{Sr}_2 \text{RuO}_4$ - $\text{Sr}_3 \text{Ru}_2 \text{O}_7$	15	-	Ar+ O <sub>2</sub> (10)	2	-	-Lamellar structure	[170]
Zn-doped $\text{CaCu}_2 \text{O}_3$	1	FR: 25 SR: 25	O <sub>2</sub> (6-7)	4	D : ~5 L : ~80	-Large size and inclusion free -Inclusions at the periphery area	[171]
CrB <sub>2</sub>	10-18	FR: 30 SR: 30	Ar (5)	4	D : ~3-5 L : ~25-30	-High quality	[172]
CuO	10	FR: 30 SR: 7	O <sub>2</sub> (35-55)	2	D : 6 L : ~40	-Cracks -No impurities	[173]
RVO <sub>4</sub> R=Rare earth elements	2-10	FR: 30 SR: 30	Air (-)	2	D : 7 L : 20-50	-Most of the crystals were low angle grain boundary free	[174]
$\text{Sr}_2 \text{RuO}_4$	30-40	-	-	-	~12 × 5 × 2	-Inclusions and precipitates	[175]
$(\text{La}_{1-x} \text{Sr}_x)_2 \text{CaCu}_2 \text{O}_{6+\delta}$ x=0.075-0.25	0.2-1	FR: 36 SR: 30	O <sub>2</sub> (1,11)	2	D : 7.8 L : 100	-Cracks and second phases -Superconductivity was obtained at oxygen pressure of 11 bar	[176]
$(\text{La}_{1-x} \text{Ca}_x)_2 \text{CaCu}_2 \text{O}_{6+\delta}$ x=0.05-0.15	0.35, 1	FR: 36 SR: 30	O <sub>2</sub> (1,11)	4	~5 × 7 × 36	-Cracks and second phases -Larger crystals were obtained at the lower growth rate of 0.35 mm/h -Superconductivity was obtained at oxygen pressure of 11 bar	[177]

Appendix B. Summary of findings from Co-doped TiO<sub>2</sub> thin films

Material (% Co content)	Preparation technique	Growth conditions			Reference
		Substrate	Temperature (° C)	Type of atmosphere and its pressure	
Co-doped anatase 0≤%Co≤8	Combinatorial laser molecular beam epitaxy (MBE)	LaAlO <sub>3</sub> (001)	677-727	Oxygen, 10 <sup>-5</sup> to 10 <sup>-6</sup> torr	[201]
		SrTiO <sub>3</sub> (001)			
		Single crystals			
<b>Results</b>					
<b>Structural characterization:</b>					
-XRD pattern of the film (%Co=8) showed only anatase phase; no evidence for clustering of Co was observed.					
-Increasing Co content increased the c-axis parameter.					
-TEM observations indicated no sign of segregation of impurity phases for %Co<8.					
-From XRD and TEM results it was concluded that the solubility of Co is up to 8%.					
<b>Magnetic characterization:</b>					
-Ferromagnetic above room temperature with a magnetic moment of 0.32 Bohr magneton per cobalt atom.					
-With increasing Co content, the magnitude of the magnetic field was enhanced as a result of the increased spontaneous magnetization.					
-T <sub>c</sub> was estimated to be >400° K					
-Ferromagnetism was attributed to the local spins of Co ions.					
Co-doped rutile 0≤%Co≤5	Laser molecular beam epitaxy	α-Al <sub>2</sub> O <sub>3</sub>	700	Oxygen, 1×10 <sup>-6</sup> torr	[202]
		(10 $\bar{1}$ 2)			
<b>Results</b>					
<b>Structural characterization:</b>					
-XRD pattern of the film confirmed the epitaxial growth of rutile phase with (101) orientation.					
-Up to 5 mole% Co doping, no impurity phase was detected in XRD patterns or from AFM and SEM measurements. Surface segregation of CoO <sub>x</sub> or CoTiO <sub>x</sub> was not observed.					
<b>Magnetic characterization:</b>					
-Ferromagnetic at room temperature with a magnetic moment of ~1.0 Bohr magneton per cobalt atom.					

Co-doped anatase %Co $\leq$ 10	Laser molecular beam epitaxy	LaAlO <sub>3</sub> (001)	650	Oxygen, 10 <sup>-5</sup> to 10 <sup>-6</sup> torr	[206]
	<b>Results</b>				
	<p><b>Structural characterization:</b>            -XRD of the film showed only sharp anatase peaks.            -No detectable phase segregation was observed in the as-grown thin film using TEM.            -Postannealing of the sample at ~400 °C under 10<sup>-6</sup> torr oxygen enhanced the clustering of Co as observed using FE-SEM.</p> <p><b>Magnetic characterization:</b>            -Magnetic moment ~0.1 Bohr magneton per cobalt atom.            -The authors suggested that ferromagnetism originated from clustered Co metal.            -Magnetic moment reached ~1.55 <math>\mu_B</math>/Co after postannealing.            -FM completely disappeared above ~400 °C under high oxygen partial pressure. This was stated to be due to oxidization of the clustered Co.</p>				
Co-doped anatase	Sputtering	LaAlO <sub>3</sub>	RT to 750	Ar, 5 × 10 <sup>-3</sup> torr	[208]
	<b>Results</b>				
	<p><b>Structural characterization:</b>            -XRD of the film showed only the anatase phase.            -SEM images showed the existence of Co clustering.</p> <p><b>Magnetic characterization:</b>            -A wide range of saturation moments up to 1.51 <math>\mu_B</math>/Co was observed, depending on both Co content and deposition parameters.            -Because a higher saturation moment was not obtained from the films with the larger and denser clustering, the authors suggested that both charge carriers and Co clustering contribute to the overall magnetism.</p>				
Co-doped anatase %Co=2 and 7	Reactive RF magnetron cosputter deposition	LaAlO <sub>3</sub> (001)	650	Ar + water vapour total pressure: 15 × 10 <sup>-3</sup> torr	[209]
	<b>Results</b>				
	<p><b>Structural characterization:</b>            -XRD data of the film indicated epitaxial anatase phase with a small amount of secondary rutile phase. (No evidence of Co or cobalt oxides was observed from the diffraction data).            -Backscattered electron images and EDS mapping indicated segregation of Co dopant atoms, while the Ti and oxygen were uniformly distributed across the film surface. These results indicated that the secondary precipitants are a Ti-Co-O phase.</p> <p><b>Magnetic characterization:</b>            -Room temperature ferromagnetism with magnetization ~0.6 <math>\mu_B</math>/Co atom was observed for the 7 at % Co-doped TiO<sub>2</sub> film.            -Increasing the Co content from 2 to 7% increased the magnetization.            -Co atoms (in the Co<sup>+2</sup> state) in the Ti-Co-O precipitate phase were reported to be responsible for the ferromagnetic behaviour.</p>				

TiO <sub>2</sub> -CoO binary compositional spread thin films %Co>50	Combinatorial laser ablation deposition	LaSrAlO <sub>4</sub> (001) Single crystal	550-750	Oxygen, 5 × 10 <sup>-5</sup> to 5 × 10 <sup>-7</sup> torr	[213]
	<b>Results</b>				
	<p><b>Structural characterization:</b> -From XRD patterns, <i>c</i>-axis oriented anatase peaks were observed up to ~50% Co content. Around this Co content, CoTiO<sub>3</sub> peaks had maximum intensity, while CoO peaks appeared at higher Co contents.</p> <p><b>Magnetic characterization:</b> -Magnetic domain structures disappeared with increasing Co content to ~50% Co (where CoTiO<sub>3</sub> peaks had maximum intensity). -The film magnetization increased with decreasing oxygen pressure during deposition.</p>				
Co-doped anatase (Ti <sub>1-x</sub> Co <sub>x</sub> O <sub>2-δ</sub> ) 1≤%Co≤15	Pulsed laser deposition	LaAlO <sub>3</sub> (001) SrTiO <sub>3</sub> (001)	700	Oxygen, 1 × 10 <sup>-5</sup> to 1 × 10 <sup>-4</sup> torr	[207]
	<b>Results</b>				
	<p><b>Structural characterization:</b> -‘<i>c</i>’-axis oriented anatase peaks were observed at 7% Co content. -STEM results from a Ti<sub>0.93</sub>Co<sub>0.07</sub>O<sub>2-δ</sub> sample indicated the presence of clusters (of size 20-50 nm) with large concentrations of Co as well as incorporation of a small fraction of Co in the remaining TiO<sub>2</sub> matrix. -Study of lattice relaxation effects indicated that the (004) lattice parameter showed concentration dependent relaxation at concentrations up to 1.5-2% (the solubility limit of Co in the as-grown films) and a saturation behaviour at higher concentrations, suggesting clustering of excess Co.</p> <p><b>Magnetic characterization:</b> -Room temperature FM with a saturation magnetic moment of ~1.4 μ<sub>B</sub>/Co atom.</p>				
Co-doped anatase 0≤%Co≤10	Oxygen plasma-assisted molecular beam epitaxy (OPA-MBE)	LaAlO <sub>3</sub> (001) SrTiO <sub>3</sub> (001)	300-750	-	[223]
	<b>Results</b>				
	<p><b>Structural characterization:</b> -A slow growth rate of ~0.01 nm/s gave films with the highest crystalline quality and most uniform distribution of Co (over a substrate temperature range of 550-600 °C), while growth at a rate of ~0.04 nm/s led to extensive formation of secondary-phase rutile nanocrystals to which Co diffused and segregated.</p> <p><b>Magnetic characterization:</b> -N/A</p>				

Co-doped rutile $1 \leq \% \text{Co} \leq 12$	Reactive co-sputtering of Ti and Co	Si (100) Quartz	250-450	Ar ( $25 \times 10^{-3}$ torr)+ O <sub>2</sub> ( $5 \times 10^{-5}$ - $3 \times 10^{-4}$ torr)	[205]
	<b>Results</b>				
	<p><b>Structural characterization:</b> -XRD patterns showed single phase polycrystalline rutile structure, with no detectable segregation of Co. From the evaluation of the (101) and (200) peak intensities, it was implied that Co atoms were doped into rutile, thereby changing the atomic scattering factor.</p> <p><b>Magnetic characterization:</b> -Room temperature M-H loops showed ferromagnetic behaviour for Co contents higher than 3%. -The magnetic moment per Co atom was estimated to be about <math>0.94 \mu_B</math>. -The temperature dependence of remanent magnetization revealed a Curie temperature higher than <math>400^\circ \text{K}</math> for a Co content of 12%.</p>				
Co-doped TiO <sub>2</sub> $1 \leq \% \text{Co} \leq 7$	Pulsed laser deposition (PLD)	LaAlO <sub>3</sub> (001) SrTiO <sub>3</sub> (001)	750	Oxygen, $1 \times 10^{-3}$ torr	[210]
	<b>Results</b>				
	<p><b>Structural characterization:</b> -XRD patterns from 0-7%Co:TiO<sub>2</sub> films grown on LaAlO<sub>3</sub>(001) showed only (001) oriented anatase peaks, while films deposited on SrTiO<sub>3</sub> substrates showed the presence of a very small amount (less than 1%) of (111) rutile in addition to (001) oriented anatase. -TEM studies showed clear evidence of the formation of Co-rich areas. Electron diffraction of these clusters suggested the presence of cobalt metal, rather than an oxide of cobalt such as Co<sub>3</sub>O<sub>4</sub> (paramagnetic) or CoO (antiferromagnetic). -Films grown at higher oxygen pressures (&gt;3 mTorr) were green in colour rather than black, suggesting that a cobalt oxide had formed.</p> <p><b>Magnetic characterization:</b> -The films were FM at room temperature with an average magnetic moment of <math>1.7 \pm 0.4 \mu_B / \text{Co atom}</math> (independent of substrate type). -A larger magnetic moment was found in films with better crystallinity. -The magnetization measurements showed a strong dependence on growth pressure. Films grown at pressures higher than <math>3 \times 10^{-3}</math> torr were nonmagnetic with a greenish tinge, compared to the greyish tinge of the ferromagnetic films grown at lower pressures.</p>				
Co-doped anatase $\% \text{Co} = 4$	Pulsed laser deposition (PLD)	SrTiO <sub>3</sub> (001) Single crystal	600	Oxygen, $10^{-7}$ to $10^{-4}$ torr	[211]
	<b>Results</b>				
<p><b>Structural characterization:</b> -XRD patterns showed only (001) peaks of the anatase phase. -As oxygen pressure decreased, the growth behaviour was changed from a 2D layer-by-layer growth with smooth surfaces to a 3D rough island-like one (width and height of the islands were found to vary from 10-100 nm using AFM).</p>					

	<p>-Rocking curves of the (004) peak showed that decreasing the oxygen pressure from <math>10^{-5}</math> to <math>10^{-7}</math> increased the FWHM from <math>0.66^\circ</math> to <math>0.86^\circ</math> respectively.</p> <p>-XTEM and EDS analysis of a film grown at a low oxygen pressure of <math>10^{-7}</math> torr showed Co-rich nanoclusters in the film.</p> <p><b>Magnetic characterization:</b></p> <p>-Decreasing the oxygen pressure resulted in an increase in the saturation magnetization (at <math>300^\circ\text{K}</math>) and conductivity.</p> <p>-It was concluded that cobalt clustering was the main cause of the observed room temperature FM.</p>				
Co-doped anatase $\sim 1\leq\%Co\leq 10$	Oxygen plasma-assisted molecular beam epitaxy (OPA-MBE)	SrTiO <sub>3</sub> (001)	300-750	Oxygen, $2 \times 10^{-5}$ torr	[214]
	<b>Results</b>				
	<p><b>Structural characterization:</b></p> <p>-The Co distribution in the film was found to depend on the way in which the growth was terminated. Stopping growth by simultaneously closing the metal source shutters, turning off the oxygen plasma, and pumping out the residual oxygen as the sample cooled produced films which were either stoichiometric or substoichiometric in Co, while terminating the growth by closing the metal shutters and allowing the sample to cool in the oxygen resulted in significant Co segregation within the near surface region.</p> <p><b>Magnetic characterization:</b></p> <p>-Samples cooled in the oxygen plasma after growth (which exhibited extensive Co diffusion to the near surface region) were nonmagnetic, while those growths terminated by extinguishing the oxygen plasma were ferromagnetic with a saturation moment of <math>1.26 \mu_B/\text{Co atom}</math> and Curie temperatures greater than <math>300^\circ\text{K}</math>.</p> <p>-The saturation moment was independent of sample temperature (between 10-300K), while the coercivity increased with decreasing temperature.</p> <p>-Bulk sensitive Co L-edge x-ray absorption spectroscopy (XAS) for a FM film (<math>\text{Co}_{0.07}\text{Ti}_{0.93}\text{O}_2</math>) revealed that Co is in the +2 oxidation state and the local coordination of Co was similar to that in <math>\text{CoTiO}_3</math>. Since the match to the reference spectra for Co metal was poor, inclusions of Co metal in the anatase lattice were ruled out as the cause of the observed FM behaviour.</p>				
Co-doped anatase	Sputtering	LaAlO <sub>3</sub>	RT to 750	Ar, $5 \times 10^{-3}$ torr	[212]
	<b>Results</b>				
	(All data reported here are from post-growth annealed films at $750^\circ\text{C}$ in high vacuum pressure ( $<10^{-6}$ Torr))				
<p><b>Structural characterization:</b></p> <p>-The film contained only single phase anatase according to XRD analysis.</p> <p>-Cross sectional TEM of the film did not show any inclusions, although surface morphology observations using AFM and SEM showed some Co-clusters.</p> <p><b>Magnetic characterization:</b></p> <p>-Saturation moment values showed a large variation ranging from <math>0.2\text{-}2.0 \mu_B/\text{Co}</math> dependent on the amount of Co clusters.</p> <p>-The saturation magnetization was insensitive to temperature (10-400 K).</p> <p>-It was suggested that the magnetization is determined by Co clustering.</p>					

Co-doped rutile	Pulsed laser deposition (PLD)	Al <sub>2</sub> O <sub>3</sub> (0001)	310	Ar+H <sub>2</sub> total pressure of $7.5 \times 10^{-2}$ torr	[217]
	<b>Results</b>				
	<p><b>Structural characterization:</b>            -XRD analysis showed that the films were rutile with preferred orientation along the [101] direction.            -The film grown in pure Ar was transparent yellow, while the film grown in Ar+H<sub>2</sub> was less transparent dark-grey (the addition of hydrogen was intended to promote oxygen vacancies).</p> <p><b>Magnetic characterization:</b>            -The room temperature saturation magnetization measured for the film grown in Ar+ H<sub>2</sub> was <math>\sim 0.25 \mu_B/\text{Co}</math>.</p>				
Co-doped TiO <sub>2</sub> Co <sub>x</sub> Ti <sub>1-x</sub> O <sub>2-δ</sub> %Co=10	Sol-gel spin coating	Si (001)	-	-	[203]
	<b>Results</b>				
	<p><b>Structural characterization:</b>            -XRD patterns showed anatase phase with a small amount of rutile with no preferred orientation. No evidence for Co or cobalt oxide phases was seen, suggesting that Co atoms were doped into titanium dioxide without clustering.            - XPS measurements indicated that neither Co nor Ti is in a metallic state.            -XRD and XPS measurements failed to detect Co clusters.</p> <p><b>Magnetic characterization:</b>            -The as-prepared films were not FM at room temperature.            -The films heat treated in air were not magnetic, but after vacuum annealing or hydrogenation, films exhibited room temperature FM with a magnetic moment of <math>\sim 0.28 \mu_B/\text{Co}</math>; it was concluded that oxygen vacancies play an important role in the generation of FM.            -No significant drop of magnetization between 5 and 300 K indicated that the Curie temperature is <math>&gt;300</math> K.            -Further work by the same author reported that the room temperature FM was partly due to the formation of Co metal [21].</p>				
Co-doped anatase	RF magnetron sputtering	LaAlO <sub>3</sub> (100)	550	Ar, $4 \times 10^{-3}$ torr	[204]
	<b>Results</b>				
	<p><b>Structural characterization:</b>            -XRD pattern showed only the anatase phase; improved crystallinity was observed with annealing at 450 C for 1 h in UHV.            -Cross sectional HRTEM and EDXS of both as-deposited and annealed films revealed a solid solution of Co dissolved in anatase, with Co concentrations ranging from <math>\sim 2</math>-7% incorporated into the lattice (there was no evidence for the presence of Co metal or Co-rich anatase clusters within the films).            -Near edge x-ray absorption fine structure analysis (NEXAFS) indicated that both as-deposited and annealed films exhibited nearly identical spectra match to a CoTiO<sub>3</sub> reference sample.</p> <p><b>Magnetic characterization:</b>            -<i>M-H</i> curves showed that spontaneous magnetization increased from 0.24 to <math>1.17 \mu_B/\text{Co}</math> atom after annealing due to both the increase in crystallinity and the creation/diffusion of defects through the lattice.</p>				

Co-doped TiO <sub>2</sub> %Co=5-8	Pulsed laser deposition (PLD)	LaAlO <sub>3</sub> (001) Si (100) SrTiO <sub>3</sub> (001)	600, 650, 700	Oxygen, 10 <sup>-5</sup> and 10 <sup>-6</sup> torr	[219]
	<b>Results</b>				
	<p><b>Structural characterization:</b> -XRD patterns revealed that films deposited at 700 °C on Si were rutile, while films deposited on LAO and STO substrates were single phase anatase.</p> <p><b>Magnetic characterization:</b> -All films deposited on different substrates were FM with Curie temperature above 400 K. -The saturation magnetization for films deposited at 700 °C on Si was 0.31 μ<sub>B</sub>/Co, while it was 0.23 μ<sub>B</sub>/Co for films on LAO and 0.16 for films on STO. -Decreasing the substrate temperature from 700 to 650 °C significantly increased the saturation magnetization to 2.8 μ<sub>B</sub>/Co on LAO. -Room temperature FM (according to XRD, magnetization and magnetic force microscopy measurements) was attributed to a doped matrix rather than dopant clusters.</p>				
Co-doped rutile %Co=5	Laser molecular beam epitaxy	α -Al <sub>2</sub> O <sub>3</sub> (10-12)	750	Oxygen, 10 <sup>-6</sup> torr	[220]
	<b>Results</b>				
	<p><b>Structural characterization:</b> -XRD pattern showed (101) oriented rutile phase without any impurity phases. -SEM from the film surface and cross sectional TEM image showed no sign of segregation of second phases and XPS studies indicated the coexistence of oxidized (Co<sup>2+</sup>) and metallic (Co<sup>0</sup>) valence states. -Extended x-ray absorption fine structure (EXAFS) spectra for the film showed the existence of metallic Co-Co bonds and oxidized Co-O bonds. -From XANES, XPS and EXAFS spectra it was concluded that Co metallic clusters and oxidized Co (which was presumed to substitute into the Ti site) coexist in the film.</p> <p><b>Magnetic characterization:</b> -Two possible magnetic origins were proposed. One involves Co ions substituting into Ti sites and the other involves Co clusters that have an unidentified interaction with the TiO<sub>2</sub> lattice.</p>				
Co-doped anatase %Co=4 -10	PLD	LaAlO <sub>3</sub> (100)	-	-	[221]
	<b>Results</b>				
	<p><b>Structural characterization:</b> Not reported.</p> <p><b>Magnetic characterization:</b> -X-ray absorption spectroscopy (XAS) and X-ray magnetic circular dichroism (XMCD) analysis demonstrated that the FM originated from clustered metallic Co, rather than the ionic oxide Co.</p>				



Co-doped anatase	co-sputtering	LaAlO <sub>3</sub> (001)	500-750	Ar, $5 \times 10^{-3}$ torr	[222]
	<b>Results</b>				
	<p><b>Structural characterization:</b>  -XRD showed the anatase structure.  -Increasing the deposition temperature increased the crystallinity (FWHM decreased).</p> <p><b>Magnetic characterization:</b>  -The saturation magnetization for the film grown at 750 °C was about 1.13 <math>\mu_B</math>/Co.  -Increasing the deposition temperature led to a higher crystallinity and increased the saturation magnetization from ~0.25 (at 450 °C) to 1.13 <math>\mu_B</math>/Co at 750 °C.</p>				

**Appendix C. Publications resulting from the work described in this thesis***Published papers:*

1. S.M. Koohpayeh, D. Fort and J.S. Abell, “***Some observations on the growth of rutile single crystals using the optical floating zone method***”, Journal of Crystal Growth 282 (2005) 190-198.
2. S.M. Koohpayeh, D. Fort, J.S. Abell, A. Williams, A. Bevan and K.K. Bamzai, “***The influence of growth rate on the microstructural and magnetic properties of float-zone grown  $\text{ErFeO}_3$  crystals***”, Journal of Magnetism and Magnetic Materials, 309 (2007) 119-125.

*Papers in preparation:*

3. S.M. Koohpayeh, D. Fort and J.S. Abell, “***The optical floating zone technique and growth parameters: A review***”, in preparation.
4. S.M. Koohpayeh, A. Bradshaw, D. Fort and J.S. Abell, “***On the link between temperature characterization of the image furnace and controllable growth parameters***”, in preparation.
5. S.M. Koohpayeh, D. Fort, A. Bevan, A. Williams and J.S. Abell, “***Study of ferromagnetism in Co-doped rutile powders and float-zone grown single crystals***”, in preparation.

*Conference presentations:*

1. S.M. Koohpayeh, D. Fort and J.S. Abell, “***The crystal growth and magnetic properties of  $\text{RFeO}_3$  ( $\text{R}=\text{Er}$  and  $\text{Y}$ )***”, 2006 annual BACG (British Association for Crystal Growth) conference, 10-12 Sept. 2006 in Edinburgh, UK.
2. S.M. Koohpayeh, D. Fort and J.S. Abell, “***The effect of optical FZ growth parameters on the microstructure of  $\text{ErFeO}_3$  single crystals***”, accepted in the 15<sup>th</sup> international conference on crystal growth, 12-17 Aug. 2007, Salt Lake City, Utah, USA.

*Poster presentation:*

1. S.M. Koohpayeh, D. Fort and J.S. Abell, “***Optimizing growth parameters for rutile single crystals by the float-zone technique using a four mirror image furnace***”, 2004 Annual Conference of the British Association for Crystal Growth, University of Leeds, UK (Sept. 5-7, 2004).

**References**

1. Y. Shiohara and A. Goodilin, Handbook on the Phys. and Chem. of Rare Earths, 30 (2000) 67.
2. H.J. Scheel, J. Crystal Growth, 211(2000) 1-12.
3. D.T.J. Hurle, Handbook of Crystal Growth, 2 (1994).
4. J.J. Gilman, The Art and Science of Growing Crystals, (1966) 347.
5. V.V. Osiko, M.A. Borik and E.E. Lomonova, Annual Rev. of Materials Sci., 17 (1987) 101-122.
6. L. Trouilleux, G. Dhalenne, J. Jegoudez and A. Revcolevschi, J. Less-Common Metals, 164-165 (1990) 526-535.
7. J. Iida, S. Takekawa and N. Kimizuka, J. Crystal Growth, 102 (1990) 398-400.
8. S. Shin, H.H. Huang, M. Ishigame and H. Iwahara, Solid State Ionics, 40-41 (1990) 910-913.
9. S. Hirosawa, M. Sagawa and T. Katayama, J. Magn. Magn. Mater., 87 (1990) 205-208.
10. M. Higuchi, T. Hosokawa and S. Kimura, J. Crystal Growth, 112 (1991) 354-358.
11. M.J.V. Menken, A.J.M. Winkelman and A.A. Menovsky, J. Crystal Growth, 113 (1991) 9-15.
12. K. Takamuku, K. Ikeda, T. Takata, T. Miyatake, I. Tomeno, S. Gotoh, N. Koshizuka and S. Tanaka, Physica C: Superconductivity, 185-189 (1991) 451-452.
13. I. Tanaka, T. Watanabe, N. Komai and H. Kojima, Physica C: Superconductivity, 185-189 (1991) 437-438.
14. M. Matsumoto, J. Shirafuji, K. Kitahama, S. Kawai, I. Shigaki and Y. Kawate, Physica C: Superconductivity, 185-189 (1991) 455-456.
15. T. Hirando, J. Less-Common Metals, 167 (1991) 329-337.
16. M. Higuchi and K. Kodaira, J. Crystal Growth, 123 (1992) 495-499.
17. M. Higuchi, J. Takahashi and K. Kodaira, J. Crystal Growth, 125 (1992) 571-575.
18. J.H.P.M. Emmen, S.K.J. Lenczowski, J.H.J. Dalderop and V.A.M. Brabers, J. Crystal Growth, 118 (1992) 477-482.
19. I. Shigaki, K. Kitahama, R. Ogawa, K. Kawate, K. Ishibashi and S. Kawai, Cryogenics, 33 (1993) 1149-1153.
20. J.H.P.M. Emmen, V.A.M. Brabers, W.J.M. de Jonge, M. Nevriya and J. Sramek, J. Alloys Comp., 195 (1993) 15-18.
21. G.D. Gu, K. Takamuku, N. Koshizuka and S. Tanaka, J. Crystal Growth, 130 (1993) 325-329.
22. G. Balakrishnan, D. McK. Paul, M.R. Lees and A.T. Boothroyd, Physica C: Superconductivity, 206 (1993) 148-154.
23. J. Yu, Y. Yanagida, H. Takashima, Y. Inaguma, M. Itoh and T. Nakamura, Physica C: Superconductivity, 209 (1993) 442-448.
24. T.W. Li, P.H. Kes, N.T. Hien, J.J.M. Franse and A.A. Menovsky, J. Crystal Growth, 135 (1994) 481-486.
25. G.D. Gu, K. Takamuku, N. Koshizuka and S. Tanaka, J. Crystal Growth, 137 (1994) 472-478.
26. K. Oka, M.J.V. Menken, Z. Tarnawski, A.A. Menovsky, A.M. Moe, T.S. Han, H. Unoki, T. Ito and Y. Ohashi, J. Crystal Growth, 137 (1994) 479-486.
27. S. Sakata, W. Itoyama, I. Fujii and K. Iishi, J. Crystal Growth, 135 (1994) 555-560.
28. R. Subramanian, M. Higuchi and R. Dieckman, J. Crystal Growth, 143 (1994) 311-316.
29. K. Ando, M. Higuchi, J. Takahashi and K. Kodaira, Mater. Res. Bull., 29 (1994) 385-391.
30. Y. Furukawa, M. Fujiyoshi, F. Nitanda, M. Sato and S. Makio, J. Crystal Growth, 143 (1994) 243-248.

31. A.M. Lejus, A.K. Harari, J.M. Benitez and B. Viana, *Mater. Res. Bull.*, 29 (1994) 725-734.
32. H. Kojima, M. Watanabe and I. Tanaka, *J. Crystal Growth*, 155 (1995) 70-74.
33. Y. Huang, M.H. Huang, K.W. Yeh and M.Y. Hong, *Mater. Chem. Phys.*, 41 (1995) 290-294.
34. J. Wada, S. Wakimoto, S. Hosoya, K. Yamada and Y. Endoh, *Physica C*, 244 (1995) 193-197.
35. M. Higuchi, R.F. Geray, R. Dieckmann, D.G. Park, J.M. Burlitch, D.B. Barber and C.R. Pollock, *J. Crystal Growth*, 148 (1995) 140-147.
36. T.R. Zhao, M. Hasegawa and H. Takei, *J. Crystal Growth*, 154 (1995) 322-328.
37. W.J. Jang, K. Imai, M. Hasegawa and H. Takei, *J. Crystal Growth*, 152 (1995) 158-168.
38. A.V. Prokofiev, A.I. Shelykh, A.V. Golubkov and I.A. Smirnov, *J. Alloys Comp.*, 219 (1995) 172-175.
39. T.L. Tsai, S.A. Markgraf and R. Dieckmann, *J. Crystal Growth*, 169 (1996) 759-763.
40. T.L. Tsai, S.A. Markgraf, M. Higuchi and R. Dieckmann, *J. Crystal Growth*, 169 (1996) 764-772.
41. I. Tanaka, Y. Shibuya and H. Kojima, *J. Crystal Growth*, 169 (1996) 469-473.
42. H. Takeya, K. Kadowaki, K. Hirata and T. Hirano, *J. Alloys Comp.*, 245 (1996) 94-99.
43. K. Zhang, R. Mogilevsky, D.G. Hinks, J. Mitchell, A.J. Schultz, Y. Wang and V. Dravid, *J. Crystal Growth*, 169 (1996) 73-78.
44. A.M. Balbashov, S.G. Karabashev, Y.M. Mukovskiy and S.A. Zverkov, *J. Crystal Growth*, 167 (1996) 365-368.
45. A. Croll, M. Schweizer, A. Tegetmeier and K.W. Benz, *J. Crystal Growth*, 166 (1996) 239-244.
46. T.R. Zhao, M. Hasegawa and H. Takei, *J. Crystal Growth*, 166 (1996) 408-413.
47. S. Tsunekawa, H. Yamauchi, K. Sasaki, Y. Yamaguchi and T. Fukuda, *J. Alloys Comp.*, 245 (1996) 89-93.
48. J.L. Mass, J.M. Burlitch, S.A. Markgraf, M. Higuchi, R. Dieckmann, D.B. Barber and C.R. Pollock, *J. Crystal Growth*, 165 (1996) 250-257.
49. K. Hatta, M. Higuchi, J. Takahashi and K. Kodaira, *J. Crystal Growth*, 163 (1996) 279-284.
50. M.K.R. Khan, Y. Mori, I. Tanaka and H. Kojima, *Physica C*, 262 (1996) 202-206.
51. H. Takeya, K. Kadowaki, K. Hirata, T. Hirano and K. Togano, *J. Magn. Magn. Mater.*, 157-158 (1996) 611-612.
52. G.D. Gu, T. Egi, N. Koshizuka, P.A. Miles, G.J. Russell and S.J. Kennedy, *Physica C*, 263 (1996) 180-184.
53. Z. Hong, Y. Huaguang, Z. Yunzhi, Z. Jianfei, X. Hongchang, W. Xing and J. Yandao, *J. Crystal Growth*, 160 (1996) 136-140.
54. W. Itoyama, K. Iishi and S. Sakata, *J. Crystal Growth*, 158 (1996) 534-539.
55. A.M. Balbashev, D.A. Shulyatev, G.Kh. Panova, M.N. Khlopkin, N.A. Chernoplekov, A.A. Shikov and A.V. Suetin, *Physica C*, 256 (1996) 371-377.
56. S. Fu and H. Ozoe, *Materials Research Bulletin*, 31 (1996) 1341-1354.
57. H. Kojima, J. Yamamoto, Y. Mori, M.K.R. Khan, H. Tanabe and I. Tanaka, *Physica C*, 293 (1997) 14-19.
58. A.M. De L. Guevara, P. Berthet, J. Berthon, F. Millot and A. Revcolevschi, *J. Alloys Comp.*, 262-263 (1997) 163-168.
59. I. Chong, T. Terashima, Y. Bando, M. Takano, Y. Matsuda, T. Nagaoka and K.I. Kumagai, *Physica C*, 290 (1997) 57-62.
60. T.R. Zhao, M. Hasegawa and H. Takei, *J. Crystal Growth*, 181 (1997) 55-60.
61. T. Tanaka, S. Okada and Y. Ishizawa, *J. Solid State Chem.*, 133 (1997) 55-58.
62. K. Takahashi and S. Kunni, *J. Solid State Chemistry*, 133 (1997) 198-200.

63. W. Mei, M. Yoshizumi, T. Okane and T. Umeda, *J. Alloys Comp.*, 258 (1997) 34-38.
64. T. Mochiku, K. Hirata and K. Kadowaki, *Physica C*, 282-287 (1997) 475-476.
65. K. Oka, Z. Zou and T. Ito, *Physica C*, 282-287 (1997) 479-480.
66. G.D. Gu, G.J. Russell and N. Koshizuka, *Physica C*, 282-287 (1997) 865-866.
67. G. Dhalenne, J.C. Rouchaud, A. Revcolevschi and M. Fedoroff, *Physica C*, 282-287 (1997) 953-954.
68. K. Kuroda, I.H. Choi, H. Unoki and N. Koshizuka, *J. Crystal Growth*, 173 (1997) 73-80.
69. N.T. Hien, J.J.M. Franse, J.J.M. Poethuizen, T.W. Li and A.A. Menovsky, *J. Crystal Growth*, 171 (1997) 102-108.
70. T. Nagata, M. Uehara, J. Goto, N. Komiyama, J. Akimitsu, N. Motoyama, H. Eisaki, S. Uchida, H. Takahashi, T. Nakanishi and N. Mori, *Physica C*, 282-287 (1997) 153-156.
71. C. Kloc, S.W. Cheong and P. Matl, *J. Crystal Growth*, 191 (1998) 294-297.
72. K. Oka, Z. Zou and J. Ye, *Physica C*, 300 (1998) 200-206.
73. T. Katsumata, T. Nabae, K. Sasajima and T. Matsuzawa, *J. Crystal Growth*, 183 (1998) 361-365.
74. U. Ammerahl, G. Dhalenne, A. Revcolevschi, J. Berthon and H. Moudden, *J. Crystal Growth*, 193 (1998) 55-60.
75. N. Ohashi, K. Fujiwara, T. Tsurumi and O. Fukunaga, *J. Crystal Growth*, 186 (1998) 128-132.
76. J.S. Gardner, B.D. Gaulin and D.McK. Paul, *J. Crystal Growth*, 191 (1998) 740-745.
77. F. Iga, N. Shimizu and T. Takabatake, *J. Magn. Magn. Mater.*, 177-181 (1998) 337-338.
78. M. Higuchi, K. Kodaira and S. Nakayama, *J. Crystal Growth*, 207 (1999) 298-302.
79. D. Shulyatev, S. Karabashev, A. Arsenov and Y. Mukovskii, *J. Crystal Growth*, 198-199 (1999) 511-515.
80. C. Marin, T. Charvolin, D. Braithwaite and R. Calemczuk, *Physica C*, 320 (1999) 197-205.
81. A. Revcolevschi, U. Ammerahl and G. Dhalenne, *J. Crystal Growth*, 198-199 (1999) 593-599.
82. H. Kageyama, K. Onizuka, T. Yamauchi and Y. Ueda, *J. Crystal Growth*, 206 (1999) 65-67.
83. Y. Nishimura, Y. Matsuoka, S. Miyashita, H. Komatsu, M. Motokawa, T. Nakada and G. Sazaki, *J. Crystal Growth*, 207 (1999) 206-213.
84. A. Maljuk, S. Watauchi, I. Tanaka and H. Kojima, *J. Crystal Growth*, 212 (2000) 138-141.
85. H. Kimura, X. Jia, K. Shoji, R. Sakai and T. Katsumata, *J. Crystal Growth*, 212 (2000) 364-367.
86. C.T. Lin, B. Liang, M. Freiberg, K. Peters and E. Schonherr, *Physica C*, 341-348 (2000) 541-542.
87. M. Imai, T. Kimura, K. Sato and T. Hirano, *J. Alloys Comp.*, 306 (2000) 197-202.
88. K.A. Soubbotin, V.A. Smirnov, S.V. Kovaliov, H.J. Scheel and E.V. Zharikov, *Optical Mater.*, 13 (2000) 405-410.
89. T. Mori, K. Aoki, N. Kamegashira, T. Shishido and T. Fukuda, *Mater. Lett.*, 42 (2000) 387-389.
90. X.L. Yan, X. Wu, J.F. Zhou, Z.G. Zhang and J. Wang, *J. Crystal Growth*, 220 (2000) 543-547.
91. M. Velazquez, C. Haut, B. Hennion and A. Revcolevschi, *J. Crystal Growth*, 220 (2000) 480-487.
92. T. Shonai, M. Higuchi and K. Kodaira, *Mater. Res. Bull.*, 35 (2000) 225-232.
93. M. Higuchi, H. Katase, K. Kodaira and S. Nakayama, *J. Crystal Growth*, 218 (2000) 282-286.
94. H. Matsumura, M. Mamiya and H. Takei, *J. Crystal Growth*, 210 (2000) 783-787.

95. M. Higuchi, K. Hatta, J. Takahashi, K. Kodaira, H. Kaneda and J. Saito, *J. Crystal Growth*, 208 (2000) 501-507.
96. Z.Q. Mao, Y. Maeno and H. Fukazawa, *Mater. Res. Bull.*, 35 (2000) 1813-1824.
97. X.L. Yan, X. Wu, J.F. Zhou, Z.G. Zhang, X.M. Wang, P.M. Fu, Y.D. Jiang, J. Hu and J.L. Qiu, *J. Crystal Growth*, 212 (2000) 204-210.
98. W. Wang, X. Yan, X. Wu, Z. Zhang, B. Hu and J. Zhou, *J. Crystal Growth*, 219 (2000) 56-60.
99. T. Fujii, T. Watanabe and A. Matsuda, *J. Crystal Growth*, 223 (2001) 175-180.
100. B. Liang, A. Maljuk and C.T. Lin, *Physica C*, 361 (2001) 156-164.
101. A. Maljuk, B. Liang, C.T. Lin and G.A. Emelchenko, *Physica C*, 355 (2001) 140-146.
102. K. Oka, H. Yamaguchi and T. Ito, *J. Crystal Growth*, 229 (2001) 419-422.
103. T.A. Campbell, M. Schweizer, P. Dold, A. Croll and K.W. Benz, *J. Crystal Growth*, 226 (2001) 231-239
  
104. T. Shonai, M. Higuchi and K. Kodaira, *J. Crystal Growth*, 233 (2001) 477-482.
105. J. Takeuchi, S. Hirahara, T.P. Dhakal, K. Miyoshi and K. Fujiwara, *J. Magn. Magn. Mater.*, 226-230 (2001) 884-885.
106. Y. Nagata, S. Yashiro, T. Mitsuhashi, A. Koriyama, Y. Kawashima and H. Samata, *J. Magn. Magn. Mater.*, 237 (2001) 250-260.
107. Y. Arita, S. Mitsuda, Y. Nishi, T. Matsui and T. Nagasaki, *J. Nuclear Mater.*, 294 (2001) 202-205.
108. S. Takekawa, Y. Furukawa, N. Kaneko and K. Kitamura, *J. Crystal Growth*, 229 (2001) 212-216.
109. T. Tanaka and A. Sato, *J. Solid State Chem.*, 160 (2001) 394-400.
110. I.M. Sutjahja, A.A. Nugroho, M. Diantoro, M.O. Tjia, H. Gelders, A.A. Menovsky and J.J.M. Franse, *Physica C*, 363 (2001) 25-30.
111. B. Liang, C.T. Lin, P. Shang and G. Yang, *Physica C*, 383 (2002) 75-88.
112. B. Liang and C.T. Lin, *J. Crystal Growth*, 237-239 (2002) 756-761.
113. G. Behr, W. Loser, H. Bitterlich, G. Graw, D. Souptel and E.V. Sampathkumaran, *J. Crystal Growth*, 237-239 (2002) 1976-1980.
114. S. Watauchi, I. Tanaka, K. Hayashi, M. Hirano and H. Hosono, *J. Crystal Growth*, 237-239 (2002) 801-805.
115. X.L. Yan, J.F. Zhou, X.J. Niu, X.L. Chen, Q.Y. Tu and X. Wu, *J. Crystal Growth*, 242 (2002) 161-166.
116. D. Prabhakaran, A.I. Coldea, A.T. Boothroyd and S.J. Blundell, *J. Crystal Growth*, 237-239 (2002) 806-809.
117. D. Prabhakaran, P. Isla and A.T. Boothroyd, *J. Crystal Growth*, 237-239 (2002) 815-819.
118. T. Mori, N. Kamegashira, K. Aoki, T. Shishido and T. Fukuda, *Mater. Lett.*, 54 (2002) 238-243.
119. K. Ihara, K. Ito, K. Tanaka and M. Yamaguchi, *Mater. Sci. Eng.*, A329-331 (2002) 222-227.
120. T. Shonai, M. Higuchi, K. Kodaira, T. Ogawa, S. Wada and H. Machida, *J. Crystal Growth*, 241 (2002) 159-164.
121. D. Souptel, G. Behr, L. Ivanenko, H. Vinzelberg and J. Schumann, *J. Crystal Growth*, 244 (2002) 296-304.
122. D. Souptel, G. Behr and A.M. Balbashov, *J. Crystal Growth*, 236 (2002) 583-588.
123. S.I. Ikeda, U. Azuma, N. Shirakawa, Y. Nishihara and Y. Maeno, *J. Crystal Growth*, 237-239 (2002) 787-791.

124. J.K. Park, K.B. Shim, K.H. Auh and I. Tanaka, *J. Crystal Growth*, 237-239 (2002) 730-734.
125. H.A. Dabkowska, A. Dabkowski, G.M. Luke and B.D. Gaulin, *J. Crystal Growth*, 234 (2002) 411-414.
126. K. Isawa, M. Nagano and K. Yamada, *J. Crystal Growth*, 237-239 (2002) 783-786.
127. D. Prabhakaran, F.R. Wondre and A.T. Boothroyd, *J. Crystal Growth*, 250 (2003) 72-76.
128. N. Kamegashira, J. Meng, T. Mori, A. Murase, H. Satoh, T. Shishido and T. Fukuda, *Mater. Lett.*, 57 (2003) 1941-1944.
129. A. Maljuk, J. Stremper and C.T. Lin, *J. Crystal Growth*, 258 (2003) 435-440.
130. P. Reutler, O. Friedt, B. Buchner, M. Braden and A. Revcolevschi, *J. Crystal Growth*, 249 (2003) 222-229.
131. L.S. Jia, X.L. Yan, J.F. Zhou and X.L. Chen, *Physica C*, 385 (2003) 483-487.
132. K. Oka, H. Shibata, S. Kashiwaya and H. Eisaki, *Physica C*, 388-389 (2003) 389-390.
133. Y. Fujita, H. Sugisaki and H. Iwasaki, *Physica C*, 388-389 (2003) 393-394.
134. G. Balakrishnan, M.R. Lees and D.McK. Paul, *J. Crystal Growth*, 256 (2003) 206-209.
135. L.S. Jia, X.L. Yan and X.L. Chen, *J. Crystal Growth*, 254 (2003) 437-442.
136. A. Maljuk, J. Stremper, C. Ulrich, A. Lebon and C.T. Lin, *J. Crystal Growth*, 257 (2003) 427-431.
137. P.I. Nabokin, D. Souptel and A.M. Balbashov, *J. Crystal Growth*, 250 (2003) 397-404.
138. S. Zhang, X. Wu, X. Yan, D. Ni and Y. Song, *J. Crystal Growth*, 247 (2003) 428-431.
139. D. Prabhakaran and A.T. Boothroyd, *J. Crystal Growth*, 250 (2003) 77-82.
140. B. Liang and C.T. Lin, *J. Crystal Growth*, 267 (2004) 510-516.
141. K.W. Yeh, Y. Huang, J.Y. Gan and Y.S. Chang, *J. Crystal Growth*, 268 (2004) 108-117.
142. K.W. Yeh, J.Y. Gan and Y. Huang, *J. Crystal Growth*, 269 (2004) 505-511.
143. Z.H. Jia, A.K. Schaper, W. Treutmann, H. Rager and W. Massa, *J. Crystal Growth*, 273 (2004) 303-310.
144. D. Souptel, G. Behr, W. Loser, A. Teresiak, S. Drotziger and C. Pfeleiderer, *J. Crystal Growth*, 269 (2004) 606-616.
145. L.S. Jia, W. Yang, X.L. Chen and X.L. Yan, *Physica C: Superconductivity*, 400 (2004) 117-121.
146. K.W. Yeh, J.Y. Gan and Y. Huang, *Mater. Chem. Phys.*, 86 (2004) 382-389.
147. D. Prabhakaran, A.T. Boothroyd, R. Coldea and N.R. Charnley, *J. Crystal Growth*, 271 (2004) 74-80.
148. M. Higuchi, H. Sagae, K. Kodaira, T. Ogawa, S. Wada and H. Machida, *J. Crystal Growth*, 264 (2004) 284-289.
149. D. Souptel, A.L. Jasper, W. Loser, W. Schnelle, H. Borrmann and G. Behr, *J. Crystal Growth*, 273 (2004) 311-319.
150. G. Balakrishnan, M.R. Lees and D.McK. Paul, *J. Magn. Magn. Mater.*, 272-276 (2004) 601-602.
151. M. Higuchi, Y. Masubuchi, S. Nakayama, S. Kikkawa and K. Kodaira, *Solid State Ionics*, 174 (2004) 73-80.
152. M. Higuchi, C. Sato and K. Kodaira, *J. Crystal Growth*, 269 (2004) 342-346.
153. J.K. Park, K.H. Kim, I. Tanaka and K.B. Shim, *J. Crystal Growth*, 268 (2004) 103-107.

154. R.S. Perry and Y. Maeno, *J. Crystal Growth*, 271 (2004) 134-141.
155. A. Maljuk, J. Stremper, C. Ulrich, M. Sofin, L. Capogna, C.T. Lin and B. Keimer, *J. Crystal Growth*, 273 (2004) 207-212.
156. M. Higuchi, K. Kodaira, Y. Urata, S. Wada and H. Machida, *J. Crystal Growth*, 265 (2004) 487-493.
157. C. Sekar, G. Krabbes and A. Teresiak, *J. Crystal Growth*, 273 (2005) 403-411.
158. M. Miclau, D. Grebille and C. Martin, *J. Crystal Growth*, 285 (2005) 661-669.
159. S.M. Koohpayeh, D. Fort and J.S. Abell, *J. Crystal Growth* 282 (2005) 190-198.
160. A.M. Balbashov, L.N. Rybina, Y.K. Fetisov, V.F. Meshcheryakov and G. Srinivasan, *J. Crystal Growth* 275 (2005) 733-738.
161. I. Mazilu, M. Frontzek, W. Loser, G. Behr, A. Teresiak and L. Schultz, *J. Crystal Growth* 275 (2005) 103-107.
162. K. Oka, H. Unoki and A. Negishi, *J. Crystal Growth* 284 (2005) 440-445.
163. S. Hara, Y. Yoshida, S.I. Ikeda, N. Shirakawa, M.K. Crawford, K. Takase, Y. Takano and K. Sekizawa, *J. Crystal Growth* 283 (2005) 185-192.
164. D. Prabhakaran, A.T. Boothroyd, F.R. Wondre and T.J. Prior, *J. Crystal Growth* 275 (2005) 827-832.
165. D.P. Chen, A. Maljuk and C.T. Lin, *J. Crystal Growth* 284 (2005) 86-90.
166. T. Tanaka, A. Sato, S. Takenouchi, K. Kamiya and T. Numazawa, *J. Crystal Growth* 275 (2005) 1889-1893.
167. M. Higuchi, T. Shimizu, J. Takahashi, T. Ogawa, Y. Urata, T. Miura, S. Wada and H. Machida, *J. Crystal Growth* 283 (2005) 100-107.
168. D. Souptel, G. Behr, A. Kreyszig and W. Loser, *J. Crystal Growth* 276 (2005) 652-662.
169. F. Servant, J.P. Brison, A. Sulpice, C. Opagiste, V. Madigou and P. Lejay, *J. Crystal Growth* 275 (2005) 739-743.
170. R. Fittipaldi, A. Vecchione, S. Fusanobori, K. Takizawa, H. Yaguchi, J. Hooper, R.S. Perry and Y. Maeno, *J. Crystal Growth* 282 (2005) 152-159.
171. C. Sekar, G. Krabbes, A. Teresiak, M. Wolf, D. Eckert and K.H. Muller, *J. Crystal Growth* 275 (2005) 1961-1965.
172. G. Balakrishnan, S. Majumdar, M.R. Lees and D.McK. Paul, *J. Crystal Growth* 274 (2005) 294-296.
173. G. Behr, W. Loser, M.O. Apostu, W. Gruner, M. Hucker, L. Schramm, D. Souptel, A. Teresiak and J. Werner, *Cryst. Res. Technol.*, 40 (2005) 21-25.
174. K. Oka, H. Unoki, H. Shibata and H. Eisaki, *J. Crystal Growth* 286 (2006) 288-293.
175. P. Guptasarma, M.S. Williamsen, B.K. Sarma, A. Suslov, M.L. Schneider, S. Sendelbach, M. Onellion and G. Taft, *J. Phys. Chem. Solids*, 67 (2006) 525-528.
176. G.D. Gu, M. Hucker, Y.J. Kim, J.M. Tranquada, Q. Li and A.R. Moodenbaugh, *J. Crystal Growth* 287 (2006) 318-322.
177. G.D. Gu, M. Hucker, Y.J. Kim, J.M. Tranquada, H. Dabkowska, G.M. Luke, T. Timusk, B.D. Gaulin, Q. Li and A.R. Moodenbaugh, *J. Phys. Chem. Solids*, 67 (2006) 431-434.
178. M. Suzana, P. Francisco and V.R. Mastelaro, *Chem. Mater.* 14 (2002) 2514-2518.
179. Y. Li and T. Ishigaki, *J. Crystal Growth*, 242 (2002) 511-516.
180. U. Diebold, M. Li, O. Dulub, E.L.D. Hebenstreit and W. Hebenstreit, *Surface Rev. and Lett.*, 7 (2000) 613-617.
181. U. Diebold, *Surface Sci. Reports*, 48 (2003) 53-229.
182. M. Shirasaki and K. Asama, *Appl. Opt.*, 21 (1982) 4296.
183. K. Sugiyama, Y. Takeuchi and Z. Kristallogr, 305 (1991) 194.



184. F.A. Grant, *Rev. Mod. Phys.*, 31 (1959) 646.
185. G.V. Samsonov, *The Oxide Handbook*, IFI/Plenum Press, New York, 1982.
186. M. Li, W. Hebenstreit, U. Diebold, A. M. Tyryshkin, M. K. Bowman, G.G. Dunham and M. A. Henderson, *J. Phys. Chem.*, B104 (2000) 4944.
187. Y. Nakazumi, K. Suzuki and T. Yajima, *J. Phys. Soc. Jpn.* 17 (1962) 1806.
188. M. Higuchi, T. Hosokawa and S. Kimura, *J. Crystal Growth* 112 (1991) 354.
189. M. Higuchi and K. Kodaira, *J. Crystal Growth*, 123 (1992) 495.
190. M. Higuchi, J. Takahashi and K. Kodaira, *J. Crystal Growth* 125 (1992) 571.
191. K. Hatta, M. Higuchi, J. Takahashi and K. Kodaira, *J. Crystal Growth* 163 (1996) 279.
192. M. Higuchi, K. Hatta, J. Takahashi, K. Kodaira, H. Kaneda and J. Saito, *J. Crystal Growth* 208 (2000) 501.
193. J.K. Park, K.B. Shim, K.H. Auh and I. Tanaka, *J. Crystal Growth* 237-239 (2002) 730.
194. J.K. Park, K.H. Kim, I. Tanaka, K.B. Shim, *J. Crystal Growth* 268 (2004) 103.
195. M. Higuchi, C. Sato, K. Kodaira, *J. Crystal Growth* 269 (2004) 342.
196. D. Fort, *J. Crystal Growth*, 94 (1989) 85.
197. F. Millot, M.G. Blanchin, R. Tetot, J.F. Marucco, B. Poumellec, C. Picard and B. Touzelin, *Progress In Solid State Chem.* 17 (1987) 263.
198. S.A. Wolf, D.D. Awschalom, R.A. Buhrman, J.M. Daughton, S.V. Molnar, M.L. Roukes, A.Y. Chtchelkanova and D.M. Treger, *Science*, 294 (2001) 1488.
199. H. Ohno, *Science*, 281 (1998) 951.
200. T. Dietl, *Semicond. Sci. Technol.*, 17 (2002) 377.
201. Y. Matsumoto, M. Murakami, T. Shono, T. Hasegawa, T. Fukumura, M. Kawasaki, P. Ahmet, T. Chikyow, S.Y. Koshihara and H. Koinuma, *Science*, 291 (2001) 854.
202. Y. Matsumoto, R. Takahashi, M. Murakami, T. Koida, X.J. Fan, T. Hasegawa, T. Fukumura, M. Kawasaki, S.Y. Koshihara and H. Koinuma, *Jpn. J. Appl. Phys.*, 40 (2001) L1204.
203. L.F. Liu, J.F. Kang, Y. Wang, H. Tang, L.G. Kong, X. Zhang and R.Q. Han, *Solid state communications*, 139 (2006) 263.
204. K.A. Griffin, A.B. Pakhomov, C.M. Wang, S.M. Heald and K.M. Krishnan, *Phys. Rev. Lett.*, 94 (2005) 157204.
205. W.K. Park, R.J. Ortega-Hertogs, J.S. Moodera, A. Punnoose and M.S. Seehra, *J. Appl. Phys.*, 91 (2002) 8093.
206. J.Y. Kim, J.H. Park, B.G. Park, H.J. Noh, S.J. Oh, J.S. Yang, D.H. Kim, S.D. Bu, T.W. Noh, H.J. Lin, H.H. Hsieh and C.T. Chen, *Phys. Rev. Lett.*, 90 (2003) 017401.
207. S.R. Shinde, S.B. Ogale, S.D. Sarma, J.R. Simpson, H.D. Drew, S.E. Lofland, C. Lanci, J.P. Buban, N.D. Browning, V.N. Kulkarni, J. Higgins, R.P. Sharma, R.L. Greene and T. Venkatesan, *Phys. Rev.*, B 67 (2003) 115211.
208. G.C. Han, Y.H. Wu, M. Tay, Z.B. Guo, K.B. Li and C.T. Chong, *J. Magn. Magn. Mater.*, 272-276 (2004) e1537.
209. B.S. Jeong, Y.W. Heo, D.P. Norton, J.G. Kelly, R. Rairigh, A.F. Hebard, J.D. Budai and Y.D. Park, *Appl. Phys. Lett.*, 84 (2004) 2608.
210. P.A. Stampe, R.J. Kennedy, Y. Xin and J.S. Parker, *J. Appl. Phys.*, 92 (2002) 7114.
211. D.H. Kim, J.S. Yang, K.W. Lee, S.D. Bu, T.W. Noh, S.J. Oh, Y.W. Kim, J.S. Chung, H. Tanaka, H.Y. Lee and T. Kawai, *Appl. Phys. Lett.*, 81 (2002) 2421.
212. G.C. Han, P. Luo, Z.B. Guo, F.U. Nahar, M. Tay, Y.H. Wu and S.J. Wang, *Thin Solid Films*, 505 (2006) 137.

213. M. Murakami, Y. Matsumoto, M. Nagano, T. Hasegawa, M. Kawasaki and H. Koinuma, *Appl. Surface Sci.*, 223 (2004) 245.
214. S.A. Chambers, S. Thevuthasan, R.F.C. Farrow, R.F. Marks, J.U. Thiele, L. Folks, M.G. Samant, A.J. Kellock, N. Ruzycski, D.L. Ederer and U. Diebold, *Appl. Phys. Lett.*, 79 (2001) 3467.
215. H. Weng, X. Yang, J. Dong, H. Mizuseki, M. Kawasaki and Y. Kawazoe, *Phys. Rev. B*, 69 (2004) 125219.
216. R. Janisch, P. Gopal and N.A. Spaldin, *J. Phys. Condens. Matter*, 17 (2005) R657.
217. N. Popovici, E. Jimenez, R.C. da Silva, W.R. Branford, L.F. Cohen and O. Conde, *J. Non-crystalline solids*, 352 (2006) 1486.
218. L.F. Liu, J.F. Kang, Y. Wang, H. Tang, L.G. Kong, L. Sun, X. Zhang and R.Q. Han, *J. Magn. Magn. Mater.*, 308 (2007) 85.
219. N.H. Hong, J. Sakai, W. Prellier and A. Ruyter, *J. Appl. Phys.*, 38 (2005) 816.
220. M. Murakami, Y. Matsumoto, T. Hasegawa, P. Ahmet, K. Nakajima, T. Chikyow, H. Ofuchi, I. Nakai and H. Koinuma, *J. Appl. Phys.*, 95 (2004) 5330.
221. Y.H. Jeong, S.J. Han, J.H. Park and Y.H. Lee, *J. Magn. Magn. Mater.*, 272-276 (2004) 1976.
222. G.C. Han, Y.H. Wu, M. Tay, K.B. Li, Z.B. Guo and T.C. Chong, *J. Magn. Magn. Mater.*, 268 (2004) 159.
223. S.A. Chambers, C.M. Wang, S. Thevuthasan, T. Droubay, D.E. McCready, A.S. Lea, V. Shutthanandan and C.F. Windisch Jr, *Thin Solid Films*, 418 (2002) 197.
224. Y.G. Joh, H.D. Kim, B.Y. Kim, S.I. Woo, S.H. Moon, J.H. Cho, E.C. Kim and D.H. Kim, *J. the Korean Phys. Society*, 44 (2004) 360.
225. J.H. Cho, B.Y. Kim, H.D. Kim, S.I. Woo, S.H. Moon, J.P. Kim, C.R. Cho, Y.G. Joh, E.C. Kim and D.H. Kim, *Phys. Stat. Sol.*, 241 (2004) 1537.
226. G.S. Hui, W.X. Wei, K.X. Ming, Z.X. Yun, X. Li, Z.Y. Lu, Y.X. Lin and Z.Y. Xuan, *Chin. Phys. Lett.*, 22 (2005) 1772.
227. N. Akdogan, B.Z. Rameev, L. Dorosinsky, H. Sozeri, R.I. Khaibullin, B. Aktas, L.R. Tagirov, A. Westphalen and H. Zabel, *J. Phys. Condens. Matter*, 17 (2005) L359.
228. Y. Matsumoto, M. Murakami, T. Hasegawa, T. Fukumura, M. Kawasaki, P. Ahmet, K. Nakajima, T. Chikyow and H. Koinuma, *Appl. Surface Sci.*, 189 (2002) 344.
229. B. Brezny and A. Muan, *J. Inorganic and nuclear Chem.*, 31 (1969). 649.
230. R.M. Bozorth, H.J. Williams and D.E. Walsh, *Phys. Rev.* 103 (1956) 572-578.
231. R.M. Bozorth, V. Kramer and J.P. Remeika, *Phys. Rev. Lett.* 1 (1958) 3-4.
232. D. Treves, *Phys. Rev.*, 125 (1962) 1843-1850.
233. Y.B. Bazaliy, L.T. Tsymbal, G.N. Nakazei and P.E. Wigen, *J. Appl. Phys.* 95 (2004) 6622-6624.
234. A.H. Bobeck, *Bell Sys. Tech. J.*, 46 (1967) 1901-1925.
235. A.H. Bobeck, R.F. Fischer, A.J. Perneski, J.P. Remeika and L.G. Van Uitert, *IEEE Trans. Magn.*, Mag-5 (1969) 544-553.
236. R.A. Laudise, *J. Crystal Growth*, 13/14 (1972) 27-33.
237. Y. Kita, F. Inose and M. Kasai, *INTERMAG Conference*, Kyoto, Japan, paper 15.2 (1972) 367-369.
238. V.G. Bar'yakhtar, M.V. Chetkin, B.A. Ivanov, S.N. Gadetskii, *Springer Tracts on Modern Phys.*, Berlin, 129 (1994).
239. S.O. Demokritov, A.I. Kirilyuk, N.M. Kreines, V.I. Kudinov, V.B. Smirnov and M.V. Chetkin, *J. Magn. Magn. Mater.* 102 (1991) 339.
240. Y.S. Didosyan, *J. Magn. Magn. Mater.*, 133 (1994) 425.
241. Y.S. Didosyan, V.Y. Barash, N.A. Boverin, H. Hauser and P. Fulmek, *Sensors and Actuator A* 59 (1997) 56-60.

242. Y.S. Didosyan, H. Hauser, J. Nicolics, V.Y. Barash and P.L. Fulmek, *IEEE Tran. on Instrument and Measurement* 49 (2000) 14-18.
243. Y.S. Didosyan, H. Hauser, J. Nicolics and F. Haberl, *J. Appl. Phys.* 87 (2000) 7079-7081.
244. Y.S. Didosyan, H. Hauser and J. Nicolics, *Sensors and Actuators* 81 (2000) 263-267.
245. Y.S. Didosyan, H. Hauser and F. Haberl, *Sensors and Actuators A* 92 (2001) 67-73.
246. Y.S. Didosyan, H. Hauser, W. Fiala, J. Nicolics and W. Toriser, *J. Appl. Phys.* 91 (2002) 7000-7002.
247. Y.S. Didosyan, H. Hauser and G.A. Reider, *IEEE Trans. on Magn.* 38 (2002) 3243-3245.
248. Y.S. Didosyan, H. Hauser, H. Wolfmayr, J. Nicolics and P. Fulmek, *Sensors and Actuators A* 106 (2003) 168-171.
249. Y.S. Didosyan, H. Hauser, G.A. Reider and W. Toriser, *J. Appl. Phys.* 95 (2004) 7339-7341.
250. S.J. Kim, G.R. Demazeau, I.G. Presniakov and J.H. Choy, *J. Solid State Chem.*, 161 (2001) 197-204.
251. M. Eibschutz, *Acta Vryst.*, 19 (1965) 337-339.
252. A. Bombik, H. Böhm, J. Kusz, A.W. Pacyna and B.M. Wanklyn, *Solid State communications* 134 (2005) 227-281.
253. K. Niels, B. Marie-Claire and D. Yves, *Experimental report 2003, Universite de Versailles-St-Quentin, Versailles Cedex.*
254. M. Eibschutz, S. Shtrikman, and D. Treves, *Phys. Rev.*, 156 (1967) 562-577.
255. I. Mikami, M. Hirano and G. Kamoshita, *Jap. J. Appl. Phys.* 12 (1973) 557-561.
256. S.J. Schneider, R.S. Roth and J.L. Waring, *J. Res. of the Natl. Bur. Standards- A. Phys. and Chem.*, 65A (1961) 345-373.
257. H.J. Van Hook, *J. Am. Ceram. Soc.*, 44 (1961) 208-214.
258. J.W. Nielsen and S.L. Blank, *J. Crystal Growth*, 13/14 (1972) 702-705.
259. P. Wu and C. Li, *Computer Coupling of Phase Diagrams and Thermochemistry*, 27 (2003) 201-211.
260. J.P. Remeika, *J. Am. Chem. Soc.*, 78 (1956) 4259.
261. A.G. Titova, *Growth of crystals 3, Consultants Bureau*, (1962) 306-308.
262. K.P. Belov, A.M. Kadomtseva, T.L. Ovchinnikova. and V.A. Timofeeva, *Fiz. Metal. Metalloved*, 19 (1965) 778.
263. R.C. Sherwood, L.G. Vanuitert, R. Wolfe and R.C. Lecraw, *Phys. Lett.*, 25 (1967) 297.
264. J.P. Remeika and T.Y. Kometani, *Mat. Res. Bull.*, 3 (1968) 895-900.
265. J.P. Remeika, E.M. Gyorgy and D.L. Wood, *Mat. Res. Bull.* 4 (1969) 51-56.
266. B.M. Wanklyn, *J. Crystal Growth*, 5 (1969) 323-328.
267. E.A. Giess, D.C. Cronemeyer, L.L. Rosier and J.D. Kuptsis, *Mat. Res. Bull.* 5 (1970) 495-502.
268. H.H. Quon, A. Potvin and S.D. Entwistle, *Mat. Res. Bull.* 6 (1971) 1175-1184.
269. J.P.M. Damen and J.M. Robertson, *J. Crystal Growth*, 16 (1972) 50-53.
270. R. Akaba, *J. Crystal Growth*, 24/25 (1974) 537-540.
271. J.P.M. Damen, *J. Crystal Growth*, 33 (1976) 266-270.
272. Y. Arai and M. Satou, *J. Crystal Growth*, 36 (1976) 358-360.
273. S. N. Barilo, A. P. Ges, S. A. Guretskii, D. I. Zhigunov, A. A. Ignatenko, A. M. Luginets and E. F. Shapovalova, *J. Crystal Growth*, 108 (1991) 309-313.

274. S. N. Barilo, A. P. Ges, S. A. Guretskii, D. I. Zhigunov, A. A. Ignatenko, A. N. Igumentsev, I. D. Lomako and A. M. Luginets, *J. Crystal Growth*, 108 (1991) 314-318
275. J.W. Nielsen and S.L. Blank, *J. Crystal Growth*, 13/14 (1972) 702-705.
276. A.M. Balbashov, 7<sup>th</sup> international conference on ferrites, Bordeaux, France, (1996).
277. T. Okada, K. Matsumi and H. Makino, *Int. Conf. Ferrites*, Kyoto, paper 7A3.2 (1970).
278. R.J. Fairholme, G.P. Gill and A. Marsh, *Mat. Res. Bull.* 6 (1971) 1131-1140.
279. A. Marsh, R.J. Fairholme and G.P. Gill, *IEEE Transactions on Magnetics*, Sept. (1971).
280. H. Makino and Y. Hidaka, *INTERMAG conference*, Kyoto, Japan, paper 25.2 (1972).
281. A.A. Mukhin, A.E. Egoyan, A. Wittlin, M.E.J. Boonman, A.M. Balbashov and I.Yu. Parsegov, *Physica B* 211 (1995) 108-111.
282. J. Takahashi, E. Matsubara, T. Arima and E. Hanamura, *Phys. Rev. B* 68 (2003) 155102.
283. A.M. Balbashov and S.K. Egorov, *J. Crystal Growth*, 52 (1981) 498-504.
284. M. Bhat, B. Kaur, R. Kumar, P.A. Joy, S.D Kulkarni, K.K. Bamzai, P.N. Kortu and B.M. Wanklyn, *Nucl. Instr. and Meth. B*, 243 (2006) 134-142.
285. L. Zhang, M.L. Jenkins and G. Taylor, *J. Crystal Growth*, 289 (2006) 308-316.
286. A. Jezierski, *Phys. Stat. Sol. (c)* 3 (2006) 225-228.
287. G. Suran, R. Krishnan, P. Gerard and H. Jouve, *IEEE Transactions on Magnetics*, Mag-17, Nov. 1981.
288. K.T. Wu, Y. D. Yao, W. C. Chang and C. Y. Chu, *J. Magn. Magn. Mater.*, 140-144 (1995) 687-688.
289. K. Qunadjela, G. Suran, and F. Machizaud, *Phys. Rev. B*, 40 (1989) 578-586.
290. [http://www.aacg.bham.ac.uk/magnetic\\_materials/origin\\_of\\_magnetism.htm](http://www.aacg.bham.ac.uk/magnetic_materials/origin_of_magnetism.htm)